

ABSTRACT

Title of Dissertation: **ON THE DYNAMICS OF BINARY ASTEROIDS
APPLIED TO DART MISSION TARGET
(65803) DIDYMOS**

Harrison F. Agrusa
Doctor of Philosophy, 2022

Dissertation Directed by: **Professor Derek C. Richardson**
Department of Astronomy

NASA's Double Asteroid Redirection Test (DART) mission will be the first full-scale demonstration of a kinetic impactor for planetary defense. On September 26, 2022, the DART spacecraft is expected to impact Dimorphos, the secondary component of the Didymos binary asteroid system. The DART impact will reduce Dimorphos's relative orbital velocity, shrinking both its semimajor axis and orbit period. The mutual orbit period will then be measured using ground- and space-based observations in order to deduce the momentum transfer efficiency, which is an important parameter in planetary defense that has never been measured experimentally at a realistic scale.

This thesis comprises a set of studies on the spin and orbital dynamics of the Didymos system conducted in support of the DART mission. Owing to the close proximity of Didymos and Dimorphos and their irregular shapes, the mutual dynamics are non-Keplerian and exhibit a high degree of spin-orbit coupling, which often requires the use of specialized numerical methods to

model the system. First, we conducted a benchmarking and sensitivity study to identify the best simulation codes for future DART-supported studies and to understand how small perturbations in the initial conditions can affect the resulting dynamical evolution of the system. Then, we demonstrated that Dimorphos can enter a wide range of post-impact spin states, including possible chaotic non-principal axis rotation, depending on its shape and the amount of momentum transferred by the DART impact. We then explored the implications of an excited spin state, including the possibility of ongoing granular motion on Dimorphos's surface resulting from the orbital perturbation induced by the DART impact.

This thesis is focused predominantly on the dynamics of the Didymos binary. However, there are many other binary systems among the near-Earth asteroid population with similar physical and dynamical properties, making the results presented here relevant to the NEA binary population in general.

On the Dynamics of Binary Asteroids Applied to DART Mission Target (65803)
Didymos

by

Harrison F. Agrusa

Dissertation submitted to the Faculty of the Graduate School of the
University of Maryland, College Park in partial fulfillment
of the requirements for the degree of
Doctor of Philosophy
2022

Advisory Committee:

Professor Derek C. Richardson, Chair/Advisor
Professor Douglas Hamilton
Professor Massimo Ricotti
Professor Christine Hartzell
Dr. Ronald Ballouz

© Copyright by
Harrison F. Agrusa
2022

Preface

The research presented in Chapters 2–5 has been previously published. Chapter 2 was published in *Icarus* as “A benchmarking and sensitivity study of the full two-body gravitational dynamics of the DART mission target, binary asteroid 65803 Didymos” (Agrusa et al., 2020). Chapter 3 was published in *Icarus* as “The excited spin state of Dimorphos resulting from the DART impact” (Agrusa et al., 2021). Chapter 4 was published in *The Planetary Science Journal* as “Dynamical evolution of the Didymos-Dimorphos binary asteroid as rubble piles following the DART impact” (Agrusa et al., 2022a). Finally, Chapter 5 was published as a letter to the Editor in *Astronomy & Astrophysics* as “Rotation-induced granular motion on the secondary component of binary asteroids: application to the DART impact on Dimorphos” (Agrusa et al., 2022b). Each chapter is presented here with minor modifications from their previously published versions.

Acknowledgments

First, I would like to thank Derek for being such an incredible advisor. He provided all the support I needed, worked hard to find funding, promoted my work, and never hesitated to introduce me to others at meetings and conferences. While at the same time, he gave me all the freedom I needed to pursue my own ideas and develop my own interests.

I'd like to also thank my groupmates Joe, Julian, and Carrie for the great discussions and your help with all the troubleshooting with PKDGRAV. To my fellow classmates Ramsey, Milena, Tomás, Julian, Guangwei, Charlotte, Sergio, thanks for making grad school so fun!

Without the contributions and support from my collaborators, much of the work presented in this thesis would not be possible. To Patrick Michel, Menios Tsiganis, Alex Davis, Alex Meyer, Yun Zhang, Ioannis Gkolias, Fabio Ferrari, Gene Fahnestock, Brent Barbee, Toshi Hirabayashi, Ryota Nakano, Guillaume Noiset, and Elisa Tasev, thanks for all your help!! Thanks to the DART Investigation Team leadership, Nancy Chabot, Andy Rivkin, and Andy Cheng for valuing and supporting my work on DART. It has been (and will continue to be) so exciting to be a part of this amazing mission.

Thanks to Rob Managan, Kirsten Howley, and Megan Bruck Syal at Lawrence Livermore National Laboratory for providing me with an incredible undergraduate research experience. It was here where I first developed an interest in planetary defense and decided to come to the University of Maryland to work on DART.

Thank you to the Agrusa, Thatcher, Novello, and Jones families for their support. I am so lucky to have all of you in my life. To Nate, Joe, Mitch, Keeton, Chris, Riley, Jack, Ian, Ricky, Taz, Kret, AC, all I have to say is... Go Bears!

Finally, I'd like to thank my partner Stephanie. None of this would have been possible without your unwavering love and support.

Table of Contents

Preface	ii
Acknowledgements	iii
Table of Contents	v
List of Tables	viii
List of Figures	ix
List of Abbreviations	xi
Chapter 1: Introduction	1
1.1 Binary Asteroids	2
1.1.1 Overview	2
1.1.2 Binary Asteroid Formation and Evolution	4
1.1.3 Binary Asteroid Dynamics	9
1.2 The Asteroid Impact Hazard	12
1.2.1 Overview	12
1.2.2 The DART and Hera Missions	14
1.2.3 The Didymos Binary Asteroid	18
1.3 This Dissertation	21
Chapter 2: Benchmarking and sensitivity study of the Didymos system	24
2.1 Chapter Preface	24
2.2 Introduction	25
2.2.1 The Didymos System	26
2.3 Methodology	27
2.3.1 The Simulation Codes	27
2.3.2 Initial Conditions	31
2.4 Results	35
2.4.1 Code Performance	35
2.4.2 The Nominal Case	36
2.4.3 Primary Rotation Phase	40
2.4.4 Dimorphos Libration	43
2.5 Conclusions	49

Chapter 3: Predicting Dimorphos’s post-impact spin state	52
3.1 Chapter Preface	52
3.2 Introduction	53
3.2.1 Background	56
3.3 Methods	60
3.3.1 Analytic Dynamics Model	61
3.3.2 Simplified 3D Dynamics Model	67
3.3.3 The GUBAS Full Two-body Problem code	68
3.3.4 Problem Set Up	68
3.4 Results	71
3.4.1 Analytic Model Results	71
3.4.2 Simplified 3D Dynamics Results	75
3.4.3 GUBAS Results	78
3.5 Discussion	83
3.5.1 Implications of a post-impact tumbling state	83
3.5.2 The Barrel Instability	86
3.6 Conclusions	92
Chapter 4: Rubble-pile modeling of the Didymos system	94
4.1 Chapter Preface	94
4.2 Introduction	95
4.3 Methodology	98
4.3.1 GUBAS	98
4.3.2 PKDGRAV	99
4.3.3 GRAINS	100
4.3.4 Problem Setup	101
4.4 Spin and Orbital Dynamics as Rubble Piles	103
4.4.1 Long-term dynamics with a point-mass Didymos	104
4.4.2 Short-term dynamics with Full Rubble Piles	117
4.5 Limits of the Rigid-body Approach	123
4.5.1 Limits on strong tidal effects	124
4.5.2 Long-term evolution of Dimorphos as an Irregularly Shaped Body	130
4.6 Conclusions and Future Work	141
Chapter 5: Rotation-induced granular motion on the Dimorphos	144
5.1 Chapter Preface	144
5.2 Introduction	145
5.3 Methods	146
5.3.1 Simulation setup	147
5.3.2 Computation of external accelerations	149
5.4 Results	150
5.4.1 A conceptual example	150
5.4.2 Dependence on momentum enhancement (β)	152
5.4.3 Dependence on the bulk density (ρ_S)	155
5.5 Discussion	157

5.6	Conclusions	160
Chapter 6: Conclusions & Future Work		161
6.1	Conclusions	161
6.2	Future Work	164
Chapter A: Appendices for Chapter 3		166
A.1	The simplified 3D model	166
A.1.1	The planar J_2 + ellipsoid model	166
A.1.2	The 3-dimensional rotation of the secondary	168
A.1.3	Uncoupled natural frequencies	171
A.2	Initial conditions optimization scheme	172
Appendix B: Appendices for Chapter 5		178
B.1	Calculation of surface accelerations and slopes	178
B.1.1	Gravitational accelerations	178
B.1.2	Rotational accelerations	180
B.2	Longer-term spin-orbit and surface slope evolution for the test case	180
B.3	Additional surface slope plots	181
Appendix C: Facilities and Software used in this Thesis		188
Bibliography		189

List of Tables

1.1	Latest Didymos system parameters	21
2.1	Didymos system parameters used in Ch. 2	28
2.2	Description of PKDGRAV particles used in benchmarking simulations	30
2.3	Initial conditions for the nominal case	33
2.4	Description of simulation cases	34
2.5	Comparison of simulation code run times	35
2.6	Simulated orbit period, semimajor axis, and eccentricity of the nominal case	36
3.1	Didymos system parameters used in Ch. 3	71
3.2	The four dominant instability-triggering resonances	77
4.1	Didymos system parameters used in Ch. 4	99
4.2	Ellipsoidal Dimorphos body shapes under consideration	106
4.3	Tidal encounter simulation results	130
4.4	Irregularly-shaped rubble piles under consideration	132
5.1	Didymos system parameters used in Ch. 5	147

List of Figures

1.1	Discovery image of the Ida-Dactyl binary asteroid	3
1.2	Radar shape models of 66391 Moshup (formerly 1999 KW ₄)	7
1.3	Images of Comet P/Shoemaker-Levy 9 and the Tunguska impact site	13
1.4	The DART Spacecraft	15
1.5	DART Impact Geometry	16
1.6	Didymos shape model	20
2.1	Shape representations of Didymos for benchmarking study	32
2.2	Schematic showing perturbations to initial conditions	34
2.3	Short-term orbital element comparison	38
2.4	Long-term orbital element comparison	39
2.5	Sensitivity of orbital phase to initial conditions	41
2.6	Orbital phase vs. initial primary rotation phase	42
2.7	Libration modes of nominal case	46
2.8	Sensitivity of libration to along-track perturbation	48
2.9	Sensitivity of libration to nonplanar perturbation	50
3.1	Diagram of Didymos system and approximate DART impact geometry	54
3.2	Attitude of Dimorphos described by the 1-2-3 Euler angle set	59
3.3	Fundamental frequencies of analytic model	73
3.4	Resonance among four fundamental frequencies	74
3.5	Fast Lyapunov indicator map	77
3.6	Libration amplitude map for planar model	78
3.7	Libration amplitude map of GUBAS simulations	79
3.8	Euler angle time-series: stable vs. unstable cases	80
3.9	Maximum Euler angle maps	82
3.10	Euler angle time-series: sensitivity to secondary shape	84
4.1	Attitude stability map for a rigid Dimorphos	105
4.2	Ellipsoidal Dimorphos rubble pile renderings	106
4.3	Euler angle time-series for $a/b = 1.2, b/c = 1.1$ in relaxed state	110
4.4	Euler angle time-series for $a/b = 1.2, b/c = 1.1, \beta = 3$	112
4.5	Euler angle time-series for $a/b = 1.2, b/c = 1.3, \beta = 3$	113
4.6	Euler angle time-series for $a/b = 1.3, b/c = 1.2, \beta = 3$	115
4.7	Euler angle time-series for $a/b = 1.4, b/c = 1.3, \beta = 3$	116
4.8	Full-rubble-pile shape representations of Didymos and Dimorphos	118
4.9	Full-rubble-pile spin and orbital evolution	119

4.10	Full-rubble-pile orbital evolution comparison with rigid body result	121
4.11	Euler angle evolution and comparison with rigid body result	122
4.12	Tidal disruption limit for a rubble-pile Dimorphos	126
4.13	Tidal encounter simulation results	128
4.14	Irregularly-shaped rubble piles under consideration	131
4.15	Spin and orbital evolution for Apophis-shaped Dimorphos	134
4.16	Spin and orbital evolution for Squannit-shaped Dimorphos	135
4.17	Maximum axis length change vs. β	137
4.18	Cumulative particle motion on scaled-Apophis	138
4.19	Cumulative particle motion on scaled-Squannit	139
5.1	Surface slope evolution example	151
5.2	Surface slope time-series	153
5.3	Maximum surface slope maps	154
5.4	Maximum surface slope vs. ρ_S and β	156
A.1	The simplified configuration of the planar J_2 -ellipsoid model.	167
A.2	Convergence of the initial conditions optimization scheme	176
A.3	Derived bulk density and libration amplitude after optimization	177
B.1	Longer term time-series plot from Fig. 5.1	182
B.2	Spin, orbit, and surface slope evolution for $\beta = 1$	183
B.3	Spin, orbit, and surface slope evolution for $\beta = 2$	184
B.4	Spin, orbit, and surface slope evolution for $\beta = 3$	185
B.5	Spin, orbit, and surface slope evolution for $\beta = 4$	186
B.6	Spin, orbit, and surface slope evolution for $\beta = 5$	187

List of Abbreviations

AIDA	The Asteroid Impact and Deflection Assessment
ASI	Agenzia Spaziale Italiana (Italian Space Agency)
BYORP	Binary YORP effect
DART	Double Asteroid Redirection Test
DEEVE	Dynamically Equivalent Equal-Volume Ellipsoid
DRA	Design Reference Asteroid
DRM	Design Reference Mission
ESA	European Space Agency
JPL	Jet Propulsion Laboratory
F2BP	Full Two-Body Problem
FLI	Fast Lyapunov Indicator
GUBAS	General Use Binary Asteroid Simulator
GRAINS	Gravitation of Rubble-pile Asteroids with Internal N-body Structure
LICIACube	Light Italian CubeSat for Imaging of Asteroids
LOC	Line of centers
MBA	Main-belt asteroid
NASA	National Aeronautics and Space Administration
NEA	Near-Earth Asteroid
NEO	Near-Earth Object
NPA	Non-principal axis
PHA	Potentially Hazardous Asteroid
PKDGRAV	Parallel K-D tree GRAVity code
SSDEM	Soft-Sphere Discrete Element Method
UCB	University of Colorado Boulder
UMd	University of Maryland
YORP	Yarkovsky-O'Keefe-Radzievskii-Paddack effect

Chapter 1: Introduction

Asteroids are fascinating small worlds, thought to be leftover planetesimals, the building blocks of our solar system that formed the planets. They undergo a range of interesting dynamical and physical processes that can be used to understand the origin and formation both the asteroids themselves and our solar system. Life on our planet is deeply intertwined with the asteroids; it is thought that asteroid impacts on the early Earth delivered the necessary ingredients for life including water (Albarède, 2009; Daly and Schultz, 2018; Sarafian et al., 2014), while at the same time asteroid impacts present a small, but nonzero threat to humanity today (Farnocchia et al., 2015; Harris et al., 2015). Most asteroids are found within the asteroid belt between the orbits of Mars and Jupiter. This thesis, however, focuses on a particular subset classified as *near-Earth asteroids* (NEAs) which encompasses all asteroids whose orbits come within 1.3 au of the Sun. Among the population of NEAs, this thesis focuses even more narrowly on binaries, in which the system consists of two asteroids orbiting one another.

1.1 Binary Asteroids

1.1.1 Overview

Speculation about the existence of binary asteroids first came from indirect evidence, including irregular lightcurve features and anomalous events during occultation events (van Flandern et al., 1979). Although none of these suspected binaries turned out to be real, they ignited a serious interest in the planetary astronomy community. Several extensive observing campaigns of main-belt asteroids (MBAs) during the 1980's failed to find any satellites, leading to doubts about their existence (Gehrels et al., 1987; Gradie and Flynn, 1988). Things changed dramatically in 1993 when the *Galileo* spacecraft, en route to the Jupiter system, flew past (243) Ida where it fortuitously imaged a smaller companion, Dactyl, shown in Fig. 1.1 (Belton et al., 1995; Chapman et al., 1995). The discovery of the Ida-Dactyl system in the main belt revolutionized asteroid science, kicking off a wave of observational campaigns in search of other binary systems. Before *Galileo*, the existence of binary asteroids remained an open question, as demonstrated by the *Asteroids II* chapter titled “Do Asteroids Have Satellites?” (Weidenschilling et al., 1989). When this question was answered by *Galileo*, the follow-up chapter in *Asteroids III* needed only minor changes to its title: “Asteroids *Do* Have Satellites” (Merline et al., 2002). No longer restricted to a theoretical curiosity, discoveries of binary systems skyrocketed and so did our understanding of their formation and evolution.

The first indications for additional binary systems came from lightcurves of NEAs containing multiple frequencies that were attributed to the presence of a second orbiting body (Pravec and Hahn, 1997; Pravec et al., 1998). In 1998, the first definitive ground-based detection of an



Figure 1.1: An image taken by the *Galileo* spacecraft of asteroid Ida and its satellite Dactyl. Image Credit: NASA/JPL/Processed by Kevin M. Gill.

asteroid satellite was (45) Eugenia's smaller companion Petit Prince, which was discovered via direct imaging (Merline et al., 1999). Soon afterwards, the first radar detections of NEA binaries were made (Nolan et al., 2000; Ostro et al., 2000). The rate of discoveries surged in the early 2000s, and binary asteroids were discovered throughout the solar system, including among the near-Earth, Mars-crossing, main-belt, and Jupiter Trojan population. At this time, the first discoveries of binary Trans-Neptunian objects (TNOs) were also announced (Veillet et al., 2002). Today, we know of hundreds of binary systems throughout the solar system in addition to several known triple systems. Just recently, a third satellite of (130) Elektra was discovered, making it the first known quadruple asteroid (Berdeu et al., 2022). The physical and dynamical properties of these multiple systems can be used to constrain their formation. By understanding the formation of binaries, we can also learn about the environments from which they formed.

1.1.2 Binary Asteroid Formation and Evolution

Here, we provide a summary for how small NEA binaries (primary diameter $\lesssim 20$ km) are thought to form. Formation mechanisms depend on both the size and heliocentric orbit of an asteroid, so we point the reader to the broader review chapter on binary asteroid formation by Walsh and Jacobson (2015) for a discussion on formation for other asteroid populations.

Approximately $\sim 10\text{--}15\%$ of Earth’s impact craters are doublets with both components having the same age, suggesting that binaries ought to make up roughly this fraction of the NEA asteroid population (Melosh and Stansberry, 1991). Similar fractions of doublet craters can also be found at Venus and Mars (Cook et al., 2003; Vavilov et al., 2022). Sure enough, both light curve and radar observations find that roughly $\sim 15\%$ of NEAs are binaries (Margot et al., 2002; Pravec et al., 1999). Additionally, Pravec and Harris (2000) found that roughly $\sim 50\%$ of NEAs with spin periods less than ~ 3.5 h were part of binary systems. If these binaries are forming after injection into near-Earth space, then these population statistics indicate that NEA binary formation is a highly efficient process, given that the typical dynamical lifetimes of NEAs are only ~ 10 Myr (Gladman et al., 2000).

Most binary NEAs have similar physical and dynamical properties. The primaries are always less than ~ 10 km in diameter and typically have a fast rotation period, somewhere between ~ 2.2 and 4.5 h. The secondary component is usually elongated, in synchronous rotation (i.e., tidally locked), and on a tight orbit with a separation of only $1.5\text{--}3$ primary diameters. These systems often have a mass ratio $M_B/M_A \leq 0.2$, where M_A and M_B are the respective masses of the primary and secondary (Pravec et al., 2016; Walsh and Jacobson, 2015). Interestingly, their total angular momentum (rotational plus orbital angular momentum) is close to, but not

exceeding, the critical spin limit if all the system's mass were contained in a single body with the same bulk density, a strong indication that these binaries formed by somehow exceeding their spin limit (Pravec and Harris, 2007). For a spherical body, this spin limit can be approximated by the threshold at which the centrifugal acceleration exceeds the self-gravitational acceleration for a test particle at the equator,

$$\omega_c = \sqrt{4\pi\rho G/3}, \quad (1.1)$$

where ρ is the body's bulk density and G is the gravitational constant.

Initially, tidal encounters with the terrestrial planets were a popular theory to explain the NEA binary population. Bottke and Melosh (1996a,b) found that planetary flybys of fast-rotating rubble-pile asteroids (approximated as a contact binary) could produce a binary in $\sim 15\%$ of encounters. With more sophisticated numerical methods, Richardson et al. (1998) found that tidal encounters were capable of producing binaries, although at a much lower frequency. In a follow-up study, Walsh and Richardson (2006) found that tidal disruption-produced binaries struggled to match the observed distributions of primary shapes, rotation periods, as well as binary semimajor axis and eccentricities. Furthermore, a Monte Carlo method found that tidal encounters could only produce a binary fraction of $\sim 1-2\%$, indicating that another formation mechanism must be dominating binary production (Walsh and Richardson, 2008). The discovery of a small binary asteroid in the main belt (where there are no planetary encounters, of course) confirmed that tidal encounters could not sufficiently explain the binary fraction among NEAs (Warner and Harris, 2007).

A more promising theory for NEA binary formation is spin-up driven by the Yarkovsky-

O’Keefe-Radzievskii-Paddack (YORP) effect. First coined by Rubincam (2000), the YORP effect is simply a result of photons carrying momentum. As an asteroid receives sunlight, some light is immediately scattered, and some is absorbed and then re-emitted in the infrared. Due to the asteroid’s irregular shape and rotation, both of these effects impart a slight torque on the asteroid. Although this torque is small, it can substantially change the spin rates of small NEAs within their dynamical lifetimes. The YORP timescale increases with asteroid radius as $\tau_{\text{YORP}} \propto R^2$ and with heliocentric distance as $\tau_{\text{YORP}} \propto a^2$, making it an effective spin-up mechanism for small NEAs and relatively unimportant in the main belt and for larger bodies (Bottke et al., 2006; Vokrouhlický et al., 2015). YORP-attributed spin-rate changes have been detected with ground-based observations (Lowry et al., 2007; Taylor et al., 2007) and in situ at Bennu with the OSIRIS-REx spacecraft (Hergenrother et al., 2019).

YORP-driven spin-up as a binary formation mechanism was first proposed in the *Asteroids III* review chapter by Bottke et al. (2002). When a detailed shape model of binary asteroid 1999 KW₄ (now named 66391 Moshup and illustrated in Figure 1.2) was made using radar during a close encounter with Earth, it was discovered that the primary had an oblate shape with a pronounced equatorial ridge (Ostro et al., 2006). It was suggested that a rotational fission event could have created the binary system, and any excess in-falling material could have formed the primary’s equatorial ridge (Scheeres et al., 2006).

This led to two schools of thought for how a binary system would form to produce a fast-rotating primary with an equatorial ridge along with a nearby secondary in synchronous rotation. The first can be referred to as “rotational fission” in which a body exceeds its spin limit leading to a single catastrophic fission event where the body splits into a binary (Scheeres, 2007). Jacobson and Scheeres (2011a) found that a single ejected fragment (i.e., the secondary) would have a

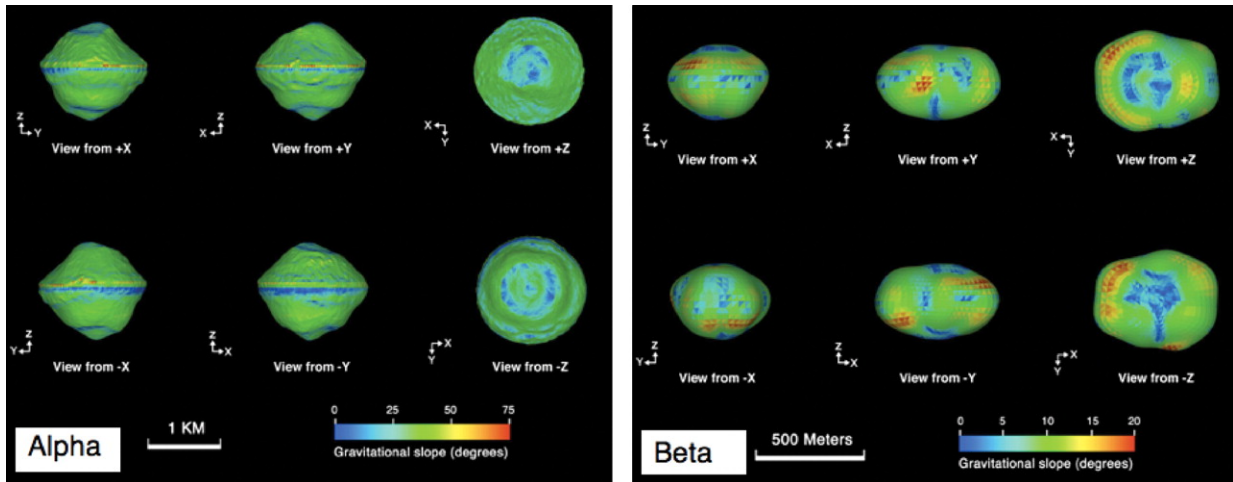


Figure 1.2: The radar-derived shape model for the primary (Alpha) and secondary (Beta) components of 66391 Moshup (formerly known as 1999 KW₄). Image Credit: Ostro et al. (2006).

positive free energy, meaning that the system was technically unbound and could not remain long-term stable. If, however, the secondary were able to undergo subsequent fissions, forming temporary triples, then this free energy could be released, allowing the secondary to finally enter a synchronous (and stable) rotation state. The third body is usually not long lived, and either gets ejected or re-impacts the primary or the secondary. They proposed that an equatorial ridge would form in cases when a fissioned body impacts the primary. In an additional study, Jacobson et al. (2016) found that this idea can sufficiently reproduce the observed population fractions of binaries as well as other subgroups (triples, pairs, etc.).

The second idea, referred to here as “mass shedding”, is where the secondary is built in orbit through gravitational accumulation of material shed from the primary (Walsh et al., 2008, 2012). In this model, the secondary is gradually built over several YORP cycles, in which a small amount of mass is shed during each event. By modeling the primary as an aggregate of thousands of constituent particles, this theory is able to produce the equatorial ridge through reshaping as it spins up and slowly loses mass.

Both models suffer some challenges when looking into the details. For example, the Jacobson and Scheeres (2011a) model is a two-dimensional dynamical model and recent work has indicated that non-planar motion may play an important roll in the spin and dynamical evolution of a secondary (Agrusa et al., 2021; Čuk et al., 2021; Quillen et al., 2022a). Davis and Scheeres (2020b) revisited the rotational fission hypothesis with a higher-fidelity, three-dimensional numerical code and found that much of the evolutionary pathways are preserved, with the relative likelihoods of secondary ejection, secondary fissions, and primary re-impacts changed slightly. In addition, extending the dynamics to three dimensions increases the timescales for these processes to occur. In both Jacobson and Scheeres (2011a) and Davis and Scheeres (2020b), the initial conditions (i.e., mass ratio, secondary shape, etc.) are user-selected and randomly generated, rather than self-consistently formed in the simulation. Given that these bodies are assumed to be rubble piles, the gravitational and contact interactions among constituent mass elements may play an important role in determining their post-fission masses, shapes, and other physical and dynamical properties. In addition, the formation of the primary’s equatorial ridge is assumed to occur, rather than explicitly modeled, anytime fissioned material re-impacts the primary. Aside from these challenges, the theory does a good job at explaining the observed population of binaries and subset populations, such as doubly synchronous systems and contact binaries.

On the other hand, the mass-shedding hypothesis arguably does a better job at self-consistently producing the equatorial ridge of the primary due to its discrete model of the gravity and contact interactions between constituent mass elements. In this way, it also “naturally” forms a secondary by allowing it to form in orbit through gravitational re-accumulation. However, the model suffers a couple drawbacks. The first is that a long-lived mass-shedding process may be inhibited by so-called “stochastic YORP”, in which both the direction and magnitude of the YORP torque are

highly sensitive to the body shape (Cotto-Figueroa et al., 2015; Statler, 2009). This means that the YORP effect may be self-limiting, as a body can spin-down just as easily as it spins-up. If the YORP torque changes each time the primary sheds some material, then it may be impossible to ever shed enough material into orbit within the asteroid’s dynamical lifetime. In any case, most evidence suggests that these binaries form predominantly through YORP spin up, although the precise details regarding their formation are still an open question.

1.1.3 Binary Asteroid Dynamics

Binaries are an extremely useful tool for studying the physical properties of asteroids. For example, the mass of the system can be obtained through Kepler’s Third Law,

$$M = \frac{4\pi^2 a^3}{GP^2}, \quad (1.2)$$

where a is the binary semimajor axis, P is the orbit period, and G is the gravitational constant. For most binaries, the mass of the primary dominates the system mass, so this usually results in a strong constraint on the primary’s mass and a relatively weak constraint on the secondary’s mass. Given estimates of the sizes (and therefore the volumes) of the binary components, a mass estimate can also be used to get a density estimate. In addition, the composition of the asteroid can be estimated with spectroscopic measurements, which can be combined with the bulk density to infer physical properties like the porosity.

Most asteroids are non-spherical, owing to their small sizes and weak self-gravity. In addition, most binaries, especially among the NEA population, are on tight orbits meaning that the two components are only separated by several primary radii. As a result, the mutual dynamics are

highly coupled and non-Keplerian. In other words, their dynamics cannot necessarily be modeled with a point-mass approximation, as the rotational motion of both bodies affects their orbital motion, and visa versa. In most cases, Kepler’s Third Law is only off by $\sim 1\%$, meaning that this does not strongly affect estimates for the system’s mass and bulk density. However, accounting for the irregular shapes of both components is important for modeling their dynamical evolution.

Generally, accounting for irregular body shapes and spin-orbit coupling requires some level of approximation and specialized numerical methods are often required. There is a wide range of analytic and numeric approaches to solving what is often called the Full Two-Body Problem (F2BP), which is briefly summarized here.

A sphere-ellipsoid model is often employed to simplify the F2BP, which treats the primary and secondary as a rigid, uniform-density sphere and ellipsoid, respectively (e.g. Scheeres, [1994](#), [2007](#)). This approximation often does a good job at capturing general dynamical properties, such as the attitude stability of the secondary, as a function of parameters like its shape and orbital eccentricity. In addition, the gravitational potential due to spheres and ellipsoids have exact analytical formulations, meaning that simulations can be extremely fast. However, as our knowledge of asteroid shapes has improved, some higher-order effects due to their irregular shapes can not be completely captured by an idealized ellipsoid approximation. Given a polyhedral shape model of an asteroid, the gravitational potential can be calculated numerically to *exact* precision, assuming that the body has a uniform bulk density (Werner and Scheeres, [1997](#), [2005](#)). Given a radar-derived shape model for example, the polyhedral gravity method can yield much higher fidelity results (Fahnestock and Scheeres, [2006](#), [2008](#)). Recent developments have significantly improved the computational speed of polyhedral methods with minimal sacrifice in fidelity or precision. For example, the “inertia integral” method can approximate the gravitational interac-

tion between polyhedral rigid bodies to a desired degree and order, in a recursive formulation that is extremely efficient (Davis and Scheeres, 2020a; Hou et al., 2017).

Other numerical methods for solving the F2BP include the Finite Element Method (FEM) (Gao et al., 2022; Nakano et al., 2022; Yu et al., 2019). One advantage with this approach is that it easily allows for irregular internal mass distributions, which can be useful to study the influence of internal structure on the system’s dynamics. The most straightforward approach to capturing irregular shapes or mass distributions in the F2BP (at least conceptually), is to approximate an irregular body as a set of point masses (or spheres), where gravity can then be found by summing over all the mass elements (Geissler et al., 1996; Rossi et al., 1999; Scheeres et al., 1998). The beauty of this “mascon” (mass concentration) approach is that the number of particles can simply be increased to obtain higher precision, however, this comes at an increased computational cost. This is especially costly when the mutual gravity between two bodies must be calculated, as the computation time scales as $\mathcal{O}(N^2)$, where N is the number of particles. Although, there are approximate methods that can improve this scaling relation at the expense of precision. However, in the case of rubble-pile asteroids, this approach can be used in which the rigid-body assumption is relaxed and contact interactions between constituent particles or “boulders” can be self-consistently modeled. This means, for example, that shape changes due to landslides can be modeled in a way that is fully coupled to the resulting dynamics (Agrusa et al., 2022a).

1.2 The Asteroid Impact Hazard

1.2.1 Overview

Perhaps the most famous asteroid impact is that which ended the reign of the dinosaurs 66 million years ago. This asteroid, estimated to be tens of kilometers in diameter, created a ~ 150 km diameter impact crater in the Yucatan Peninsula of Mexico (Alvarez et al., 1980; Bottke et al., 2007; Desch et al., 2021). Today, there are only $\sim 1,000$ NEOs greater than 1 km in diameter, of which $\sim 95\%$ have been discovered with none posing a realistic threat (Harris and D’Abramo, 2015; Harris and Chodas, 2021). Owing to the collisional evolution of small bodies in the solar system, there are far more small asteroids than there are large asteroids (Bottke et al., 2005, 2015). There are an estimated $\sim 25,000$ NEOs greater than 140 m diameter, of which only $\sim 1/3$ have been found. At this size scale, an Earth impact would be capable of causing regional devastation. Similarly, $\sim 100,000$ NEOs larger than 50 m in diameter are thought to exist and only $\sim 2\%$ have been discovered. These sized impactors are capable of destroying a urban area. Not only are these smaller NEOs numerous, they are also much dimmer owing to their smaller surface area, making them extremely challenging to detect and track.

Asteroid impacts are a low-probability, yet extremely high-consequence risk. Although a devastating asteroid impact is unlikely to occur within our lifetimes, they are the *only* natural disaster that is entirely preventable. We are always periodically reminded of the existential threat that asteroids pose, such as the 1908 Tunguska event that leveled 2000 km^2 of forest (Chyba et al., 1993; Kulik, 1927), the 2013 Chelyabinsk air burst (Popova et al., 2013), and the tidal disruption and impact of comet P/Shoemaker-Levy 9 with Jupiter (Hammel et al., 1995; Weaver

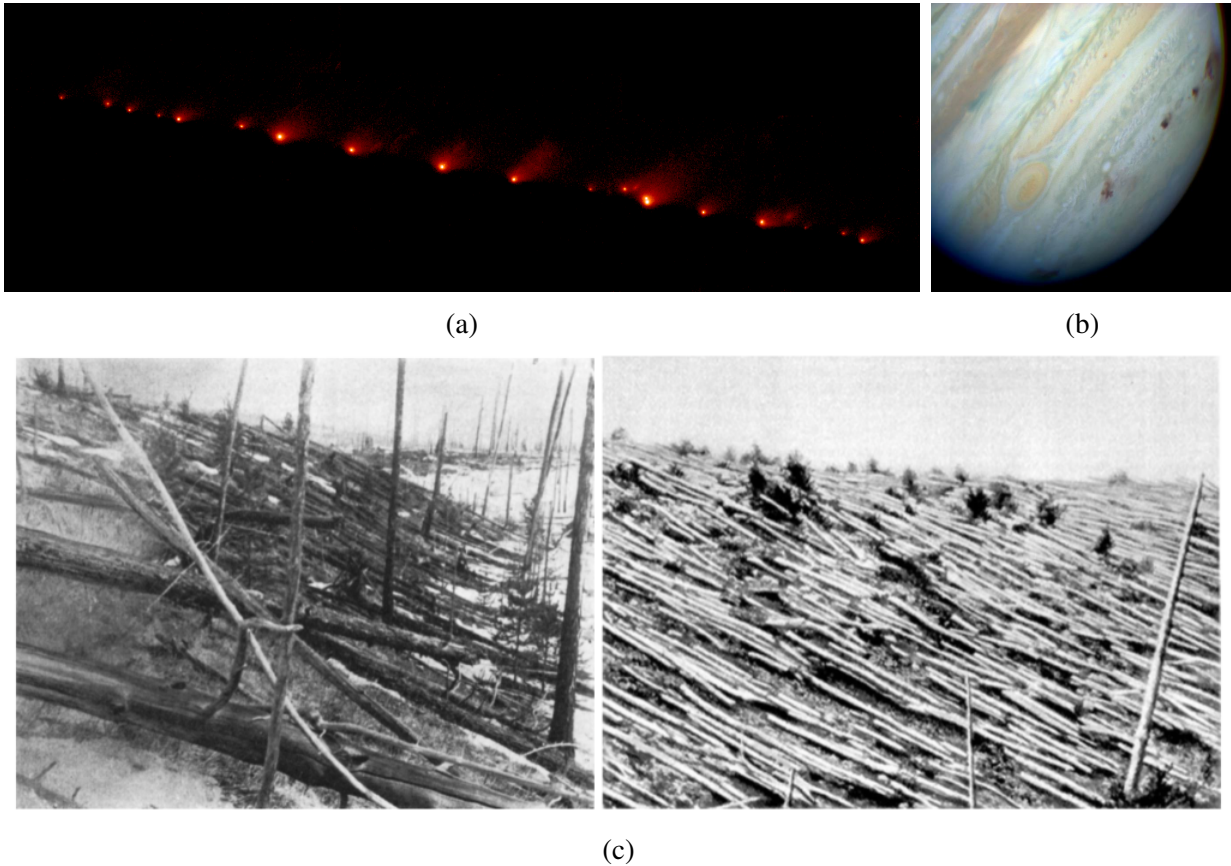


Figure 1.3: (a) Tidally-disrupted fragments of Comet P/Shoemaker-Levy 9 prior to impacting Jupiter. Image credit: NASA/ESA/STScI. (b) Images of Jupiter where the impact sites can be seen as dark brown spots. Image credit: NASA/ESA/STScI. (c) Photographs taken at the Tunguska impact site, showing thousands of trees that were knocked down. Image credit: Leonid Kulik.

et al., 1994). Images of Shoemaker-Levy 9's impact on Jupiter and photos from the Tunguska impact site are shown in Figure 1.3. In 2029, the ~ 350 meter diameter potentially hazardous asteroid (PHA) (99942) Apophis will pass within Earth's geosynchronous orbit (Farnocchia et al., 2013; Giorgini et al., 2008). This encounter is so close that tidal forces will be strong enough to potentially alter Apophis's spin and surface features (DeMartini et al., 2019; Yu et al., 2014).

In 2016, NASA created the Planetary Defense Coordination Office. And for the first time, the Planetary Science and Astrobiology Decadal Survey included a dedicated chapter for planetary defense (National Academies of Sciences and Medicine, 2022). In recent years, planetary

defense has become a flourishing field that the Decadal Survey aptly described as “applied planetary science”. NEO detection, characterization, and mitigation all rely heavily on a deep scientific understanding of NEOs, including their dynamical, compositional, and geophysical properties.

1.2.2 The DART and Hera Missions

The Double Asteroid Redirection Test (DART) mission is planetary defense demonstration mission that will assess a kinetic impactor as a viable mitigation strategy (Cheng et al., 2016; Cheng et al., 2018; Rivkin et al., 2021). A kinetic impactor or kinetic deflector is a technique to simply ram a spacecraft into an asteroid at a high-enough speed to sufficiently alter its orbit and prevent an eventual collision with the Earth. The DART spacecraft, shown in Fig. 1.4, successfully launched from Vandenberg Space Force Base on November 24, 2021. It is expected to impact Dimorphos, the secondary component of the Didymos binary asteroid, on September 26, 2022 with an estimated mass and relative speed of ~ 535 kg and ~ 6.15 km/s. The impact will be approximately head-on, decreasing Dimorphos’s orbital speed, shrinking the binary semimajor axis and orbit period. Figure 1.5 shows a schematic of the expected geometry of the Sun, Earth, Didymos system, and the DART spacecraft at impact. Several days before DART strikes Dimorphos, it will deploy the Light Italian CubeSat for Imaging of Asteroids (LICIACube), managed by the Italian Space Agency (ASI). LICIACube will fly by the system, capturing images of the early phases of crater formation and ejecta production, as well as image the backside of Dimorphos (Dotto et al., 2021). With ground-based observations, the new orbit period can be measured, from which the momentum enhancement factor, commonly referred to as β , can be estimated.

The momentum enhancement factor, β , is a dimensionless parameter describing the effec-



(a)



(b)

Figure 1.4: (a) Computer rendering of the DART spacecraft with its solar panels fully deployed. Image credit: NASA/Johns Hopkins APL. (b) The DART spacecraft as it was being loaded into the rocket fairing. Image credit: NASA/Johns Hopkins APL/Ed Whitman.

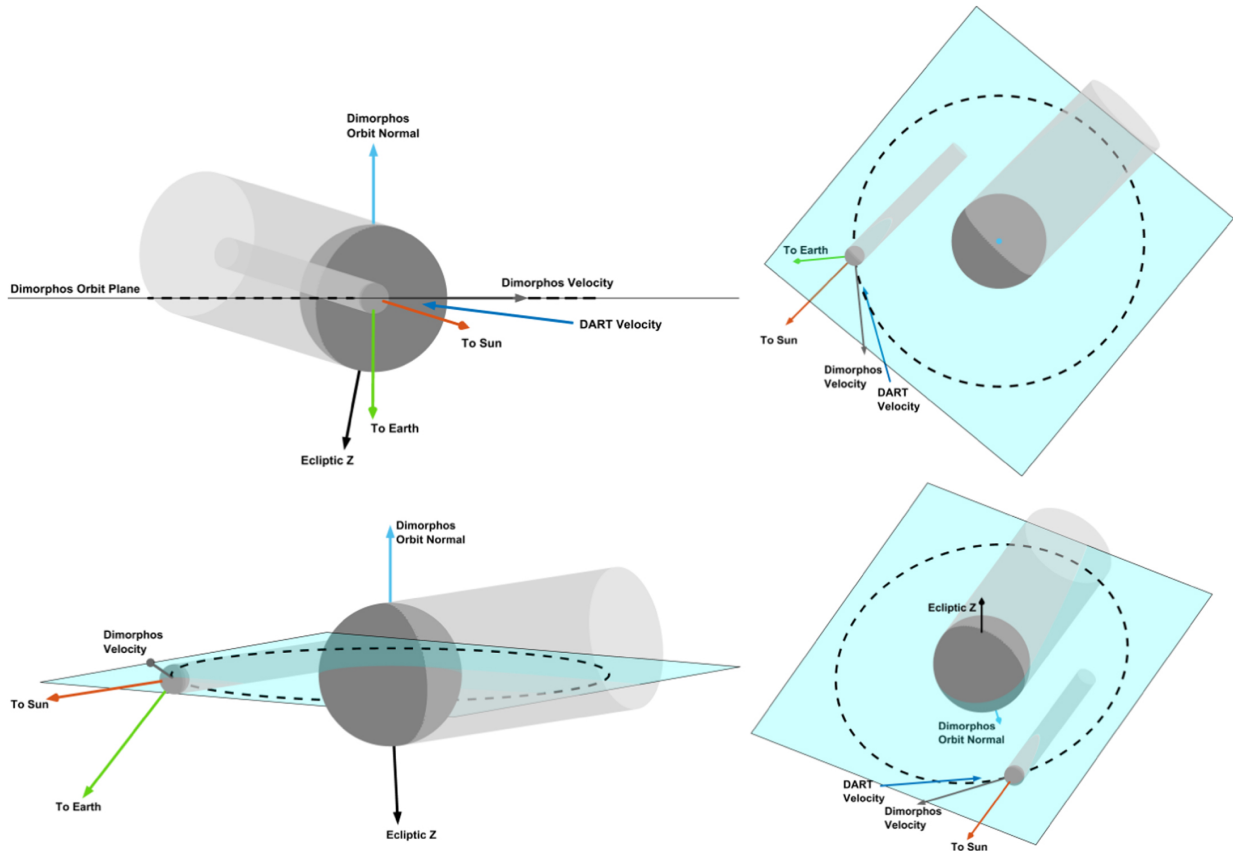


Figure 1.5: Expected geometry for the DART impact. The impact will be nearly opposite the orbital motion of Dimorphos. This figure is taken from Rivkin et al. (2021).

tiveness of a kinetic impactor and can conceptually be thought of as the ratio of net momentum imparted to the target divided by the momentum delivered to the target. In a perfectly inelastic collision, β is simply equal to 1. In a realistic impact, a crater is formed and ejecta is produced that travels in a direction (generally) opposite the motion of the kinetic impactor. Any ejecta exceeding the escape velocity will contribute to the net momentum transfer, thus “enhancing” the kinetic impact and making β exceed 1. For our purposes, β can be thought of as a scalar quantity. In reality, however, β is a three-dimensional vector that depends on a range of parameters including target material properties, impact geometry, spacecraft mass, velocity, and shape. In an

ideal, one-dimensional case, β can be written as,

$$\beta = 1 + \frac{p_{\text{ejecta}}}{p_{\text{sc}}}, \quad (1.3)$$

where p_{ejecta} is the momentum carried by the escaping ejecta, which is traveling opposite to the momentum of the spacecraft, p_{sc} . Then, for an idealized head-on impact, the change in Dimorphos's orbital speed can be written as,

$$\Delta v = -\frac{M_{\text{sc}}v_{\text{sc}}}{M_{\text{target}}}\beta, \quad (1.4)$$

where M_{sc} and v_{sc} are the spacecraft (i.e., DART) mass and speed, and M_{target} is the target (i.e., Dimorphos) mass. This Δv results in a change in orbit period of approximately,

$$\frac{\Delta P}{P} = 3\left(\frac{v}{an}\right)^2 \frac{\Delta v}{v}, \quad (1.5)$$

where v is Dimorphos's pre-impact orbital speed, a is the pre-impact semimajor axis, and n is the pre-impact mean motion. This series of equations makes a number of assumptions,

1. The DART impact is head-on, exactly opposite the orbital motion of Dimorphos.
2. All ejecta travels exactly opposite to the incoming DART momentum vector.
3. The impact is also aligned with Dimorphos's center of mass, such that there is no imparted torque.
4. The impact can be treated as an instantaneous event, such that Dimorphos's velocity changes immediately according to Δv .

5. The binary orbit is Keplerian, where the two components behave as ideal point-masses and there is no spin-orbit coupling. The binary orbit is also circular.
6. The change in orbit period ΔP is small compared to the orbit period, P .

Although all of these assumptions introduce some level of error, the uncertainty in the mass of Dimorphos (which will not be measured by DART or LICIACube) will likely dominate the uncertainty in the determination of β . In practice, the formula that will be used to determine β for the DART mission accounts for the three-dimensional nature of the momentum enhancement factor (i.e., assumptions 1 and 2 are not made) (Rivkin et al., 2021).

The European Space Agency (ESA) will launch the Hera mission in 2024, which will arrive at the Didymos system in late 2026, roughly ~ 4 years after the DART impact (Michel et al., 2018, 2022). Its principal objectives are to characterize the dynamical and physical properties of the system. One of the principal measurements that Hera will make is the mass of Dimorphos, which will substantially improve upon DART's estimate for β . In addition to being the first full-scale demonstration of a kinetic deflection, DART will also be the first mission to a near-Earth binary asteroid while Hera will be the first to comprehensively characterize a binary, making for an exciting technological and scientific opportunity.

1.2.3 The Didymos Binary Asteroid

(65803) Didymos was first discovered at Kitt Peak Observatory in 1996 (Alday et al., 1996). Didymos is classified as both a NEA and PHA, as the intersection of its orbit and Earth's comes within 0.05 au, although it poses no threat to Earth. In 2003, it was discovered that Didymos was a binary asteroid (Pravec et al., 2003). Its provisional name was originally 1996 GT, but was

renamed to Didymos, which means “twin” in Greek, after its binary nature was discovered. The word “Didymos” is used interchangeably to refer to the entire binary system, or just the main body or the “primary”. The primary has also been referred to as Didymos A in the literature. The official IAU designation for the name of Didymos’s satellite, or “secondary”, is (65803) Didymos I Dimorphos, or more informally, simply “Dimorphos”. Dimorphos is a Greek word for “having two forms”, a nod to how its form will change following the DART impact. Dimorphos has been colloquially referred to in the literature as “Didymos B” or “Didymoon”, but Dimorphos is now the officially adopted name.

The system has a heliocentric semimajor axis, eccentricity, and inclination of 1.64 au, 0.384, and 3.4° , respectively. The primary (Didymos) and the secondary (Dimorphos), have respective diameters of ~ 780 and ~ 160 m, and are separated by only ~ 1200 m or ~ 3 primary radii. The radar-derived shape model for Didymos shows that it is oblate, and has a slight equatorial ridge, which is typical for NEA binaries (Naidu et al., 2020a). Didymos is a fast-rotator, with a spin period of 2.26 h. Based on the ~ 11.92 h binary orbit period, semimajor axis, and estimated body volumes, the system has a bulk density of ~ 2.2 g cm $^{-3}$. Figure 1.6 shows Didymos’s net surface gravity given its estimated shape, bulk density, and spin rate. Due to the strong centrifugal acceleration, the net gravity is zero at the equator indicating that Didymos is nominally exceeding its critical spin limit. In order to maintain its structural stability, this implies that Didymos must have some combination of (a) a higher bulk density than estimated, (b) some degree of interparticle cohesion, and/or (c) the primary is actively shedding mass (Zhang et al., 2017, 2018, 2021). The shape of the secondary is not yet known, so it is assumed to have an approximate ellipsoidal shape in accordance with similar systems, with axis ratios $a/b = 1.3$ and $b/c = 1.2$, where a , b and c are its respective long, intermediate, and short axis lengths. The

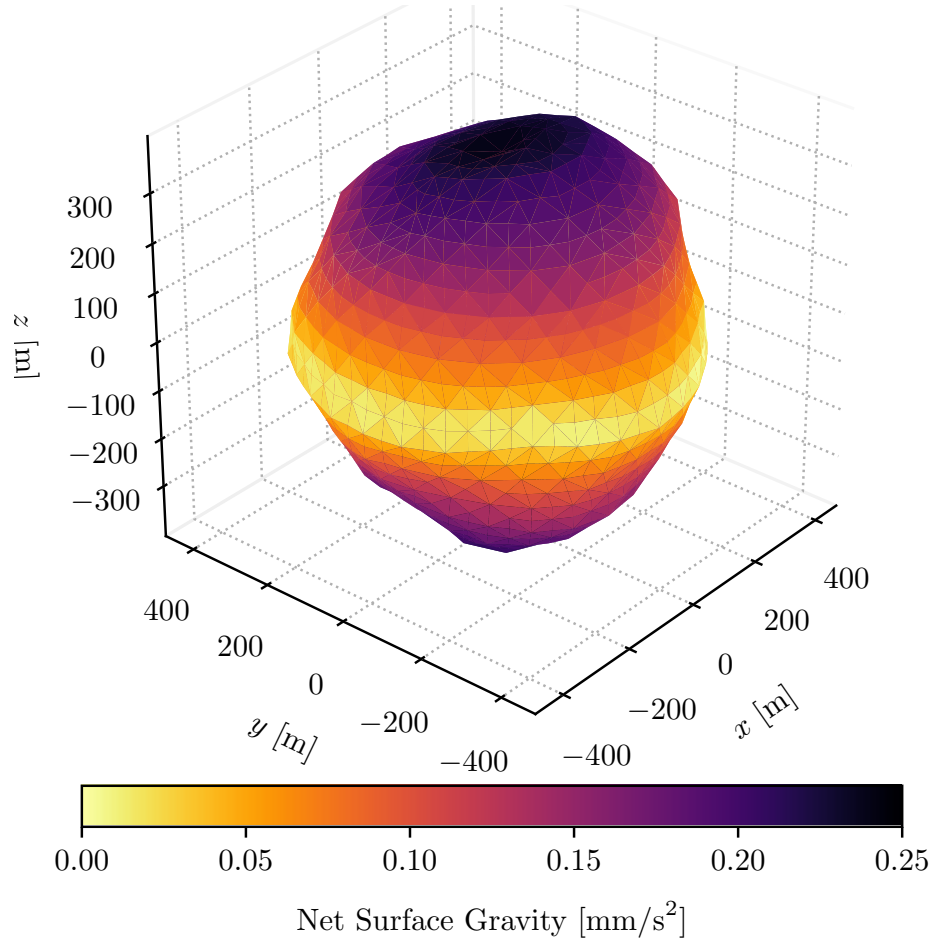


Figure 1.6: The radar-derived shape model for Didymos from Naidu et al. (2020a). The x , y , and z axes are coordinated in the body-fixed frame such that z is parallel to the spin axis and x points along Didymos’s longest axis length. The facet colors show the net surface gravity at Didymos’s 2.26 h rotation period at the nominal bulk density of 2.2 g cm^{-3} . At the equator, the centrifugal acceleration is so strong that it cancels out the gravitational acceleration.

secondary’s spin is assumed to be synchronous with the ~ 11.92 h mutual orbit period, although this has not been directly confirmed. Table 1.1 lists the current best estimates of the physical and dynamical properties of the system.

Owing to the irregularly shaped bodies and their close separation, the system experiences a high degree of spin-orbit coupling and non-Keplerian motion. As a result, the system’s dynamical evolution is highly sensitive to Dimorphos’s unknown shape and spin state. Adequately capturing the mutual dynamics for these types of systems often requires the use of high-fidelity F2BP codes.

Table 1.1: The current best estimates for the physical and dynamical parameters of the Didymos system as of Didymos Reference Asteroid (DRA) v. 3.21. Some of these parameters will likely change shortly after this thesis is published when DART arrives. Reported uncertainties are 1σ .

Parameter	Value
Volume-Equivalent Diameter of Primary D_P	780 ± 30 m
Volume-Equivalent Diameter of Secondary D_S	164 ± 18 m
Bulk Densities of Components ρ_P	2200 ± 350 kg m ⁻³
Mean Separation of Component Centers a_{orb}	1.20 ± 0.03 km
Secondary Shape Elongation $a_S/b_S, b_S/c_S$	$1.3 \pm 0.2, 1.2$ (assumed)
Total Mass of System M	$(5.55 \pm 0.42) \times 10^{11}$ kg
Secondary Orbital Period P_{orb}	11.9216289 ± 0.0000028 h
Secondary Orbital Eccentricity e_{orb}	< 0.03
Primary Rotation Period P_P	2.2600 ± 0.0001 h
Secondary Rotation Period P_S	P_{orb} (assumed tidally locked)
Secondary Orbital Inclination i_{orb}	0° (assumed)

Didymos’s close distance from the Earth at the time of the DART impact, combined with the fact that Dimorphos has a relatively short orbit period, makes it an ideal testbed for a kinetic impactor. If DART instead deflected a single asteroid, it would require a measurement of the change of the asteroid’s heliocentric orbit, which is both challenging and time consuming, potentially taking years to observe a noticeable change (e.g., Makadia et al., 2022). Instead, by impacting Dimorphos, the binary orbit period will change by several minutes compared to its initial ~ 11.92 h orbit period, something that can be readily measured with Earth-based observations in the weeks following the impact (Naidu2022; Rivkin et al., 2021; Scheirich and Pravec, 2022).

1.3 This Dissertation

The work presented in this dissertation consists of several projects related to the dynamics of the Didymos system that were conducted in support of the DART Mission. Although the chapters focus exclusively on the Didymos-Dimorphos binary, the methods and much of the con-

clusions apply broadly to binary systems in general. All chapters were previously published in peer-reviewed journals and are presented here with minimal modification. Chapter 2 presents a benchmarking and sensitivity study of the full two-body dynamics of the Didymos system. The main goals of this chapter were to determine the optimal F2BP code to inform future studies and to understand the sensitivity of the system dynamics to the initial conditions. During this study, we found that the spin or libration state of Dimorphos is very sensitive to its initial orbital velocity. Given that the DART impact will substantially change Dimorphos’s orbital velocity, this finding naturally led to the investigation described in Chapter 3. Here, we studied the spin state of Dimorphos as a function of its unknown shape and β (which corresponds directly to the change in orbital velocity) using GUBAS, the F2BP code that was adopted after the benchmarking exercise of Chapter 2. We found that the post-impact spin state is highly sensitive to both the shape and β , and that various spin-orbit resonances could potentially lead to chaotic rotation as a result of the DART impact. Given the possibility of a highly excited post-impact spin and orbital state, Chapter 4 relaxed the rigid-body assumption of previous studies and simulated the mutual dynamics with one or both components treated as rubble piles. We found the same general result, that the post-impact spin may become chaotic for certain values of β and body shape, which further confirms the predictions of Ch. 3. Due to the excited post-impact spin and tidal environment, we also found that long-term granular motion on the surface of Dimorphos is plausible, depending on the body shape and β . The numerical approach used in Ch. 4 likely underestimates any surface motion for reasons explained in the chapter. To explore the possibility of dynamically triggered surface motion further, Chapter 5 explores the evolution of accelerations felt on Dimorphos’s surface as a function of β and the bulk density. We find that surface motion is plausible, although the likelihood and magnitude depends strongly on the bulk density and shape, both of which are

not yet well-constrained. Finally, Chapter 6 summarizes this thesis and briefly discusses potential future work, related to both Didymos and binary asteroids in general.

Chapter 2: Benchmarking and sensitivity study of the Didymos system

2.1 Chapter Preface

This chapter was published in *Icarus* under the title, “A benchmarking and sensitivity study of the full two-body gravitational dynamics of the DART mission target, binary asteroid 65803 Didymos” (Agrusa et al., 2020). This benchmarking study was assigned to the Dynamics Working Group (WG) as part of DART’s Investigation Task Plan. The main goals of the study were to understand the sensitivity of the system’s dynamics to different initial conditions and to identify the best simulation code for future studies in support of DART. I led the analysis, wrote the manuscript, and ran one of the four simulation codes. However, this study would not have been possible without major contributions from Alex Davis, Gene Fahnestock, and Toshi Hirabayashi.

The following chapter appears nearly unaltered with respect to its journal version. However, since the manuscript was published, “Dimorphos” was selected as the official name for the secondary component of the Didymos system. In its published version, this manuscript referred to the primary as “Didymos A” and the secondary as “Didymos B”. Any references to “Didymos A” have been replaced with “Didymos” and “Didymos B” has been replaced with “Dimorphos”. The reader will notice however, that some of the figures still contain the original naming scheme. Also, the “UCB” simulation code was given the official name “GUBAS” after this paper was published. However, we keep the original nomenclature in this manuscript, as the other three

simulation codes are also referred to based on their institution of origin. Some of the introductory material may be somewhat repetitive with Chapter 1, so the reader may skip to Section 2.3 if desired.

As a further point of clarification, the eccentricity reported in Table 2.6 and Figures 2.3 and 2.4 is the *Keplerian* eccentricity. In other words, the eccentricity is computed based on the respective positions and velocities of the center of masses of the two binary components. Due to the system's non-Keplerian dynamics, this differs slightly from the *geometric* eccentricity. In addition, the orbit period reported in Table 2.6 is simply in inverse of the average angular velocity of the orbit. It should be noted that this period is not perfectly fixed, and that the mutual orbit period varies with time as a result of spin-orbit coupling. We point the reader to Meyer et al. (2021) for further discussion on this caveat. In subsequent chapters, the precise definition of the eccentricity, orbit period, and other orbital elements is specified as appropriate.

2.2 Introduction

The Asteroid Impact & Deflection Assessment (AIDA) collaboration is a NASA- and ESA-supported effort to test the capability of a kinetic impactor for hazardous asteroid mitigation. NASA will lead the Double Asteroid Redirection Test (DART) mission, which will achieve a kinetic impact on the secondary (Dimorphos) of 65803 Didymos, a near-Earth binary asteroid, in the fall of 2022 (Cheng et al., 2018). ESA will lead Hera, a follow-up mission to rendezvous with Didymos to characterize the system and visible effects of the impact (Michel et al., 2018). The main goal of the DART mission is to demonstrate the kinetic impactor technique by intercepting the secondary, causing a change in the binary orbital period that can be measured with ground-

based observations.

In this work, we present results from a suite of benchmarking simulations conducted by the DART Investigation Team’s Dynamics Working Group to better understand the complex mutual dynamics, to constrain the sensitivity of the simulated Didymos system to initial conditions, and to identify the appropriate numerical methods to fully capture the dynamics. In Section 2.2.1 we describe the physical and dynamical properties of the Didymos system. Section 2.3 introduces the four dynamics models used in this study and the initial conditions of the simulation cases. The results are presented in Section 2.4. Finally, we discuss future work to better understand the Didymos binary in Section 2.5.

2.2.1 The Didymos System

Discovered in 1996, 65803 Didymos is classified as a near-Earth object and potentially hazardous asteroid with a heliocentric semi-major axis of 1.644 au (Alday et al., 1996). In 2003, it was discovered that Didymos is a binary system (Pravec et al., 2003). The binary has a mutual orbit period of $P_{\text{orb}} \sim 11.9217$ h and a semi-major axis of $a_{\text{orb}} \sim 1.19$ km (Naidu et al., 2020a; Pravec et al., 2006). According to the binary mean separation and orbital period, Kepler’s third law for assumed point masses implies a system mass of $M_{\text{sys}} \sim 5.37 \times 10^{11}$ kg.

The primary (Didymos) is ~ 780 m across and has an oblate shape and equatorial ridge, and the secondary (Dimorphos) is approximately 164 m across and we assume an ellipsoidal shape similar to that of other NEO binary secondaries. Didymos is a fast rotator, with a spin period of 2.26 h. A polyhedral shape model with 1996 facets was derived by Naidu et al. (2020a) from combined radar and light curve data. In the simulations presented here, Dimorphos is assumed to

be synchronous (i.e., tidally locked) with its long axis initially aligned with the line of centers. It is also assumed that both bodies are in principal axis rotation and that their spin poles are initially aligned with the binary orbit normal.

Table 2.1 summarizes the relevant physical and dynamical parameters of the Didymos system. These are the nominal system parameters adopted by the DART investigation team at the current time and will be updated throughout the DART mission as new measurements become available.

2.3 Methodology

The Didymos binary is an example of the full two-body problem (F2BP), where the rotational and translational dynamics are fully coupled, due to the objects' irregular shapes and the close proximity of the components. As a result, the system's dynamical evolution is especially sensitive to the shapes and initial positions and orientations of each component, thus F2BP simulation codes are necessary to fully capture the system's dynamics.

2.3.1 The Simulation Codes

Four different codes were tested in this study, each developed by team members at NASA JPL, University of Colorado Boulder (UCB), Auburn University, and the University of Maryland (UMd), respectively. Only some of these codes have official names, so we refer to each code by the institution that developed it for simplicity. Brief descriptions of the codes are given below.

NASA JPL The JPL code is based on the formulation of the mutual gravitational potential between two polyhedral bodies developed by Werner and Scheeres (2005). It calculates the

Symbol	Parameter	Value	Comments/References
a_{orb}	Semi-major Axis	1.19 ± 0.03 km	(Naidu et al., 2020a)
$c : b : a$	Secondary Axis Ratios	1:1.2:1.56	Assumed, based on other binary systems.
D_{P}	Diameter of Primary	780 ± 30 m	(Naidu et al., 2020a)
D_{S}	Diameter of Secondary	164 ± 18 m	Derived from D_{P} and $D_{\text{S}}/D_{\text{P}}$
$D_{\text{S}}/D_{\text{P}}$	Size Ratio	0.21 ± 0.01	(Scheirich and Pravec, 2009)
e_{orb}	Binary Orbit Eccentricity	$e_{\text{orb}} < 0.03$	Upper limit, assumed zero. (Scheirich and Pravec, 2009)
i_{orb}	Binary Orbit Inclination	0.0	Assumed.
(λ, β)	Mutual Orbit Pole	$(310^\circ, -84^\circ) \pm 10^\circ$	Ecliptic coordinates, (Naidu et al., 2020a; Scheirich and Pravec, 2009)
M_{sys}	Total System Mass	$(5.37 \pm 0.44) \times 10^{11}$ kg	Derived via Kepler's 3rd Law with P_{orb} and a_{orb} .
P_{orb}	Binary Orbit Period	11.9217 ± 0.0002 h	One possible orbit solution. (Scheirich and Pravec, 2009)
P_{P}	Primary Spin Period	2.2600 ± 0.0001 h	(Pravec et al., 2006)
P_{S}	Secondary Spin Period	11.9217 h	Assumed.
ρ_{P}	Primary Bulk Density	2170 ± 350 kg m ⁻³	Derived based on D_{P} and M_{sys} .
ρ_{S}	Secondary Bulk Density	2170 ± 350 kg m ⁻³	Assumed.

Table 2.1: Physical and dynamical parameters of the Didymos System. These are the current nominal values adopted by the DART investigation team. Because these parameters are constantly being refined by ongoing observations, these are not exactly the same parameters used in this study. The initial conditions of the simulations presented here differ slightly, but remain within the uncertainty bounds given here. (See Table 2.3 for the simulation initial conditions.)

mutual gravitational potential and its gradients through a Legendre polynomial series expansion, truncated to a desired order, and integrates the discrete-time Hamiltonian equations of motion using the Lie-Group Variational Integrator (LGVI) developed by Lee et al. (2007). This code was written in C++ and parallelized to run on a cluster computer environment, due to the high computational cost of the potential and gradients evaluation at each timestep.

University of Colorado Boulder (UCB) The recently developed UCB code utilizes inertia integrals to expand the mutual gravitational potential according to the formalism derived by Hou et al. (2017). This tool, known as the General Use Binary Asteroid Simulator (GUBAS), is now publicly available¹ and can easily be run on a single desktop computer. Despite the different mathematical formulations for the mutual gravitational potential and its gradients between the JPL and UCB codes, they agree to near-machine precision for the same given expansion order of the mutual potential, since they used the same numerical integrator (LGVI) for the simulations run herein. However, the inertia integral formulation allows for the attitude and mass distribution to be decoupled and computed separately, which allows for a more computationally efficient implementation and thus faster runtimes. The present study served as a convenient test to confirm that the UCB code does in fact achieve the same result as the JPL code.

Auburn University The Auburn code is a simplified version of the UCB code. It expands the inertia integrals only to second order according to the formulation given by Hirabayashi and Scheeres (2013). The equations of motion are solved with an 8th-order Runge-Kutta scheme. This code can be thought of as evaluating the mutual gravitational potential of the system as if the Didymos shape model were replaced with a best-fit ellipsoid. Although the Auburn code

¹<https://github.com/alex-b-davis/gubas>

	Primary	Secondary
N	3355	3546
$\rho_{\text{bulk}} [\text{g cm}^{-3}]$	2.104	2.104
$\rho_{\text{particle}} [\text{g cm}^{-3}]$	3.8947	3.7329
$r_{\text{avg}} [\text{m}]$	21	4.4

Table 2.2: Physical parameters for PKDGRAV particles. All particles in each respective body are given a uniform particle density in order to achieve the desired bulk density of 2.104 g cm^{-3} . r_{avg} is the mean particle radius. The particle size distributions for the primary and secondary are sampled from a normal distribution with mean $\mu = 21 \text{ m}$, standard deviation $\sigma = 4.2 \text{ m}$ and $\mu = 4.4 \text{ m}$, $\sigma = 0.88 \text{ m}$, respectively. The size distributions both have $\pm 1\sigma$ cutoffs.

does not fully capture perturbations due to the asymmetric shape of the primary, it is extremely fast and is a useful reference point to understand the effect of higher-order perturbations due to Didymos’s shape.

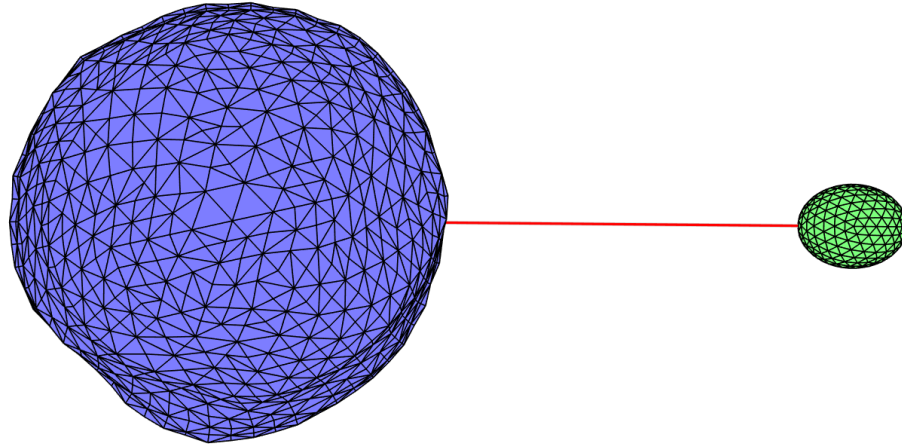
University of Maryland (UMd) Unlike the other three codes that represent the primary and secondary as monolithic and homogeneous bodies of some arbitrary polyhedral or ellipsoidal shape, the UMd code treats each body as a rigid aggregate of many spherical particles. The code, called PKDGRAV, is a parallel N -body tree code (Richardson et al., 2000; Stadel, 2001). The UMd code uses a primary consisting of ~ 3500 particles in order for the average particle diameter ($\sim 42 \text{ m}$) to be within the spatial resolution of the radar shape model ($\sim 50 \text{ m}$). Details of UMd’s representation of each body are shown in Table 2.2. The translational motion is integrated with a fixed-step second-order leapfrog integrator, while the rotational motion is integrated with a time-adaptive fourth-order Runge-Kutta scheme within each leapfrog step (Richardson et al., 2009). Note that PKDGRAV’s k-d tree is not used, so the forces and torques are computed by summing over every particle at every timestep to ensure the highest possible accuracy at the expense of speed.

Snapshots of the simulations of Didymos are shown in Fig. 2.1. The key differences are that

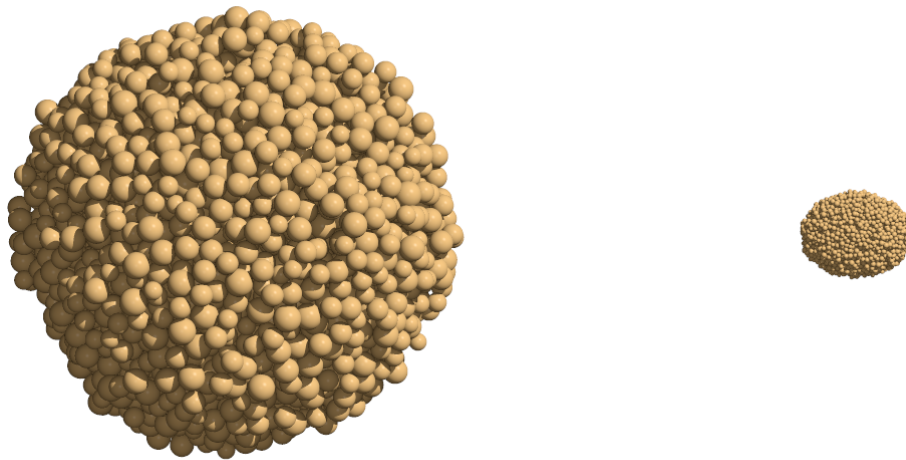
JPL, UCB, and Auburn simulate the full radar-derived Didymos shape model with an ellipsoidal Dimorphos, with the mutual gravitational potential expanded to some desired order of accuracy. The UMd method fills a volume with randomly packed spherical particles, then carves each body to match the desired shape and computes the mutual gravitational potential of the packed spheres exactly without truncation to any order. Because of the different mass representations of each method, there will be inherent variations between these approaches.

2.3.2 Initial Conditions

The 11 simulations presented here comprise a small subset of cases that the Dynamics Working Group has studied thus far. These simulations were selected to compare code performance and better understand the system’s sensitivity to uncertainty in its initial state. Using the nominal values for the mass of each body and their separation, we computed the initial conditions to approximately put the system on a circular Keplerian orbit. This is considered the “nominal” simulation case. More details on the initial conditions for the nominal case are shown in Table 2.3. We then give these initial conditions slight perturbations to test the system’s sensitivity to the initial relative velocity of the secondary and the initial rotation phase of the primary. See Table 2.4 for details of the 11 test cases, along with a schematic in Fig. 2.2. Each group selected a timestep for their respective code, based on numerical convergence and runtime constraints, with each code conserving energy to one part in a million or better over the entire simulation. Each of the 11 test cases was simulated for a total of 150 days of simulation time. All codes modeled the system as two rigid bodies interacting purely through their mutual gravity, with all additional forces or torques such as solar tides, BYORP, or internal dissipation turned off.



(a) Radar shape model of Didymos and the assumed ellipsoidal shape of Dimorphos. JPL, UCB, and Auburn simulate the full radar-derived primary shape model with the mutual potential expanded to various orders of accuracy.



(b) The UMd representation of the binary, where randomly packed spherical particles fill the shapes of each body and the potential is computed explicitly over every particle.

Figure 2.1: Representations of the Didymos binary among the different codes. Both of these images are a top-down view (i.e. from the mutual orbit north pole) at the start of the simulation.

Parameter	Value	Notes
System Mass	5.276428×10^{11} kg	
Primary Mass	5.228011×10^{11} kg	
Secondary Mass	4.841661×10^9 kg	
Primary Bulk Density	2103.4 kg m ⁻³	
Secondary Bulk Density	2103.4 kg m ⁻³	
Secondary Axis Lengths	$a = 103.16$ m $b = 79.35$ m $c = 66.13$ m	a is oriented along line of centers at $t = 0$.
Initial Body Separation	1.18 km	
Initial Relative Velocity	0.17275 m s ⁻¹	Relative velocity of the body centers. Derived to achieve circular Keplerian orbit with period of 11.9216 h.
Primary Spin Angular Velocity	0.0007723 rad s ⁻¹	Equivalent to a 2.26 h spin period. Aligned with mutual orbit pole.
Secondary Spin Angular Velocity	0.0001464 rad s ⁻¹	Equivalent to a spin period of 11.9216 h, in order to match the Keplerian orbit period. Aligned with orbit pole.

Table 2.3: Initial conditions of the nominal simulation.

Each group output previously agreed-upon state variables at a 1-minute cadence (except for UMD which had hourly outputs due to data storage constraints). With such a high output cadence, we were able to compare both short- and long-term evolution of the binary system with each simulation code. The JPL and UCB codes were run with the mutual gravity expansion set to 4th order; this choice is accurate enough to capture the dynamics with high fidelity while keeping the computation time manageable. UCB also repeated the nominal case with the gravity expansion order set to 8th order to confirm that the choice of 4th order was indeed sufficient to accurately model the system. Again, the Auburn code is limited to 2nd order, while the UMD code has no order truncation.

Name	Description
nominal	The nominal, unperturbed initial state. The initial conditions are calculated using Newton's version of Kepler's Third Law to give a circular orbit based on the total system mass and mean separation.
posR, negR	The initial velocity of the secondary's barycenter is perturbed by ± 0.0005 m/s in the instantaneous orbital radial direction.
posT, negT	The initial velocity of the secondary's barycenter is perturbed by ± 0.0005 m/s in the instantaneous orbital tangential direction (along-track).
posN, negN	The initial velocity of the secondary's barycenter is perturbed by ± 0.0005 m/s in the instantaneous orbital normal direction (out-of-plane).
ph+1, ph+3, ph-1, ph-3	the initial rotation phase of primary shape model is adjusted by rotating ± 1 or ± 3 degrees from nominal, around the primary spin pole.

Table 2.4: Description of the 11 simulation cases.

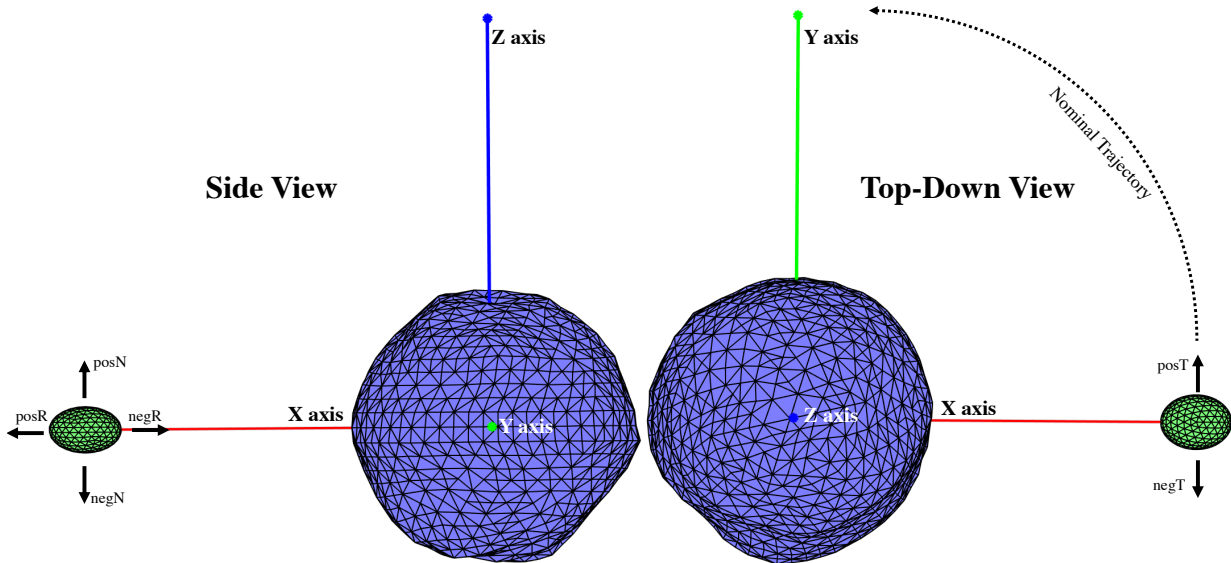


Figure 2.2: Schematic of the perturbations to Dimorphos. The X, Y, and Z axes are the three principal axes of Didymos. The nominal case has the long axes of both bodies aligned. The $ph\pm 3$ and $ph\pm 1$ cases have Didymos rotated about its spin axis such that its X axis is pointed ± 3 or ± 1 degrees away from the direction to Dimorphos.

	# Processors	timestep [s]	# timesteps	wallclock [h]
Auburn	1	60	216,000	~several min
NASA JPL (4th Order)	512	40	324,000	38.0
UCB (4th Order)	1	40	324,000	5.6
UCB (8th Order)	1	40	324,000	111.55
UMd	4	1.875	6,912,000	702.0

Table 2.5: Each code’s performance for its nominal run, with a total integration duration of 150 d.

2.4 Results

2.4.1 Code Performance

Since each code was run on different machines (see acknowledgments) with different timesteps and numerical routines, normalized performance comparisons can be troublesome. In Table 2.5, we simply show the runtimes for the nominal case along with the number of processors and timesteps used by each code. The Auburn code is orders of magnitude faster than the other codes, given its 2nd-order approximation of the mutual potential. This makes it a useful tool for quick tests, however it does not capture higher-order perturbations due to the asymmetric shape of the primary. It should also be noted that the UCB or JPL codes would have similar performance if the mutual potential approximation were set to 2nd order. The UMd code had the longest runtime, due to a combination of its small timestep and requirement to compute the gravitational potential on a particle-by-particle basis. The 4th-order UCB code offers the best combination of speed and accuracy, as we will see in the following section. Therefore, the Dynamics Working Group has recommended that the UCB code be adopted for future rigid-body dynamics studies related to DART.

	Orbit Period [h]	Semi-Major Axis [km]	Eccentricity
Auburn	11.8138797	1.1747401	0.0055961390
NASA JPL	11.8062721	1.1743513	0.0059765762
UCB (4th Order)	11.8062824	1.1743520	0.0059765772
UCB (8th Order)	11.8053794	1.1743062	0.0060210983
UMd	11.8211246	1.1750370	0.0051450228
Kepler Orbit	11.9216030	1.1800000	0.0000000000

Table 2.6: Simulated time-averaged orbital period, semi-major axis, and eccentricity for the nominal case. All codes use exactly the same initial conditions and body masses, so the deviations from a Keplerian orbit and among the codes themselves are due to different mass representations of the primary and secondary. Each quantity is rounded to enough decimal points to show deviation between nearly identical numbers.

2.4.2 The Nominal Case

The orbit period, semi-major axis, and eccentricity for each code’s nominal case is shown in Table 2.6 along with what those values would be if the system were Keplerian. As expected, the NASA JPL and UCB (4th Order) results are nearly identical. They also match closely to the 8th-order result, indicating that the 4th-order approximation is capturing the mutual gravitational potential with high fidelity. The deviations in the orbit period and semi-major axis are driven by each code’s representation of the mass distribution, and thus the mutual potential, of the two bodies.

Figure 2.3 shows the evolution of the system over 2 d (~ 4 orbital periods) as determined by each simulation code for the nominal case. Since the bodies do not follow a precise Keplerian orbit due to their irregular shapes, the orbital eccentricity and inclination are *osculating*—they are instantaneous values evaluated based on the position and motion of the body centers for each simulation output.

Since each group used a numerically converged timestep, the differences they show in the system’s orbital evolution are attributable to how each code represents the mass distribution of

each body. The oscillations in the various orbital elements are small and are driven by the shape perturbations of the primary. The bottom two plots in Fig. 2.3 show the obliquities of each body, defined as the angle between the body's spin axis and the mutual orbit pole. Due to its 2nd-order gravity approximation, the Auburn code shows negligible out-of-plane motion, indicating that the small changes in the inclination and obliquities with the other three codes are mainly driven by asymmetries in the primary shape.

The NASA JPL and UCB codes at 4th order are indistinguishable in Fig. 2.3 and the 8th-order version shows almost no appreciable difference. All codes show qualitative agreement, given their known differences. Because the UMD code had an output frequency of one hour, the inclination and obliquity plots look artificially jagged.

To study the orbital elements over longer time scales, we take a running average to remove short-term behavior. This is shown for the nominal case over the full 5-month simulation in Fig. 2.4. The long-term evolution is quite stable, with the orbital elements remaining constant or drifting by a very small amount. One apparent effect is that each code has a different average semi-major axis and eccentricity. This is again a result of different mass representations, which sets the initial mutual potential, and thus the eccentricity and equilibrium separation. This highlights the influence of the primary's shape on the orbital properties of the system. In general, the codes agree well, with differences attributable to their respective representations of each body. Because we expect the Didymos binary to be stable over long periods, our ability to capture long-term stability in its mutual orbit is reassuring.

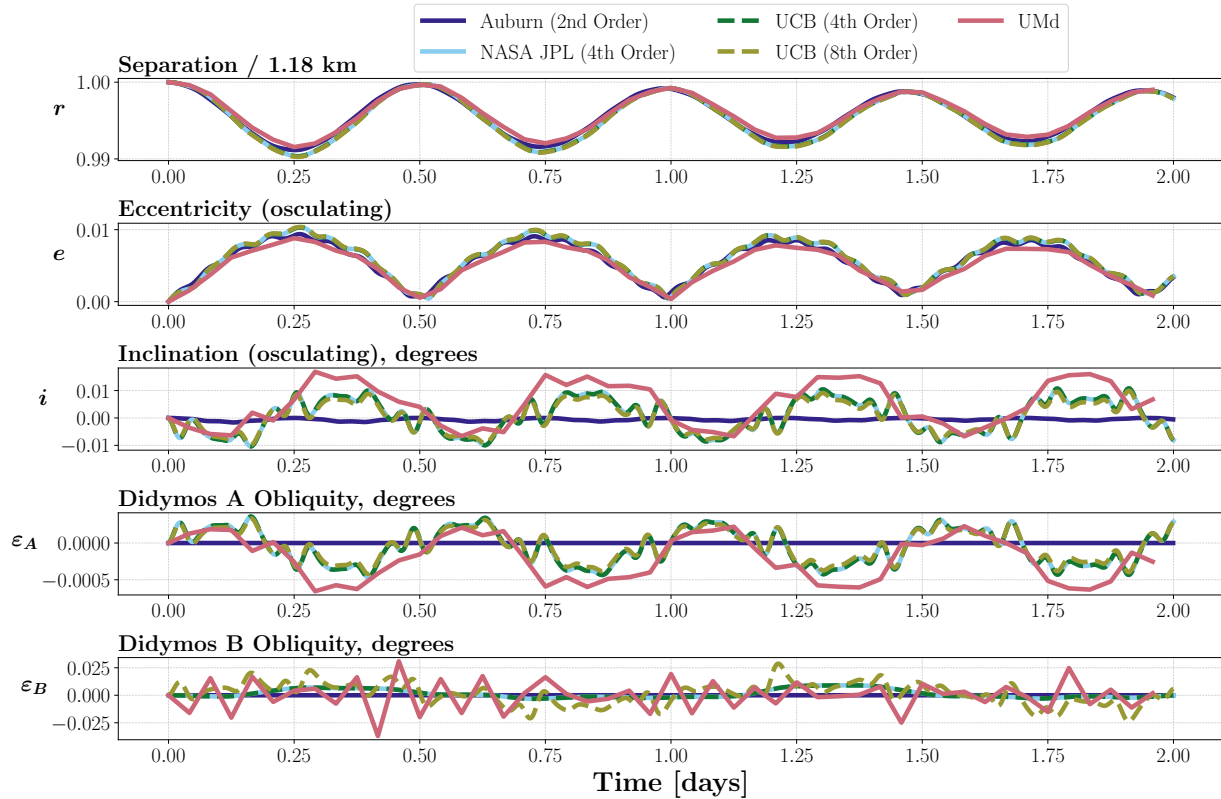


Figure 2.3: The nominal case over 2 d (~ 4 orbital periods). The NASA JPL and UCB codes show perfect agreement at 4th order, and the UCB 8th-order version matches closely as well. The Auburn code is evaluating the mutual gravitational potential to 2nd order, so it doesn't capture higher-order effects of the primary's asymmetric shape on the mutual orbit. The choppy noise in UMd's plot of Dimorphos's Obliquity is a result of its coarser output cadence.

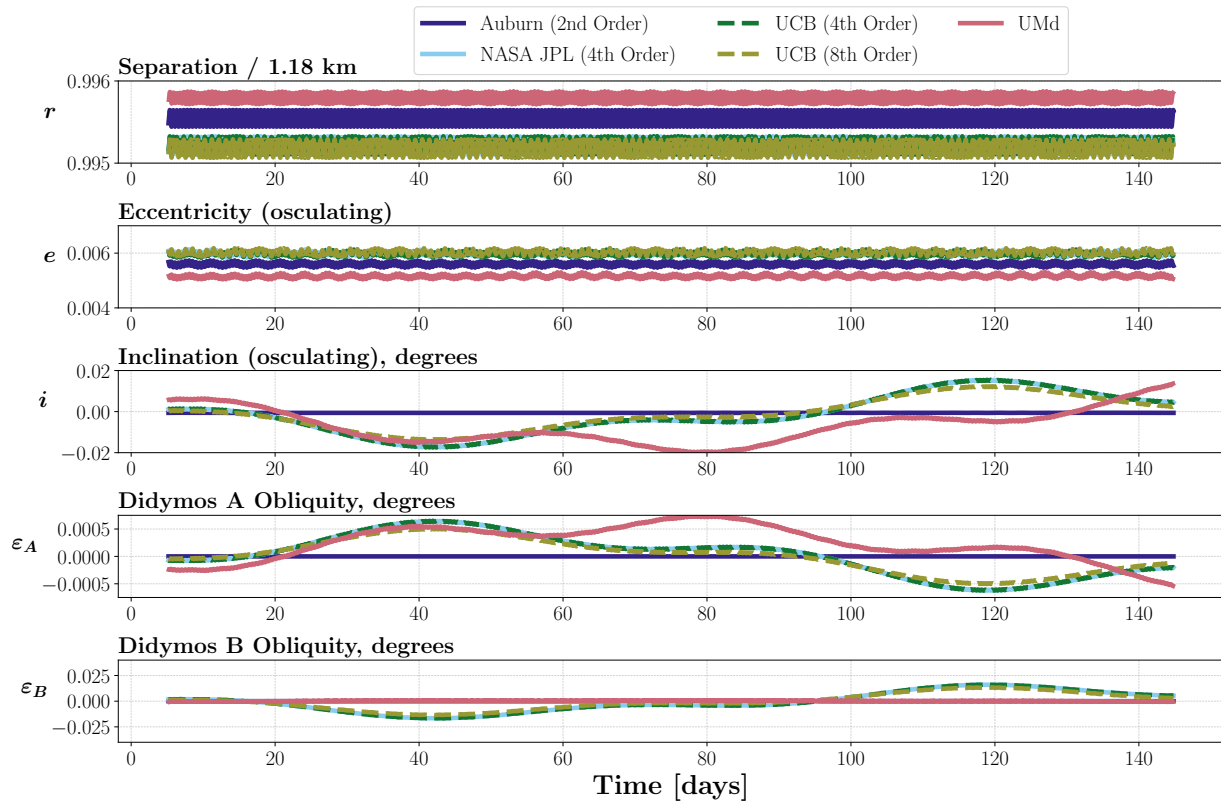


Figure 2.4: A running average of orbit parameters for the nominal case over 5 months. The first and last 10 d of data are cut off due to the running average using ~ 10 days worth of data (20 orbital periods).

2.4.3 Primary Rotation Phase

The only constraints we place on the orientations of the primary and secondary are that their spin axes be initially aligned with the mutual orbit pole. In our nominal case, the primary's long axis is aligned with the line of centers at $t = 0$, but this choice is arbitrary. A precise measurement of the primary's orientation relative to the secondary at a given epoch with ground-based observations prior to the DART impact will be very challenging, so we treat the primary's initial rotation phase as a free parameter. Therefore, understanding the system's sensitivity to the initial primary rotation phase is essential to developing methods for predicting the position of the secondary at later times.

To test this sensitivity, we varied the initial primary rotation phase with respect to the nominal case by $\pm 3^\circ$ and $\pm 1^\circ$. All codes showed a non-negligible dependence on this slight change. Fig. 2.5 shows the orbital phase (angular position of secondary) relative to *each code's* respective nominal case. The Auburn code is comparatively insensitive to the initial primary phase since it is only approximating the mass distribution to second order. NASA JPL and UCB have identical results, and UMD is slightly more sensitive to the initial primary phase.

If the initial primary rotation phase is altered, the initial mass distribution will be slightly different, resulting in a different mutual potential and thus a different orbital period. Due to the asymmetry of the primary and the binary's small separation, this is a non-negligible effect, especially if we want to accurately predict the position of the secondary.

After determining that the orbit may be sensitive to the initial primary rotation phase, we performed another set of simulations over a wider range of initial rotation phases with the UMD code only. The results in Fig. 2.6 show that the initial primary rotation phase has a significant

Orbit Phase vs. Initial Primary Rotation Phase

All quantities are relative to their respective nominal run

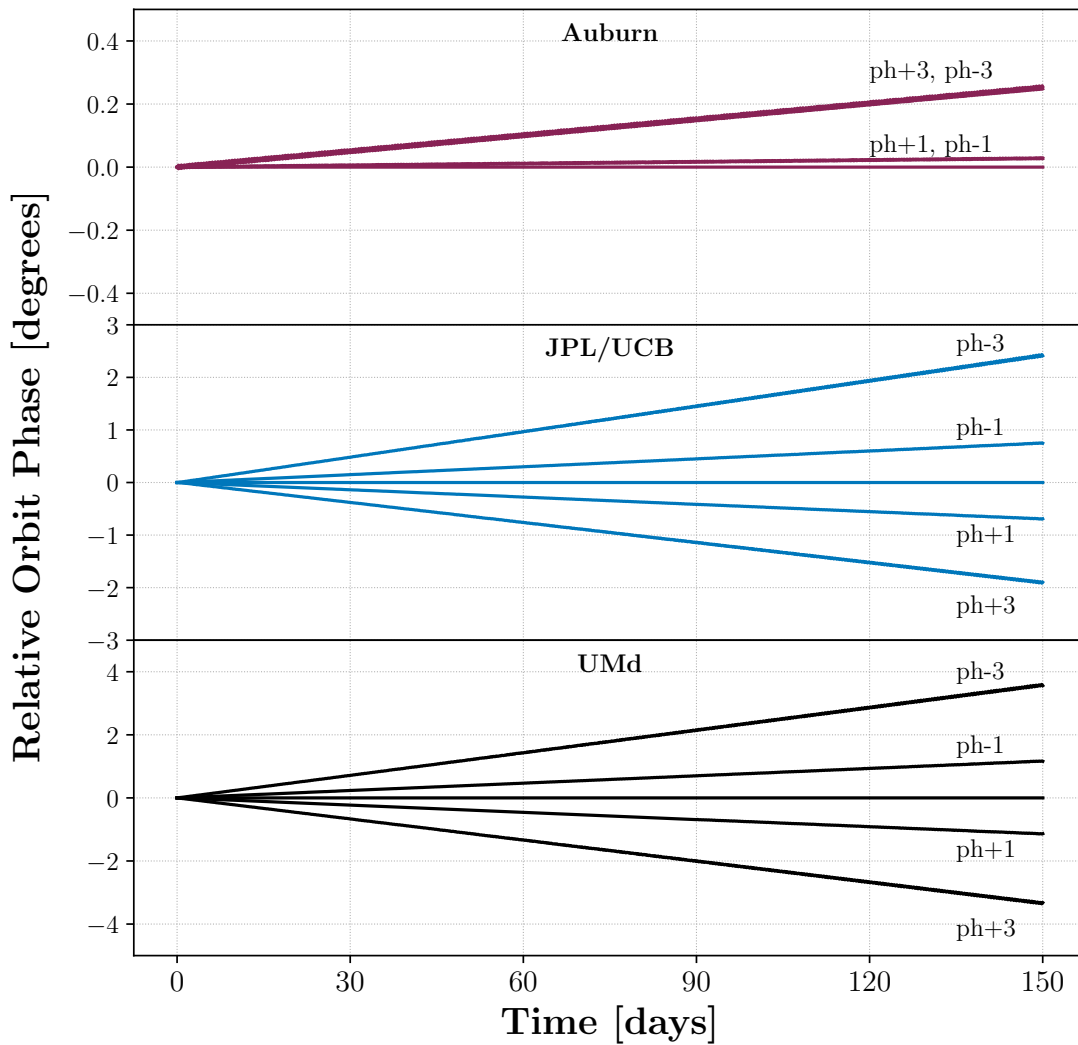


Figure 2.5: Orbit phase relative to each code's nominal run (the horizontal line). Small differences in the initial primary rotation phase give a slightly different orbital period, making it difficult to predict the position of the secondary at later times. Note the differences in vertical scale between codes.

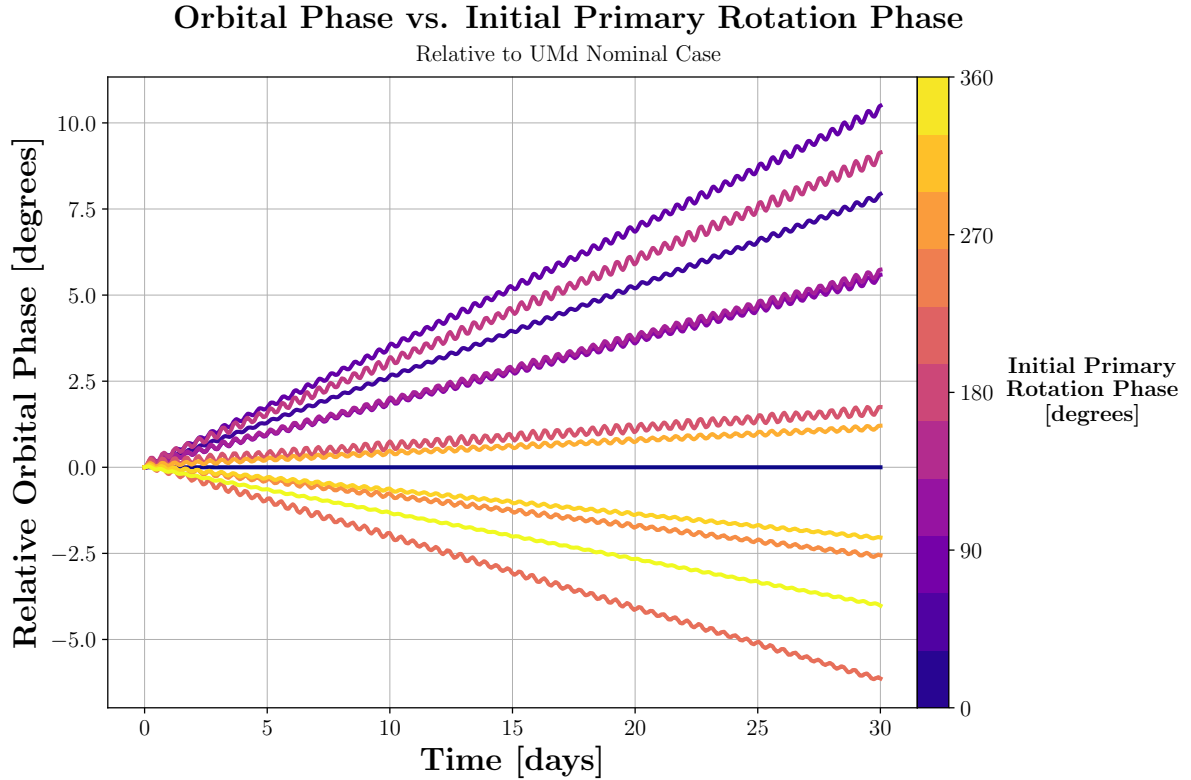


Figure 2.6: Orbit phase relative to nominal run, for initial primary rotation phases spanning 360° , using the UMd code. This represents the spread in the possible locations of Dimorphos after a fixed interval of time given some random initial primary rotation phase.

influence on the orbital evolution of the secondary. After an integration time of only 30 d, there is a spread of $\sim 15^\circ$ in the relative positions of the secondaries. The DART Investigation Team has a requirement to predict the orbit phase at the impact epoch to within $\pm 45^\circ$ 60 days prior to launch and to within $\pm 15^\circ$ 55 days prior to impact (3σ errors). The high sensitivity to Didymos's initial rotation phase means that it will likely be impossible to meet this requirement with dynamical simulations, especially considering the uncertainties in the other initial conditions. However, the Observing Working Group should be able to meet this orbital phase prediction requirement through fitting a weighted least-squares model to observed timing of mutual events (Naidu et al., 2020b).

2.4.4 Dimorphos Libration

Through tidal dissipation, we expect that the mutual orbit has circularized, the secondary is tidally locked, and any libration of the secondary's spin state has damped to a minimum. So the Didymos system should be in or close to a dynamically relaxed state prior to the DART impact. The impact will nearly instantaneously reduce the instantaneous orbital velocity of the secondary, decreasing the orbit period and increasing the eccentricity. Therefore, significant libration of the secondary should be induced. A libration angle is a measure of the orientation of a satellite's long axis relative to the line of centers between the two components' centers of mass. In the following analysis, we show only results from the UCB 4th order code for brevity, although we note that all 4 codes show good agreement, given the known differences among the codes.

In the coupled spin-orbit problem in which a synchronous, ellipsoidal secondary orbits a spherical or point-mass primary with its spin axis aligned with the mutual orbit pole, there are two modes of libration: *excited* and *relaxed*. In the decoupled spin-orbit problem, the excited and relaxed modes are analogous to free and forced librations, respectively. See Naidu and Margot (2015) for a detailed discussion on these two libration modes in both the coupled and uncoupled scenarios.

The frequency of free libration for a synchronous satellite on a circular orbit is given by,

$$\omega_0 = n \left(3 \frac{\mathcal{B} - \mathcal{A}}{\mathcal{C}} \right)^{1/2}, \quad (2.1)$$

where n is the mean motion, and \mathcal{A} , \mathcal{B} , and \mathcal{C} are the three principal moments of inertia of the secondary, where $\mathcal{A} < \mathcal{B} < \mathcal{C}$ (Murray and Dermott, 2000). This mode is analogous to a

pendulum's natural frequency, depending on its length and the gravitational acceleration. This libration mode is thought to be damped away due to tidal friction, especially if the secondary has a rubble-pile structure (Goldreich and Sari, 2009; Murray and Dermott, 2000). However, the *forced (relaxed) mode* necessarily exists for a synchronous secondary on an eccentric orbit. The secondary will feel a periodic restoring torque, with a frequency equal to the mean motion, due to the misalignment of the long axis with the line of centers, resulting from the orbital angular velocity varying over the course of a single orbit.

This picture is complicated when we consider libration in the *full* two-body problem. The theory on spin-orbit coupling discussed above makes two critical assumptions: 1) that the orbit is fixed (no apsis precession) and 2) that the ellipsoidal secondary is orbiting a *spherically symmetric* primary (Wisdom, 1987b). As a result, we will see some differences between the classic theory and our simulation results.

The nominal DART spacecraft impact is designed to hit the secondary's center-of-figure, in a direction nearly opposite its orbital motion at a 15-to-25-degree angle with respect to the orbital plane (depending on DART's trajectory), imparting a near-instantaneous change to its orbital velocity without significantly altering its spin state (Cheng et al., 2018). This will induce both longitudinal (in-plane) and latitudinal (out-of-plane) librations that will have *both* relaxed and excited components. By changing the mean motion without a matching change in the secondary's spin rate, we introduce excited (free) libration modes on top of those that exist already (if any). Further, the impact will increase the eccentricity of the system, exciting a stronger relaxed (forced) libration mode. Therefore, studying the resulting libration for the benchmarking cases where we perturb the orbital motion of the secondary reveals the extent to which DART may effect a libration in the secondary. Further, understanding the behavior of induced libra-

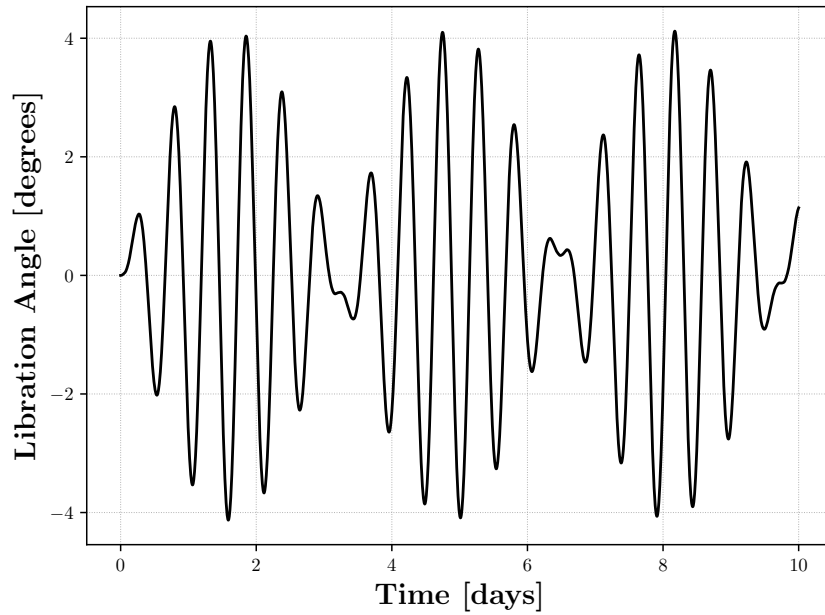
tions may be an important tool for interpreting the results of the DART impact, if the libration amplitude or frequency is observable.

The longitudinal libration for the nominal case is shown in Fig. 2.7a for the first 10 days of the simulation. The distinct beating pattern in the libration is a signature of both excited-mode and relaxed-mode librations (Naidu and Margot, 2015). A Fourier transform of the libration pattern shows the two distinct libration modes (Fig. 2.7b).

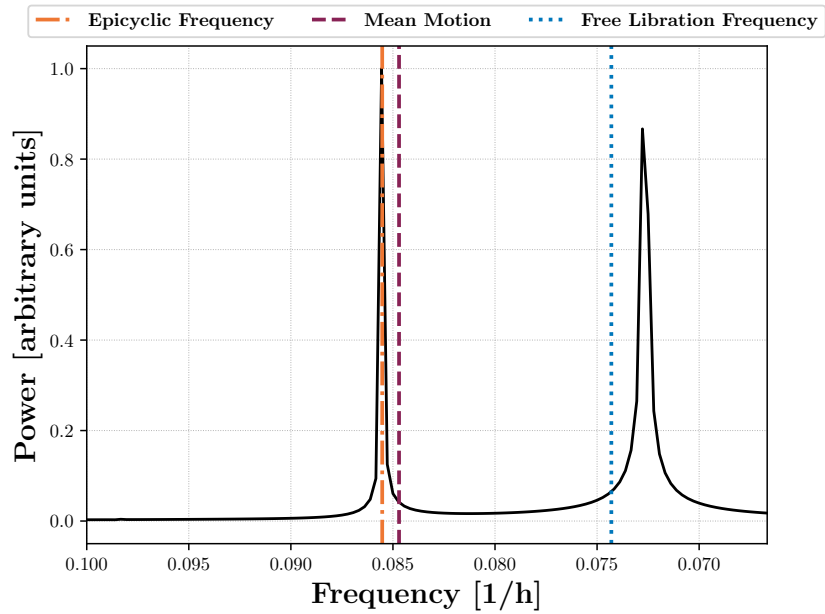
The frequency of the relaxed (forced) mode is the frequency at which the orbital angular velocity oscillates, which in this case is the epicyclic or radial frequency. A key assumption in the classic spin-orbit problem is that the orbit is fixed (i.e., no apsidal precession), in which case the epicyclic frequency would match the mean motion. However, the oblate shape of the primary and the close orbit of the secondary results in an extremely fast precession of the periaapse. In the nominal case, the mean motion differs from the epicyclic frequency by $\sim 1\%$, which corresponds to a precession rate of $\sim 3.5^\circ$ per *orbit*.

The excited (free) libration mode has a frequency close to the theoretical prediction given by Eq. 2.1. These frequencies don't match perfectly because Eq. 2.1 assumes a spherically symmetric primary on a fixed orbit. Because this excited libration frequency will depend on the secondary's moments of inertia in a fashion similar to Eq. 2.1, it may be possible to infer something about the mass distribution and interior structure from a careful measurement of the libration frequency with Hera.

Fig. 2.8 shows the libration for the nominal case and the 2 cases where the secondary was given an along-track velocity perturbation (posT/negT). The libration amplitude is driven by the initial difference between the orbital angular velocity and the secondary's spin rate. The posT case is where the secondary is given a slightly larger initial tangential velocity, so its orbit



(a) Longitudinal libration of UCB nominal case over 10 days. The libration pattern is consistent over the full 150-day simulation.



(b) Fourier transform of longitudinal libration.

Figure 2.7: The Fourier transform of the longitudinal libration reveals the two libration modes. The relaxed (forced) mode is driven by the epicyclic (radial) frequency, while the excited (free) mode is controlled by the moments of inertia of the secondary. The theoretical free libration frequency doesn't match the excited mode perfectly because its derivation assumes a spherically symmetric primary.

expands, increasing the orbital period to ~ 11.911 h, closely matching Dimorphos's initial spin period and thus decreasing the libration amplitude. The negT case is the opposite: a smaller initial tangential velocity shrinks the orbit and shortens the orbital period (~ 11.703 h), producing a larger discrepancy between the secondary's initial spin and orbital periods, thus a libration amplitude reaching $\sim 8^\circ$ at its maximum.

The perturbation to the secondary's linear momentum in the posT and negT cases is approximately one-half of the momentum carried by the DART spacecraft, so these perturbations are of the same order of magnitude that DART may produce. Since the posT case has a relatively small libration amplitude, we can think of it as being close to the "true" relaxed state of the system (in which the excited libration mode has nearly damped away but relaxed librations persist). Then, the jump from the posT to the negT cases corresponds to a rough conservative estimate of the effect of the DART impact on the libration, when the momentum perturbation to the secondary is approximately equal to the momentum carried by the DART spacecraft. In reality, we would expect the momentum perturbation to the secondary to be considerably larger, due to the contributions of ejecta to the net momentum transfer. Further, if the DART spacecraft impacts several meters off of center-of-figure, which terminal guidance simulations at JHU/APL suggest is likely, the torque applied to the secondary will also alter its spin state, nearly instantaneously. The DART terminal guidance system will likely result in an impact location biased toward the illuminated portion of the secondary, which will be the side opposite the primary based on DART's viewing geometry at the impact epoch. Therefore, such an off-center impact is likely to reduce the secondary's angular velocity, further increasing the maximum possible libration amplitude. For these reasons, the simulations presented here are a conservative estimate of the possible post-impact libration state of Dimorphos, given our current knowledge of the state of the system. It is

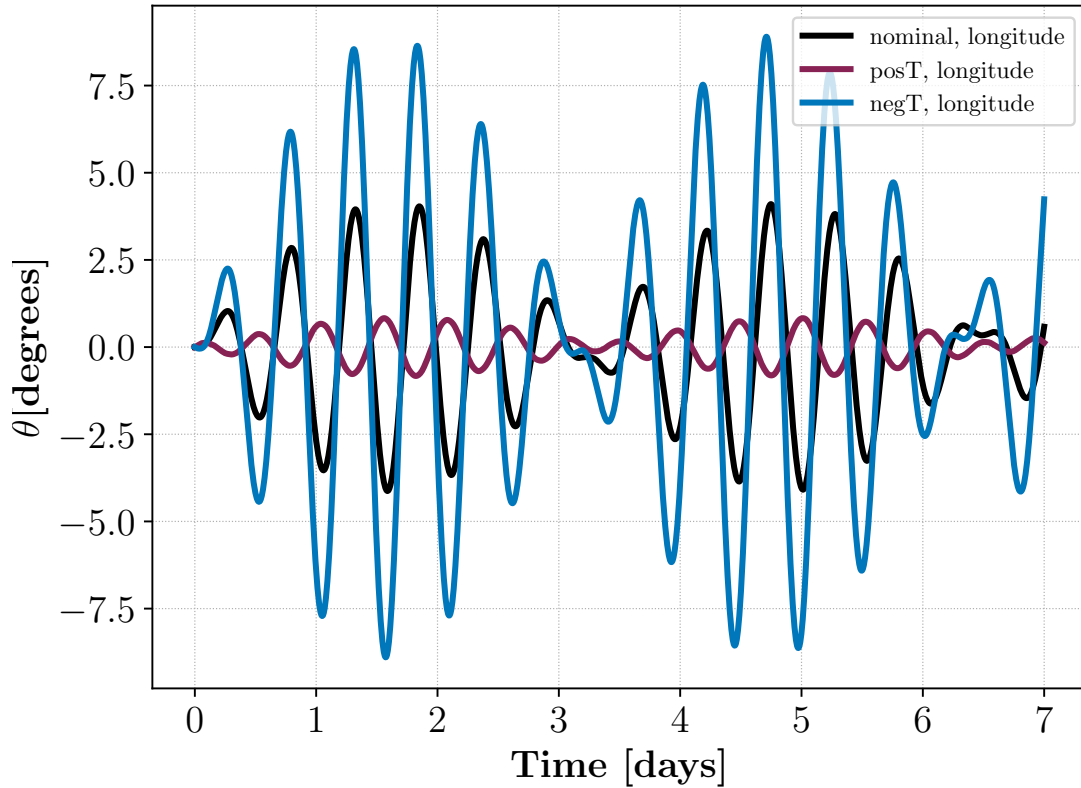


Figure 2.8: Longitudinal libration angles as function of time for the nominal run and tangential (along-track) perturbations, using the UCB code.

also important to note, that the libration amplitude and frequency are dependent on Dimorphos’s moments of inertia which are computed based on our assumptions of constant density and its ellipsoidal shape. Studying the dependence of Dimorphos’s libration on its mass distribution is planned for a future study.

Naidu and Margot (2015) show that the libration of a synchronous satellite may be detectable with radar, if the secondary is large enough compared to the primary ($D_S/D_P \gtrsim 0.2$). This threshold is barely satisfied by the Didymos system and therefore the libration may be measurable with radar, given adequate observing conditions, a favorably shaped secondary, and a sufficiently large momentum transfer.

When the secondary is given a normal (out-of-plane) perturbation, we are inducing out-of-

plane motion in the secondary and therefore a noticeable, but small, latitudinal libration in the secondary, while the longitudinal libration is effectively unchanged (see Fig. 2.9). The librations resulting from the benchmarking cases where we apply radial velocity perturbations (posR/negR) and different primary rotation phases ($ph\pm 3$ and $ph\pm 1$) show almost no sensitivity, so we exclude showing them here.

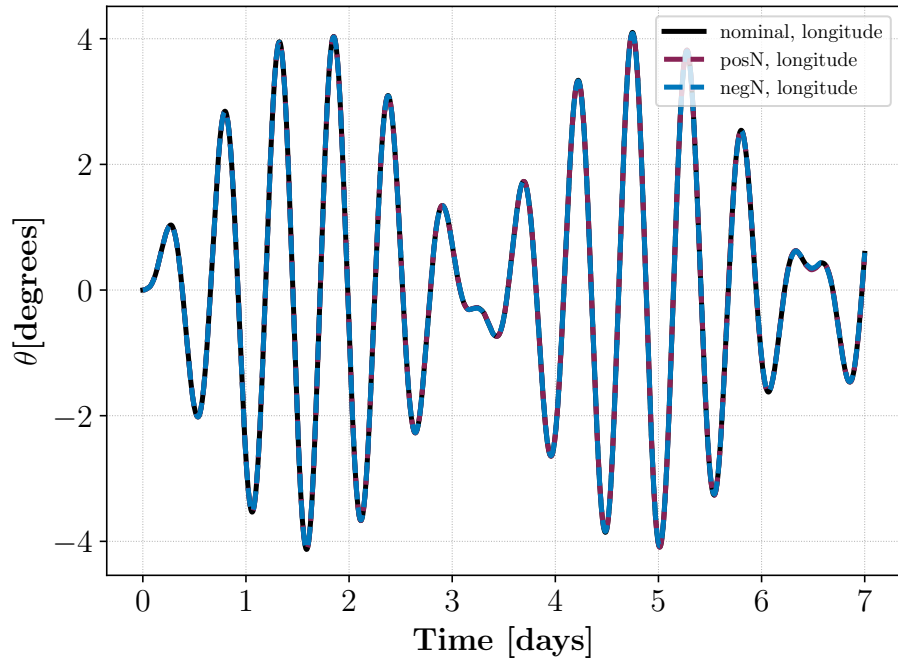
2.5 Conclusions

In this work, we found that the simulation package provided by UC Boulder is well-suited to studying the orbital dynamics of the Didymos system, due to its accuracy and speed. The Dynamics Working Group has recommended the adoption of this code for future dynamics studies in support of DART.

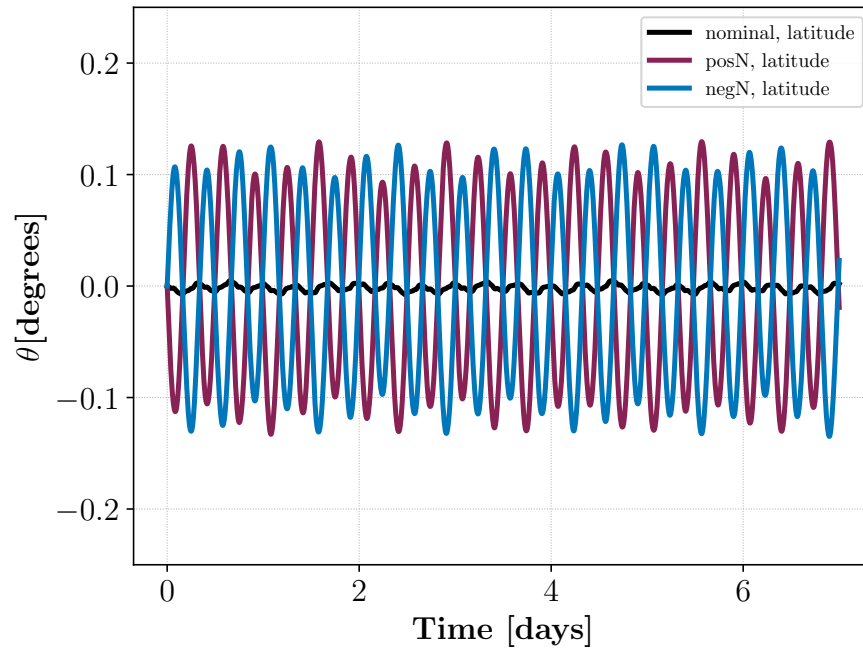
The results of this benchmarking study show that: 1) shape perturbations cause a non-negligible deviation from a Keplerian orbit; 2) the orbit phase of the secondary is highly dependent on the initial orientation of the primary; and 3) the system will be highly susceptible to induced librations resulting from the DART impact, which may be measurable from ground-based radar or with Hera. If measurable, Dimorphos's libration may be a useful probe of its internal structure.

The first two results indicate that predicting the orbital phase of the secondary may not be feasible with numerical simulations, given the uncertainties in the initial conditions and body shapes. However, the Observing Working Group will be able to meet this orbital phase prediction requirement through fitting an analytic model to observed timing of mutual events.

We have begun a comprehensive study with the UCB code on the strength and frequency



(a) Longitudinal libration for out-of-plane perturbations.



(b) Latitudinal libration for out-of-plane perturbations.

Figure 2.9: Longitudinal and latitudinal libration vs. time for normal (out-of-plane) perturbations, using the UCB code. The longitudinal libration is insensitive to the normal perturbation as expected, while the small induced latitudinal libration is caused by initial out-of-plane motion of the secondary.

of post-impact librations as a function of the mass distribution of Dimorphos and momentum transferred by DART. This study will be used to constrain the range of possible impact outcomes in order to better infer the result of the actual DART experiment.

In reality, Didymos is likely a rubble pile given its shape and fast rotation. A rubble-pile structure may play an important role for the binary dynamics due to processes such as landslides (Hirabayashi and Scheeres, 2019) and tidal dissipation. Dimorphos may also be a rubble pile in which case its free libration modes will dampen via internal friction. Therefore, we also plan to use PKDGRAV with an implementation of a soft-sphere discrete element method to numerically investigate whether this damping may be a noticeable effect over the timescales between the DART and Hera missions.

Chapter 3: Predicting Dimorphos’s post-impact spin state

3.1 Chapter Preface

This chapter was published in *Icarus* under the title, “The excited spin state of Dimorphos resulting from the DART impact” (Agrusa et al., 2021). This paper was written as part of another DART Investigation Task Plan assignment to predict the post-impact dynamical state of the Didymos system, including Dimorphos’s expected libration state. Although I led the study, much of it would have been impossible without major contributions from my collaborators. Alex Meyer and Dan Scheeres supplied the “analytic model” (Sections 3.3.1 and 3.4.1) and Ioannis Gkolias and Menios Tsiganis supplied the “simplified 3D model” (Sections 3.3.2 and 3.4.2), including all the text and figures for those respective subsections. Although these sections were not my own work, they are included in order to understand and interpret the results of the higher-order dynamics model. The following chapter appears nearly unaltered with respect to its journal version. Some of the introductory material may be somewhat repetitive with Chapter 1, so the reader may skip to Section 3.2.1 if desired. The appendices associated with this chapter are located in Appendix [A](#)

3.2 Introduction

NASA’s Double Asteroid Redirection Test (DART) mission will be the first to demonstrate asteroid deflection by kinetic impact as a realistic assessment for planetary defense. The DART spacecraft will intercept the secondary (Dimorphos) of the near-Earth binary asteroid system 65803 Didymos in the fall of 2022 (Cheng et al., 2018). The European Space Agency’s (ESA) Hera mission will arrive at the binary ~ 4 years later to investigate the resulting dynamical and geophysical changes to the system (Michel et al., 2018). The nominal DART trajectory is an approximate head-on collision with Dimorphos, impulsively reducing its relative orbital speed, and thereby shortening the mutual orbit period and semimajor axis. The binary orbit eccentricity and inclination will also change, depending on the impact circumstances (Cheng et al., 2016).

Figure 3.1 shows a sketch of the binary system and the geometry of the problem. The change in orbit period will be measured with ground-based observations in order to infer β , the momentum transfer efficiency. The change in velocity of an asteroid in response to a kinetic impact can be written as (Cheng et al., 2020; Feldhacker et al., 2017),

$$\Delta\vec{v} = \frac{m}{M} \left(\vec{u} + (\beta - 1)(\hat{n} \cdot \vec{u})\hat{n} \right), \quad (3.1)$$

where m is the impactor mass, M is the target mass, \vec{u} is the impactor velocity, and \hat{n} is the outward surface normal at the impact site. The first term represents the incident momentum of the spacecraft, and the second term is the contribution of escaping momentum, which is assumed to be along the surface normal. β can then be written as the ratio of the total transferred momentum to the momentum delivered by the impactor:

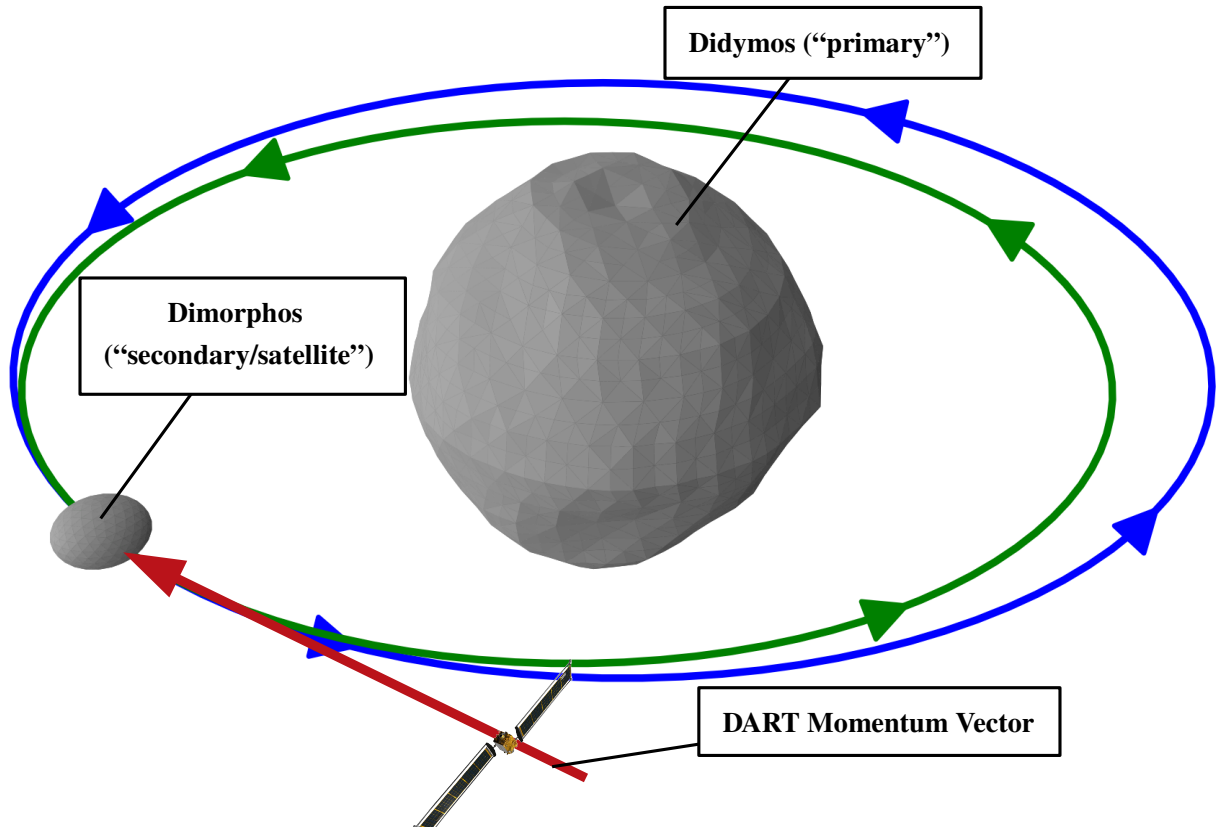


Figure 3.1: Diagram showing the geometry of the problem and some terminology. In this work, “Didymos” or “primary” refers to the more massive, central component of the *Didymos binary system*, while “Dimorphos”, “secondary”, or “satellite” refers to its smaller companion. The term “impactor” refers to the DART spacecraft. The red line denotes DART’s momentum vector. In this work, this vector is assumed to lie within the plane of the mutual orbit, however the actual DART trajectory will have a nonzero inclination relative to the orbit plane. The blue line shows the shape and direction of the nominally assumed circular pre-impact orbit, while the green line shows an exaggerated post-impact orbit. This diagram shows the radar-derived polyhedral primary shape model from (Naidu et al., 2020a) along with an assumed triaxial shape for the secondary. The body shapes and their mutual separation are to scale, while the DART spacecraft and post-impact orbit path are not. The spin poles of both bodies are assumed to be aligned with the mutual orbit pole.

$$\beta = \frac{M(\hat{n} \cdot \Delta\vec{v})}{m(\hat{n} \cdot \vec{u})}. \quad (3.2)$$

In reality, β is a complicated function of the material properties and geometry of both the target and impactor (Stickle et al., 2020). If we assume a head-on impact on a flat surface (allowing us to ignore the impact geometry), we can express β as a simple function of scalars,

$$\beta = 1 + \frac{p_{\text{ejecta}}}{p_{\text{DART}}}, \quad (3.3)$$

where p_{DART} is the scalar momentum carried by the DART spacecraft, and p_{ejecta} is the scalar momentum carried by impact ejecta (which travels in the opposite direction). This expression for β is much simpler than the equation used in practice, as it assumes that p_{ejecta} and p_{DART} are perfectly anti-aligned. However, this version is sufficient for describing *why* β is important: it tells us how much momentum is transferred to the target as a function of the impactor and ejecta momenta. For a more formal description and derivation of β , see Rivkin et al. (2021).

Due to the irregular shapes of both components and their close proximity, the spin and orbit of Dimorphos are highly coupled and non-Keplerian, meaning the dynamics cannot be treated as a simple point-mass 2-body problem. Therefore the use of high-fidelity, full-two-body-problem (F2BP) codes is crucial to understanding the complex dynamics (Agrusa et al., 2020). Further, the shape of Dimorphos is still unknown and could have a major effect on the system’s dynamics. With an assumed triaxial ellipsoid shape for Dimorphos, we explore the post-impact dynamical evolution of the system as a function of the possible axial ratios of the secondary and the momentum transferred by the DART impact (β). In Section 3.2.1, we give some brief background on the Didymos binary and the DART impact’s implications for the secondary’s libration state.

Then Section 3.3 introduces our novel analytic approach and two numerical methods for studying the spin dynamics of Dimorphos. The results for each of these three methods are presented in Section 3.4. Finally, we discuss the implications of our results in Section 3.5.

3.2.1 Background

Although it has not yet been confirmed with observations we nominally assume that Dimorphos is in the 1:1 spin-orbit resonance (i.e., tidally locked)¹. Didymos’s spinning-top shape and fast rotation are suggestive of a rubble-pile structure, owing to likely formation scenarios such as spin-up-driven mass loss (followed by gravitational accumulation of the secondary), or gravitational reaccumulation after a catastrophic disruption (Richardson and Walsh, 2006). In addition, its spin rate exceeds the spin barrier at the nominal bulk density of $\sim 2.17 \text{ g cm}^{-3}$, implying some level of interparticle cohesion and/or higher bulk density (Zhang et al., 2017, 2018, 2021). If Dimorphos and Didymos have a common origin, this suggests that Dimorphos is also a rubble pile. The highly dissipative nature of rubble-pile asteroids implies that the system has had sufficient time for Dimorphos to become tidally locked and enter a dynamically relaxed state (Goldreich and Sari, 2009; Jacobson and Scheeres, 2011a). For these reasons we assume the system’s pre-impact dynamical state is relaxed, meaning the mutual orbit is well-circularized with the secondary in the 1:1 spin-orbit resonance and any free libration is minimized. However, it should be noted that observations have not confirmed such a relaxed state, rather it just has not been ruled out (Naidu et al., 2020a; Pravec et al., 2006; Scheirich and Pravec, 2009). If, upon arrival at the Didymos system, we find that the mutual orbit and secondary spin are already excited,

¹Naidu et al. (2020a) find that the radar bandwidth of secondary is consistent with a spin period equal to the orbit period, suggesting Dimorphos may be in synchronous rotation.

the DART impact will likely further excite the mutual dynamics. Therefore, the results presented in this work should be interpreted as a conservative estimate of the possible impact outcomes.

3.2.1.1 Libration Concepts

The angle between the line-of-centers (LOC) and the secondary’s long axis is commonly referred to as a *libration* angle. In the classic (uncoupled) spin-orbit problem, there are two distinct libration modes: *free* and *forced* (Murray and Dermott, 2000; Naidu and Margot, 2015). Although this paper explores the dynamics of the fully coupled spin and orbital dynamics of the Didymos-Dimorphos system, the insights from the classic spin-orbit problem provide useful intuition for understanding the dynamics when we consider the full problem. For a circular, uncoupled planar orbit, a first-order approximation for the frequency of free libration is given by (see Ch. 5 of Murray and Dermott (2000)),

$$\omega_{\text{lib}} = n \left(\frac{3(B - A)}{C} \right)^{1/2}, \quad (3.4)$$

where n is the mean motion, and A , B , and C are the secondary’s three principal moments of inertia (which correspond to the axis lengths $a \geq b \geq c$). For certain combinations of the three moments of inertia, the free libration frequency can become resonant with the forced libration frequency (i.e., the mean motion) and a *secondary* resonance can occur (Gkolias et al., 2019; Melnikov, 2001). This can lead to an intricate dynamical environment, which only becomes more complicated when we allow for non-zero eccentricity, out-of-plane motion, and a full coupling between the mutual orbit and the spin states of both bodies.

It is important to note that the DART impact will excite both free and forced libration

modes, even if they have been damped to a minimum prior to the impact. The velocity perturbation from DART will increase the binary eccentricity (Cheng et al., 2016), increasing the *forced* libration mode, due to the restoring torque that the secondary feels as it becomes misaligned with the LOC as the orbital angular velocity changes throughout the orbit. With a nearly instantaneous perturbation to the orbital velocity of the secondary, DART will also induce *free* libration modes by creating a difference in its instantaneous orbital and spin angular velocities.

In reality, Dimorphos’s attitude has three degrees of freedom relative to the uniformly rotating orbit frame (roll, pitch, and yaw) and the system could have a nonzero eccentricity and inclination. Therefore, its spin evolution will be more complicated than the two idealized libration modes used here as a conceptual example. Namely, the excited planar libration modes, for particular shapes of the secondary, can induce significant out-of-plane rotation (Eapen et al., 2021; Kane, 1965). Moreover, energy transitions can happen between the planar and out-of-plane rotational degrees of freedom that is attributed to resonant phenomena (Breakwell and Pringle, 1965). We will see that the excitation of Dimorphos’s libration state, primarily due to the excitation of nonplanar rotation, can lead to chaotic motion. Chaotic rotation has been observed for many other bodies in our solar system such as the triple system (47171) Lempo, Saturn’s Hyperion, and Pluto’s outer four satellites, to name a few examples (Correia, 2018; Showalter and Hamilton, 2015; Wisdom et al., 1984).

3.2.1.2 Euler Angles

In this work, we treat the “libration angle” as simply the angle between the long-axis of the secondary and the line-of-centers. As described above, in the classic spin-orbit problem, this

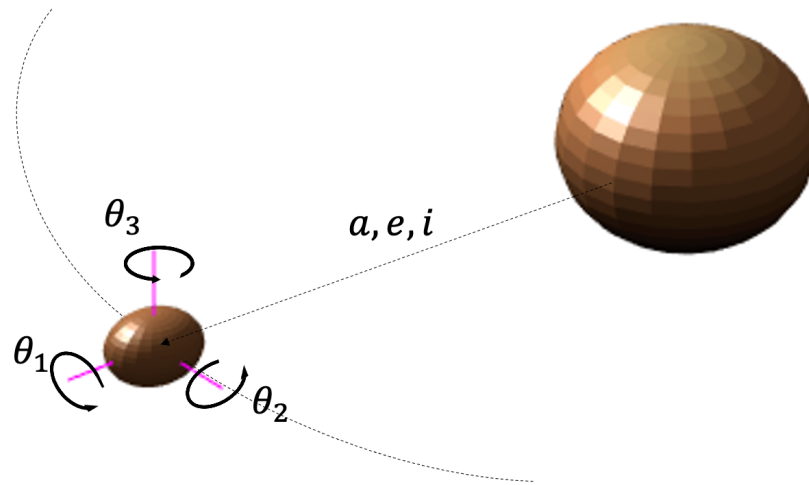


Figure 3.2: Schematic showing the Euler angle set for Dimorphos. θ_1 is the roll angle, θ_2 is pitch, and θ_3 is yaw. In the diagram, the pink axis markers point *out* of Dimorphos, and the angles rotate in the sense of the right-hand rule. The angles are defined such that all three angles are equal to zero when the secondary’s body-fixed frame is aligned with the orbital frame. (Image credit: Meyer and Scheeres (2021))

angle would be purely within the plane of the orbit. However, we will see that this angle will have nonplanar components if the secondary’s attitude becomes unstable.

Instead of just looking at the libration angle, we can examine all three Euler angles that make up the secondary’s attitude. We use the 1-2-3 Euler angle set (roll-pitch-yaw) shown in the diagram on Fig. 3.2, where the Euler angles give Dimorphos’s attitude in the frame rotating with the orbit. At each simulation output the rotating frame is defined as follows: the x -axis points along the LOC, the z -axis is the direction of the mutual orbit pole (i.e., the orbital angular momentum vector), and the y -axis completes the right-handed triad. A direction cosine matrix between the secondary’s body-fixed frame to the rotating frame is constructed, from which the three Euler angles are computed. See Appendix B of Schaub et al. (2009) for the precise mathematical derivation of this Euler angle set.

The Euler angles θ_2 (pitch) and θ_3 (yaw) can be thought of as two libration angles; θ_2 is

analogous to an out-of-plane (latitude) libration, and θ_3 is analogous to the planar (longitude) libration. Due to the ordering sequence of the Euler angles, this is only technically true when θ_1 is exactly zero, which we will see is not the case. However, thinking about θ_3 and θ_2 as the respective planar and non-planar components of the secondary’s libration can be a useful conceptual tool.

3.3 Methods

In Section 3.3.1, we use an analytic approach to investigate the attitude stability and presence of resonant libration frequencies of Dimorphos, under the assumption that the primary is a uniform sphere and that the system is in an equilibrium state (i.e., a circular orbit)². Then we employ two numerical codes to study the attitude dynamics of Dimorphos following a DART-like perturbation to the relative velocity of Dimorphos. The first code, described in Section 3.3.2, computes a coupled planar (2D) orbit between an oblate spheroid (Didymos) and a triaxial ellipsoid (Dimorphos) and parametrically inserts the solution into Euler’s rigid body equations to follow Dimorphos’s attitude in 3D. In Section 3.3.3, we introduce the second numerical code, which uses the radar-derived shape model for Didymos and computes the fully coupled spin and orbital evolution of the system. To clarify, all three models used in this work have at least some degree of spin-orbit coupling, each with increasing levels sophistication. Finally, our approach to

²The assumption that the pre-impact orbit is relaxed and circular is made for a few reasons. First, ground-based observations have not placed a lower limit on the mutual eccentricity and three studies have derived upper limits of 0.03, 0.04, and 0.05 (Scheirich and Pravec (2009), Fang and Margot (2012), Naidu et al. (2020a), respectively). Second, if the two components are rubble piles (for reasons laid out in Section 3.2.1), then we would expect tides to quickly damp the system to an equilibrium state (Goldreich and Sari, 2009). Third, assuming a relaxed pre-impact state means that the post-impact dynamics predicted by this work can be interpreted as a conservative estimate. In other words, the predictions made in this work should be considered a “lower limit” for the excitation of Dimorphos’s spin state resulting from the DART impact. If the binary is already excited prior to DART, then the impact may only further excite the system.

setting up the initial conditions for the numerical simulations is detailed in Section 3.3.4.

3.3.1 Analytic Dynamics Model

Here we develop an analytic, linearized approach to calculating Dimorphos's fundamental frequencies as a function of its semi-axes. Previous work has addressed this problem using a variety of simplifying assumptions. The first to estimate the uncoupled frequencies was Lagrange in his 1764 essays on the libration of the Moon (**fraser1983**). Modern day derivations can be found in various textbooks; Murray and Dermott (2000) provide the planar libration frequency (i.e., Eq. (3.4)) and Curtis (2020) gives the non-planar frequencies. Also, Fleig (1970) derives fundamental frequencies for a triaxial satellite, with a good discussion on the role of resonances with the offplane frequencies (see Appendix A.1.3). Scheeres (2006) developed an approach for this computation using an arbitrary body and a sphere, which is used by Fahnestock and Scheeres (2008) to solve for analytic expressions of the four fundamental frequencies around a synchronous equilibrium applied to the binary system Moshup (previously 1999 KW4). In the simplest analytic approximation, Fahnestock and Scheeres (2008) assume a spherical primary and report the frequencies as a function of the secondary's shape. This is further expanded to fourth-order by Boué and Laskar (2009), where the mutual interactions between the bodies are considered and report good estimates for the precession and nutation frequencies for Moshup. For our purposes, the simpler approach outlined in Scheeres (2006) and Fahnestock and Scheeres (2008) is sufficient to provide an idea of the expected behavior in the system, which we expand upon here.

The potential energy between two bodies taken to a second-order approximation is (Scheeres,

2009):

$$V = \frac{-GM_1M_2}{R} - \frac{G}{2R^3}[M_1\text{Tr}(I_2) + M_2\text{Tr}(I_1)] + \frac{3G}{2R^5}\vec{R} \cdot [M_1A_2^T I_2 A_2 + M_2A_1^T I_1 A_1] \cdot \vec{R} \quad (3.5)$$

where A_i is the matrix transforming from the frame in which the relative position vector \vec{R} is specified to body-fixed coordinates, with the subscript 1 and 2 referring to the primary and secondary, respectively. The inertia tensors of the primary (I_1) and secondary (I_2), are written in their respective body-fixed frames. For the spherical restricted full two-body problem, body 1 is a sphere while body 2 is an arbitrary 3D massive asteroid. Since body 1 is a sphere, the term $\vec{R} \cdot A_1^T I_1 A_1 \cdot \vec{R}$ can simply be written as $R^2 I_S$ where I_S is the diagonal entry of I_1 (i.e., the moment of inertia of a uniform sphere) and $\text{Tr}(I_1)$ reduces to $3I_S$, thus the higher-order terms involving body 1 disappear.

If the position vector \vec{R} is written in the frame of body 2, A_2 then becomes the identity matrix. With these simplifications, the second-order potential energy becomes:

$$V = \frac{-GM_1M_2}{R} - \frac{G}{2R^3}[M_1\text{Tr}(I_2)] + \frac{3G}{2R^5}\vec{R} \cdot [M_1 I_2] \cdot \vec{R}. \quad (3.6)$$

The equations of motion for this model, taken in the body-fixed frame of the secondary, are:

$$\ddot{\vec{R}} + 2\vec{\Omega} \times \dot{\vec{R}} + \dot{\vec{\Omega}} \times \vec{R} + \vec{\Omega} \times (\vec{\Omega} \times \vec{R}) = -\frac{1}{m} \frac{\partial V}{\partial \vec{R}}, \quad (3.7)$$

$$I\dot{\vec{\Omega}} + \vec{\Omega} \times I\vec{\Omega} = \vec{R} \times \frac{\partial V}{\partial \vec{R}}, \quad (3.8)$$

where we drop the subscript on I , which is the inertia tensor of the secondary (body 2). Here, $\vec{\Omega}$ is the angular velocity of the frame of the secondary and m is the reduced mass: $m = \frac{M_1 M_2}{M_1 + M_2}$.

This problem can be normalized by introducing a length scale α (equal to the body separation) and mean motion $n = \sqrt{G(M_1 + M_2)}/\alpha^3$. With this convention, we define,

$$r \equiv \frac{R}{\alpha} \quad (3.9)$$

$$\omega \equiv \frac{\Omega}{n} \quad (3.10)$$

$$\mathcal{I} \equiv \frac{I}{M_2 \alpha^2}. \quad (3.11)$$

The equations of motion can now be rewritten as,

$$\ddot{\vec{r}} + 2\vec{\omega} \times \dot{\vec{r}} + \dot{\vec{\omega}} \times \vec{r} + \vec{\omega} \times (\vec{\omega} \times \vec{r}) = -\frac{\partial \mathcal{V}}{\partial \vec{r}}, \quad (3.12)$$

$$\mathcal{I} \dot{\vec{\omega}} + \vec{\omega} \times \mathcal{I} \omega = \nu \vec{r} \times \frac{\partial \mathcal{V}}{\partial \vec{r}}, \quad (3.13)$$

where we introduce a mass fraction $\nu = \frac{M_1}{M_1 + M_2}$ ($\nu \simeq 0.99$ for the Didymos system) and the normalized potential energy,

$$\mathcal{V} = \frac{-1}{r} - \frac{1}{2r^3} [\text{Tr}(\mathcal{I})] + \frac{3}{2r^5} \vec{r} \cdot [\mathcal{I}] \cdot \vec{r}. \quad (3.14)$$

Defining the state vector as $\vec{X} = [\vec{r}, \dot{\vec{r}}, \vec{\omega}]^T$, the state dynamics can thus be written as,

$$\dot{\vec{X}} = \begin{bmatrix} \dot{\vec{r}} \\ -2\tilde{\omega}\dot{\vec{r}} + \tilde{r}\dot{\omega} - \tilde{\omega}\tilde{\omega}\vec{r} - \frac{\partial \mathcal{V}}{\partial \vec{r}} \\ \mathcal{I}^{-1} \left[-\tilde{\omega}\mathcal{I}\vec{\omega} + \nu\vec{r} \times \frac{\partial \mathcal{V}}{\partial \vec{r}} \right] \end{bmatrix} = \vec{F}(\vec{X}), \quad (3.15)$$

where we introduce the tilde notation for the cross product skew-symmetric operator. Then, the equilibrium conditions are:

$$\dot{\vec{r}} = \dot{\omega} = 0 \quad (3.16)$$

$$\tilde{\omega}\tilde{\omega}\vec{r} = -\frac{\partial \mathcal{V}}{\partial \vec{r}} \quad (3.17)$$

$$\tilde{\omega}\mathcal{I}\vec{\omega} = \nu\vec{r} \times \frac{\partial \mathcal{V}}{\partial \vec{r}}. \quad (3.18)$$

With these equilibrium conditions, the linearized dynamics matrix at equilibrium can be calculated:

$$\frac{\partial \vec{F}}{\partial \vec{X}} \Big|_{\vec{X}_0} = \begin{bmatrix} [\mathbf{0}]_{3 \times 3} & [\mathbf{U}]_{3 \times 3} & [\mathbf{0}]_{3 \times 3} \\ \nu\tilde{r}\mathcal{I}^{-1} \left[\tilde{r}\frac{\partial^2 \mathcal{V}}{\partial \vec{r}^2} - \frac{\partial \mathcal{V}}{\partial \vec{r}} \right] - \tilde{\omega}\tilde{\omega} - \frac{\partial^2 \mathcal{V}}{\partial \vec{r}^2} & -2\tilde{\omega} & \tilde{r}\mathcal{I}^{-1} \left[-\tilde{\omega}\mathcal{I} + \mathcal{I}\tilde{\omega} \right] + \tilde{\omega}\tilde{r} + \tilde{\omega}\tilde{r} \\ \nu\mathcal{I}^{-1} \left[-\frac{\partial \mathcal{V}}{\partial \vec{r}} + \tilde{r}\frac{\partial^2 \mathcal{V}}{\partial \vec{r}^2} \right] & [\mathbf{0}]_{3 \times 3} & \mathcal{I}^{-1} \left[-\tilde{\omega}\mathcal{I} + \mathcal{I}\tilde{\omega} \right] \end{bmatrix}, \quad (3.19)$$

where $[\mathbf{U}]_{3 \times 3}$ is the unitary matrix. This gives the linearized dynamics equation about the equi-

librium:

$$\begin{bmatrix} \delta \dot{\vec{r}} \\ \delta \ddot{\vec{r}} \\ \delta \dot{\vec{\omega}} \end{bmatrix} = \left. \frac{\partial \vec{F}}{\partial \vec{X}} \right|_{\vec{x}_0} \begin{bmatrix} \delta \vec{r} \\ \delta \dot{\vec{r}} \\ \delta \vec{\omega} \end{bmatrix}. \quad (3.20)$$

Fahnestock and Scheeres (2008) calculate the dynamics matrix to obtain a simplified expression, from which they derive equations for the four fundamental frequencies after reducing the matrix to 8×8 . We will step through the process of reducing this matrix using the angular momentum integral. However, rather than obtaining expressions for the frequencies, we will directly solve for them using spectral decomposition of the reduced dynamics matrix.

The magnitude of the angular momentum provides an integral of motion allowing us to reduce the dynamics matrix from 9×9 to 8×8 . In practice, this leads to eliminating the ω_3 (x_9) contribution, which would otherwise result in a zero eigenvalue. To reduce the matrix, we can break the problem up as:

$$\delta \dot{\vec{X}} = \begin{bmatrix} A_y & A_{8 \times 1} \\ A_{1 \times 8} & A_9 \end{bmatrix} \begin{bmatrix} \delta \vec{y} \\ \delta x_9 \end{bmatrix} \quad (3.21)$$

where \vec{X} is the state, \vec{y} is the first 8 states (excluding x_9), and the full linearized dynamics matrix is called A , which we have broken up into convenient submatrices. This allows us to write

$$\delta \dot{\vec{y}} = A_y \delta \vec{y} + A_{8 \times 1} \delta x_9. \quad (3.22)$$

The angular momentum magnitude integral, H , is linearized and written as,

$$\frac{\partial H}{\partial \vec{X}} \delta \vec{X} = 0, \quad (3.23)$$

where the angular momentum vector is defined as,

$$\vec{H} = \mathcal{I} \vec{\omega} + \nu \vec{r} \times (\dot{\vec{r}} + \vec{\omega} \times \vec{r}). \quad (3.24)$$

This can be expanded by again splitting the state:

$$\frac{\partial H}{\partial \vec{y}} \delta \vec{y} + \frac{\partial H}{\partial x_9} \delta x_9 = 0. \quad (3.25)$$

Finally we can write:

$$\delta x_9 = \frac{\partial H}{\partial \vec{y}} \delta \vec{y} \left(\frac{-\partial H}{\partial x_9} \right)^{-1}. \quad (3.26)$$

Substituting this in gives,

$$\delta \dot{\vec{y}} = A^* \delta \vec{y}, \quad (3.27)$$

with,

$$A^* = A_y - A_{8 \times 1} \frac{\partial H}{\partial \vec{y}} \left(\frac{\partial H}{\partial x_9} \right)^{-1}. \quad (3.28)$$

At an equilibrium point it becomes possible to calculate the A^* matrix and in turn find its spectral decomposition, with the zero eigenvalue corresponding to ω_3 removed. The presence of real components in any of the eigenvalues of A^* would correspond to unstable motion. Furthermore, the eigenvalues can be leveraged to find resonances between the system's fundamental fre-

quencies. Using this approach, we can compute the fundamental frequencies of the secondary’s motion as a function of its axial ratios a/b and b/c . The results of this analytic approach will be described later in Section [3.4.1](#).

3.3.2 Simplified 3D Dynamics Model

The “simplified 3D model” is an efficient approximation of the mutual spin-orbit dynamics that captures Dimorphos’s libration behavior. First, the mutual orbit is integrated based on the equations of motion in which the mutual potential is expanded to second-order, accounting for the primary’s J_2 moment and the secondary’s ellipsoidal shape (McMahon and Scheeres, [2013](#)). Although the full shape model of Didymos is not used, its J_2 moment alone is a reasonable approximation due to its fast rotation. The equations of motion for the orbit are described in detail in Appendix [A.1.1](#).

The 3D spin and attitude of the secondary are then integrated via Euler’s rigid-body equations for a triaxial ellipsoid (Wisdom et al., [1984](#)), using the mutual orbit found in the previous integration (see Appendix [A.1.2](#)). It is important to note that for small variations from the planar solution (small obliquity of the spin axis) the rotation of Dimorphos matches the planar one very closely. Only when the precession of the spin axis is significantly excited does the model fail to produce the correct 3D spin-orbit coupled motion, due to the lack of conservation of the total angular momentum of the system. However, because it is unlikely that the DART impact will induce an *immediate* large-amplitude precession in the secondary, this simplified approach lends itself to being an extremely efficient way of studying the secondary’s attitude dynamics, over a wide range of possible shapes and other parameters. In any case, this approach is valid for

small deviations from the planar case or short-term integrations and is sufficient for deducing the attitude stability properties under perturbations. For this purpose, it is necessary to derive also the linearized (variational) equations of the system, which are integrated simultaneously with the equation of motion, to derive the stability properties (see Appendix [A.1.2](#)).

3.3.3 The GUBAS Full Two-body Problem code

The General Use Binary Asteroid Simulator (GUBAS) is a novel F2BP code that uses the inertia integral method for evaluating the mutual potential between two arbitrary rigid bodies. The mathematical formulation for inertia integrals is described in Hou et al. (2017) and implemented in a fast, open-source³ C++ code with a Python-based user interface (Davis and Scheeres, 2020a). The code has several options for integration scheme, body-shape representations, and gravity expansion order. In the results presented here, we use the Lie group variational integrator and a fixed timestep of 40.0 seconds, which has been shown to give numerically converged results for this system (Agrusa et al., 2020). The primary is represented by its radar-derived shape model (Naidu et al., 2020a), the secondary is a triaxial ellipsoid with adjustable axial ratios, and the mutual gravity is expanded to 4th order. The equations of motion are then integrated, with the mutual orbit and body spins fully coupled. See Davis and Scheeres (2020a) for more details on this code.

3.3.4 Problem Set Up

In this paper, we are exploring the binary orbital evolution solely under the influence of the mutual gravitational potential. Both bodies are considered to be fully rigid with the same

³The code is available at <https://github.com/alex-b-davis/gubas>

bulk density. This study considers much shorter timescales than those associated with higher-order perturbations such as mutual tides, YORP, BYORP, and solar gravity, which are ignored here. In the simulations presented in this work, we use an integration time of one year. This timescale is long enough to allow for any strong attitude instabilities to set in, but short enough that higher-order perturbations to the mutual orbit can be safely ignored.

We assume that the mutual orbit is initially planar, with the spin poles of both bodies aligned with the mutual orbit pole. Further, we assume the pre-impact orbit is nearly circular and that the secondary is in the 1:1 spin-orbit resonance with the libration amplitude damped to a minimum. We adopt the latest observed parameters from the DART Design Reference Asteroid (DRA), namely, the primary and secondary sizes, the binary semimajor axis, and the binary orbit period. These parameters are listed and referenced in Table 3.1. In order to achieve the assumptions listed above, and to match the observed DRA parameters (namely the measured orbit period, which has been measured to high precision), we use an optimization scheme to determine our initial conditions for the GUBAS simulations⁴. A naive approach using Kepler’s 3rd law to derive the mass of the system is invalid due to the non-spherical shapes and close proximity of the two components. Therefore, our initial-conditions-optimization scheme adjusts the total mass of the system (assuming the primary and secondary have the same bulk density), until it finds a mass where the simulated orbit period matches the observed period. This process is able to generate initial conditions that match the observed orbit period to high precision that also have a small libration amplitude and nearly circular orbit. This means that when the shape of the secondary is changed (although its total volume is conserved), the system mass and bulk density change

⁴This procedure is only required for GUBAS, as it uses the polyhedral shape model for the primary and evaluates the mutual gravity to 4th order. However, this procedure can be done analytically for the simplified 3D model (see Appendix A.1.1).

slightly. The mass and density adjustments are small ($< 1\%$) and allow us to match the observed orbit period to the highest precision possible because the orbit period is so well constrained. The details of this optimization routine can be found in Appendix [A.2](#).

For each choice of the secondary’s axis ratios a/b and b/c , the optimization scheme is used to derive the pre-impact relaxed state of the system. Then, the orbital speed of the secondary is altered according to our choice for β . Based on the most recent DART flight plans at the time of this writing, the choice for spacecraft mass and relative speed were 535 kg and 6.6 km s^{-1} , respectively. These values are subject to change by small amounts, but are not expected to change drastically. With the head-on, planar impact considered in this work, Eq. (3.1) can be simplified to give the perturbation to the secondary’s orbital speed:

$$\Delta v = -\beta \frac{M_{\text{DART}} v_{\text{DART}}}{M_{\text{B}}}, \quad (3.29)$$

where M_{DART} and v_{DART} are the respective mass and speed of the DART spacecraft, and M_{B} is the mass of Dimorphos. The change in speed is negative because the nominal impact trajectory impacts the leading face of Dimorphos (head-on impact), causing it to slow down, fall onto a tighter orbit, and reduce the orbit period. The real DART trajectory will result in an impact with Dimorphos at an angle relative to the mutual orbit plane that varies with launch date within a range of roughly 5–30 degrees. However, in this work, we assume an idealized head-on impact with no out-of-plane component. We also assume that the impact is aligned with the center of mass, such that there is no instantaneous torque imparted to Dimorphos. We leave the more realistic treatment of the impact geometry to future work. We note that a non-planar and off-center impact will likely excite the secondary’s spin state significantly more than in an idealized, head-

Parameter	Value	Reference(s)
Diameter of Primary D_P	780 ± 30 m	Naidu et al. (2020a) (equivalent spherical diameter)
Diameter of Secondary D_S	164 ± 18 m	Naidu et al. (2020a) and Scheirich and Pravec (2009)
Semi-major Axis a_{orb}	1.19 ± 0.03 km	Naidu et al. (2020a)
Binary Orbit Period P_{orb}	11.9217 ± 0.0002 h	Scheirich, P., personal communication (2020) ^a
Primary Spin Period P_P	2.2600 ± 0.0001 h	Pravec et al. (2006)

Table 3.1: Physical parameters of the Didymos binary based on lightcurve and radar observations. We assume that the binary eccentricity and inclination are both zero. The initial conditions for the simulations presented here match all of these parameters, and all other initial conditions (i.e., masses and velocities) are derived from these parameters.

^aThe best available orbital solution at the time of this work.

on impact. Therefore, the results presented in this work may be *underestimating* the perturbation to Dimorphos’s spin state.

3.4 Results

3.4.1 Analytic Model Results

We performed a grid search over the solution space of axis ratios, ranging from $1 < a/b < 1.5$ and $1 < b/c < 1.5$. Due to the lack of a well-constrained shape for Dimorphos, the parameter space was instead selected because of an observed upper-limit of binary asteroid satellites with elongations $a/b > 1.5$ in the near-Earth, Mars-crossing, and small main belt populations (Pravec et al., 2016). For each value of a/b and b/c , the inertia tensor is computed for a uniform triaxial ellipsoid and normalized. The dynamics matrix, A^* (Equation (3.28)), is then evaluated for each value of a/b and b/c at their respective equilibrium points. We find that all eigenvalues over this solution space are purely imaginary, which indicates stable motion about the equilibrium point.

Because the spectral decomposition produces eight conjugate frequencies, there are only four unique values leading to four fundamental frequencies. The four fundamental frequencies from this analysis are represented by their period in Fig. 3.3. These four frequencies correspond to the in-plane free libration (i.e., Equation (3.4)), the orbital frequency (mean motion), and two out-of-plane frequencies, related to the precession and nutation of the secondary.

Although the eigenvalue analysis naively indicates stable motion about the equilibrium (due to imaginary eigenvalues), we find a multitude of resonances among the fundamental frequencies upon closer examination. The resonance locations can be found by simply searching for locations in the solution space where one fundamental frequency becomes commensurate with another. These resonances indicate areas in the solution space in which this linear model is no longer accurate, and nonlinear effects become important. Figure 3.4 shows each resonance between the various fundamental frequencies up to 5:1. It will turn out that some of these resonances will drive unstable motion in the full nonlinear problem, with the single 1:1 and three of the 2:1 resonances being the most dominant.

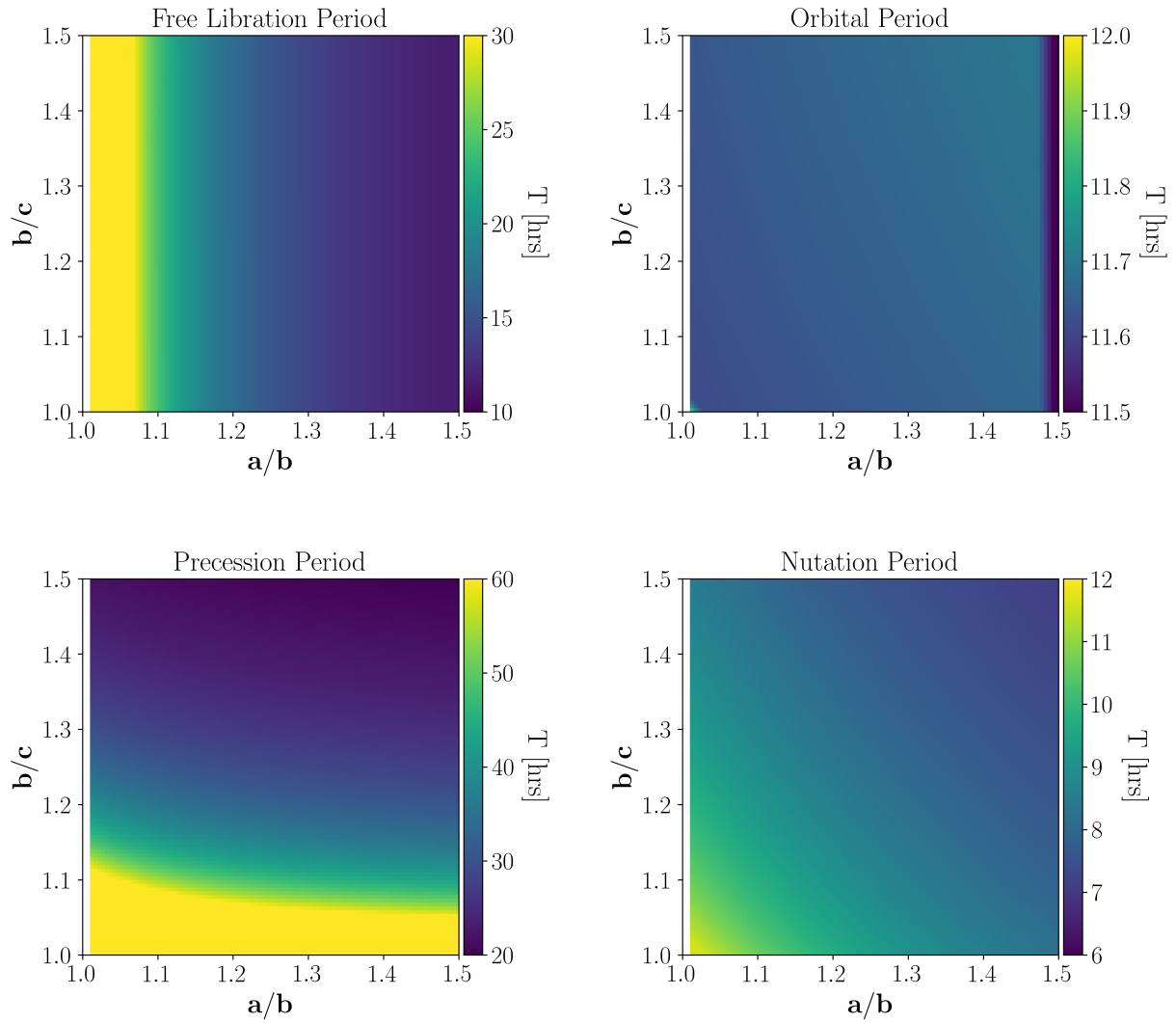


Figure 3.3: The four fundamental periods of motion about the equilibrium point, shown in hours. The free libration period is very similar to the frequency given in Eq. (3.4). The two nonplanar periods correspond to the secondary’s spin precession and nutation periods.

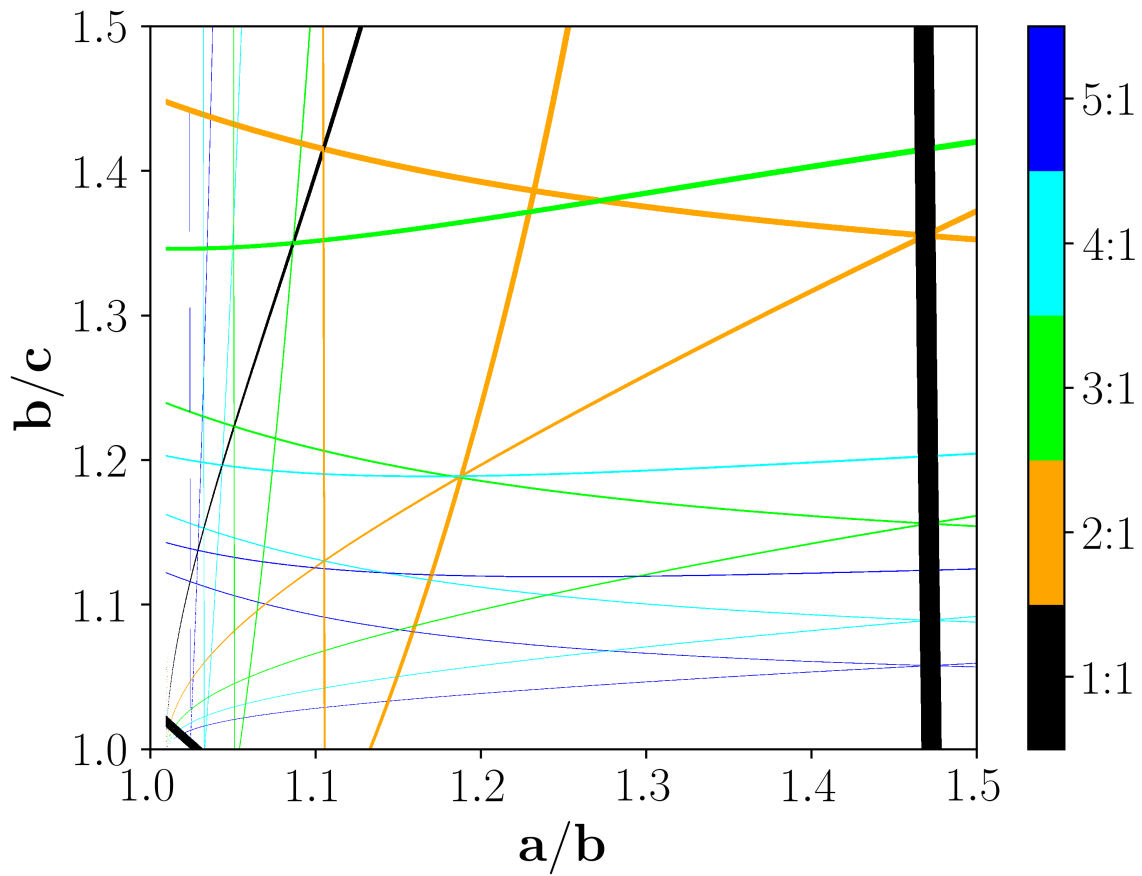


Figure 3.4: The resonances of the four fundamental frequencies up to 5:1. The line weight is a reflection of the width of each resonance region, although each resonance is ideally a line. Thus, thicker lines allow for a wider range of secondary shapes to excite that resonance. Note that these lines are all continuous, and any lines that look dotted or dashed are due to the resonance width being smaller than the resolution of the grid search.

3.4.2 Simplified 3D Dynamics Results

To be clear, in the previous section, we found the fundamental frequencies and resonance locations for Dimorphos at equilibrium (i.e., a uniform, circular orbit). Then, with the simplified 3D model (and later with GUBAS), we add a perturbation to Dimorphos’s relative velocity according to a given choice for β to study the post-impact attitude stability. The results of Section 3.4.1 do not depend on β and only apply to the case the pre-impact circular orbit. However, Section 3.4.1 provides insight for understanding the mechanisms that drive attitude instability when Dimorphos’s orbit is perturbed.

Using the simplified 3D model, we first computed the fast Lyapunov indicator (FLI) for each combination of a/b and b/c using the simplified 3D model for $\beta = 1$ and $\beta = 3$. The FLI is a useful and widely used tool for detecting weak chaos in dynamical systems (Froeschlé et al., 1997), and is a measure of the exponential divergence in phase space of two solutions with infinitesimally separated initial conditions. The resulting FLI map is shown in Fig. 3.5. It should be noted that a run for $\beta = 0$ (i.e., the pre-impact, relaxed state) yields a fully regular phase space. This has further been confirmed via a Floquet analysis of the relaxed states, which showed that all computed eigenvalues indicated stable motions. Moreover, this finding is in agreement with the analytical approach of Section 3.4.1.

Based on the shape of the instability region identified in the FLI analysis, the chaotic motion seems to be primarily driven by four key resonances, which are given on Table 3.2. It should first be noted that the frequencies and resonances given in Table 3.2 are the uncoupled frequencies described in Appendix A.1.3. In reality, the true frequencies and resonance locations are slightly different (and more complicated) and the uncoupled frequencies are only meant to be a

qualitative indicator here. In this case, the uncoupled resonances do an adequate job in predicting the locations of resonances.

The three prominent frequencies seem to be the mean motion, n^{uc} , the free libration frequency, ω_{lib}^{uc} , and the secondary's spin precession frequency, ω_{prc}^{uc} . These frequencies have the superscript uc to indicate that they are *uncoupled* and merely an approximation to the real frequency. To first order, the free libration frequency is approximated by Eq. (3.4). For a uniform triaxial ellipsoid, the principal moments of inertia can be rewritten in terms of the corresponding semi-axis lengths a , b , and c . The libration frequency, ω_{lib}^{uc} is in a 1:1 resonance with the mean motion when $a/b = \sqrt{2}$ and a 2:1 resonance when $a/b = \sqrt{13/11}$. These resonances appear as two faint vertical lines on Fig. 3.5a and are referred to as \mathcal{R}_4 and \mathcal{R}_3 , respectively, in Table 3.2.

The secondary's spin precession frequency, ω_{prc}^{uc} , is more complicated and is given in Appendix A.1.3. For certain combinations of a/b and b/c , ω_{prc}^{uc} can enter a 2:1 resonance with ω_{lib}^{uc} or a 2:1 resonance with n . These two resonances make up the two wing-like structures in Fig. 3.5a and are called \mathcal{R}_1 and \mathcal{R}_2 , respectively, in Table 3.2. These four resonances among the three frequencies are certainly not the only ones playing a role in the structure of the instability region, but seem to be the dominant contributors.

The maximum libration angle achieved for each secondary shape after a one-year simulation is shown in Fig. 3.6. This angle is not necessarily entirely within the orbit plane and can have nonplanar components that we investigate later. When the libration angle exceeds 90° , we consider Dimorphos to have broken from synchronous rotation, which is shown in white on the plot. Even for $\beta = 1$, we see there are a significant number of cases in which the libration angle has exceeded 90° , and when $\beta = 3$, nearly half of the parameter space has exceeded 90° . We find that the cases where the libration amplitude exceeds 90° are largely correlated to chaotic

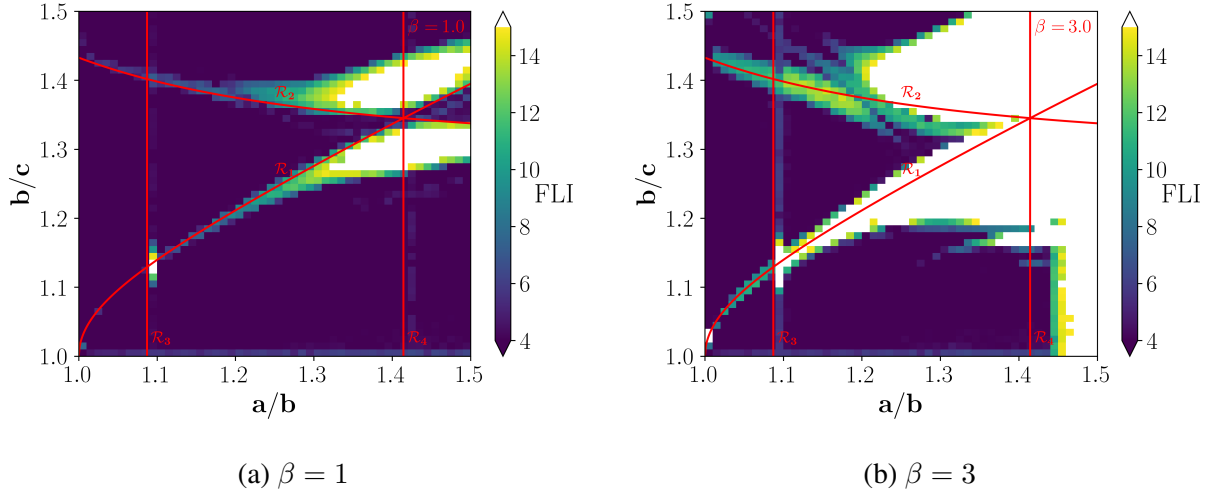


Figure 3.5: A fast Lyapunov indicator map of the parameter space, with larger values indicating unstable, chaotic motion in the secondary’s spin state. The uncoupled resonance locations from Table 3.2 are overlaid to show the dominant drivers of instability.

Name	Resonance
\mathcal{R}_1	$\omega_{\text{lib}}^{uc} = 2\omega_{\text{prc}}^{uc}$
\mathcal{R}_2	$n^{uc} = 2\omega_{\text{prc}}^{uc}$
\mathcal{R}_3	$n^{uc} = 2\omega_{\text{lib}}^{uc}$
\mathcal{R}_4	$\omega_{\text{lib}}^{uc} = n^{uc}$

Table 3.2: The four main resonances driving Dimorphos’s attitude instability. ω_{lib}^{uc} is the free libration frequency of the secondary, n^{uc} is the mean motion, and ω_{prc}^{uc} is the spin precession frequency of the secondary. We use the superscript uc to indicate that these frequencies are uncoupled and are only approximations of their real value in the fully coupled problem.

motion identified by the FLI. The four resonances identified in the FLI analysis are overlaid onto the libration plots to show the qualitative agreement between the analytic, uncoupled resonance locations and the instability regions. However, when the secondary’s spin state becomes significantly excited (i.e., large nonplanar oscillations), the simplified 3D model is no longer valid, requiring the use of a fully coupled solver.

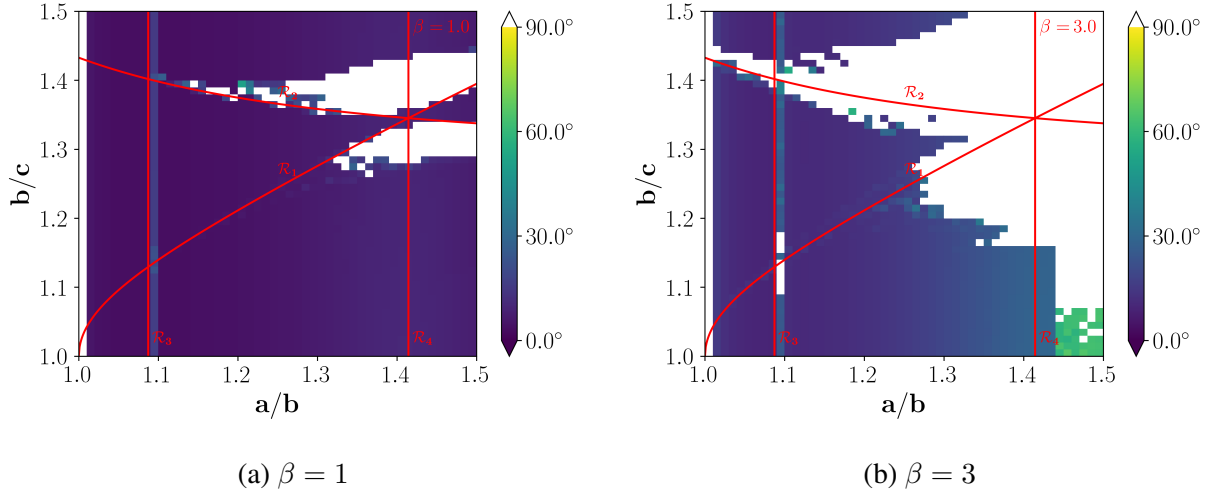


Figure 3.6: The maximum libration amplitude for $\beta = 1$ and $\beta = 3$ as a function of the secondary’s axial ratios a/b and b/c , according to the simplified 3D model. When the libration angle exceeds 90° , the satellite has broken from synchronous rotation. The *uncoupled* resonance locations from Table 3.2 are overlaid to show the dominant drivers of instability.

3.4.3 GUBAS Results

Equivalent simulations were run in GUBAS over the full parameter space of a/b and b/c for β values of 1, 3, and 5. The core differences between the two simulation codes is the use of the radar-derived polyhedral shape model for the primary, expansion of the mutual gravitational potential to higher order (4th), and full coupling between the body spins and mutual orbit. The maximum libration amplitude achieved over the course of the one-year simulations is shown in Fig. 3.7 for $\beta = 1$ and $\beta = 3$. Again, the libration angle is considered to be the angle between Dimorphos’s long axis and the LOC, which is not necessarily planar. When $\beta = 1$, no cases exceed 90° and only a select few do at $\beta = 3$. The libration amplitudes are quite large, but much smaller than those in the simplified 3D model runs. This is a direct result of Dimorphos traveling on a fully coupled orbit rather than the predetermined one in the simplified model. Put simply, the secondary transfers excess spin energy to the mutual orbit, keeping the libration amplitude

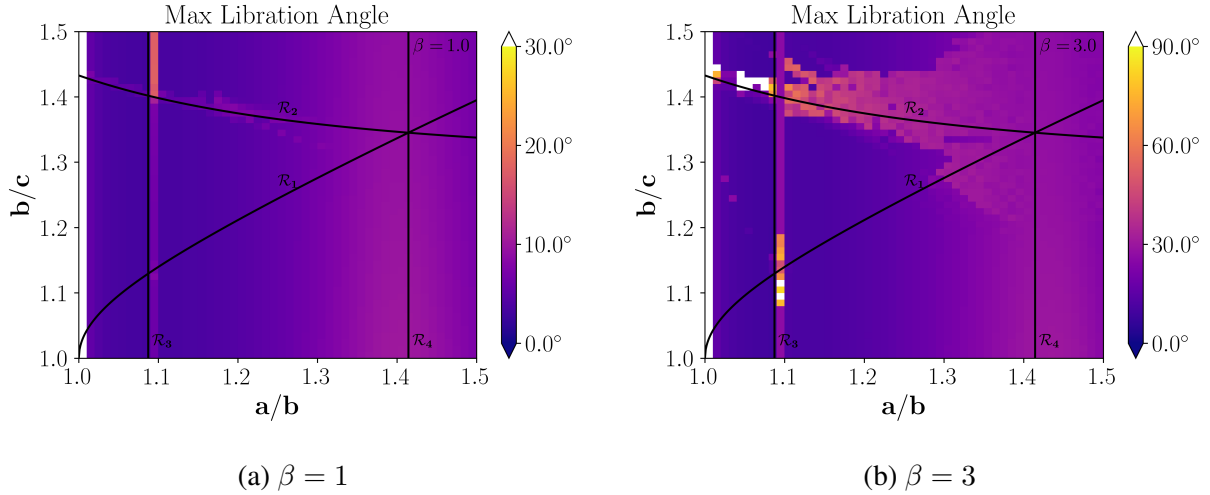


Figure 3.7: The maximum libration amplitude in GUBAS simulations with the theoretical resonances from Table 3.2 overlaid. We recover the same general dynamical structure seen in the simplified 3D model. However, the libration amplitudes are far smaller than those in the simplified model (Fig. 3.6), and only a few cases ever exceed the 90° threshold for leaving synchronous rotation. Note the different colorbar scales for 3.7a and 3.7b.

from exceeding 90° . The libration amplitudes are still relatively large however, and given the chaotic nature of Dimorphos’s tumbling state, it is possible that these cases could break from synchronous rotation after longer integration times.

3.4.3.1 Dimorphos’s attitude instability

Instead of looking at just the libration angle defined as the angle between Dimorphos’s long axis and the LOC, we can examine the 1-2-3 Euler angle set that make up the secondary’s attitude as described in Section 3.2.1. Figure 3.8 shows a time series of the three Euler angles for the simulation where $\beta = 1$ for two different shapes of the secondary. Fig. 3.8a shows the Euler angles for a secondary in which $a/b = 1.3$ and $b/c = 1.2$, which represents a typical simulation in which the secondary’s attitude remains stable. The roll and pitch angles remain small, hovering around zero, while the yaw angle steadily librates around an equilibrium. Changing the shape

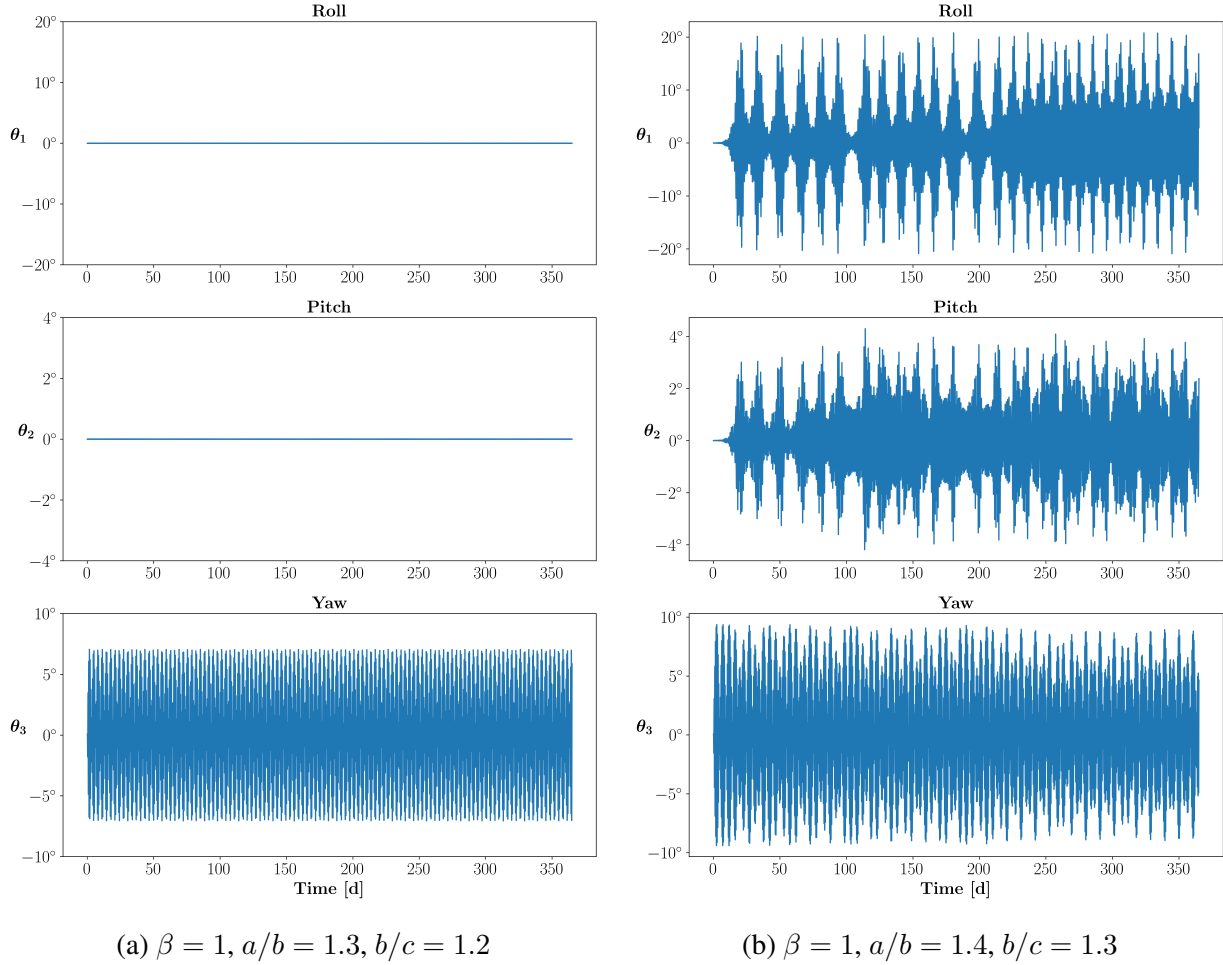


Figure 3.8: Time-series plots of the secondary’s three Euler angles for two different secondary shapes: $a/b = 1.3, b/c = 1.2$ (a typical stable case) and $a/b = 1.4, b/c = 1.3$ (a typical unstable case). Note the difference in angle-axis scales for each Euler angle. The time axis shows the time since the DART impact (impact occurs at time = 0).

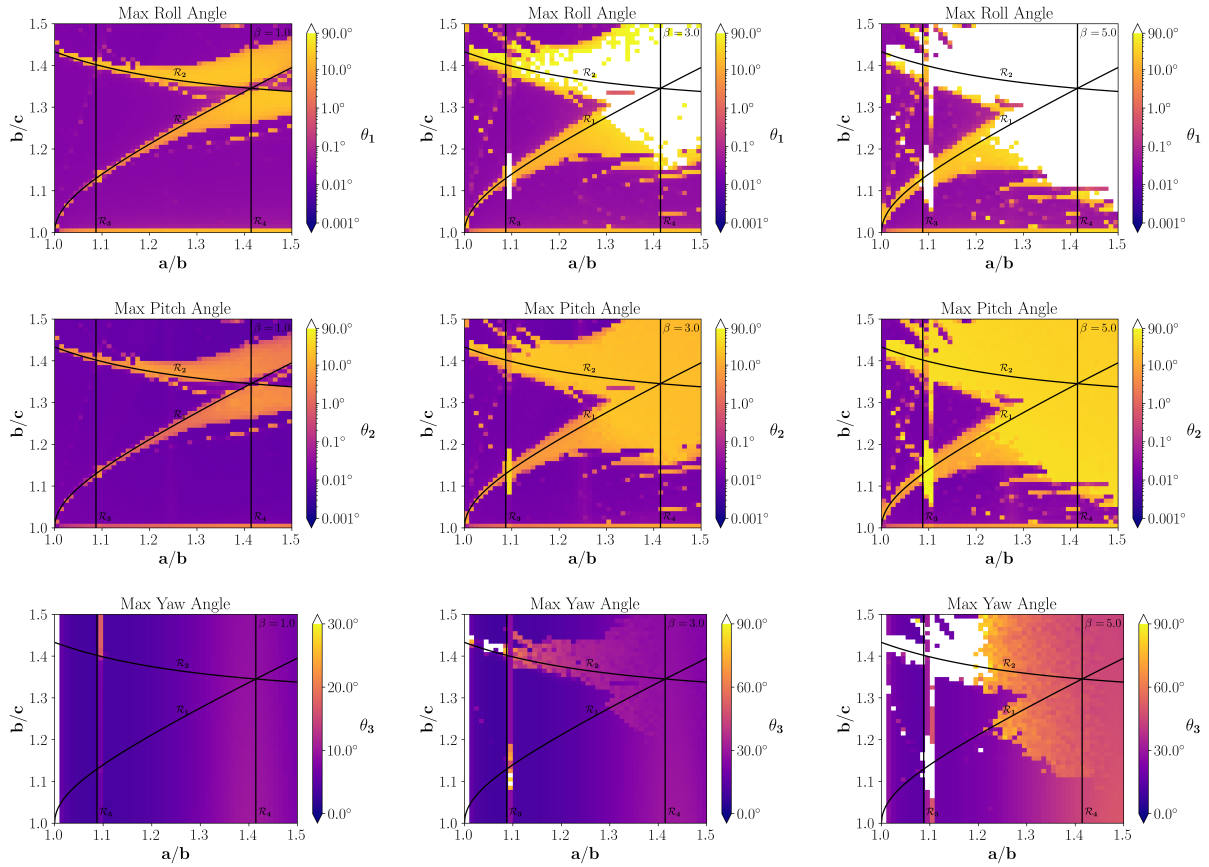
only slightly to $a/b = 1.4$ and $b/c = 1.3$, Fig. 3.8b shows a typical example where the secondary’s attitude becomes unstable. Roughly ~ 10 days after the DART impact, the secondary’s roll and pitch angles become excited, reaching angles of $\sim 20^\circ$ and $\sim 4^\circ$ respectively. After the initial excitement of the roll and pitch angles, there is a continuous energy exchange between the planar and nonplanar degrees of freedom, indicated by the simultaneous changes in the roll and pitch angles.

The attitude stability over the full parameter space when $\beta = 1$ is shown on Fig. 3.9a,

with the maximum roll, pitch, and yaw angles achieved by Dimorphos over the full simulation. When Dimorphos’s attitude is broken into its constituent components, we can see very clearly that the same resonances found with the simplified 3D model are driving the instabilities in the fully coupled problem. The most significant result here is the tendency for more-elongated secondaries to roll about their long axis, reaching angles of nearly 90° (almost rolling over), an effect that would have gone unnoticed by just computing the libration angle.

Figure 3.9b shows the maximum Euler angles when $\beta = 3$. Note the difference in color-bar scale for the yaw angle between Figs. 3.9a and 3.9b. When β is increased to 3, we see the overall shape of the instability region stay the same, with the size of the region and magnitude of the maximum angle increasing. The most obvious difference is that many of the more-elongated secondaries exceed a roll angle of 90° , indicating that they have either rolled over or are continuously rolling. In most of these cases, the secondary has rolled over without technically breaking from synchronous rotation (defined by the libration angle exceeding 90°). The implications for this are discussed in Section 3.5.2. We also see that a select few cases have exceeded 90° in yaw near the intersection of resonances.

Finally, for completeness, we show the same maximum Euler angle plots when $\beta = 5$ in Fig. 3.9c, where over half of the parameter space has become unstable and exhibits chaotic tumbling motion. To get a rough understanding of what this tumbling motion looks like over time, we show time-series plots of the three Euler angles for two shapes of the secondary on Fig. 3.10. Fig. 3.10a corresponds to $a/b = 1.29$ and $b/c = 1.30$, which lies in the “stable island” near the middle of the parameter space from Fig. 3.9c. This subplot shows regular, stable motion over the course of the entire year. Shown in Fig. 3.10b, the attitude instability sets in after ~ 15 days, with long-axis rolling commencing at ~ 60 days when the b/c axis ratio is changed only



(a) Max Euler angles, $\beta = 1$. (b) Max Euler angles, $\beta = 3$. (c) Max Euler angles, $\beta = 5$.

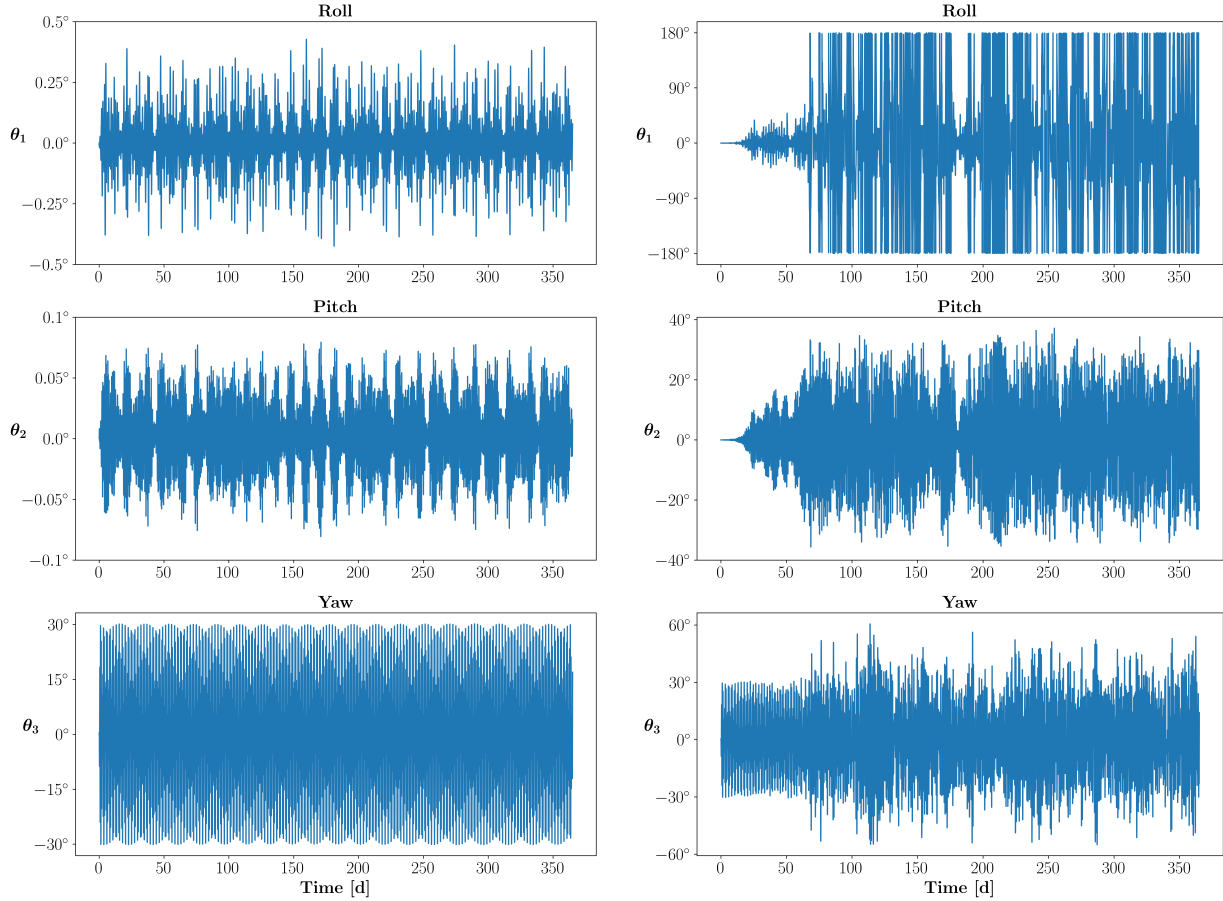
Figure 3.9: The maximum Euler angles over a one-year simulation for $\beta = 1, 3$ and 5 . Cases that exceed 90° are shown in white. The pitch angle (θ_2) is defined between 0° and 90° , and therefore never exceeds 90° . The uncoupled, analytic resonance locations from Table 3.2 are overlaid. Over half of the parameter space is attitude unstable, dominated by rolling about the secondary's long axis, when $\beta = 5$.

slightly from 1.30 to 1.31. This highlights how sensitive the instability can be to the shape of the secondary. To put this in perspective, the physical extents along each axis of these two body shapes differ by a fraction of a meter compared to the ~ 100 m scale of the full axes, yet one enters a chaotic spin state and the other remains stable.

3.5 Discussion

3.5.1 Implications of a post-impact tumbling state

One concern about a post-impact tumbling state is that the periodic (and chaotic) exchange of angular momentum between the mutual orbit and Dimorphos's spin state could affect the post-impact ground-based measurements of the orbit period. This could cause a portion of the orbit period change to be misattributed to the DART impact, and complicate the estimate of β based on the orbit period change, which is a Level 1 mission requirement. To get a rough idea of how important this effect might be, we compare the energy of the mutual orbit (which determines the orbit period) with Dimorphos's spin energy. To first order, we can estimate the energy in the mutual orbit by assuming the bodies behave as point-masses, so the problem reduces to a Keplerian orbit. Then the orbital energy can be written as $E_{\text{orb}} \simeq -\frac{GM_{\text{A}}M_{\text{B}}}{2r}$, where M_{A} and M_{B} are the respective body masses, r is the binary semimajor axis, and G is the standard gravitational parameter. The secondary's spin energy can be written as $E_{\text{B}} = \frac{1}{2}C\omega^2$, where C is Dimorphos's largest principal moment of inertia, and ω is the spin rate. If Dimorphos is a uniform ellipsoid in synchronous rotation, we can write $E_{\text{B}} = \frac{1}{2}\frac{M_{\text{B}}}{5}(a^2 + b^2)\left(\frac{2\pi}{P_{\text{orb}}}\right)^2$, where a and b are Dimorphos's semimajor and semi-intermediate axis lengths, and P_{orb} is the binary orbit period. Choosing axial ratios for Dimorphos that lie in the middle of the parameter space studied



(a) $\beta = 5$, $a/b = 1.29$, $b/c = 1.30$
 $a = 105.40597$ m
 $b = 81.71005$ m
 $c = 62.85389$ m

(b) $\beta = 5$, $a/b = 1.29$, $b/c = 1.31$
 $a = 105.67555$ m
 $b = 81.91903$ m
 $c = 62.53361$ m

Figure 3.10: Time-series plots of the secondary's three Euler angles for two different secondary shapes: $a/b = 1.29$, $b/c = 1.30$ (a stable case) and $a/b = 1.29$, $b/c = 1.31$ (an unstable case). The physical semi-axis lengths are listed in the subcaptions. Although these two shapes differ by a fraction of a meter in their respective semi-axes lengths, their attitude evolutions vary drastically. Note the different angle-axis scales on each plot. Again, the DART impact occurs at time = 0.

in this work ($a/b = b/c = 1.25$) along with nominal parameters for the system,⁵ we find a value of $E_B/E_{\text{orb}} \simeq 0.25\%$ ⁶, meaning that the energy in Dimorphos’s rotation is much less than the energy of the mutual orbit. This indicates that even relatively large changes in Dimorphos’s spin state should be small compared to the energy in the mutual orbit, meaning that any spin-state-induced changes to the orbit period should be a small effect. In other words, spin-orbit coupling or a chaotic tumbling state is unlikely to affect the Level 1 requirement to measure β . The uncertainties in the β measurement will be dominated by uncertainties in Dimorphos’s mass, the impact location and surface normal, and the ejecta cone geometry (Rivkin et al., 2021). However, a focused study on secular changes to the mutual orbit resulting from a tumbling secondary could be valuable. This effort is planned for future work, as this study concentrated only on Dimorphos’s spin state resulting from the DART impact.

If Dimorphos begins chaotically tumbling, it is possible but highly unlikely to be detected via ground-based observations, given the required precision to measure sufficiently small fluctuations in the lightcurve (Pravec, P., personal communication, 2021). Of course, this is dependent on the details of Dimorphos’s shape, the observing geometry, and available telescope facilities, but even under ideal conditions, such a measurement is likely unachievable from the ground during the first few years after the impact. However, if the tumbling persists for several years, Hera will be able to provide detailed measurements upon arrival (Michel et al., 2018). In particular, the Hera mission design requirements state that the spin pole orientation shall be measured to a precision of 1° , and therefore, Hera will be able to accurately characterize any deviation larger than that. The visible and infrared cameras as well as the radio science on-board Hera can all be

⁵Based on current observations and an assumed Keplerian orbit, we have $M_{\text{sys}} = 5.37 \times 10^{11}$ kg, $M_B = 4.97 \times 10^9$ kg, $r = 1190$ m, $P_{\text{orb}} = 11.9217$ h. Further, if $a/b = b/c = 1.25$, we have $a = 101.875$ m and $b = 81.5$ m.

⁶A similar approach can be used for the spin and orbital angular momenta, where we get $L_B/L_{\text{orb}} \simeq 2 \times 10^{-5}$.

used to constrain Dimorphos’s spin state, provided sufficient accuracy in the orientation and position of the spacecraft. Hera’s two CubeSats, especially once landed on the surface, will increase the measurement precision of Dimorphos’s spin state. The synergies between the instruments of Hera will thus offer the opportunity to investigate the rotational state of Dimorphos, checking the predictions and consequences of the DART impact. We note that a chaotic tumbling state should not influence most of Hera operations. However, if Dimorphos is tumbling, the attitude reconstruction of Hera will have to rely on star tracking until the rotation state is constrained well enough to rely on landmarks. Only during very close proximity operations, like close flybys, will Dimorphos’s spin state need to be taken into account. This could potentially add challenges for close operations with the CubeSats and their landing trajectories.

3.5.2 The Barrel Instability

The “barrel instability” is a low-energy instability in which an elongated secondary in an eccentric orbit enters a long-axis rotation state while remaining tidally locked (Ćuk et al., 2020). We find similar behavior in the simulations presented here (indicated by large roll angles), suggesting that a post-impact rolling state about the long axis is a possible outcome. The GUBAS simulations show that the secondary can rotate about its long axis, even if the secondary’s long axis remains aligned with the line of centers (i.e., libration angle $< 90^\circ$).

Through the YORP effect, the spins of asteroids can be altered by the absorption of sunlight and anisotropic re-emission as thermal radiation resulting in a net torque (Rubincam, 2000). This process has an analog for binary systems, commonly referred to as the binary-YORP or BYORP effect, whereby a tidally-locked satellite’s thermal emission contributes a net torque to

the mutual orbit, leading to secular changes in the mutual orbit’s semimajor axis and eccentricity (Ćuk and Burns, 2005). Because the BYORP effect requires a synchronous secondary, a rolling or tumbling state resulting from a DART-like impact would terminate the BYORP process, even if the secondary’s long axis remains aligned with the LOC.

The orbital solution for the Didymos binary is achieved by fitting the timing of mutual events to an orbit model (Scheirich and Pravec, 2009). The model includes the quadratic drift of the secondary’s mean anomaly due to secular changes in the semimajor axis that result from the combined effect of BYORP and tides. Based on historical data and recent observations during the 2020–2021 apparition, the latest best-fit solution to Dimorphos’s mean anomaly acceleration is $0.13 \pm 0.14 \text{ deg yr}^{-2}$ (Scheirich and Pravec, personal communication, 2021). The mean anomaly acceleration corresponds to a drift in the mean motion of $\dot{n} = 4.45 \pm 4.91 \times 10^{-18} \text{ rad s}^{-2}$ and a drift in the semimajor axis of $\dot{a} \simeq -0.076 \text{ cm yr}^{-1}$. The measured mean anomaly acceleration is extremely small, with the 3-sigma uncertainty including zero, meaning that any secular changes to the orbit are small, if not zero. This implies that Dimorphos may be in (or very close to) a BYORP-tide equilibrium, a state predicted analytically by Jacobson and Scheeres (2011b) in which tides and BYORP effectively cancel each other. If the DART impact excites an attitude instability, the resulting rolling and/or tumbling motion of Dimorphos would shut off the BYORP process (Ćuk et al., 2020). Because secular changes in the semimajor axis due to tides do not require a synchronous secondary⁷ (Goldreich and Sari, 2009; Murray and Dermott, 2000), the termination of BYORP would allow the mutual orbit to begin to evolve solely under the influence of tides. It should be noted here that we do not know how effective the tides are at suppressing

⁷Although spin synchronization of the secondary is the fastest tidal process, it is not a prerequisite for the mutual orbit to expand through tides. So the mutual orbit would evolve concurrently as the secondary begins to re-synchronize.

Dimorphos's attitude instability. It may be possible, but unlikely, that tides could shrink the parameter space of cases that become attitude unstable to begin with. Or, tides may suppress the attitude instability after it has begun, so that the system finds the BYORP-tide equilibrium again. In either case, this knowledge could be used to place a constraint on the tidal parameters of the system.

If, however, the BYORP effect is terminated due to an attitude instability, it could present a unique opportunity to constrain the tidal parameters of the system. Under the assumption that Didymos is currently in a BYORP-tide equilibrium, the quantity BQ/k can be estimated from observable quantities, where B is the BYORP coefficient, Q is the tidal quality factor, and k is the tidal Love number. The BYORP coefficient, B , is a unitless parameter that depends only on the shape of the secondary and quantifies the degree of symmetry of the body. The quality factor Q describes the efficiency of energy dissipation through tides (Goldreich and Soter, 1966). Finally, the Love number k describes the gravitational response of a body to tides and can be thought of as the ratio of additional gravitational potential produced by a body in response to the perturbing potential to the perturbing potential itself. Jacobson and Scheeres (2011b) derive an equation for BQ/k_p for a binary asteroid in BYORP-tide equilibrium,

$$\frac{BQ}{k_p} = \frac{2\pi\omega_d^2\rho R_p^2 q^{4/3}}{H_\odot (a/R_p)^7}, \quad (3.30)$$

where k_p is the Love number of the primary, ω_d is the spin-disruption limit, ρ is the bulk density of both bodies, R_p is the radius of the primary, q is the secondary-to-primary mass ratio, H_\odot is the radiation pressure, and a is the binary semimajor axis. The spin disruption limit can be written as $\omega_d = \sqrt{4\pi G\rho/3}$ and we assume that both the primary and secondary have the same bulk density,

so there is only one value for ρ . We can also write $H_{\odot} = F_{\odot}/(a_{\odot}^2\sqrt{1-e_{\odot}^2})$, where a_{\odot} and e_{\odot} are the heliocentric semimajor axis and eccentricity, and F_{\odot} is the solar radiation constant, which is $\sim 10^{22}$ g cm s⁻² (McMahon and Scheeres, 2010).

Based on nominal parameters for Didymos from the literature, we have $\rho = 2.17$ g cm⁻³, $R_p = 390$ m, $q = 0.00926$, $a_{\odot} = 1.644$ au, and $e_{\odot} = 0.384$ (Naidu et al., 2020a; Pravec et al., 2006; Scheirich and Pravec, 2009)⁸. Plugging in numbers, we find $BQ/k_p \simeq 555$. A proper treatment of error propagation would show that the uncertainties on BQ/k can be relatively large (Jacobson and Scheeres, 2011b), due to the uncertainties in all the observable parameters. However, these will decrease with future ground-based observations and DART imagery leading up to the moment of impact.

If the secondary then enters a tumbling state following the DART impact, BYORP will shut off and the system will evolve primarily through tides. After such an excitation, the tides between the binary components will dissipate energy working to bring it back to a minimum energy state. Spin synchronization, the fastest-evolving tidal process, will be driven by tides raised on the secondary by the primary. Meanwhile, tides raised on the primary by the secondary will act to increase the mutual semi-major axis and eccentricity. However, tides raised on the secondary will act to damp the eccentricity along with the radial and librational tides (Goldreich and Sari, 2009; Murray and Dermott, 2000). The “barrel instability”, or rolling about the secondary’s long axis will not be damped by any of these tides. However, it is sensitive to obliquity tides so long as the secondary’s spin axis is unaligned with the mutual orbit pole. Given the limited knowledge of Q/k for asteroids and the relative strengths of each tidal mechanism, we provide a simple order-

⁸These values are derived or taken from the listed references. Note that they may be slightly different than the values used in the simulations presented in this paper

of-magnitude estimate for only the rate of change in the semimajor axis due to the tides raised on the primary by the secondary. If the tides are strong enough, then it may be possible to measure a secular change in the mean anomaly (and therefore the semimajor axis), either through ground-based observations or when Hera makes its rendezvous in 2026. If a change in the semimajor axis can be measured ($\frac{da}{dt}$), then it would be possible to estimate Q/k to constrain the tidal properties of the system. For low eccentricity, the rate of change in the semimajor axis can be approximated as (Goldreich and Sari, 2009),

$$\frac{1}{a} \frac{da}{dt} = 3qn \frac{k_p}{Q} \left(\frac{R_p}{a} \right)^5, \quad (3.31)$$

where n is the mean motion. Although the ratio k/Q (or Q/k) is commonly used to parameterize a body's tidal response, its value and scaling relationship with other physical properties remain open questions for rubble piles. For example, Goldreich and Sari (2009) find that k should scale linearly with the body's radius, while Jacobson and Scheeres (2011b) find that the scaling should vary inversely with the radius. For a Didymos-like system, Nimmo and Matsuyama (2019) suggest that $Q/k \sim 10^5$. For the sake of demonstration, we can plug this value into Eq. (3.31) to get an estimate of $\frac{da}{dt} \simeq 0.58 \text{ cm yr}^{-1}$. Although this is a small number, a value of $\sim 1 \text{ cm s}^{-1}$ has been measured for near-Earth binary Moshup through ground-based measurements of the system's mean anomaly acceleration (Scheirich et al., 2021). In addition, the rendezvous of the Hera spacecraft will make it possible to make much-higher-precision measurements than are possible from the ground. Furthermore, spin synchronization is the fastest-evolving tidal process, meaning that Hera should be able to measure a secular change to Dimorphos's spin if its semimajor axis drift is also measurable.

The BYORP coefficient, B , depends only on the secondary's shape, and can therefore be calculated from a shape model which will become available after the DART impact (and refined with Hera measurements). Scheirich et al. (2015) show that an independent measurement of B derived from a shape model can be combined with an independent measurement of BQ/k at the BYORP-tide equilibrium to obtain a non-degenerate solution for both B and Q/k . When a shape model for Dimorphos is created, it will be possible to do this, so long as the system is actually in the BYORP-tide equilibrium prior to impact. Although this approach will be dependent on the resolution scale of the shape model and further complicated by the fact that the crater formed by DART will slightly alter Dimorphos's shape and affect B . If the barrel instability is triggered following the impact, a separate, independent measurement of Q/k can be made using Eq. (3.31). Therefore it may be possible to have three independent measurements constraining the BYORP and tidal evolution of the system: BQ/k prior to impact, Q/k after impact, and B from the secondary's shape model.

Such a measurement of the tidal and BYORP parameters of the system is of course complicated by a variety of factors. First, an excitation of the secondary's spin state could induce local slope failure, leading to possible deformation and surface motion. This would create a direct dynamical effect on the system's evolution if the secondary's shape changes plus additional energy dissipation due to surface motion that would muddle any measurement of tidal dissipation. Second, the crater created by the DART impact could have a minor effect on the secondary's mass distribution and potentially a major effect on its BYORP coefficient, given the high sensitivity of B to the body shape. Third, the primary's spin rate sits right at the critical spin limit for a non-cohesive spherical body, meaning that the acceleration required to loft material near the surface is quite small. There is a possibility that "tidal saltation", a process by which the tidal acceleration

of the secondary lofts material off the surface of the primary (Harris et al., 2009). This results in a transfer of angular momentum from the primary to the mutual orbit as the material is lofted and falls back to the surface. This process would enhance the effect of tidal evolution in addition to serve as a 'breaking' mechanism that prevents YORP spin-up from driving the primary beyond its critical spin limit. A related effect could be larger global-scale reshaping of Didymos and its effect on the mutual orbit (Hirabayashi et al., 2017, 2019). These examples are only a select few effects that could lead to long-term changes to Dimorphos's mutual orbit and spin state that could complicate any future measurements of the system's tidal parameters. “

3.6 Conclusions

We presented three independent methods—one analytic and two numerical—to study the attitude dynamics of Dimorphos. The analytic model found four fundamental periods of motion relating to the mean motion and the free libration, precession, and nutation frequencies of the secondary. At the resonance locations among these various frequencies, we predicted that unstable motion could be possible. Then, using the “simplified 3D model”, we simulated the post-impact attitude evolution of the secondary when $\beta = 1$ and 3, where we found several of the predicted resonances and verified that they did produce unstable motion. Using fast Lyapunov indicators, we demonstrated that the secondary's attitude evolves chaotically at the resonance locations. Then, using GUBAS, we verified the results of the simplified 3D model. We found that the simplified 3D model predicted the instability regions correctly but overestimated the magnitude in the libration amplitudes, but GUBAS (or any other fully-coupled F2BP code) is necessary to accurately predict the amplitude of oscillations in the instability regions. The GUBAS simula-

tions also demonstrated that the secondary is especially prone to unstable rotation about its long axis. The implications for a post-impact tumbling and/or rolling state were discussed, including the consequences for Hera, the possibility of terminating any BYORP drift, and measuring the tidal parameters of the system.

In this work, we assumed an idealized impact in which the DART momentum is transferred entirely within the mutual orbit plane with no instantaneous change to the secondary's spin (i.e., a centered impact). In reality, the DART momentum vector will nominally be misaligned with respect to the mutual orbit plane by an angle between 5° and 30° with respect to the orbit plane, imparting some nonplanar motion to the mutual orbit. In addition, the DART impact is unlikely to be perfectly aligned with the center of mass, and will deliver an instantaneous torque to the secondary. We expect that these effects will lead to the development of attitude instabilities at earlier times and make a larger portion of the parameter space unstable. In addition, the pre-impact state of the system was in an idealized relaxed dynamical state. For these reasons, the results presented in this work should be viewed as a *lower bound* on Dimorphos's post-impact spin dynamics. The exploration of non-planar, off-center impacts, including non-relaxed pre-impact states is planned for future work.

Finally, with ongoing GUBAS code development, including a tidal evolution model, we plan to explore the role that tides may play in the Didymos system. As a function of the tidal parameters k and Q , we will investigate the likelihood of exciting the attitude instabilities demonstrated in this work, and predict the dissipation of Dimorphos's spin state, if excited. This may make it possible to predict the binary orbital evolution on timescales relevant to the Hera mission.

Chapter 4: Rubble-pile modeling of the Didymos system

4.1 Chapter Preface

This chapter was published in *The Planetary Science Journal* under the title, “Dynamical evolution of the Didymos-Dimorphos binary asteroid as rubble piles following the DART impact” (Agrusa et al., 2022a). This paper was written as a follow-up to Agrusa et al. (2021) (Chapter 3) in order to fulfil another DART Investigation Task Plan item to understand the role that a “rubble pile” structure might play in the ensuing post-impact dynamics. The first part of this paper verified the post-impact spin state predictions of the previous rigid-body simulations. Then the second half explored regimes where the rubble-pile nature of either Didymos or Dimorphos may play an important role in the dynamics, where we found that an unusual secondary shape or a high value of β may necessitate the use of the N -body methods to treat each component as a gravitational aggregate. However, in “typical” circumstances, we found that the rigid-body methods of previous studies should be sufficient to propagate the post-impact spin and orbital evolution of Dimorphos.

Although I led the study, much of it would have been impossible without major contributions from my collaborators. Fabio Ferrari provided Sections 4.3.3 and 4.5.1 and Yun Zhang provided Section 4.4.2. This chapter is presented with minimal modification from its previously published version. Some of the introductory material may be somewhat repetitive with the Chap-

ter 1, so the reader may skip to Section 4.3 if desired.

4.2 Introduction

Launched on November 24, 2021 and arriving at the Didymos system on September of 26, 2022, NASA's Double Asteroid Redirection Test (DART) will be the first planetary defense-oriented mission to conduct a kinetic impact on an asteroid (Cheng et al., 2018; Rivkin et al., 2021). The target of the mission is Dimorphos, the smaller component of the binary asteroid 65803 Didymos. The DART spacecraft will intercept Dimorphos, making an approximate head-on impact, which will slow Dimorphos's relative speed, leading to a reduction in the mutual semimajor axis and orbit period of the binary system. The change in orbit period can then be measured using ground-based observations (Naidu2022; Pravec et al., 2022) to ultimately infer the momentum enhancement factor, β , a unitless quantity that describes how much net momentum is transferred to the target body (Rivkin et al., 2021; Stickle et al., 2022). Prior to DART's kinetic impact, the spacecraft will deploy the Light Italian CubeSat for Imaging of Asteroids (LICIAcube) cubesat, which will fly by the system, imaging the early stages of the cratering process as well as provide images of the system from different angles to improve Dimorphos's shape determination, and possibly provide information on the surface characteristics. (Cheng et al., 2022; Dotto et al., 2021; Pajola et al., 2022). Lead by the European Space Agency, the Hera spacecraft will then visit Dimorphos 4 yr after the DART impact. Hera consists of an orbiter and two cubesats, called Juventas and Milani, that will fully characterize the physical (including interior), compositional, and dynamical states of the system (Michel et al., 2018). Hera will also further assess the impact effects, in particular the size and morphology of the crater left by DART

in addition to a precise measurement of Dimorphos’s mass in order to improve the estimate of β (Michel et al., 2022). Together, DART and Hera constitute the Asteroid Impact and Deflection Assessment (AIDA) cooperation between the two space agencies.

The shape, spin, and size of Didymos in addition to the mutual orbit period and average separation of the binary are relatively well understood (Fang and Margot, 2012; Naidu et al., 2020a; Scheirich and Pravec, 2009, 2022). However, both the shape and spin state of Dimorphos are poorly constrained. It is often assumed that Dimorphos is in a relaxed, tidally locked state, meaning that its spin period matches the measured mutual orbit period of ~ 11.9216 hr and its libration amplitude is small, although this has not yet been directly confirmed (Richardson et al., 2022). Regardless of Dimorphos’s preimpact dynamical state, DART’s perturbation to the mutual orbit will likely excite Dimorphos’s spin state as a result of the high degree of spin-orbit coupling due to the irregular shapes of both components and their close proximity. The degree of excitation will be highly dependent on the magnitude of β , in addition to Dimorphos’s shape, which is assumed to be a tri-axial ellipsoid and commonly parameterized by its ellipsoidal axis ratios a/b and b/c , with $a \geq b \geq c$. Using rigid, full two-body simulations, Agrusa et al. (2021) demonstrated that Dimorphos can become attitude unstable, and its spin state could evolve chaotically as a result of the impact, depending on its shape (i.e., moments of inertia). However, it is unclear how relaxing the rigid-body formalism to allow the bodies to behave as rubble piles will affect the binary dynamics and attitude-stability properties of Dimorphos.

The fast rotation rate and oblate shape of Didymos is indicative of a rubble-pile structure (Walsh, 2018). Furthermore, if Dimorphos has a common origin (YORP-induced fission or mass loss and subsequent reaccumulation in orbit, for example), then it is quite plausible that both bodies are rubble piles (Jacobson and Scheeres, 2011a; Walsh et al., 2008). Therefore, extending

previous rigid-body studies to include granular physics while maintaining high-fidelity modeling of the mutual spin and orbital dynamics represents an important next step in simulating the post-impact evolution of the Didymos binary. This work presents our first steps at studying and constraining the dynamical implications of a rubble-pile treatment. Therefore, we focused our efforts on understanding the limits at which rubble-pile effects are important. Assuming that Didymos and/or Dimorphos are confirmed to be rubble piles upon DART’s arrival, the parameter space of possible body shapes, particle-size distributions, etc., will also be greatly reduced, allowing us to eventually have a better handle on the relative importance of rubble-pile effects.

As a point of clarification, this work focuses on the dynamical evolution of the system when one or both bodies are treated as rubble piles and allowed to deform *over time*. In this work, we do not consider immediate deformation due to the DART impact itself. We refer the reader to the companion papers by Hirabayashi et al. (2022) and Nakano et al. (2022) that model the direct deformation of Didymos or Dimorphos due to the DART impact and propagate the resulting system as rigid bodies. The degree of shape deformation that DART will cause is unclear, as it depends on many unknowns such as the bulk density, cohesion, boulder distribution, among many other parameters. Recent numerical simulations by Raducan and Jutzi (2022) indicate that a DART-scale impact could significantly deform and resurface Dimorphos if it has low cohesive strength. This nonzero possibility of significant impact-induced shape change is something to consider in future work, depending on the outcome of the DART impact. Combined imagery from DART and LICIAcube will be crucial in determining the impact outcome prior to Hera’s arrival.

In Section 4.3, we introduce the simulation codes employed in this work and briefly describe how these simulations are set up. Section 4.4 compares the mutual dynamics of the system

when treated as rubble piles versus rigid bodies and finds that rigid-body and rubble-pile models are in broad agreement in typical circumstances. Then, Section 4.5 explores the limits at which the rubble-pile structure of Didymos or Dimorphos may affect the dynamics and, conversely, the limits at which the dynamics may affect the structure of either body. Finally, Section 4.6 summarizes this research and discusses future work to follow after the DART impact.

4.3 Methodology

We study the dynamics of the Didymos binary system with self-gravitating, rubble-pile models of Didymos and Dimorphos using the N -body granular physics codes PKDGRAV and GRAINS. In addition, the GUBAS full two-body problem (F2BP) code is used as an additional point of comparison with rigid-body results. For convenience, we provide the current best estimates for the physical and dynamical parameters at the time of this writing in Table 4.1. These parameters can also be found in Appendix A of Rivkin et al. (2021), but are updated here with the latest values as of this writing based on the Design Reference Asteroid v. 3.2 (DRA; DART mission internal document). These values may not necessarily match *exactly* those used in the simulations presented here, although they are all close and within the estimated uncertainties of the system. The three codes used in this work are briefly described below.

4.3.1 GUBAS

The General Use Binary Asteroid Simulator (GUBAS) is an open-source¹ simulation tool that can quickly solve for the coupled spin and orbital motion of two arbitrarily shaped rigid

¹The code is available at <https://github.com/alex-b-davis/gubas> and can be effectively run with a single core on a desktop computer.

Parameter	Value
Volume-equivalent Diameter of Primary D_P	780 ± 30 m
Volume-equivalent Diameter of Secondary D_S	164 ± 18 m
Bulk Densities of Components ρ_P	2170 ± 350 kg m ⁻³
Mean Separation of Component Centers a_{orb}	1.20 ± 0.03 km
Secondary Shape Elongation $a/b, b/c$	$1.3 \pm 0.2, 1.2$ (assumed)
Total Mass of System M	$(5.55 \pm 0.42) \times 10^{11}$ kg
Secondary Orbital Period P_{orb}	11.9216289 ± 0.0000028 h
Secondary Orbital Eccentricity e_{orb}	< 0.03
Primary Rotation Period P_P	2.2600 ± 0.0001 h
Secondary Rotation Period P_S	P_{orb} (assumed tidally locked)
Secondary Orbital Inclination i_{orb}	0° (assumed)

Table 4.1: Selected dynamical parameters from Rivkin et al. (2021) and updated with the latest values of this writing (DRA v. 3.2).

masses with high fidelity (Davis and Scheeres, 2020a, 2021). GUBAS has been benchmarked against other F2BP codes, formally adopted for rigid-body modeling of the Didymos system for the DART mission (Agrusa et al., 2020), and successfully used to model the Didymos–Dimorphos binary (Agrusa et al., 2021; Meyer et al., 2021). In this work, we consider the motion of the two bodies solely under their mutual gravity.

4.3.2 PKDGRAV

PKDGRAV is a massively parallel N -body tree code that can represent each component of the Didymos system as an aggregate of many spherical particles (Richardson et al., 2000; Stadel, 2001). In this work, the k -d tree code is not used, so the gravitational forces on each particle are computed by summing directly over all particles at each time step to ensure the highest possible accuracy at the expense of computational speed (i.e., the full $\mathcal{O}(N^2)$ N -body problem). The contact forces on interacting particles are handled using the soft-sphere discrete element method (SSDEM), which allows for particles to slightly overlap each other with a mediating spring force

as a proxy for particle deformation (Schwartz et al., 2012). With SSDEM, a user can set parameters such as the restoring spring constant and coefficients of rolling and twisting friction to achieve the desired material properties (Zhang et al., 2017). Following common practice, we set the spring constant such that the overlap between two particles never exceeds 1% of the smallest particle’s radius. As will be discussed later, this approach may lead to an artificially deformable body, but it allows us to adequately resolve interparticle contacts without having to resort to prohibitively short time steps. It is also possible to include interparticle cohesive forces in PKDGRAV (Zhang et al., 2018). Here, we ignore any potential cohesion in Dimorphos in order to observe the maximum possible effect of its rubble-pile treatment. In all PKDGRAV simulations presented herein, we select the friction parameters that represent a gravel-like material and yield a friction angle of $\sim 38^\circ$ (Zhang et al., 2018). PKDGRAV has already been used and validated in rigid F2BP studies of the Didymos system (Agrusa et al., 2020), and here we extend our analysis by enabling the code’s SSDEM feature to fully model Didymos and Dimorphos as rubble piles, rather than rigid bodies.

4.3.3 GRAINS

GRAINS is a N -body code that accounts for both gravitational and granular physics interactions between a large number of nonspherical particles (Ferrari et al., 2017). Gravity computations are done using either a direct N^2 algorithm, which accounts for the mutual gravity between all particles in the system, or by using a GPU-based octree implementation of the Barnes–Hut algorithm (Ferrari et al., 2020). As done with PKDGRAV, we do not use the tree implementation in order to ensure the highest accuracy of mutual gravity computations in this work. Contact and

collision interactions are handled using the Smooth Contact Method module of the open-source multiphysics code CHRONO (Tasora et al., 2016). GRAINS has been used recently to study the stability and internal structure of Didymos (Ferrari and Tanga, 2022; Hirabayashi et al., 2022). In this work, we use GRAINS to model Dimorphos as a gravitational aggregate of irregularly shaped, meter-sized boulders. Each boulder has a different polyhedral shape with about 10 vertices on average, and an aspect ratio (smallest to largest dimension) between 0.7 and 1. The individual shape of each fragment is built as the convex hull of a randomly generated cloud of points. This makes each boulder unique, although all of them are similar in size. The contact parameters are set to reproduce the properties of gravel-like material and are based on previous benchmarking studies (Ferrari and Tanga, 2020; Fleischmann et al., 2015; Pazouki et al., 2017). The cohesion between fragments is set to zero in GRAINS, as cohesive effects are not considered in this work.

4.3.4 Problem Setup

Due to the high computational cost of N -body problems, the number of cases and integration times had to be limited. Due to this constraint, we employ several simulation approaches to model different aspects of the system’s dynamics. All things being equal, PKDGRAV simulations run much faster than GRAINS due to PKDGRAV’s treatment of constituent particles as spheres rather than polyhedral shapes. Therefore we rely on PKDGRAV to conduct long-term simulations (~ 1 yr) or for simulating both bodies as rubble piles at high resolution. In this work, GRAINS is employed in specific shorter-term cases to understand the influence of irregular particle shapes where computationally feasible. In general, the long-term simulations that focus on Dimorphos’s spin and attitude properties use PKDGRAV and treat Didymos as a point mass to increase the com-

putational speed. The exact details and initial conditions for each set of simulations are explained within their respective subsections to avoid confusion.

In all simulations presented herein, we assume that Dimorphos’s preimpact spin period matches the observed mutual orbit period. Although a synchronously rotating Dimorphos has not been directly confirmed with radar and photometry, there is good theoretical and observational evidence to indicate that this is the most likely preimpact state for Dimorphos. This assumption is addressed with more detail in a companion paper by Richardson et al. (2022). Some of the theoretical justifications include the relatively low frequency of natural impacts and close planetary fly-bys (Fuentes-Muñoz and Scheeres, 2020; Meyer and Scheeres, 2021), and efficient tidal dissipation in rubble piles (Goldreich and Sari, 2009; Nimmo and Matsuyama, 2019). The observational evidence includes a measured upper limit on the binary eccentricity of 0.03 (Scheirich and Pravec, 2022), as well as the abundance of synchronous rotators in other close binary systems (Pravec et al., 2016). Furthermore, the best-fit orbital solution indicates a quadratic drift in the mean anomaly of $\Delta M_d = 0.15 \pm 0.14 \text{ deg yr}^{-2}(3\sigma)$, implying that outward tidal expansion is being overcome by inward BYORP drift (Scheirich and Pravec, 2022). If BYORP is acting in the system, then this would require a tidally locked secondary (Ćuk and Burns, 2005). However, there are also good theoretical arguments that a nonsynchronous spin state could be easily excited and long lived (Ćuk et al., 2021; Quillen et al., 2022a). If, upon DART’s arrival, there is a reasonable indication that Dimorphos is in nonsynchronous rotation, then new models will be needed to incorporate this effect. Furthermore, in all simulations, we assume that the DART impact will impart an instantaneous Δv to Dimorphos’s orbital velocity. We neglect any instantaneous changes to Dimorphos’s spin that could result from an off-center impact that imparts a torque to the body, as such a torque is expected to be relatively small. If, however, DART impacts

farther than expected from the body’s center-of-mass, then accounting for this torque may be a topic of future work, depending on the impact outcome. Further discussion of this assumption, as well as other approximations for the dynamics of the system, is available in Richardson et al. (2022).

4.4 Spin and Orbital Dynamics as Rubble Piles

As previously mentioned, it is not feasible to treat both bodies as rubble piles over long integrations while maintaining high resolution and numerical accuracy. Therefore, we take two approaches to model the system, i.e., the *full-rubble-pile* approach, in which both Didymos and Dimorphos are modeled as rubble piles, and the *single-rubble-pile* approach, where only Dimorphos is a rubble pile and Didymos is treated as a point mass. The full-rubble-pile approach is applied to assess the dynamics on short timescales (days to weeks), and the single-rubble-pile approach can be used to study the system on longer timescales (years). Although the latter approach fails to capture any dynamical effects due to Didymos’s higher-order gravity moments, it still adequately captures the attitude-stability properties of Dimorphos, since this is predominantly determined by its own shape and the mutual eccentricity (Agrusa et al., 2021; Wisdom, 1987a). However, the higher-order gravity effects, such as those due to Didymos’s J_2 and C_{22} gravity coefficients are captured with the full-rubble-pile approach as well as rigid-body simulations presented in other works (Agrusa et al., 2021; Meyer et al., 2021; Richardson et al., 2022)

4.4.1 Long-term dynamics with a point-mass Didymos

Agrusa et al. (2021) found that the attitude stability of Dimorphos is highly sensitive to its shape (i.e., moments of inertia). This is a result of resonances that can occur among the orbital, libration, spin precession, and nutation frequencies of Dimorphos that can trigger attitude instabilities. Aside from the orbital frequency (mean motion), these frequencies depend directly on Dimorphos’s moments of inertia (i.e., shape), which are unknown. In order to extend the results of Agrusa et al. (2021), we select four possible ellipsoidal shapes for Dimorphos: two in which previous rigid-body simulations predict the presence of an attitude instability, and two of which are expected to remain stable at an eccentricity of $e \sim 0.025$ (i.e., a perturbation to a circular orbit consistent with $\beta = 3$). The four selections for the shape of Dimorphos are listed on Table 4.2. These four cases were selected in order to sample both the unstable and stable configurations in many parts of the parameter space surveyed by Agrusa et al. (2021). Given that nonprincipal axis rotation of Dimorphos is commonly observed in simulations (Agrusa et al., 2021; Ćuk et al., 2021; Quillen et al., 2022a), comparing cases across different attitude-stability regimes is important for benchmarking the rigid-body and rubble-pile approaches. Figure 4.1 shows a modified version of a plot from Agrusa et al. (2021) that displays the maximum Euler angles achieved by Dimorphos for a year following a DART-like impact in which $\beta = 3$ based on GUBAS rigid-body simulations. Overlaid on the plot are the four Dimorphos shapes considered in this section. Renderings of the four shapes are shown on Fig. 4.2. Case ab1.4bc1.3 is the most elongated shape considered in this study, and is expected to enter the “barrel instability,” a phenomenon in which a satellite enters a rolling state about its long axis, which is described in greater detail in Ćuk et al. (2021) and indicated by the roll angle exceeding 90° in Fig. 4.1.

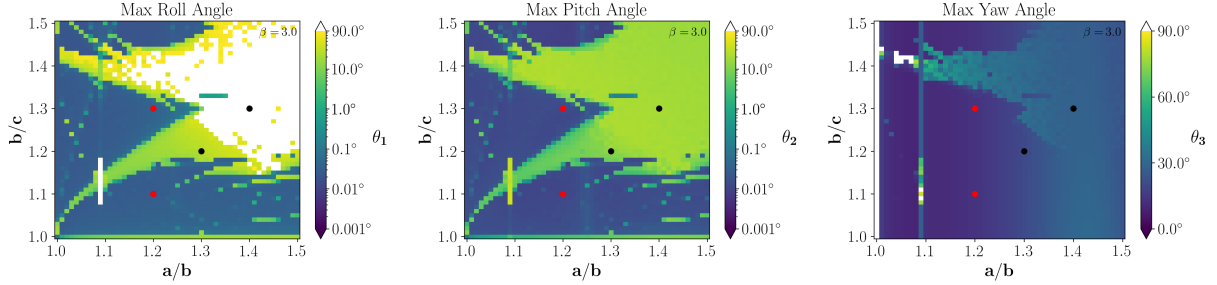


Figure 4.1: From Agrusa et al. (2021), the maximum Euler angles (roll, pitch, and yaw) achieved by Dimorphos over a 1 yr simulation in GUBAS following a DART-like perturbation to the mutual orbit with $\beta = 3$. The overlaid dots show the four shapes under consideration in this study with the two expected attitude-stable cases ($ab1.2bc1.3$ and $ab1.2bc1.1$) in red and the two expected attitude-unstable cases ($ab1.4bc1.3$ and $ab1.3bc1.2$) in black. The structure of the attitude-stability region is a result of various resonances between the mean motion and Dimorphos’s libration, spin precession, and nutation frequencies.

Case $ab1.3bc1.2$ was selected to provide an additional attitude-unstable case and because it is the nominal shape used by the mission in the DRA. Due to the lack of observational constraints for Dimorphos, this particular shape was selected for the DRA based on the observed elongations of the secondary component of other binary systems (Pravec et al., 2016). Finally, cases $ab1.2bc1.3$ and $ab1.2bc1.1$ were selected due to their strong attitude-stability properties according to GUBAS rigid-body simulations and to see whether the rubble-pile codes reproduce the same predicted stability.

Since the attitude-stability properties of Dimorphos are driven primarily by its own shape, accounting for the oblate shape of Didymos is not necessary, allowing us to simply treat it as a point mass. The set of PKDGRAV runs presented in this subsection performs a given simulation two times: once as a rigid body in which all the constituent particles of Dimorphos are locked together into a rigid aggregate; and once using PKDGRAV’s SSDEM package where Dimorphos is treated as a rubble pile. This allows for a direct *apples-to-apples* comparison in which the rigid and SSDEM cases have identical initial shapes. We also simulate a matching case in GUBAS,

Name	$a/b, b/c$	a, b, c [m]	N	M_B [10^9 kg]	Agrusa et al. (2021) prediction for $\beta = 3$
ab1.4bc1.3	1.40, 1.30	111.3, 79.5, 61.2	3737	4.8788	Unstable
ab1.3bc1.2	1.30, 1.20	103.2, 79.4, 66.1	3739	4.8831	Unstable
ab1.2bc1.3	1.20, 1.30	100.4, 83.7, 64.4	3742	4.8847	Stable
ab1.2bc1.1	1.20, 1.10	95.0, 79.2, 72.0	3719	4.8872	Stable

Table 4.2: The body shapes for Dimorphos considered in this section, informed by the larger parameter sweep used in Agrusa et al. (2021). a/b and b/c are the ellipsoidal axis ratios for each body shape along with their physical lengths, a , b , and c . We also report the total number of particles, N that make up the body, as well as the total mass of the body, M_B . The body masses vary slightly in the simulation in order to produce a dynamically relaxed preimpact state of the system. Note that all four bodies are constructed from the same power-law particle-size distribution and that the bulk size of Dimorphos remains conserved between all cases.

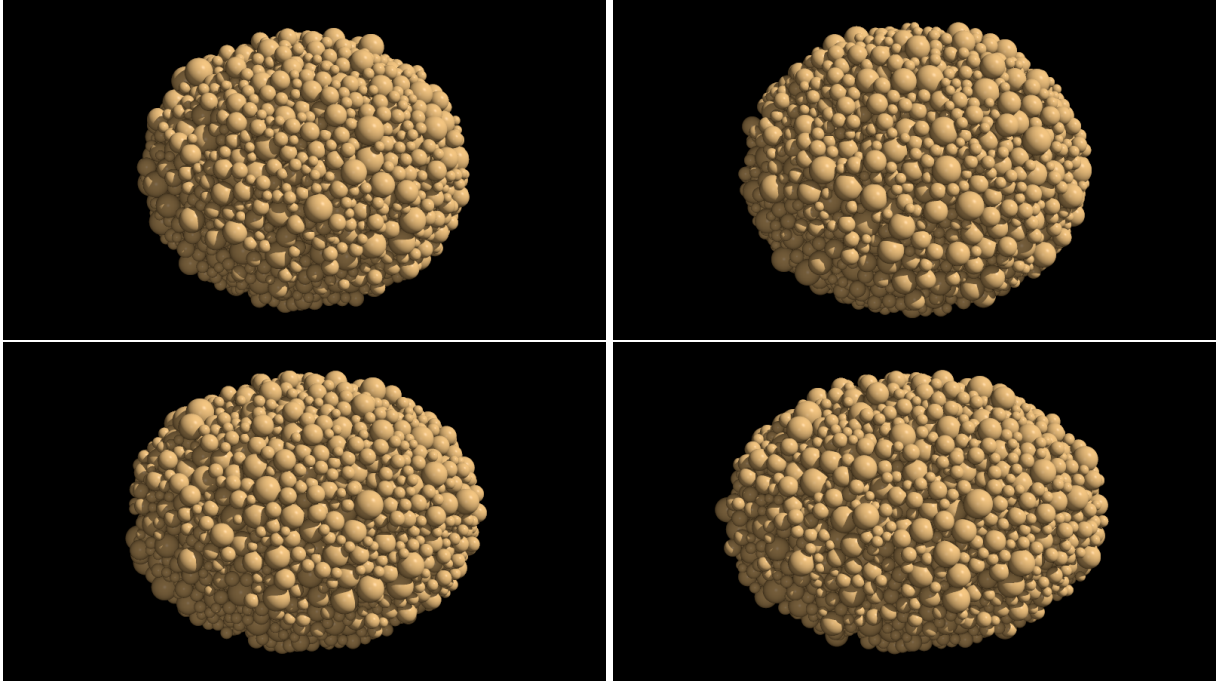


Figure 4.2: The four ellipsoidal representations of Dimorphos in PKDGRAV considered in this section. Each body is drawn from the same power-law particle-size distribution with an index of -3 and an average particle radius of ~ 4.2 m. These are *top-down* views, meaning that the camera is situated above Dimorphos’s spin pole. Top left: ab1.2bc1.1. Top right: ab1.2bc1.3. Bottom left: ab1.3bc1.2. Bottom right: ab1.4bc1.3.

although these cases do not match *exactly* because Dimorphos’s shape is treated as an idealized ellipsoid. When interpreting the results of this section, the difference between a GUBAS and a rigid PKDGRAV case shows the fundamental differences between the two codes and their respective shape representation of Dimorphos, while the differences between the SSDEM and rigid PKDGRAV cases show any effects due to the deformability of Dimorphos.

This leads to one additional complication: when the rubble-pile Dimorphos is placed into orbit around Didymos, it suddenly feels a tidal force that acts to slightly deform its shape into a new equilibrium configuration. This change is extremely small, but in order to directly compare with the SSDEM and rigid PKDGRAV cases, we must make sure both bodies have the *exact same* starting shape. This is achieved by simulating the preimpact system for 24 hr (~ 2 orbit periods) with Dimorphos as a rubble pile, which is sufficiently long for the particles to reach a new relaxed state. Then the simulation is halted, the constituent particles of Dimorphos are locked into a rigid aggregate (or left alone for the SSDEM cases), and a Δv is applied to the orbital velocity of Dimorphos as a proxy for the DART impact. Finally, the simulation is restarted and allowed to propagate for 1 yr of simulation time.

To summarize, simulations are set up as follows:

1. PKDGRAV particles are generated from a power-law particle-size distribution with an index of -3.0 and an average particle radius of 4.2 m. The maximum and minimum possible particle radii are 8.4 and 2.8 m. The power-law index was chosen to be similar to the boulder-size distribution exponents observed on the surfaces of several asteroids (e.g., Michikami et al., 2010, 2019; Walsh et al., 2019), and the size cutoffs were chosen such that each realization of Dimorphos would contain $\sim 4,000$ particles to keep the computational costs

reasonable. The cloud of particles is allowed to collapse (with all friction parameters set to zero) to form an approximately spherical body. Then the desired ellipsoidal shape for Dimorphos is *carved out* of this rubble pile by simply deleting any particles that lie outside of its surface.

2. After Dimorphos is carved into its desired shape, friction is turned on, and the body is simulated on its own (no Didymos) to allow it to come to an equilibrium configuration under self-gravity and spin.
3. The initial conditions for the binary orbit were generated using GUBAS and the optimization routine described in Agrusa et al. (2021). In this case, the optimization routine used a point-mass primary and ellipsoidal secondary to derive the initial conditions such that the resulting system has a spin-synchronous secondary with a mutual semimajor axis and orbital period that match their respective observed values in Table 4.1.
4. The simulation is then started in PKDGRAV and stopped after 24 hr of simulation time (~ 2 orbit periods). This allows for the rubble-pile model of Dimorphos to come to equilibrium after it is suddenly feels the tidal stress resulting from being placed in an orbit around the point-mass Dimorphos.
5. After all settling is complete, Dimorphos is given an instantaneous Δv as a proxy for the DART impact. The change in velocity is determined based on the expected mass and relative velocity of the DART spacecraft, as well as a guess for β ($\beta = 3$ is assumed for

these particular simulations).² Here, we assume that DART imparts all of its momentum within the mutual orbit plane and opposite Dimorphos’s motion. Due to DART’s expected near-head-on impact geometry, this planar approximation is not expected to significantly alter the dynamics (Richardson et al., 2022).³

6. The simulation is then restarted and run for 1 yr of integration time, once as a rigid body and once using the SSDEM feature. These simulations are run with a time step of ~ 0.86 s, which is small enough to adequately resolve interparticle contact interactions and is also well below the 1.875 s time step that was found to be appropriate for accurately modeling the mutual orbital dynamics with PKDGRAV by Agrusa et al. (2020).

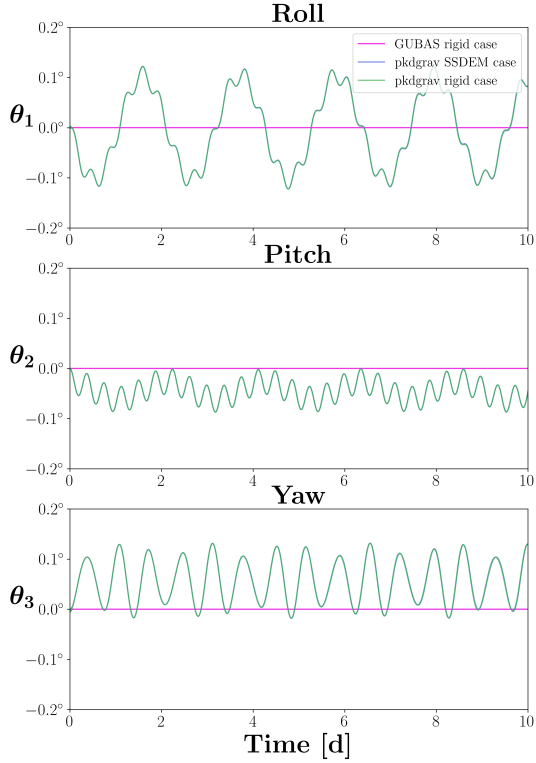
4.4.1.1 Attitude-stable cases

Based on rigid-body simulations, we expect cases ab1.2bc1.1 and ab1.2bc1.3 to remain attitude stable against a DART-like impact. Here we show that PKDGRAV simulations reproduce the same behavior, both as a rigid body and as a rubble pile using SSDEM.

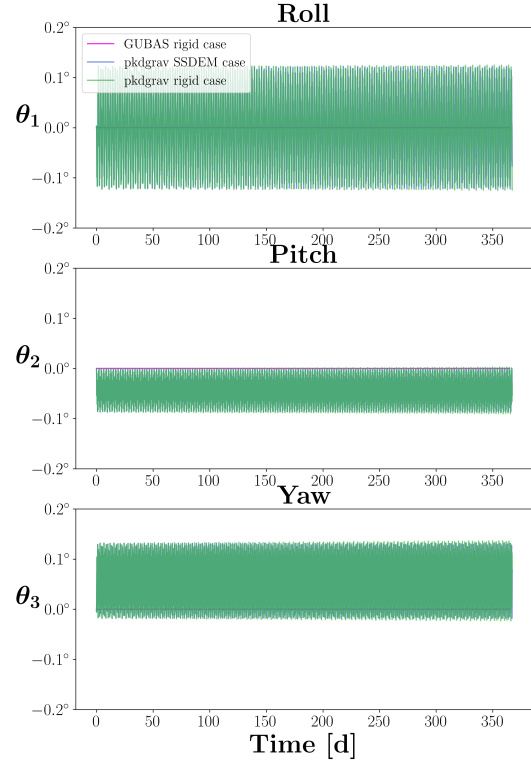
Figure 4.3 shows Dimorphos’s Euler angles (roll, pitch, and yaw) when it has the shape ab1.2bc1.1 and the system is in the relaxed state (i.e., no DART impact). The GUBAS results show *perfect* tidal locking (all Euler angles being zero) due to the idealized symmetry: a spherical primary, a smooth ellipsoidal secondary, and a circular orbit. As discussed earlier, the rubble-pile realization of Dimorphos does not *exactly* match the mass distribution of the GUBAS case, mean-

²The mass and relative velocity of the DART spacecraft are assumed to be 535 kg and 6.6 km s⁻¹, respectively. Since the time this investigation was begun, the best estimate of the mass and relative velocity has changed to 536 kg and 6.15 km s⁻¹ respectively. Therefore, for a given value of β and mass of Dimorphos, these simulations slightly overestimate the Δv that Dimorphos will receive.

³For a simplified, head-on impact, Dimorphos receives $\Delta v = -\beta \frac{M_{\text{DART}} v_{\text{DART}}}{M_{\text{B}}}$, where M_{DART} and v_{DART} are the spacecraft’s respective mass and velocity, and M_{B} is Dimorphos’s mass.



(a) `ab1.2bc1.1` in its relaxed state simulated with PKDGRAV for the first 10 days.



(b) `ab1.2bc1.1` in its relaxed state simulated with PKDGRAV for 1 year.

Figure 4.3: Evolution of Dimorphos’s Euler angles for `ab1.2bc1.1` when the system is in a dynamically relaxed state. The GUBAS rigid case shows *perfect* tidal locking since the system is idealized: a circular orbit, spherical primary, and smooth ellipsoidal secondary. The PKDGRAV simulations (both as a rigid aggregate and SSDEM body) are not quite as relaxed since their mass distributions do not perfectly match the equivalent GUBAS simulations.

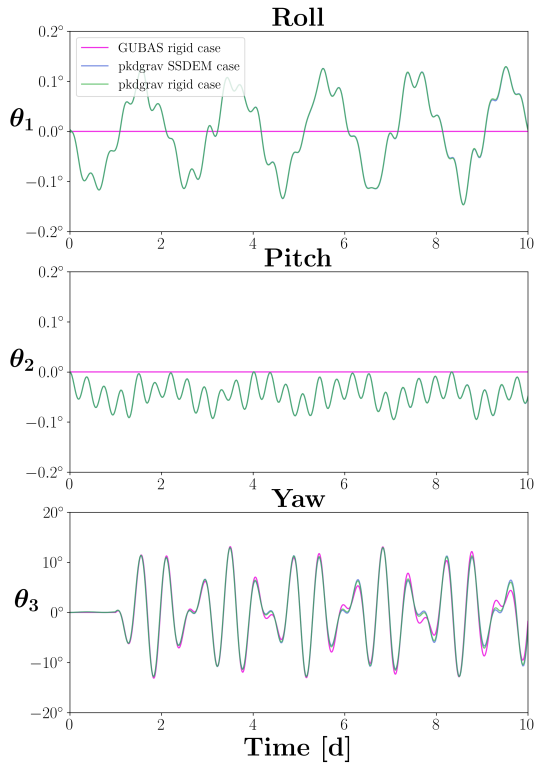
ing that the dynamics are not perfectly relaxed. This is also the reason that the pitch and yaw angles oscillate around a nonzero value. Although the Euler angle amplitudes are nonzero, the PKDGRAV simulations are in qualitative agreement with GUBAS, with any minor deviations being attributable to differences in the shape representations. Furthermore, the rigid and SSDEM PKDGRAV results are nearly identical and hard to distinguish, meaning that the rigid-body approximation is more than adequate in this scenario, as we would expect.

We also show the same model for Dimorphos (ab1.2bc1.1) following a DART-like perturbation consistent with $\beta = 3$ on Fig. 4.4. The DART perturbation is applied at $t = 1$ day and leads to an eccentricity of the mutual orbit of $e \sim 0.025$. The effect of this can be seen on the yaw-angle plot in Fig. 4.4a, where Dimorphos starts librating after 1 day. Both PKDGRAV simulations as well as GUBAS show attitude stability and the same libration amplitude (given by yaw angle). Furthermore, the rigid and SSDEM PKDGRAV cases are nearly identical, again indicating that Dimorphos is behaving as a rigid body and that the rigid-body approximation is adequate for simulating the post-impact attitude dynamics in this case.

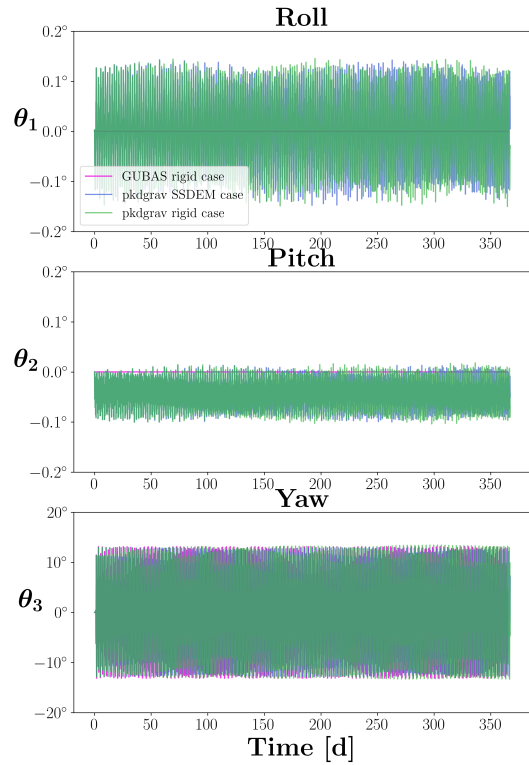
Fig. 4.5 shows the post-impact spin evolution of Dimorphos for $\beta = 3$ but with the ab1.2bc1.3 shape representation. Here, we see similar behavior: the PKDGRAV cases show strong qualitative agreement with the matching GUBAS simulation, with minor deviations due to differences in the body shape representations and the codes themselves. Furthermore, the rigid and SSDEM PKDGRAV cases show nearly identical behavior, indicating that the rigid-body approximation is valid in the regime of attitude stability.

4.4.1.2 Attitude-unstable cases

Previous work has shown that Dimorphos's spin state can evolve chaotically after its attitude becomes unstable. This means that Dimorphos's spin evolution is highly sensitive to any small changes in the system or the initial conditions. Therefore, it is impossible for the PKDGRAV and GUBAS simulations to match exactly since they do not have the *exact* same initial conditions, nor the same numerical integrator. However, we find *qualitative* agreement between the GUBAS simulation and both the rigid and SSDEM PKDGRAV simulations for ab1.3bc1.2

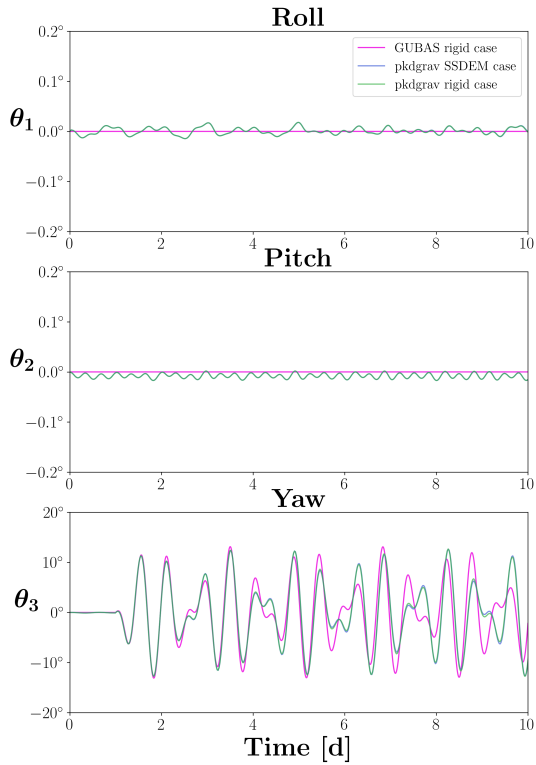


(a) $ab1.2bc1.1$ after the mutual orbit is perturbed by $\beta = 3$ for the first 10 days.

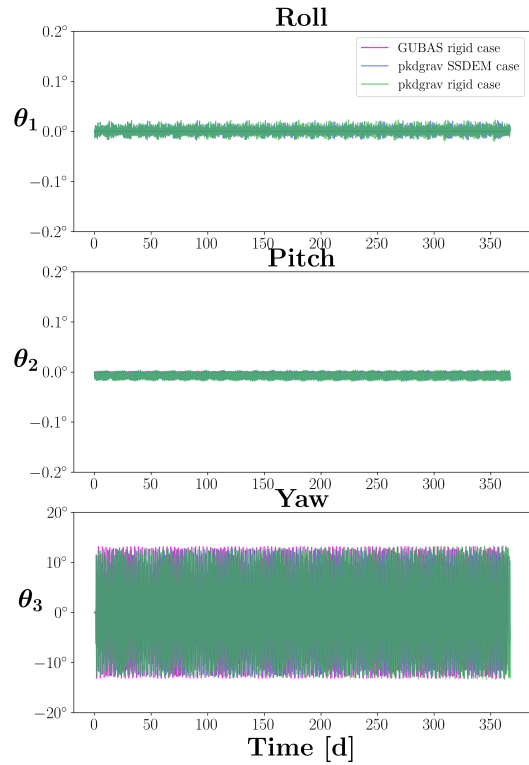


(b) $ab1.2bc1.1$ after the mutual orbit is perturbed by $\beta = 3$ over 1 year.

Figure 4.4: Evolution of Dimorphos's Euler angles for $ab1.2bc1.1$ when Dimorphos's orbital velocity is perturbed consistent with a DART impact with $\beta = 3$. In other words, the mutual orbit has an eccentricity of ~ 0.025 . The DART impact is applied at $t = 1$ day, which is when Dimorphos begins significantly librating.



(a) ab1 . 2bc1 . 3 after the mutual orbit is perturbed by $\beta = 3$ for the first 10 days.



(b) ab1 . 2bc1 . 3 after the mutual orbit is perturbed by $\beta = 3$ over 1 year.

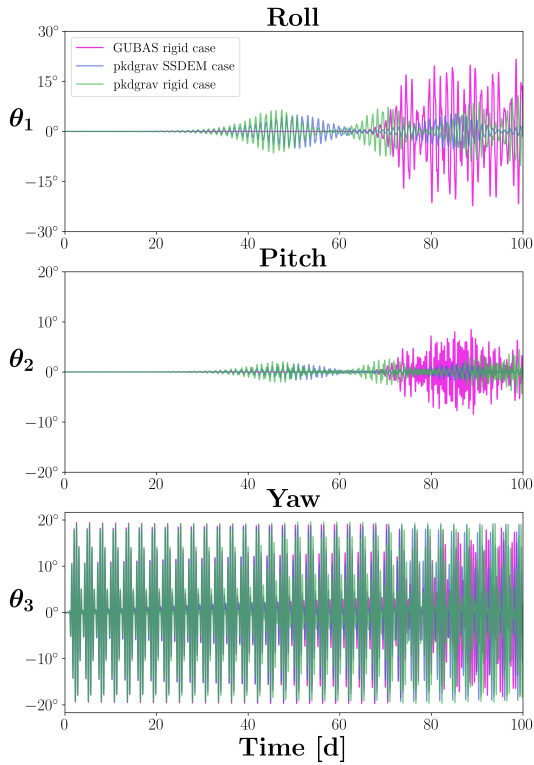
Figure 4.5: Evolution of Dimorphos's Euler angles for ab1 . 2bc1 . 3 when Dimorphos's orbital velocity is perturbed consistent with a DART impact with $\beta = 3$. In other words, the mutual orbit has an eccentricity of ~ 0.025 . The DART impact is applied at $t = 1$ d, which is when Dimorphos begins significantly librating.

and $a b 1.4 b c 1.3$. Generally speaking, if GUBAS predicts a given configuration to be attitude unstable, we see the same behavior with PKDGRAV.

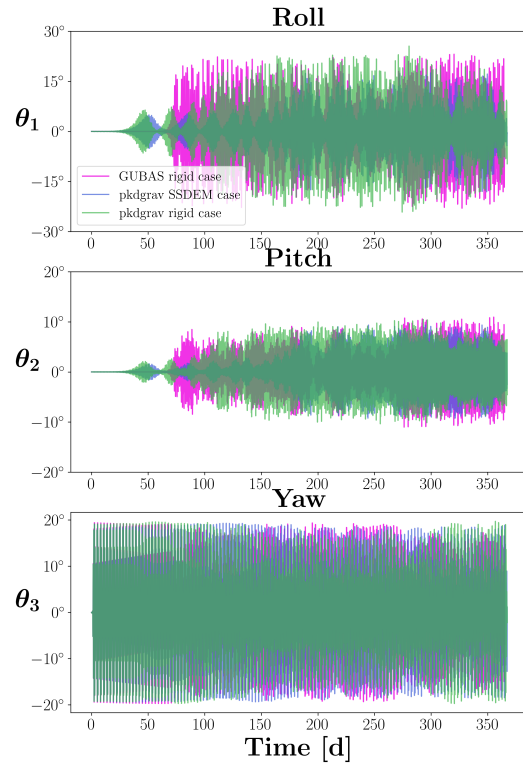
Figure 4.6 shows the post-impact evolution of Dimorphos’s Euler angles with the shape $a b 1.3 b c 1.2$ after a DART-like perturbation of $\beta = 3$. Both PKDGRAV simulations and GUBAS reveal that Dimorphos should become attitude unstable for this shape and show approximately the same post-impact libration amplitude of $\sim 20^\circ$ (yaw angle). In addition, they are in broad agreement for the amplitude of roll and pitch oscillations once Dimorphos enters the attitude instability. The main difference between the codes is in the timing of the instability, which is technically impossible to predict given the chaotic nature of the system. Additionally, the codes use different numerical integrators, were simulated on different machines, and the rubble-pile Dimorphos doesn’t have the *exact* same mass distribution as the idealized ellipsoid, so there is no reason for us to expect the timing of the instability to match.

Following a DART-like impact, $a b 1.4 b c 1.3$ is expected to not only be attitude unstable but should also enter the so-called “barrel instability”, characterized by rotation about the secondary’s long axis (Ćuk et al., 2021). Indeed, PKDGRAV finds the same behavior both when Dimorphos is treated as a rigid body and a deformable rubble pile, as seen in Fig. 4.7. Although each case enters the instability at different times, all three cases show the same qualitative behavior, with Dimorphos episodically rotating about its long axis (roll angle hitting 180°) and the pitch and yaw amplitudes capped at $\sim 20^\circ$ and $\sim 25^\circ$, respectively.

In conclusion, the rubble-pile approach reproduces the same qualitative behavior seen in equivalent rigid-body simulations. This indicates that the rigid-body approach is appropriate, at least for moderate values of β and an ellipsoidal secondary.

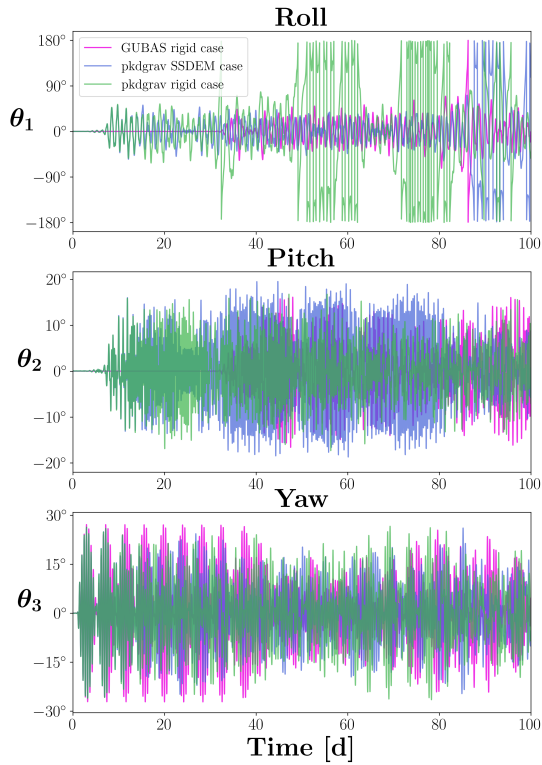


(a) $ab1.3bc1.2$ after the mutual orbit is perturbed by $\beta = 3$ for the first 100 days.

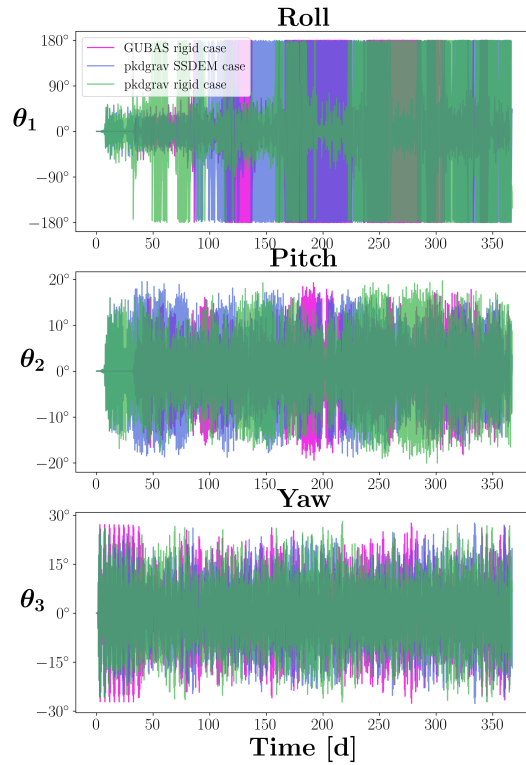


(b) $ab1.3bc1.2$ after the mutual orbit is perturbed by $\beta = 3$ over 1 year.

Figure 4.6: Evolution of Dimorphos’s Euler angles for $ab1.3bc1.2$ for $\beta = 3$. The GUBAS and PKDGRAV simulations are in broad agreement, both showing attitude instability with about the same amplitudes in the three Euler angles. The deviations between the three simulations are attributable to differences between the codes and the shape representation of Dimorphos.



(a) $ab1.4bc1.3$ after the mutual orbit is perturbed by $\beta = 3$ for the first 10 days.



(b) $ab1.4bc1.3$ after the mutual orbit is perturbed by $\beta = 3$ over 1 year.

Figure 4.7: Evolution of Dimorphos's Euler angles for $ab1.4bc1.3$ for $\beta = 3$. The GUBAS and PKDGRAV simulations are in broad agreement, both showing the barrel instability, although the instability occurs at different times. The deviations between the three simulations are attributable to differences between the codes and the shape representation of Dimorphos.

4.4.2 Short-term dynamics with Full Rubble Piles

Increasing in complexity, we then simulate the system with *both* Didymos and Dimorphos modeled as rubble piles. A rubble-pile model composed of 13,049 particles is constructed based on the radar-derived shape model of Didymos (Naidu et al., 2020a) to capture its irregular top-like shape. This choice of particle number represents the optimal compromise between the model resolution and computational cost. The sizes of these particles range from ~ 7.8 to ~ 31.2 m following a differential power-law distribution with an exponent of -3 (the same as for Dimorphos in the single-rubble-pile runs). Dimorphos is assumed to be a rubble-pile ellipsoid consisting of 504 particles with the same power-law distribution but smaller sizes, i.e., ~ 5.4 to ~ 16.0 m, to better characterize its shape.⁴ Given that the tidal interaction raised by the primary is expected to drive the secondary’s spin toward synchronization much more efficiently than in the case of a monolithic secondary and that the presence of a rubble-pile primary can cause changes in the orbital semimajor axis and eccentricity more rapidly (Goldreich and Sari, 2009), we focus on a post-impact attitude-unstable case in this section to investigate the effect of the rubble-pile binary. A shape with $a \approx 109.93$ m, $b \approx 81.41$ m, $c \approx 60.21$ m, is selected to represent the shape of Dimorphos (similar to the attitude-unstable $ab1.4bc1.3$ case shown in Table 4.2).

The two rubble-pile models were generated via the gravitational collapse and shape-carving procedure introduced in Section 4.4.1. A quasi-static spin-up procedure (see Section 2.2 in Zhang et al., 2021) was applied to settle the two models separately to their respective equilibrium state with the corresponding spin rate, i.e., ~ 2.26 hr for Didymos and ~ 11.91 hr for Dimorphos. Then, the two models were combined in one simulation by assigning the movement of their mass

⁴Due to the increased computational cost of simulating Didymos as a rubble pile, we simulate Dimorphos at lower particle resolution than in the previous section.

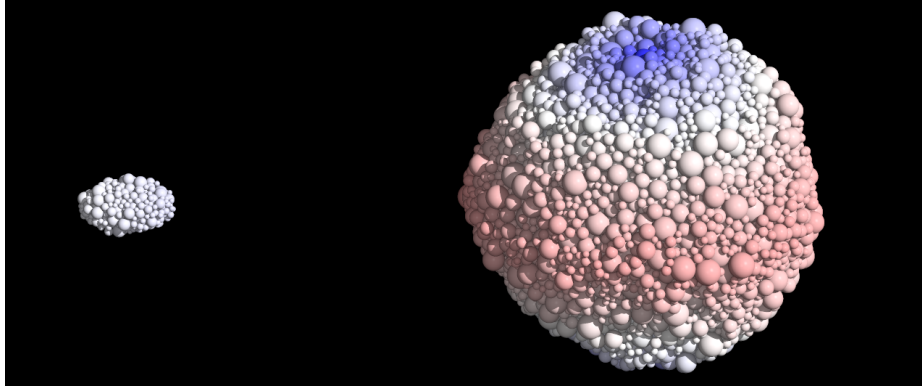


Figure 4.8: Rubble-pile representations of Didymos and Dimorphos in PKDGRAV considered in the full-rubble-pile approach (Section 4.4.2). Each body is drawn from the same power-law particle-size distribution with an index of -3 and particle radii of ~ 7.8 to ~ 31.2 m (Didymos) and ~ 5.4 to ~ 16.0 m (Dimorphos). Particles are color-coded by the speed magnitude to show the spin orientation of Didymos and the relative orbital speed of Dimorphos. The camera is tilted $\sim 23^\circ$ above the equatorial plane to better present the two bodies’s shapes.

centers according to the orbital dynamics of the Didymos-Dimorphos system derived from the point-mass-Didymos approach (see Section 4.4.2). Due to its fast rotation, the Didymos rubble pile needs some amount of material cohesion to maintain its stability at its assumed density. Adopting from our previous study (Zhang et al., 2021), we use a macroscopic cohesion of 20 Pa and a friction angle of 38° to represent the material properties of Didymos. Dimorphos is modeled with the same friction angle but zero cohesion to provide for the maximum possible effect of the rubble-pile structure. The full-rubble-pile models were allowed 24 hr to settle down under their mutual gravity, and then the velocity of Dimorphos was modified along the instantaneous orbital direction to capture the momentum-change effect of the DART impact (the same procedure as introduced in Section 4.4.1). Figure 4.8 shows the initial configuration of the full-rubble-pile model. Simulations were run for 30 days to reveal the short-term dynamics of the rubble-pile structure.

To investigate the effect of the impact momentum transfer efficiency, we carried out simula-

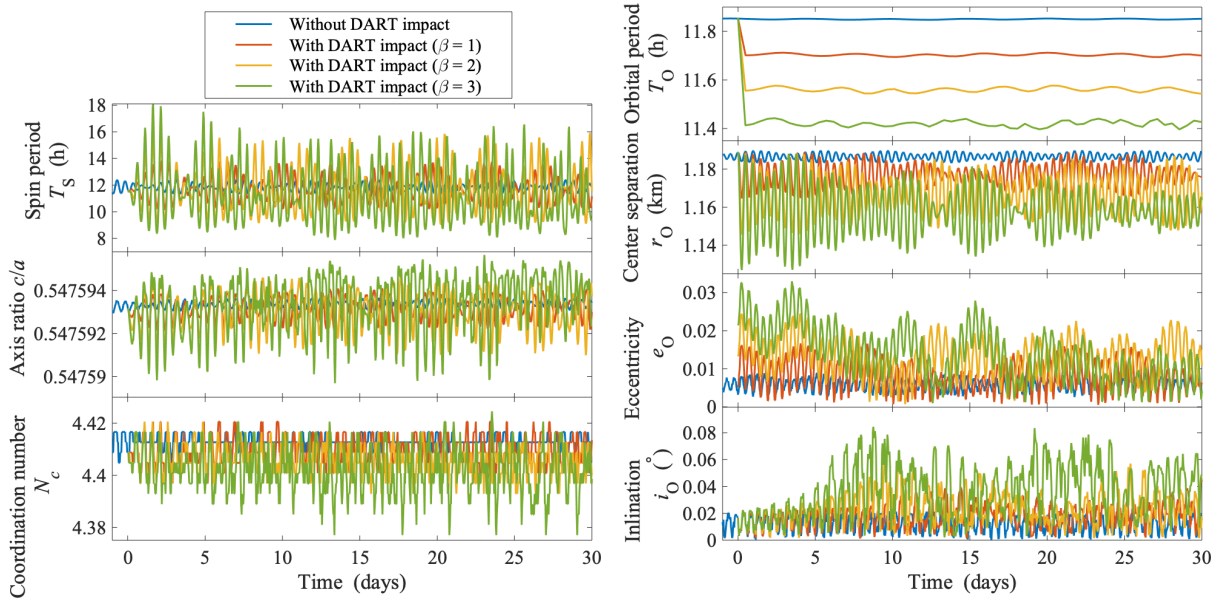


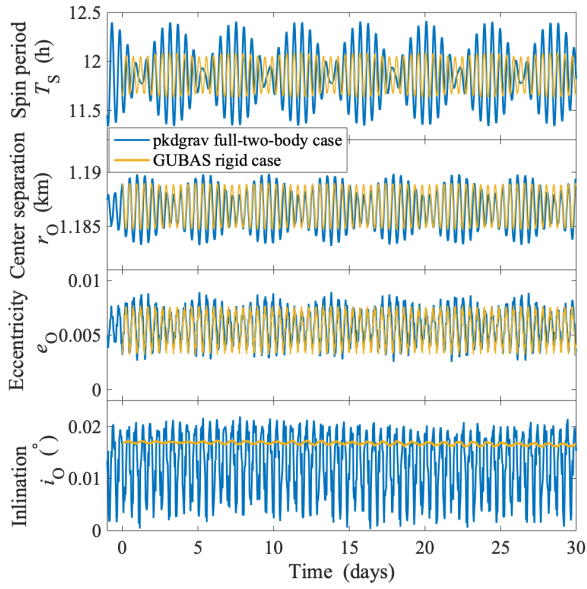
Figure 4.9: Evolution of Dimorphos’s spin, shape, coordination number (i.e., the averaged contact number of the rubble pile), and orbital parameters of the full-rubble-pile model. The blue curves show the evolution without DART impact while the remaining three colors represent the results of instantaneous DART impacts with different β values. We note that e_O is the Keplerian eccentricity, computed at each output based on the instantaneous body position and velocity vectors.

tions for one case without the DART impact and three cases with the DART impact and different values of β . Figure 4.9 shows the evolution of the spin periods, axis ratios, coordination number, and various orbital parameters of Dimorphos. Considering that the binary orbit deviates from a Keplerian orbit, the orbital period is evaluated as the time it takes for Dimorphos to complete each successive 360° revolution, following the orbit period formalism of Meyer et al. (2021). The orbit is time-varying due to periodic exchanges of angular momentum between the mutual orbit and Dimorphos’s spin.

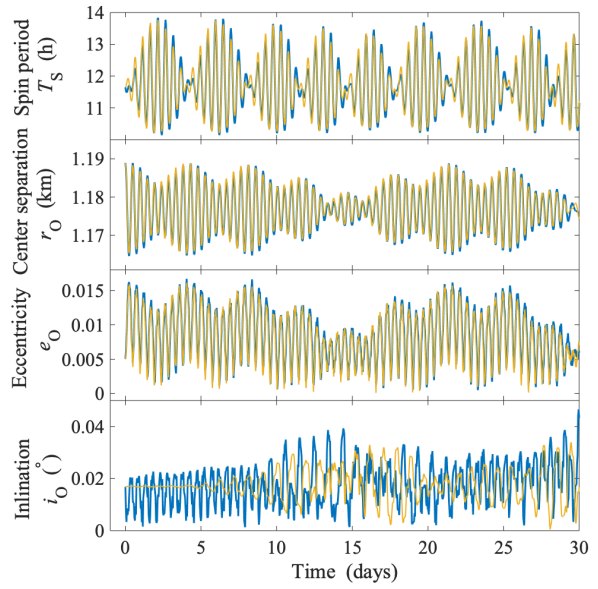
As shown in Figure 4.9, without being perturbed by the DART impact, the state of Dimorphos stays near the nominal observational values oscillating with small magnitudes due to the deviation of Didymos’s gravity field from the point mass, as shown by the blue curves. The

rubble-pile Dimorphos behaves like an elastic body, and its shape (c/a) and averaged contact number (N_c) expand and shrink in response to its orbital position and rotational state. The orbit and rotation can be further excited by the DART impact. As shown by the curves marked with different β values, the oscillation magnitudes after DART impact increase substantially and monotonically with larger β . In the case of $\beta = 1$, the averaged orbital period of Dimorphos decreases to ~ 11.7 hr, meaning that the DART impact causes a ~ 720 s change, which is one order of magnitude larger than the Level 1 requirement of the DART mission Rivkin et al. (2021). With $\beta = 3$, this change increases to ~ 1800 s, and the center separation between the two bodies is decreased by ~ 0.03 km on average. The orbital eccentricity is elevated immediately due to the instantaneous change of orbital speed and then oscillates as angular momentum is exchanged between the mutual orbit and Dimorphos's spin state. Due to the irregular gravity field, the orbital evolution of Dimorphos is not perfectly planar, and the orbital inclination can also be excited by the DART impact, despite an assumed planar impact. These results are consistent with previous analyses based on rigid-body dynamics (Agrusa et al., 2021; Meyer et al., 2021; Richardson et al., 2022).

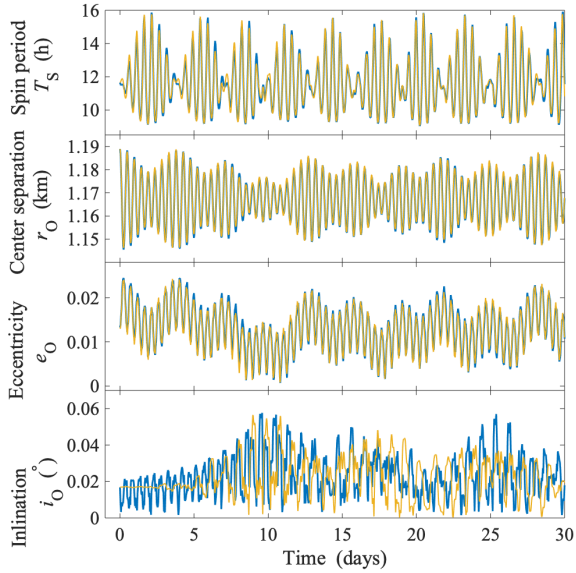
To better understand the role that the full-rubble-pile model plays in the binary system dynamics, we carried out matching rigid-body simulations using GUBAS with both Didymos and Dimorphos modeled as dynamically equivalent equal-volume ellipsoids (DEEVES). The body masses, DEEVE shapes, positions, velocities, spins, and orientations of the GUBAS model are set to match the initial state of the full-two-rubble-pile model. Figures 4.10 and 4.11 compare the post-impact spin and orbital evolution of Dimorphos for the unperturbed and three β cases predicted by the full-two-rubble-pile model against the GUBAS rigid-body model. In general, these two models show strong qualitative agreement with each other (even quantitative in the



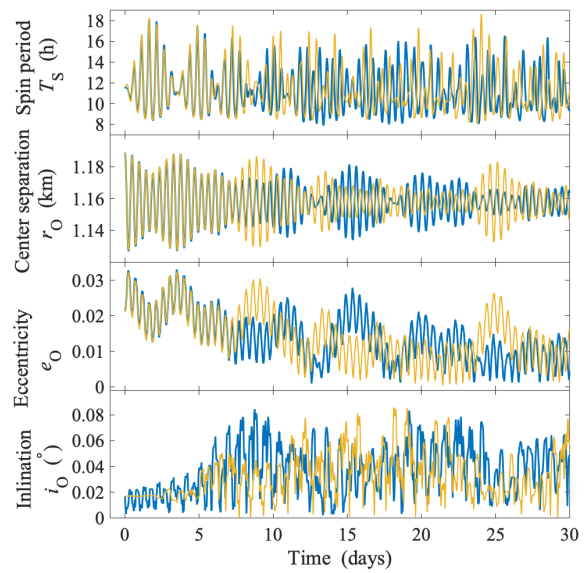
(a) Without DART impact (unperturbed).



(b) With DART impact ($\beta = 1$).

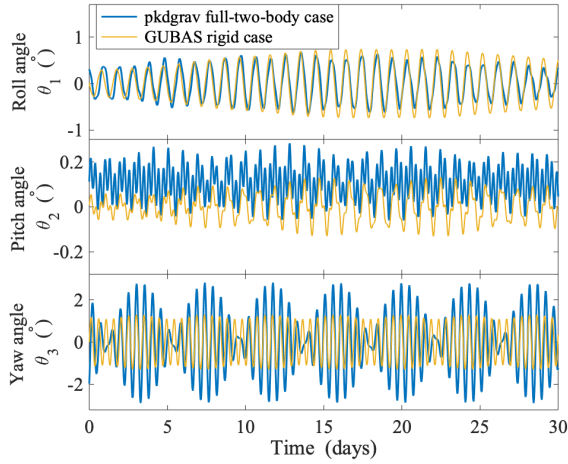


(c) With DART impact ($\beta = 2$).

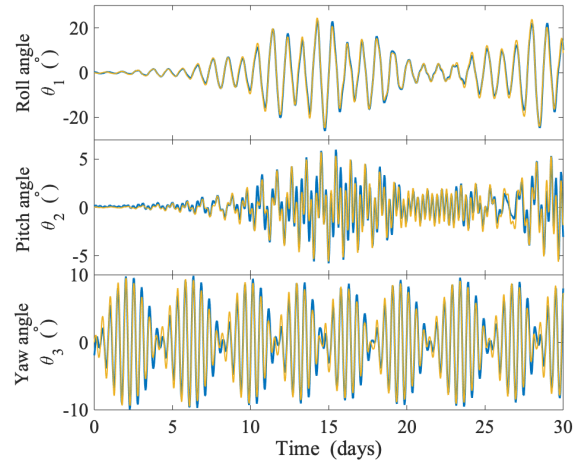


(d) With DART impact ($\beta = 3$).

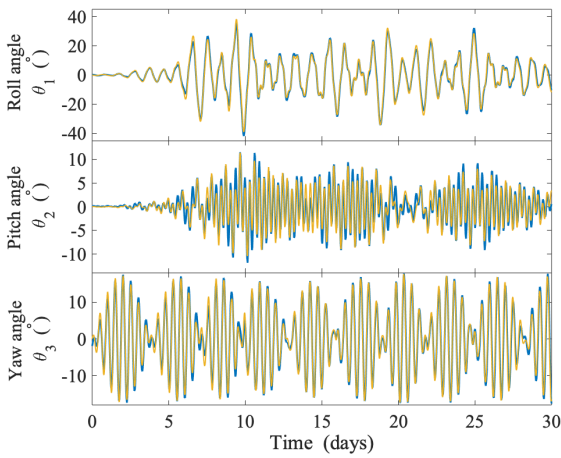
Figure 4.10: Dimorphos's spin and orbital evolution for different β values: the full-two-rubble-pile model (the blue curves) vs. the GUBAS model (the yellow curves). The GUBAS and PKDGRAV simulations are in good agreement, both showing large orbital oscillation induced by the DART impact.



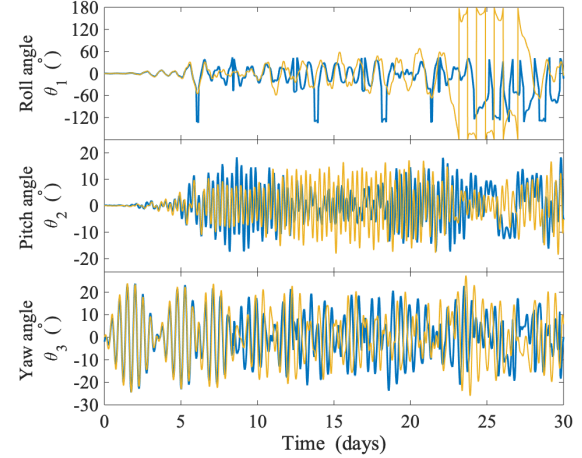
(a) Without DART impact (unperturbed).



(b) With DART impact ($\beta = 1$).



(c) With DART impact ($\beta = 2$).



(d) With DART impact ($\beta = 3$).

Figure 4.11: Evolution of Dimorphos's Euler angles with the full-two-rubble-pile model for different β values. The GUBAS and PKDGRAV simulations are in good agreement, both showing large librations with about the same amplitudes and phases for $\beta = 1, 2$ and the barrel instability for $\beta = 3$.

case of $\beta = 1, 2$; the small deviation in the inclination is mainly due to the different treatment in approximating the non-point-mass gravity field of Didymos). The consistency in the eccentricity evolution indicate that the variations in e_O mainly come from the exchange of angular momentum between Dimorphos’s rotational and orbital states, rather than tidal dissipation due to their rubble-pile treatment. This agrees with the previous theoretical understanding of the rubble-pile–tidal interaction, whose timescales on affecting the binary dynamics would be on the order of megayears (Goldreich and Sari, 2009). The barrel instability predicted by the rigid-body approach is also observed in the rubble-pile simulation, although Dimorphos never completes a full rotation about its long axis over the 30 days time frame. Given that the barrel instability is observed in the 1 yr simulations presented in Section 4.4.1, this is likely due to the chaotic nature of its spin evolution rather than the fact that we are considering the full-rubble-pile approach here. These results further confirm that the rigid-body approximation is valid in terms of predicting the general attitude evolution and stability of the binary system.

4.5 Limits of the Rigid-body Approach

In Section 4.4, we showed that under moderate conditions (a typical β value and ellipsoidal-shaped secondary) that the rubble-pile models are in broad, qualitative agreement with equivalent rigid-body simulations. This likely means that faster rigid F2BP codes are adequate for predicting the dynamical state of the system following the DART impact. In this section, we explore the limit at which this assumption may break down and rubble-pile models of the system are required. DART’s arrival at the Didymos system will confirm whether the two components are in fact rubble piles. If they are rubble piles (as we expect), the DART imagery will also greatly re-

duce the range of possible shapes for Dimorphos as well as constrain its boulder-size–frequency distribution, which will provide a much better picture of the importance of rubble-pile effects. Therefore, the results presented in this section are just preliminary and meant to guide future studies of the binary system following the DART impact.

4.5.1 Limits on strong tidal effects

As a result of DART’s near-head-on impact, the orbital speed of Dimorphos will be reduced, causing it to fall on a tighter orbit with a decreased pericenter distance. In this context, it is worth exploring the tidal interactions between Dimorphos and Didymos, to the limiting distances that would affect the stability of Dimorphos’s interior structure or surface material. According to the classic theory of Roche (1847), a minimum distance exists for a purely fluid body below which tidal forces are greater than self-gravity, causing breakup. Holsapple and Michel (2006, 2008) provide a more specific theoretical framework, based on the Drucker-Prager strength model, suited to solid objects undergoing tidal stress, relying on parameters such as the internal friction angle and cohesion. Although these models provide theoretical insights to the tidal interaction problem, they both rely on assumptions that greatly simplify the treatment of the complex granular dynamics occurring within rubble-pile objects. In fact, it is reasonable to assume that rubble piles behave neither as a fluid nor as a solid, but rather as a complex granular system where long-range force chains may manifest and evolve. In this context, the theoretical predictions provided by Roche (1847) and Holsapple and Michel (2006, 2008) theories can be compared to the outcome of N -body granular simulations, which provide a better treatment of granular physics (e.g., Asphaug and Benz, 1994; Movshovitz et al., 2012; Yu et al., 2014; Zhang

and Michel, 2020).

In this section, we estimate the limiting distance between Dimorphos and Didymos where tidal effects are relevant to the stability of Dimorphos’s internal structure and surface material. We use GRAINS to take advantage of the nonspherical shapes of the fragments, whose effect has shown to be relevant in short-term tidal interaction problems (e.g., the case of comet Shoemaker-Levy 9; Movshovitz et al. (2012)). We model Dimorphos as a full rubble-pile object made of approximately 2000 meter-sized fragments. Tidal forces are automatically computed by the explicit N -body solver, as each fragment of rubble-pile Dimorphos interacts gravitationally with Didymos, which is modeled as a point-mass gravity source. We run 12 simulations in total, covering three different bulk density values (lower-bound 1820 kg/m^3 ; nominal 2170 kg/m^3 ; upper-bound 2520 kg/m^3) for Dimorphos. Each simulation lasts 12 hr (approximately one preimpact orbital period), and starts with Dimorphos at its nominal preimpact orbital location. The DART impact is modeled by means of an instantaneous change of Dimorphos’s orbital velocity, which is selected to reach different pericenter distances (400, 500, 600, 800 m). For a direct comparison, we choose the pericenter distances to fall within the range provided by theoretical estimates based on Holsapple and Michel (2006, 2008) and Roche (1847).

Figure 4.12 shows the qualitative results of GRAINS simulations and their direct comparison to theoretical estimates based on Roche (1847) and Holsapple and Michel (2008) models as a function of Dimorphos’s bulk density. In particular, the Roche limit (represented by a green line) ranges between $\sim 600\text{--}700$ m, depending on the bulk density of Dimorphos ($\rho_B = 2170 \pm 350 \text{ kg m}^{-3}$). The colored region represents the disruption limits for a range of cohesion values, based on Holsapple and Michel (2006, 2008), and aggregates with a friction angle of 25° . In this case, the cohesionless breakup limit (upper edge of colored region) is consistently lower than

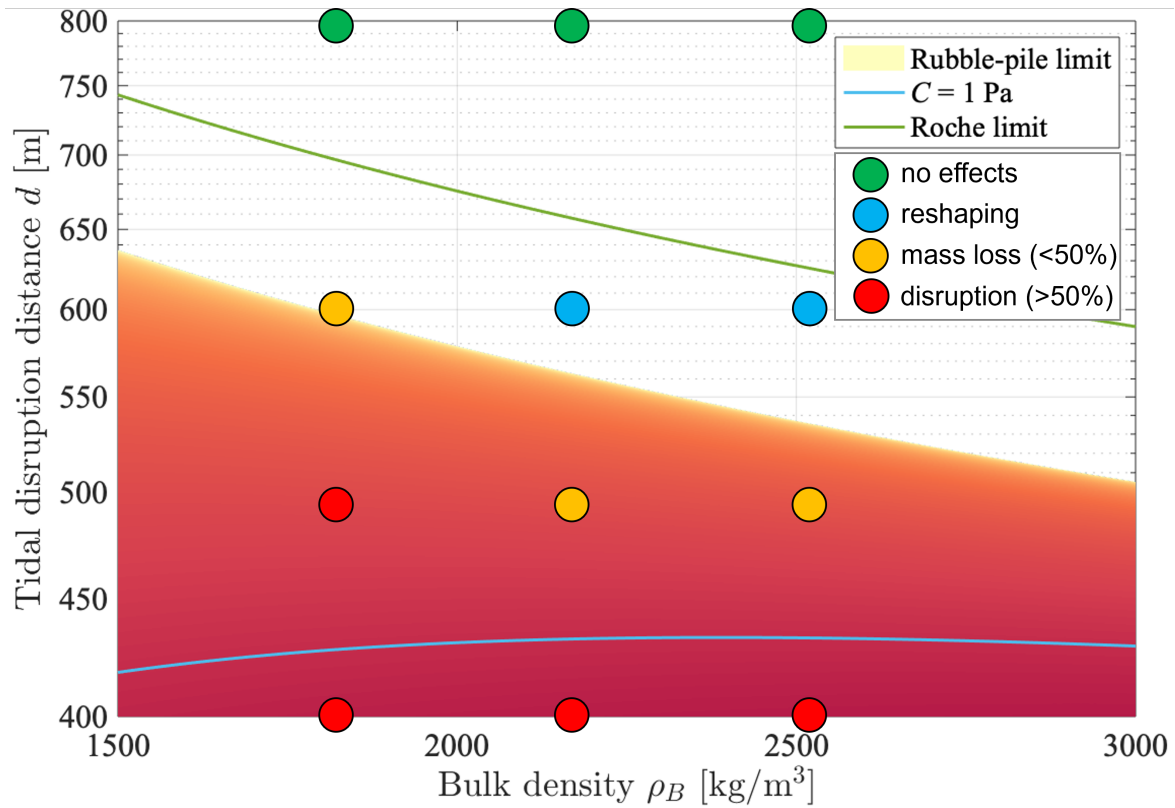


Figure 4.12: Tidal disruption distance as function of bulk density ρ_B for the case of Dimorphos. The distance is considered here between the center of mass of Dimorphos and Didymos. The green line represents the Roche limit for fluid bodies (Roche, 1847). The colored area represents disruption limits for aggregates with cohesion (the darker the color, the more cohesion is required to keep the aggregate stable) based on Holsapple and Michel (2006, 2008), where the upper limit represents a cohesionless aggregate and the blue curve shows an example for a cohesion of 1 Pa. Colored circles represent results of numerical simulations of cohesionless aggregates using GRAINS, where the colors are representative of the qualitative outcome of the simulation on a four-level scale (no effects/reshaping/mass loss/disruption).

the Roche limit for fluids. Also, according to Holsapple and Michel (2008) theory, the amount of cohesion needed to prevent breakup is extremely small, even at very low distances: e.g., a cohesion of 1 Pa is sufficient to prevent breakup at $\sim 400\text{--}450$ m (blue line). The colored circles represent the outcome of GRAINS simulations in terms of their qualitative behavior on a four-level scale: *no effects*, where the aggregate's shape is largely preserved and little to no motion is observed on its surface; *reshaping*, where the aggregate's shape is considerably affected, but no mass loss is observed; *mass loss*, where some amount of mass (less than/equal to 50%) is lost by Dimorphos; and *disruption*, where more than 50% of Dimorphos's mass is lost. We remark here that these results refer only to short-term tidal interactions, i.e., to effects observed within 12 hr from the simulated DART impact. There may be additional disturbances to Dimorphos's structure or surface on subsequent pericenter passages.

In this context, very weak or no effects are observed on aggregates orbiting with a pericenter of 800 m, while some effects are visible after a close passage at 600 m. In this case, depending on the density of Dimorphos, the aggregate experiences mass loss (lower-density case), or reshaping without mass loss (nominal- and higher-density cases). A pericenter at 500 m produces disruption of a low-density aggregate or a consistent mass loss in case the density is higher. For a lower pericenter, the consequences are more dramatic as the aggregate is completely shattered after a close passage at 400 m, for any density value within the range considered. Figure 4.13 shows the snapshots from three GRAINS simulations, with nominal bulk density of Dimorphos. They show the binary system 12 hr after instantaneous velocity change is applied, leading to, from left to right: a 600, 500, and 400 m pericenter orbit. As mentioned, the aggregate is heavily reshaped but with no mass loss in the 600 m case (left). On the other hand, we observe a significant mass loss in the 500 m case (center) and for lower pericenter distances, up to major shattering

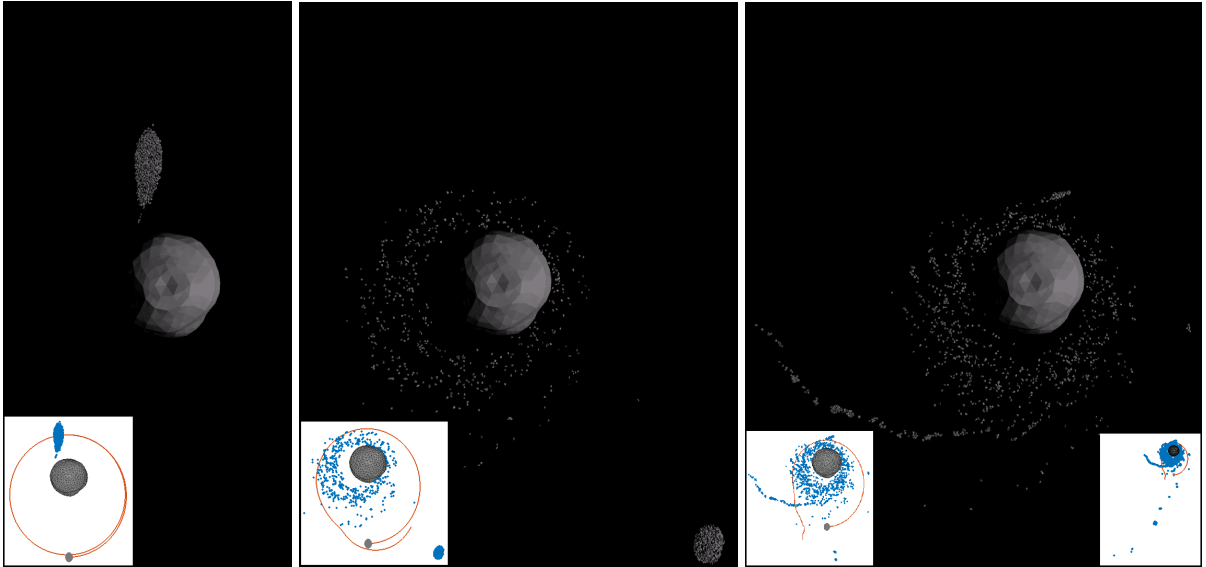


Figure 4.13: Snapshots of GRAINS simulations 12 hr after an instantaneous velocity change is applied on Dimorphos rubble-pile aggregate with nominal bulk density. From left to right: pericenter at 600 (reshaping with no mass loss), 500 (significant mass loss), 400 m (disruption). We show the physical extent of Didymos in scale for comparison. Didymos’s shape model is used for collision computations, but not for gravity computations, which are done using a point-mass source. Thumbnails report the orbital trace of Dimorphos barycenter in red (including all particles that belonged to Dimorphos at the beginning of the simulation), and the initial position of Dimorphos before the instantaneous velocity change (gray ellipsoid).

in the 400 m case (right). The physical extent of Didymos is shown: we recall that gravity is computed using a point-mass source, while the contact/collision interactions take into account the full polyhedral-shape model of Didymos, as shown in the figures. Thumbnails report the orbital trace of Dimorphos’s barycenter in red, as well as the initial position of ellipsoidal Dimorphos in gray, before the instantaneous velocity change is applied.

Both the theoretical and numerical models predict strong tidal effects to occur in a close-proximity region, within 800 m from Didymos barycenter, i.e., approximately within a distance of 400 m from Didymos surface. As Dimorphos’s preimpact orbit has a semi-major axis of approximately 1200 m, it is clear that a significant perturbation is required to reach the <800 m region. It is now worth interpreting these results in the context of the DART mission, by consid-

ering realistic orbit changes expected from DART impact itself. The β value can be computed as a function of masses and speeds of both Dimorphos and DART:

$$\beta = \frac{\Delta v \cdot M_{\text{B}}}{v_{\text{DART}} \cdot M_{\text{DART}}} \quad (4.1)$$

where Δv represents the change in Dimorphos’s orbital speed produced by the DART impact. Using this simple relation, we compute β values required to reach the region where strong tidal effects are relevant.

Table 4.3 reports the values of orbital period change (ΔT), semimajor-axis change (Δa), and β value required to reach a given pericenter distance (800, 600, 500, 400 m). It is worth noting that β depends on Dimorphos’s mass, which is highly uncertain and will only be measured with high accuracy by the Hera mission 4 yr after the impact. This uncertainty is propagated to the value of β , which varies by approximately 40% depending on Dimorphos’s mass. We report β values for the limiting cases of low ($\rho_{\text{B,lo}} = 1820 \text{ kg m}^3$), nominal ($\rho_{\text{B,nom}} = 2170 \text{ kg m}^3$), and high ($\rho_{\text{B,hi}} = 2520 \text{ kg m}^3$) bulk density. As anticipated, the orbital change required to enter the region where strong tidal effects are relevant is very high. In the worst-case scenario (low Dimorphos mass), $\beta = 21$ is required to reach a 800 m close passage. This value is an order of magnitude higher than the typical expected values, where β ranges typically from 1 to 5 and hardly reaches values as high as 10 (Stickle et al., 2022). Based on these considerations, it appears very unlikely for Dimorphos to enter the 800 m region, relevant for strong tidal effects, after DART’s impact. Therefore, we can safely assume that both its internal structure and outer surface will not be affected in a relevant manner by short-term tidal interactions with Didymos, so long as ρ_{B} is not significantly less than anticipated. However, we note that the simulations

presented in this section are limited in their duration. Over longer integration times, it may be possible that Dimorphos’s internal structure could be altered after subsequent pericenter passages as its spin and orbit evolves, even for the 800 m pericenter cases.

Pericenter [m]	ΔT [hr]	Δa [m]	β		
			$\rho_{B,lo}$	$\rho_{B,nom}$	$\rho_{B,hi}$
800	2.7	190	21	24	29
600	4.1	290	36	43	51
500	4.7	340	47	55	65
400	5.3	390	59	70	82

Table 4.3: Orbital variation corresponding to a post-impact orbit of Dimorphos with pericenter values ranging from 400 to 800 m. β values associated with such variations are computed for the limiting cases of low ($\rho_{B,lo} = 1820 \text{ kg m}^3$), nominal ($\rho_{B,nom} = 2170 \text{ kg m}^3$), and high ($\rho_{B,hi} = 2520 \text{ kg m}^3$) bulk density.

4.5.2 Long-term evolution of Dimorphos as an Irregularly Shaped Body

We also study the possibility of shape or surface changes to Dimorphos over longer timescales resulting from its post-impact rotation state. Previous rigid-body work has shown that the DART impact will cause Dimorphos to librate and possibly enter a chaotic rotation state, depending on its shape and β . Here we explore whether Dimorphos’s post-impact rotation state can affect its internal structure or surface. We take a similar approach to the one described in Section 4.4.1, where we use PKDGRAV with a point-mass Didymos and rubble-pile Dimorphos. We also use the same particle-size–frequency distribution and friction parameters described in that section. However, instead of using the idealized ellipsoidal rubble piles, we instead use the radar-derived shape models of two near-Earth asteroids scaled to the volume of Dimorphos. Using a more realistic body shape allows parts of the surface to achieve higher surface slopes to allow us to find reasonable limits at which the rubble-pile nature of the secondary may become important. The

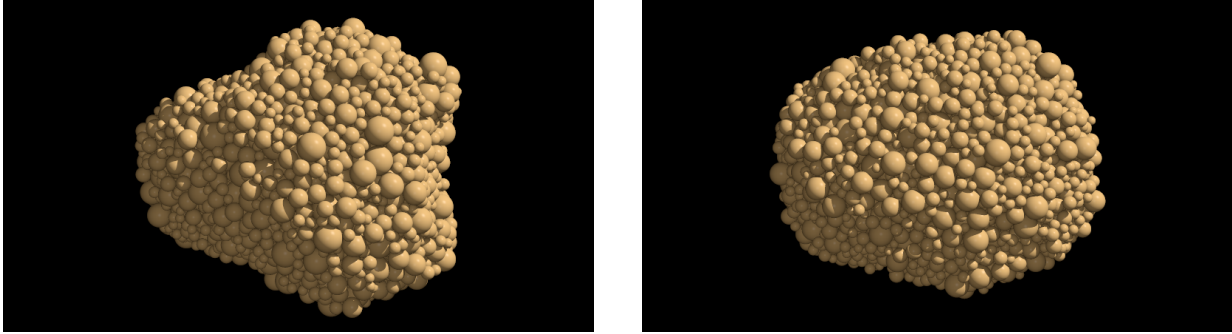


Figure 4.14: Top-down views of the rubble-pile models of Apophis and Squannit, scaled to the dimensions of Dimorphos. These bodies are built from the same particle-size distribution described in Section 4.4.1 and also have the same material parameters.

two radar-derived shape models we selected are Squannit, the secondary component of 66391 Moshup (Ostro et al., 2006), and 99942 Apophis (Brozović et al., 2018). Squannit was chosen because it is the secondary component of a system quite similar to Didymos and because its shape is expected to be attitude unstable in the Didymos system for an eccentricity of $e \sim 0.025$ ($\beta = 3$). A scaled Apophis shape model was chosen because it has an irregular shape despite a relatively low shape elongation, and its DEEVE semiaxis lengths indicate that it should remain attitude stable within the Didymos system for $\beta = 3$.⁵ PKDGRAV representations of these two bodies, scaled to the volume of Dimorphos, are shown in Fig. 4.14 and Table 4.4 provides some quantitative descriptions of the two bodies.

Figure 4.15 is a mosaic of plots showing the evolution of the system for varying values of β for the scaledApophis realization of Dimorphos. In each subfigure, the top plot shows Dimorphos’s instantaneous spin rate along with the mutual orbital angular speed. The middle plot shows the instantaneous separation between Didymos and Dimorphos. The DART perturba-

⁵Assuming a uniform bulk density, Squannit’s DEEVE axis lengths indicate it would be unstable within the Didymos system according to the analysis of Agrusa et al. (2021). Similarly, Apophis’s DEEVE axis lengths indicate that it should be attitude stable as Didymos’s secondary following a DART impact with $\beta = 3$

⁶These objects were not actually simulated in Agrusa et al. (2021) but their DEEVE semiaxes indicate stable/unstable attitudes respectively.

Name	$a/b, b/c$	a, b, c [m]	N	M_B [10^9 kg]	Agrusa et al. (2021) Prediction for $\beta = 3^6$
scaledApophis	1.25, 1.07	100.8, 80.5, 75.3	3801	4.8524	Stable
scaledSquannit	1.32, 1.32	109.7, 83.0, 63.0	3834	4.8664	Unstable

Table 4.4: The body shapes for Dimorphos considered in this section. The shape models for the real Apophis (Brozović et al., 2018) and Squannit (Ostro et al., 2006) were scaled to match the expected volume of Dimorphos. The rubble-pile models for `scaledApophis` and `scaledSquannit` were simply created by deleting any PKDGRAV particles that lay outside the respective scaled shape models. The reported dimensions ($a, b, c, a/b, b/c$) are based on the DEEVE semiaxis lengths of the rubble piles and do not necessarily match the *exact* dimensions of the shape models used to create those rubble piles. N and M_B are the respective number of particles and mass of the body.

tion is applied after 24 hr of simulation time, which is why the orbital separation starts off near 1200 m, then drops to a lower value. The binary eccentricity is computed based on the periapse and apoapse of the orbit⁷ (which can change due to spin-orbit coupling). The binary eccentricity is reported on each subfigure and is computed based on the first several orbit periods immediately following the DART perturbation. Finally, the third plot shows the change in Dimorphos’s DEEVE semiaxis lengths, relative to their starting value. Rather than plot the changes to the body’s moments of inertia, we instead plot the DEEVE axis lengths, since they have dimensions of length and are easier to conceptualize, although there is a straightforward correspondence between an arbitrarily shaped body and its DEEVE axis lengths.⁸

In Fig. 4.15, we see that, in the `scaledApophis` case, the secondary’s spin rate oscillates around the mean motion up to $\beta = 5$ since the body is stably librating. At $\beta = 7$, Dimorphos has become attitude unstable, and the spin rate can diverge from the mean motion. The same trend is

⁷Since the mutual orbit is non-Keplerian, we report a geometric eccentricity rather than the Keplerian eccentricity. The geometric eccentricity of the orbit is a simple function of the maximum and minimum separations (periapse and apoapse) of the orbit. It can be written as $e = 1 - \frac{2}{r_a/r_p + 1}$, where r_a and r_p are the respective apoapse and periapse distances.

⁸For a body of mass m and principal moments of inertia A, B, C , its corresponding dynamically equivalent equal-volume ellipsoid axis lengths a, b, c are given by the following relations: $A = \frac{m}{5}(b^2 + c^2)$, $B = \frac{m}{5}(a^2 + c^2)$, $C = \frac{m}{5}(a^2 + b^2)$.

true for the binary separation: the body separation uniformly oscillates due to the eccentricity of the orbit and the periodic exchange of angular momentum between Dimorphos's spin state and the mutual orbit. When Dimorphos becomes attitude unstable, its spin state becomes chaotic, as does the binary separation due to the strong spin-orbit coupling. The most interesting feature of these plots is the significant changes and oscillations in Dimorphos's DEEVE axis lengths (i.e., moments of inertia). Even when Dimorphos is stably librating, the moments of inertia are also oscillating as the body feels time-varying stresses due to oscillations in the tidal potential and its spin state. This effect can be thought of as the body *breathing* or *flexing* in response to these stresses. This is a result of SSDEM, where particles are able to overlap by a small amount, which is mediated by a restoring spring force. As the tides or the body's spin change, the particles are able to make small adjustments to find a new equilibrium. When the body becomes attitude unstable, this effect becomes much more significant, and we see permanent changes to the DEEVE axis lengths indicating that some particles have actually been displaced, which will be discussed shortly.

Figure 4.16 shows the same mosaic of plots for the `scaledSquannit` realization of Dimorphos. Qualitatively, these plots are very similar, with the main difference being that Squannit becomes attitude unstable at lower values of β due to its shape and thus has larger variations in its DEEVE semi axis lengths.

It should be noted that these results likely *exaggerate* the oscillations in the DEEVE axis lengths. In terms of axis-length change, the tidal response of a rubble pile is highly dependent on its Young's modulus, which relates its strain (axis-length change) to stress (applied force per unit area). In PKDGRAV, the Young's modulus is not an input parameter but is related to the spring constant, k_n , that mediates particle overlaps. The Young's modulus (Y) can be approximated as

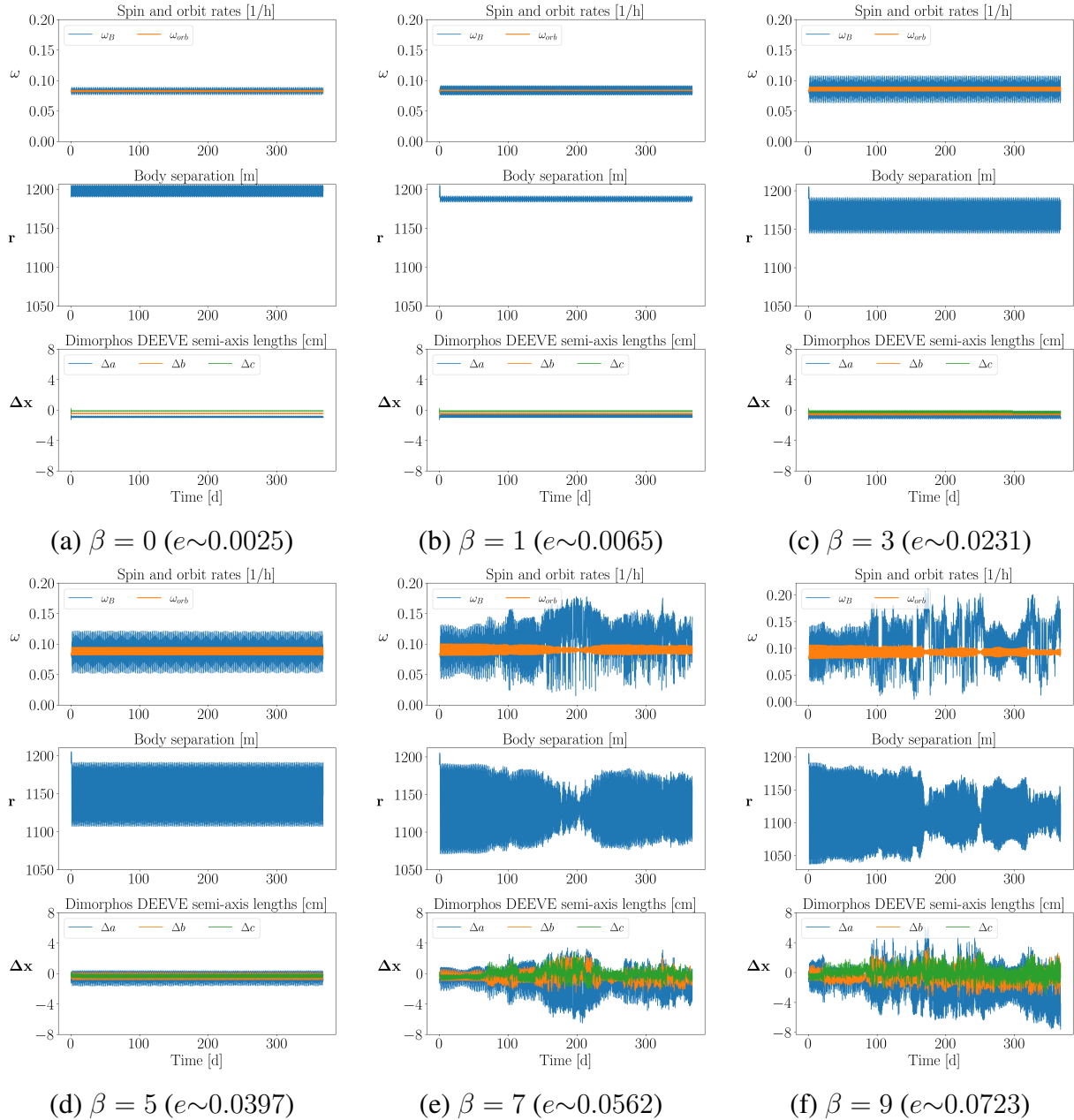


Figure 4.15: Evolution of the secondary’s spin rate (top plots), orbital separation (middle plots), and change in DEEVE semi-axis lengths (bottom plots), for an Apophis-shaped Dimorphos with values of β ranging from 0 to 9. For each value of β , we also report the binary orbital eccentricity e , based on the first several orbit periods following the DART-like perturbation. As β increases, the body eventually becomes attitude unstable allowing relatively large deviations in the body’s DEEVE axis lengths. All plots have the same y-axis scales to allow for direction comparisons.

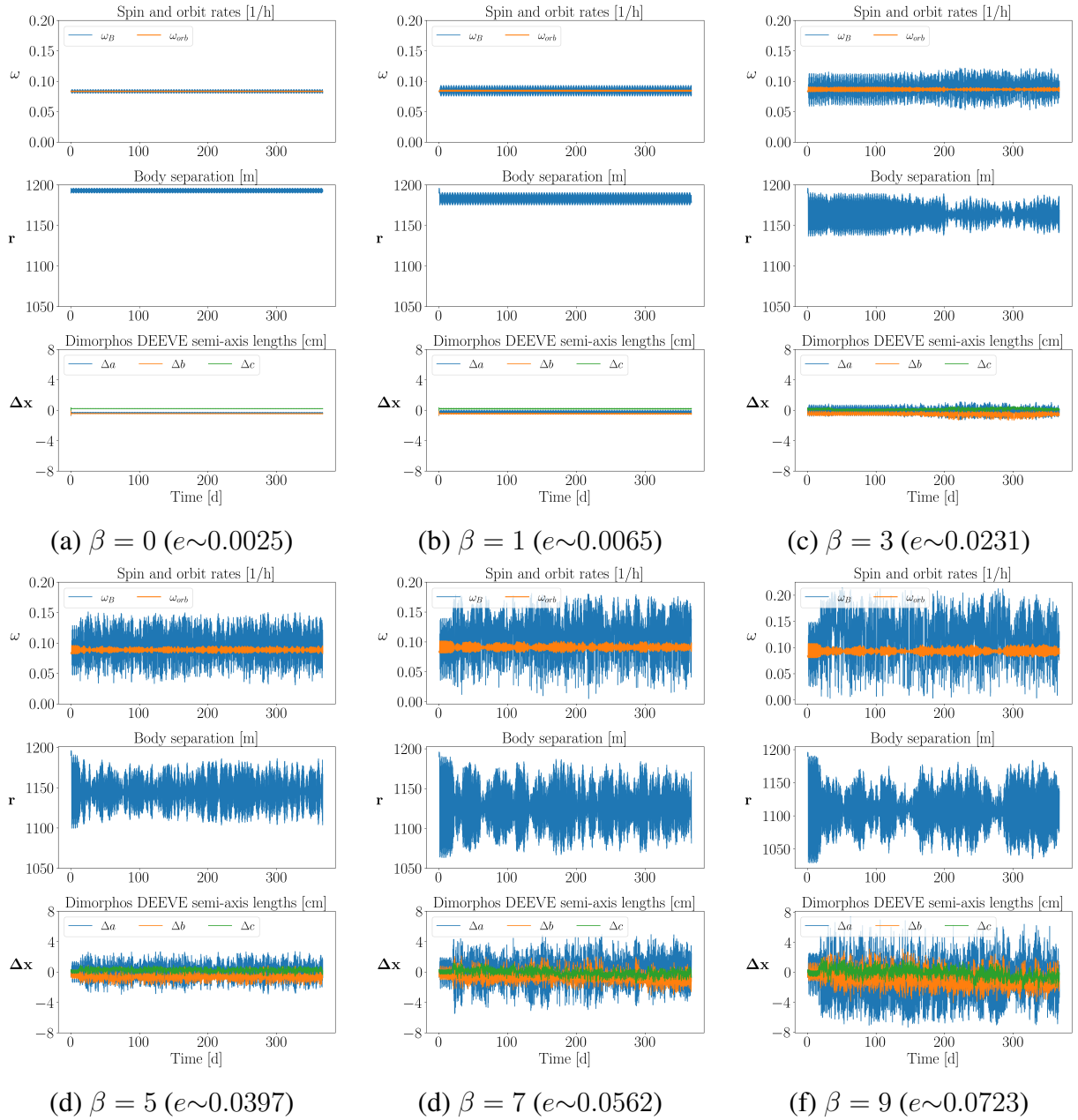
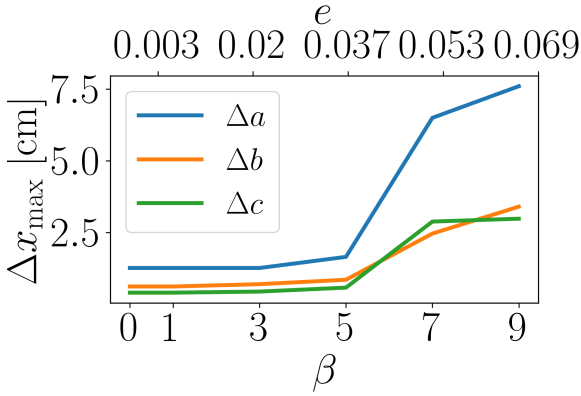


Figure 4.16: Evolution of the secondary’s spin rate (top plots), orbital separation (middle plots), and change in DEEVE semi-axis lengths (bottom plots), for an Squannit-shaped Dimorphos with values of β ranging from 0 to 9. For each value of β , we also report the binary orbital eccentricity e , based on the first several orbit periods following the DART-like perturbation. All plots have the same y-axis scales to allow for direction comparisons.

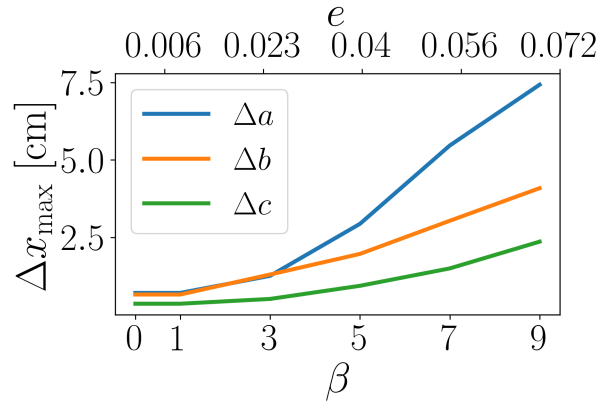
$Y \sim \frac{k_n}{\pi R}$, where R is the typical particle radius (DeMartini et al., 2019). In other words, a weaker spring constant means the material is weaker and easier to deform. In these simulations, the average particle radius is 4.2 m, and the spring constant is $k_n \sim 1.45 \times 10^4 \text{ N m}^{-1}$, corresponding to a Young's modulus of $\sim 1.1 \text{ kPa}$. This value is quite small for granular material, although not completely unrealistic; a value on the order of 1 MPa or greater is probably more realistic (Möhlmann et al., 2018). The low value for the spring constant (and therefore Young's modulus) was chosen out of computational necessity. A higher spring constant means higher restoring forces between particles, which requires a shorter time step to adequately resolve the particle interactions (Schwartz et al., 2012). This means that the time step needs to be reduced by a factor of ten if we want to increase the spring constant (and therefore the Young's modulus) by a factor of 10, which makes long-term simulations too slow.⁹ Conveniently, previous work has shown that the axis-length changes scale linearly with the Young's modulus (DeMartini et al., 2019). So if Dimorphos has a Young's modulus of $Y \sim 1 \text{ MPa}$, then we would expect the deviations in its DEEVE axis lengths to be a factor of $\sim 10^{-3}$ times smaller than what is shown here, for example. Figure 4.17 shows the maximum change in axis length over the entire simulation as a function of β for the two body shapes under consideration. Although the artificially low Young's modulus exaggerates the magnitudes in the axis length change, these plots illustrate the strong dependence on β . An equivalent plot with a more realistic Young's modulus would qualitatively look similar, with the y-axis scaled to lower values.

Based on these simulations, it seems that the oscillations in Dimorphos's DEEVE axis lengths are caused by time-varying stresses due to spin and tides, while the magnitude of the

⁹The simulations presented here used 4 CPU cores in parallel, and took ~ 3 months to complete a 1 yr simulation. All things being equal, it would take ~ 250 yr of wall-clock time to repeat these simulations with a more realistic Young's modulus of $\sim 1 \text{ MPa}$.



(a) Apophis-shaped Dimorphos



(b) Squannit-shaped Dimorphos

Figure 4.17: Maximum DEEVE axis-length changes as a function of β or the binary eccentricity e . The axis-length change for $\beta = 0$ is nonzero since the system is not *perfectly* relaxed and has a nonzero eccentricity and libration. As β or e is increased, the DEEVE axis lengths have larger oscillations, and the trend jumps up sharply when the body becomes attitude unstable. In these simulations, Dimorphos’s Young’s modulus is ~ 1 kPa and likely *overestimates* the axis-length changes for reasons explained in the text. For higher values of the Young’s modulus, we would expect lower magnitudes in axis-length oscillations, although the general trend would not change.

oscillations is highly dependent on the material properties of the body. Now, we turn to briefly investigate the cause of the permanent changes to the DEEVE axis lengths. We find that the cause is likely small particle motions on the surface of the body that lead to small changes in the body’s moments of inertia (and therefore DEEVE semiaxis lengths). In Fig. 4.18, we plot the number of particles that have moved by a given distance for the Apophis-shaped Dimorphos, for $\beta = 5, 7, 9$. In order to calculate whether a particle has moved, we compute its position in the body-fixed frame at each output and compare it to its position when the DART perturbation was first applied. It is important to keep in mind that the body-fixed frame is constructed by computing the body’s principal rotation axes at each time step, which depend on the body’s moments of inertia. Because the principal axes are able to change in direction, the body-fixed frame is not perfectly fixed. Due to this effect, this approach is not sensitive to small particle motions. However, the average particle size is 4.2 m, meaning that the sensitivity to small-scale motion is limited anyways.

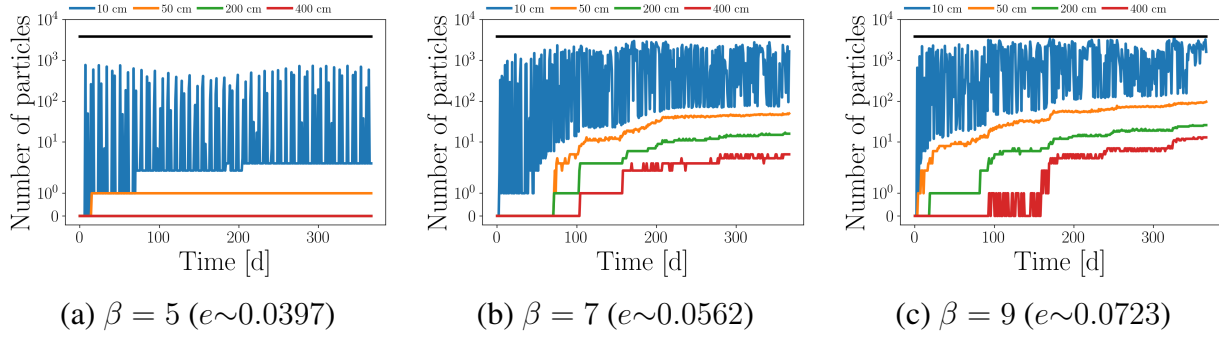


Figure 4.18: Particles that have moved by more than a given distance for the scaled Apophis case. As β (or equivalently the binary eccentricity e) is increased, more particles are able to move from their original location. These motions are ongoing and occur hundreds of orbit periods after the DART perturbation is applied. However, the average particle radius is 420 cm, meaning that these motions are very small. The large number of particles that are moving by 10 cm or more indicates that we are not sensitive to motion at this scale due to the combination of limited particle resolution and the fact that the body’s moments of inertia (which form the fixed-body coordinate frame) are changing.

In Fig. 4.18(a) ($\beta = 5$), we see that no particles have moved more than 400 or 200 cm, one has moved more than 50 cm, and many particles have moved by 10 cm or more. Figs. 4.18(b) and 4.18(c) show that more particles are able to move from their original location when the binary eccentricity (i.e., β) is increased. The same results are shown in Fig. 4.19 for the Squannit-shaped Dimorphos with largely the same conclusion: a more eccentric and tighter orbit leads to more particle motion. It is important to keep in mind that the typical particle radius is 4.2 m, meaning that these particles are not traveling large distances on the surface. Rather, these are particles making small adjustments, typically moving less than a single particle radius.

4.5.2.1 Interpretation of results

Here, we provide a guide for interpreting the results of this subsection in the context of the various choices and compromises in simulation settings.

1. The large oscillations in the number of particles that move ≥ 10 cm (Figs. 4.18 and 4.19)

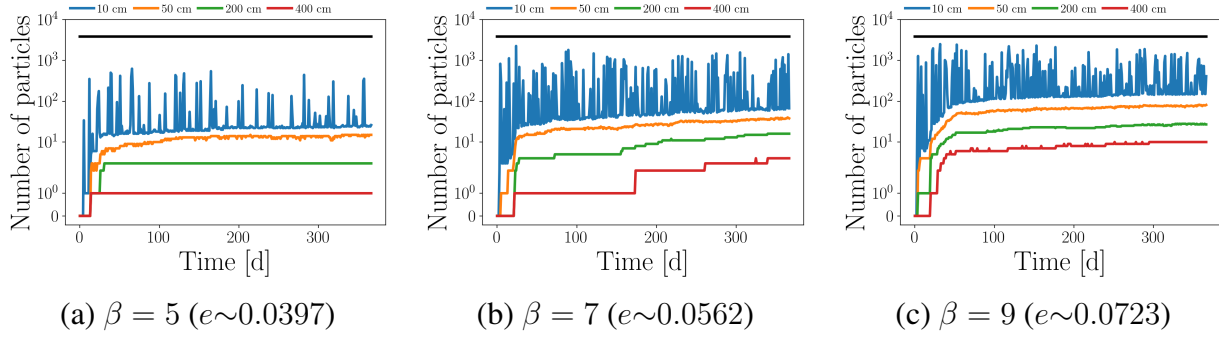


Figure 4.19: Particles that have moved by more than a given distance for the scaled Squannit case.

indicate that the simulations are not sensitive to small-scale particle motion. This is due to a combination of the coarse particle resolution and the fact that Dimorphos’s body-fixed frame is not technically fixed. At each simulation output, Dimorphos’s body-fixed frame is defined using its principal rotation axes, which depend on its time-varying inertia tensor.

2. The artificially low value of the Young’s modulus (~ 1 kPa here) means that the simulated rubble piles are likely overly deformable, meaning that we are *overestimating* the tidal response of Dimorphos. This choice in Young’s modulus was required to reduce the computational costs. However, it has been shown that the Young’s modulus is directly proportional to the maximum axis-length change (DeMartini et al., 2019). This means that the DEEVE axis-length changes can be scaled down to approximate a more realistic axis-length change. Something on the order of millimeters (or less) seems probable. Such a small effect is unlikely to be measurable with Hera. Although, in theory, an in situ seismometer would be capable of detecting this signal.
3. The coarse particle size (~ 4 m radii) was chosen to limit the computational costs as well. This means these simulations likely *underestimate* the particle motion on the surface. This is because many surface particles are sitting in deep gravitational wells and have to be lifted

out of a meters-deep crevice before they can move along the surface. Of course, if DART imagery indicates a lack of sub-meter-sized boulders, then this is no longer an issue as it would represent a realistic treatment of Dimorphos’s surface. However, if Dimorphos has smaller-sized particles on its surface, then a higher-resolution simulation (or an alternative approach) is necessary to fully quantify the amount of surface motion that may occur as a result of Dimorphos’s post-impact dynamical state.

4. All these simulations use *gravel-like* friction parameters that yield a friction angle of $\phi \sim 38^\circ$ —a lower friction angle would increase the odds that a portion of Dimorphos’s surface could exceed its angle of repose while tumbling, leading to surface motion.

For these reasons, we conclude that DART-induced particle motion on Dimorphos is a possibility under the right circumstances, although a more detailed investigation is required. In addition, the fact that the tumbling, and therefore particle motion, is long-lived indicates that ESA’s Hera mission may observe this effect in real time upon rendezvous in 2026. After DART’s arrival, the parameter space of possible body shapes and boulder-size ranges will shrink dramatically (Daly et al., [2022](#)), making this problem more tractable. If preliminary DART imagery suggests that Dimorphos is indeed a rubble pile, that its body shape indicates post-impact tumbling, and that it has a shape with high surface slopes, then the possibility of surface particle motion will be explored with much higher fidelity. Full-scale PKDGRAV-like simulations with a more realistic Young’s modulus and particle-size distribution, in addition to high-resolution localized granular bed simulations at particular locations on Dimorphos’s surface, could be used to investigate the likelihood of long-term surface particle motion. However, given that Dimorphos’s shape and boulder-size–frequency distribution are still unknown, such a high-fidelity study is unwarranted

at this point.

4.6 Conclusions and Future Work

In Section 4.4.1, we conducted *long-term* (1 yr) simulations with Dimorphos as a rubble pile having the shape of a tri-axial ellipsoid following the DART impact. We found that, for a momentum enhancement factor, β , on the order of 3, Dimorphos’s evolution as a rubble pile is not appreciably different than its evolution as a rigid body. This holds true in cases where Dimorphos is in a stable libration state and when it rotates chaotically. We extended this study in Section 4.4.2 to include a rubble-pile treatment for Didymos and found no substantial differences, although these simulations were limited to only 30 days due to the increased number of particles and computational cost. These results indicate that the much faster rigid-body approach is an appropriate tool for modeling the post-impact dynamics of the Didymos binary following the DART impact.

In Section 4.5, we explored the limits at which a rubble-pile treatment might be necessary. In Section 4.5.1, we showed that β would have to be unrealistically large ($\beta \gtrsim 20$) in order for the mutual tides to cause significant structural changes to Dimorphos, at least over short timescales and for the expected range in bulk density. We then simulated Dimorphos as an irregular shape using scaled shape models of Squannit and Apophis over a wider range of β values ($0 < \beta < 9$) to place rough constraints on how the excitation due to DART will affect Dimorphos over longer timescales. We found that the mass distribution of Dimorphos (i.e., its moments of inertia), measurably changes in response to the time-varying spin and tidal environment. Even for small values of β , we observed the DEEVE semiaxis lengths of Dimorphos oscillate as its spin rate

and orbital separation are periodically changing. However, the magnitude of these oscillations are probably overexaggerated in these simulations due to the unavoidable selection of material parameters. Oscillations on the order of millimeters are probably more likely than the centimeter-scale oscillations presented here, although this is all highly dependent on Dimorphos's (unknown) material strength and interior structure. For $\beta \gtrsim 5$, we also saw small permanent changes to the semiaxis lengths as a result of small motions of particles at the surface. Due to Dimorphos's rapidly changing spin state when its attitude becomes chaotic, as well as the periodically varying tidal force, these particles feel high-enough accelerations that enable them to move on the surface. These motions are small and are typically less than a single particle radius. However, the limited particle resolution underestimates this effect, making it difficult to draw any firm conclusions. In any case, these simulations indicate that, under the right circumstances, the motion of particles on the surface is plausible and that a more focused investigation is required. If surface motion does occur, we showed that it could be a long-lived process, meaning that it is something that Hera may be able to observe upon arrival in late 2026. There is also the prospect that any regolith motion could alter the shape of the DART impact crater, prior to Hera's arrival in a manner analogous to surface refreshment at Stickney Crater on Phobos (Ballouz et al., 2019).

To summarize, we identify four key results of this work:

1. We find that a rubble-pile approach is not required to capture Dimorphos's post-impact spin and orbital evolution, so long as β is not unexpectedly large. Therefore, faster rigid-body codes should be more than adequate for predicting the system's post-impact dynamical state.
2. If β is *significantly* larger than expected ($\beta \geq 20$) or Dimorphos is highly underdense

(or undermassive), then significant reshaping, mass loss, or disruption would be possible. However, we find that such an outcome is unlikely given experimental and numerical predictions for β (Stickle et al., 2022; Walker et al., 2022).

3. Depending on the internal structure and material properties of Dimorphos and the level of excitation to its spin and orbital state, a large tidal response may be induced. In theory, this could be measured with a seismometer. In practice, this effect will likely not be measurable with Hera.
4. Depending on Dimorphos's shape and post-impact spin state, granular motion on the surface is a possibility. We expect that the methodology used in this work *underestimates* any motion on the surface. This effect requires more thorough investigation, which is currently underway. If surface motion occurs, it presents a unique possibility that Hera may observe this effect by characterizing the surface color and grain flow patterns.

Chapter 5: Rotation-induced granular motion on the Dimorphos

5.1 Chapter Preface

This chapter was published as a letter in *Astronomy & Astrophysics* under the title, “Rotation-induced granular motion on the secondary component of binary asteroids: Application to the DART impact on Dimorphos” (Agrusa et al., 2022b). The findings of Agrusa et al. (2022a) (Chapter 4) indicated the possibility of boulder motion on Dimorphos’s surface depending on its post-impact spin and orbital state. To better understand the magnitude and likelihood of any dynamically triggered granular motion, we put together this short study to look at Dimorphos’s possible post-impact surface slope evolution as a function of its unknown bulk density and β . This was a short paper to demonstrate a range of possibilities that will enable future studies once Dimorphos’s geophysical properties and the DART impact outcome are better understood. This chapter is presented with minimal modification from its published version. Some of the introductory material may be somewhat repetitive with Chapter 1, so the reader may skip to Section 5.3 if desired. The appendices associated with this chapter are located in Appendix B.

5.2 Introduction

On September 26, 2022, NASA’s Double Asteroid Redirection Test (DART) mission will kinetically deflect Dimorphos, the smaller component of the binary asteroid 65803 Didymos, as a planetary defense demonstration test (Rivkin et al., 2021). Prior to the impact, DART will deploy the Light Italian CubeSat for Imaging of Asteroids (LICIACube), which will fly by the system to image the initial phase of the cratering process as well as improve Dimorphos’s shape determination (Cheng et al., 2022; Dotto et al., 2021). Following the impact, the change in the mutual orbit period will be measured via ground-based observations and used to infer the momentum enhancement factor, commonly referred to as β (Rivkin et al., 2021). Due to the contribution of ejecta that exceeds the escape speed, β is expected to exceed 1. Four years after DART, the European Space Agency’s Hera mission will rendezvous with Didymos to characterize the physical, dynamical, and compositional properties of the system. Hera will also measure in detail the effects of the DART impact, including the crater’s properties and the mass of Dimorphos, allowing for a more precise determination of β (Michel et al., 2022).

In addition to abruptly reducing the binary semimajor axis and orbit period, the impact will also change the eccentricity and inclination (Cheng et al., 2016). Due to a high degree of spin-orbit coupling, the dynamical evolution of Dimorphos strongly depends on the initial conditions at the time of impact and the body’s shape, which are currently unknown (Agrusa et al., 2020). Depending on β and Dimorphos’s shape, it is possible that Dimorphos may enter a chaotic rotation state following the DART impact (Agrusa et al., 2021; Richardson et al., 2022). Furthermore, numerical simulations that treat Dimorphos as a rubble pile indicate that boulders may move on the surface, depending on Dimorphos’s spin state, bulk shape, and material properties (Agrusa

et al., 2022a). In this study, we take a closer look at the possibility of post-impact surface motion on Dimorphos as a function of its complex spin and orbital environment.

Observational evidence and theoretical arguments both indicate that chaotic rotation is not uncommon for secondaries in tight binary systems (Ćuk et al., 2021; Pravec et al., 2016; Quillen et al., 2022a; Seligman and Batygin, 2021), and it is plausible that many synchronous secondaries have undergone some level of chaotic rotation in their past or during their formation (Davis and Scheeres, 2020b; Jacobson and Scheeres, 2011a; Wisdom, 1987a). Therefore, the methods and results presented here are also broadly applicable to the general binary asteroid population.

5.3 Methods

Focusing on the DART impact, we first ran a simulation to capture the system’s dynamics, from which the local slopes can be computed, in an approach analogous to previous studies of dynamically triggered regolith motion (Ballouz et al., 2019; Yu et al., 2014). In order to capture the coupled spin and orbital motion of the secondary, we used the General Use Binary Asteroid Simulator (GUBAS), an efficient rigid full two-body problem (F2BP) code (Davis and Scheeres, 2020a, 2021). GUBAS has been benchmarked against other F2BP simulation codes and has been used extensively to study the dynamics of Didymos and other binary systems (Agrusa et al., 2020; Davis and Scheeres, 2020b; Meyer et al., 2021; Meyer and Scheeres, 2021). In accordance with previous studies, the GUBAS simulations expand the gravitational potential of the polyhedral shape models to degree and order 4 to adequately capture their irregular gravity fields. All simulations presented herein were run for 1 yr of integration time.

Parameter	Value
Primary bulk density (ρ_P)	2.2 g cm ⁻³
Secondary bulk densities (ρ_S)	[1.85, 2.20, 2.55] g cm ⁻³
Primary mass (M_P)	5.47×10^{11} kg
Secondary masses (M_S)	[4.20, 4.99, 5.78] $\times 10^9$ kg
Primary Diameter (D_P)	780 m
Secondary Diameter (D_S)	164 m
Initial body separation (a_{orb})	1200 m
Initial Orbital Period (P_{orb})	11.92 h
Primary Spin Period (P_P)	2.26 h
Secondary Spin Period (P_S)	11.92 h
Assumed DART Mass (M_{DART})	536 kg
Assumed DART Speed (v_{DART})	6.15 km/s

Table 5.1: Selected physical and dynamical parameters used for the simulated Didymos system, consistent with the current best estimates (Rivkin et al., 2021). The body diameters are the volume-equivalent spherical diameters. A synchronous spin state for Dimorphos is assumed, and we refer the reader to Richardson et al. (2022) for further discussion on this assumption.

5.3.1 Simulation setup

In the F2BP simulations, the primary’s gravity is modeled using Didymos’s radar-derived polyhedral shape model (Naidu et al., 2020a). Dimorphos’s shape is still unknown, so we used the radar shape model for Squannit, the secondary component of the binary asteroid (66391) Moshup, scaled to the expected volume of Dimorphos. Squannit is arguably the best available analog for Dimorphos. Both the Didymos and Moshup systems are S types (Binzel et al., 2004; Dunn et al., 2013) and have similar properties, including a fast-rotating primary with a raised equatorial ridge and a tidally locked secondary component on a tight, approximately circular orbit (Scheeres et al., 2006).¹ Squannit is the only currently available secondary shape model for a near-Earth binary and contains ~ 2300 facets (Ostro et al., 2006). Radar data tend to smooth and flatten surface features, making the surface slope analysis presented here somewhat conservative.

¹There are no observations that show Dimorphos is spin locked, but circumstantial evidence indicates that this is likely. We refer the reader to Richardson et al. (2022) for a detailed discussion on this assumption.

When scaled to the dimensions of Dimorphos, Squannit’s average facet has a surface area of $\approx 38 \text{ m}^2$. Schematics showing the shape models for the primary and secondary are shown in Fig. 5.1(a-c).

We focused this short study on the role of β and Dimorphos’s bulk density (ρ_s) as they play a significant role in determining the surface slope evolution of Dimorphos. The bulk density sets the mass and therefore the self-gravity of the body, which has a significant effect on the surface slope of a given shape model (Richardson and Bowling, 2014; Richardson et al., 2019). For a fixed β , a smaller bulk density (i.e., lower mass) will result in a larger perturbation to the mutual orbit, which can lead to larger changes in surface slopes over time. We tested values of β in the range $0 \leq \beta \leq 5$, in accordance with the best estimates from hydrodynamic simulations of the DART impact (Raducan et al., 2022; Stickle et al., 2022). Based on light curve and radar observations, the Didymos system is expected to have a bulk density with 1σ uncertainties of $\rho \approx 2.2 \pm 0.35 \text{ g cm}^{-3}$ (Naidu et al., 2020a; Rivkin et al., 2021). Assuming Dimorphos has a bulk density within this range, we tested values of 1.85, 2.2, and 2.55 g cm^{-3} . It should be noted that the reported uncertainties are for the bulk density of the entire system, which is of course dominated by the primary, and it is certainly possible for Dimorphos to have a bulk density outside of the range explored here (see the discussion on Dimorphos’s density in Rivkin et al. (2021)). Table 5.1 provides the adopted physical and dynamical parameters for this study.

First, the binary was given dynamically relaxed initial conditions (i.e., a circular orbit with a synchronous secondary). Then, a change in velocity ($\Delta\vec{v}$) was applied to the secondary’s instantaneous orbital velocity consistent with a head-on DART impact and a given selection for

β and ρ_S .² This $\Delta\vec{v}$ reduces Dimorphos’s velocity, causing the body to fall into a tighter, more eccentric orbit.³ Due to the increased eccentricity, Dimorphos then begins librating and can also enter a chaotic non-principal axis (NPA) rotation state at later times depending on its shape. The attitude instability that leads to NPA rotation is driven by intersections of various spin-orbit resonances among Dimorphos’s frequencies of free libration, spin precession, nutation, and mean motion — more details can be found in Agrusa et al. (2021). In results presented here, we give both the value for β and the corresponding binary eccentricity, e , in an effort to make the results of this paper broadly applicable to other similar binary systems. Due to the non-Keplerian nature of small binary systems, we report e as the geometric eccentricity, which is a function of the periapsis (r_p) and apoapsis (r_a) distances: $e = (r_a - r_p)/(r_a + r_p)$.

5.3.2 Computation of external accelerations

At each timestep, the GUBAS code outputs the full state of the system, including the body locations, orientations, velocities, and spins, from which the net surface accelerations of the secondary can be readily computed. The net acceleration is evaluated at the center of each triangular facet (indexed by i) of the shape model at each timestep (indexed by t) and can be written as

$$\mathbf{a}_{i,t}^{\text{net}} = \mathbf{a}_{i,t}^{\text{grav}} + \mathbf{a}_{i,t}^{\text{tides}} + \mathbf{a}_{i,t}^{\text{cent}} + \mathbf{a}_{i,t}^{\text{Euler}}, \quad (5.1)$$

²The DART impact will not be ideally head-on and centered, but recent work indicates that these effects should be negligible in terms of determining the system’s bulk dynamical properties (Richardson et al., 2022).

³ $\Delta\vec{v}$ is dependent on β , the impactor mass and velocity, as well as the secondary’s mass. In a simplified scalar form, it can be written as $\Delta v = -\beta M_{\text{DART}} v_{\text{DART}} / M_S$, where the negative sign indicates that Dimorphos’s speed is reduced.

where the vectors $\mathbf{a}_{i,t}^{\text{grav}}$, $\mathbf{a}_{i,t}^{\text{tides}}$, $\mathbf{a}_{i,t}^{\text{cent}}$, and $\mathbf{a}_{i,t}^{\text{Euler}}$ are the secondary's self-gravity, the primary's tidal acceleration, the centrifugal acceleration, and Euler acceleration, respectively. The Coriolis acceleration is neglected because this study is focused on the conditions to trigger surface motion, rather than details of the motion itself (Kim et al., 2021). The details of how each respective acceleration was computed can be found in Appendix B.1. On each facet, the surface slope is then defined as

$$\theta_{i,t} = \hat{\mathbf{n}}_i \cdot \hat{\mathbf{a}}_{i,t}^{\text{net}}, \quad (5.2)$$

where $\hat{\mathbf{n}}_i$ is the surface normal and $\hat{\mathbf{a}}_{i,t}^{\text{net}} = \frac{\mathbf{a}_{i,t}^{\text{net}}}{\|\mathbf{a}_{i,t}^{\text{net}}\|}$.

5.4 Results

5.4.1 A conceptual example

To demonstrate how the various acceleration components affect the surface slope, we show time-series plots for a scenario in which $\beta=2$ and $\rho_S=2.2 \text{ g cm}^{-3}$ in Fig. 5.1. The initial slopes of the secondary are shown in Fig. 5.1(c), and the post-impact spin and orbital evolution is shown in Fig. 5.1(d). The slope and accelerations are shown in Fig. 5.1(e) for the facet shown in white in Fig. 5.1(c), which has a longitude and latitude of $(\phi, \lambda) \approx (0^\circ, 45^\circ)$. This particular example was chosen to illustrate the relative importance of the various accelerations considered here, as well as the sensitivity of the slope evolution to the spin and orbit of Dimorphos.

The DART perturbation reduces the semimajor axis and increases the eccentricity to $e \sim 0.023$, the effect of which can be seen in the top plot of Fig. 5.1(d). Through spin-orbit coupling, Dimorphos's spin state is also excited, and it begins librating while its spin rate oscillates. In only

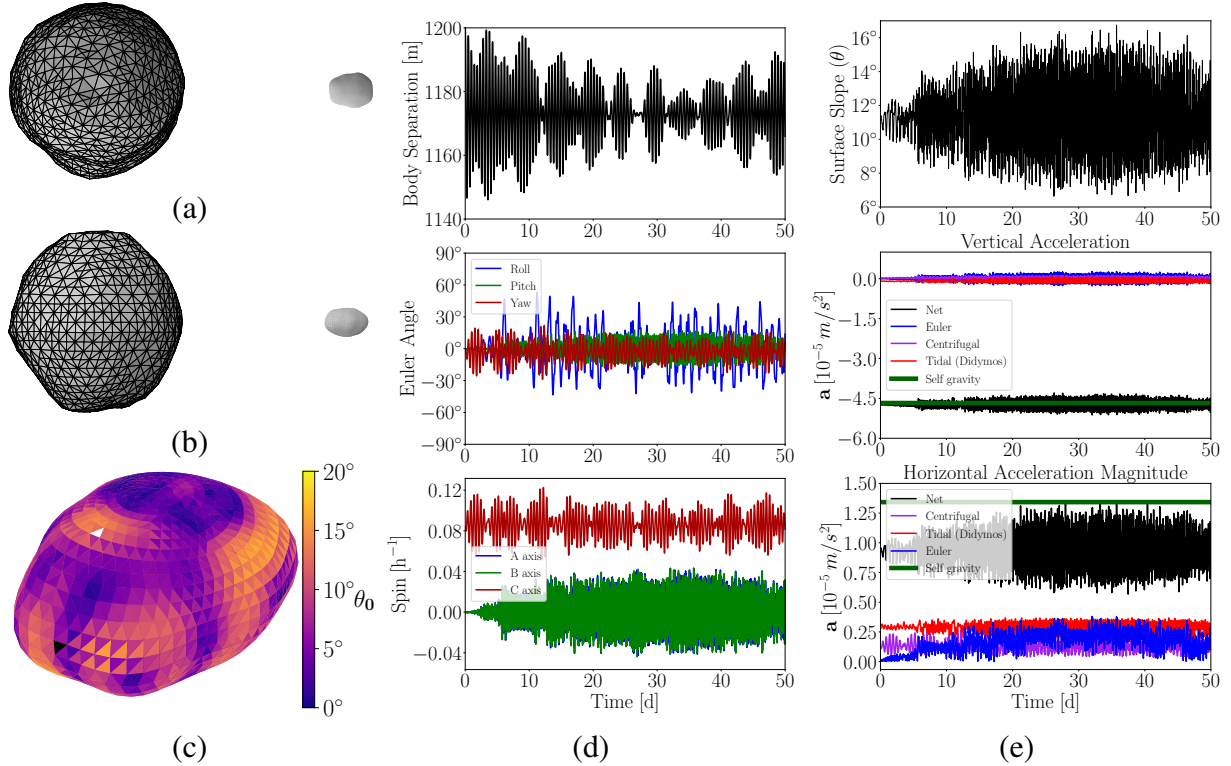


Figure 5.1: Surface slope evolution as a function of Dimorphos’s dynamical evolution. (a) Top-down view of the “Didymos-Squannit” system. From this view, the spin and mutual orbit poles are pointing out of the page. (b) Side view. (c) Surface slopes for a Squannit-shaped Dimorphos with a bulk density of $\rho_S = 2.2 \text{ g cm}^{-3}$ in an idealized, relaxed dynamical state. The black facet corresponds to the sub-Didymos point (at zero libration amplitude) with a longitude and latitude of $\phi \approx \lambda \approx 0^\circ$. The white facet has a longitude and latitude of $(\phi, \lambda) \approx (0^\circ, 45^\circ)$ and corresponds to the time-series plots in part (e). (d) Spin and orbital evolution for the Squannit-shaped Dimorphos when $\beta = 3$ ($e = 0.023$). The Euler angles are the 1-2-3 Euler angle set (roll-pitch-yaw) expressed in the rotating orbital frame, while the body spin rates are in the secondary’s body-fixed frame. (e) Slope and surface accelerations on the white facet from part (c). The vertical accelerations point along the facet’s surface normal and are generally dominated by self-gravity. The horizontal accelerations are expressed as magnitudes and point parallel to the surface. Initially, the Euler acceleration is relatively small and the tides are the dominant time-varying acceleration. After about 5 days, Dimorphos enters NPA rotation, and the Euler accelerations become comparable to both the tidal and centrifugal accelerations. We refer the reader to Appendix B.1 for an identical plot showing the full 365 d simulation.

~ 5 d, the secondary becomes attitude unstable, as indicated by the nonzero roll and pitch angles, although Dimorphos technically remains in the 1:1 spin-orbit resonance (yaw angle $< 90^\circ$). The influence of these dynamical changes can be seen on the surface slope plot at the top of Fig. 5.1(e). At early times, changes in the surface slope are dominated by the tidal acceleration. When Dimorphos enters slight NPA rotation, the centrifugal and Euler accelerations become much more important, leading to abrupt and chaotic surface slope changes.

5.4.2 Dependence on momentum enhancement (β)

In Fig. 5.2 we show time-series plots of the change in surface slope ($\Delta\theta = \theta(t) - \theta_0$) of each surface facet for $\beta = 1$ and $\beta = 3$ with ρ_S fixed at 2.2 g cm^{-3} . The color of each line corresponds to the slope at the start of the simulation, θ_0 . When $\beta = 1$, the orbit is not significantly perturbed. As such, the tidal acceleration is weak and Dimorphos exhibits little NPA rotation, resulting in small surface slope changes of $\Delta\theta \lesssim 2^\circ$. When $\beta = 3$, then the tidal environment becomes strong and Dimorphos enters NPA after only ~ 5 d, resulting in surface slope changes as large as $\Delta\theta \sim 10^\circ$.

The results of Fig. 5.2 highlight the strong temporal dependence of the surface slopes. The surface slope evolution is also spatially dependent, as demonstrated by Fig. 5.3. These plots show the maximum slope achieved over the same simulations shown in Fig. 5.2. The arrows on the plot indicate the down-slope direction. These plots suggest that the highest slopes are achieved in regions that start off with a high slope. For this particular shape and assuming loose regolith covering the surface, we would expect most motion near the equator and mid-latitudes, and very little, if any, near the poles. This spatial dependence may have implications for inferred

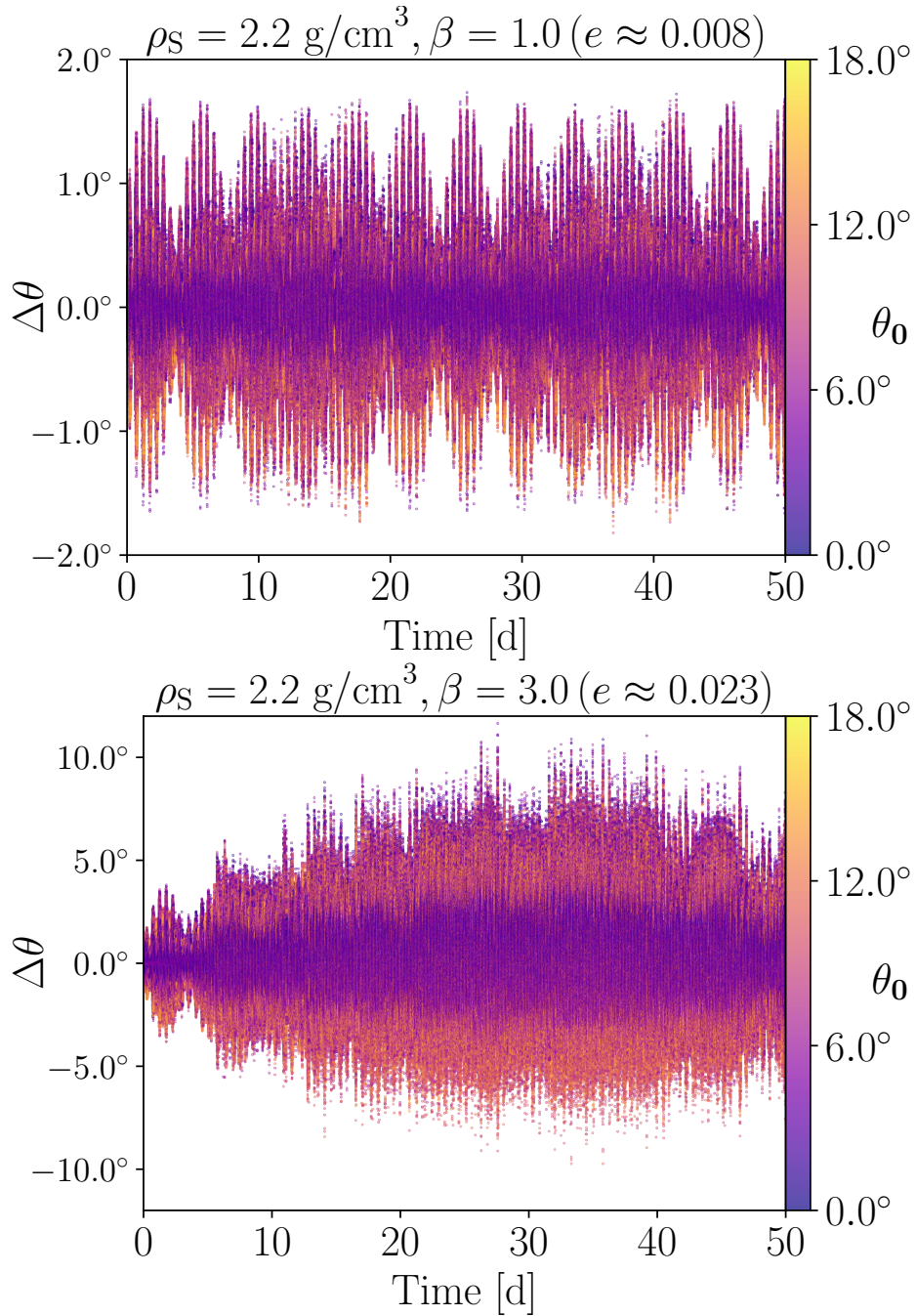


Figure 5.2: Time-series plots of the change in surface slope ($\Delta\theta$) of each facet in the secondary shape model. Each line is colored based on its initial surface slope (θ_0). As β (or e) increases, we see much larger changes in surface slope. The bulk density is $\rho_S = 2.2 \text{ g cm}^{-3}$. See Appendix B.3 for equivalent plots showing the full 365 d simulation and additional values for β .

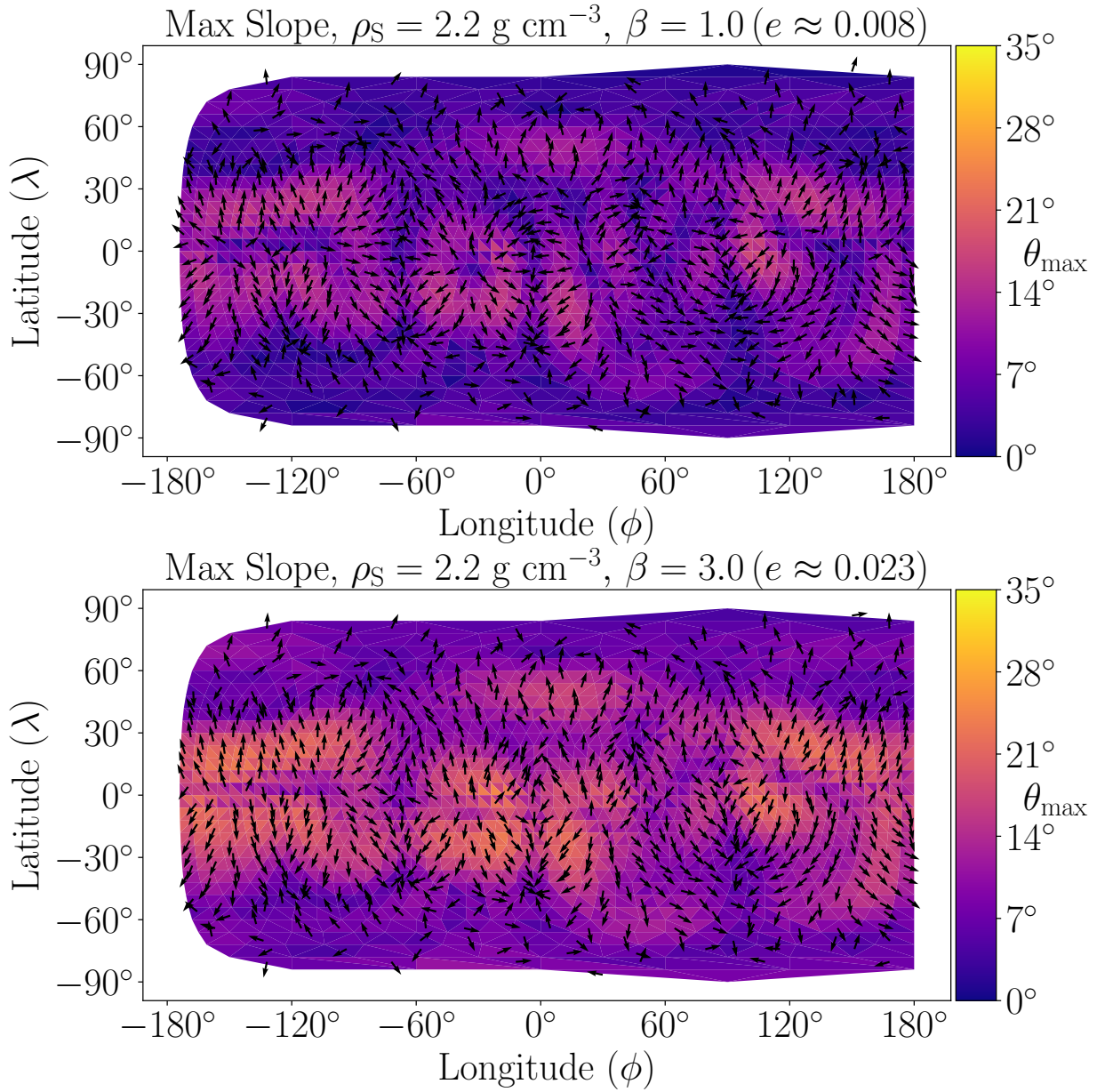


Figure 5.3: Maximum slope achieved after a 365 d simulation, with arrows indicating the down-slope direction. See Appendix B.3 for equivalent plots for other values of β .

crater ages in different regions of Dimorphos’s surface. In addition, the spatial dependence on the surface slope evolution could be leveraged to distinguish between causes of surface refreshment. For example, we might expect surface motion triggered by the re-accretion of impact ejecta to occur over much of Dimorphos’s surface, while tidal and rotationally induced surface motion may be restricted to regions that can achieve high slopes. We refer the reader to Appendix B.3 for additional plots that show the surface slopes for other values of β .

5.4.3 Dependence on the bulk density (ρ_S)

The surface slopes of a given shape are highly dependent on the body’s bulk density (Richardson and Bowling, 2014; Susorney and Teanby, 2022). It sets the mass and self-gravity, which partially determine the initial slope of each facet. On a related note, a low density means that the self-gravity is weaker, making the accelerations due to tides and rotation stronger in comparison and in turn allowing larger slope changes. Finally, a low density (i.e., a low mass) means a higher eccentricity (and shorter periapsis distance) for a fixed value of β . Therefore, a lower density will result in a more perturbed orbit, in which the tidal and rotational accelerations play an increasingly important role. For these reasons, the possibility and magnitude of any granular motion will be highly dependent on Dimorphos’s bulk density.

We see precisely this result in Fig. 5.4, which shows the maximum surface slope achieved as a function of ρ_S and β . The color of the dots indicates the eccentricity of the particular orbit, which depends on both β and ρ_S . We see that the surface slopes increase dramatically as a function of β , especially for $\rho_S = 1.85 \text{ g cm}^{-3}$, reaching $\sim 40^\circ$ for high β due to the higher eccentricity and resulting in stronger tidal and rotational forces.

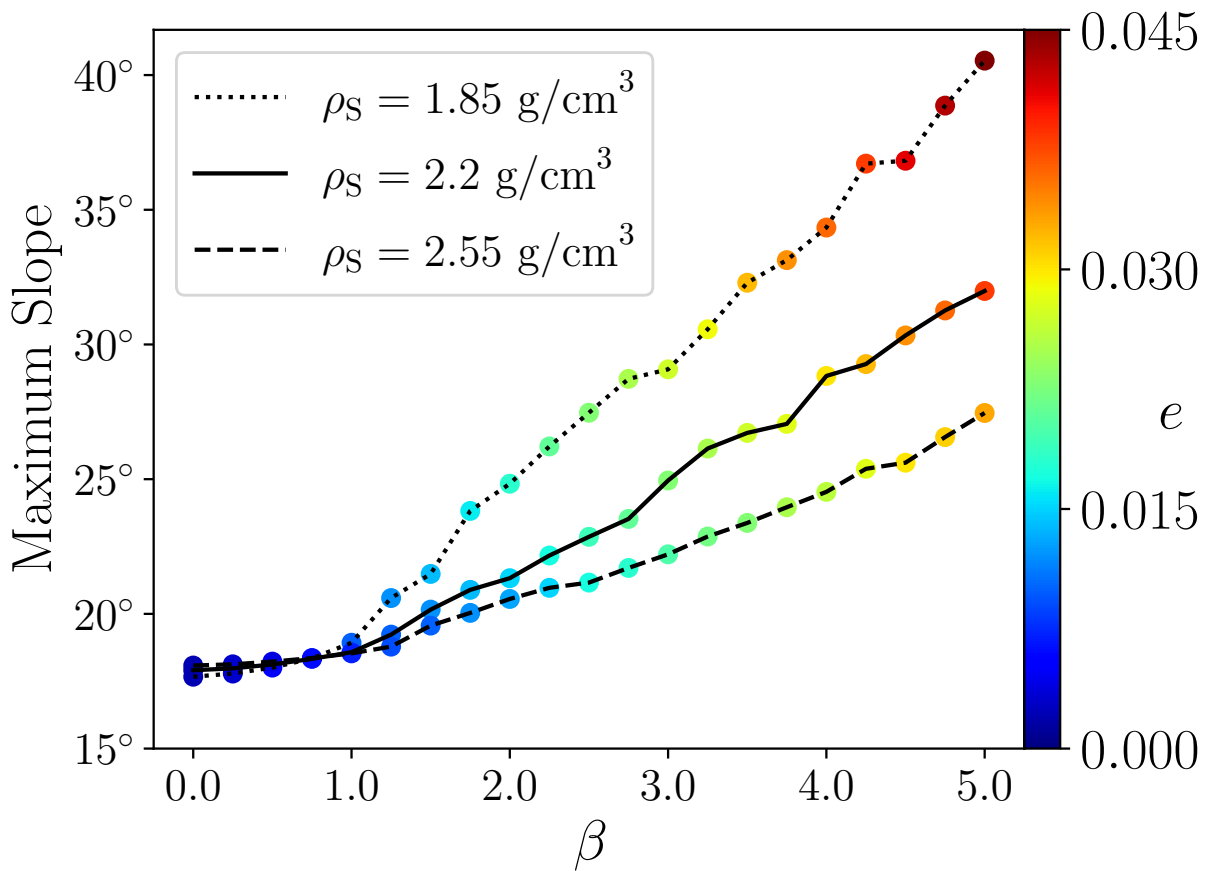


Figure 5.4: Maximum slope as a function of β and ρ_s . The slope over a given simulation increases with β due to the spin and orbit of Dimorphos being more excited. Lower densities achieve higher slopes due to the higher orbital eccentricity for a given β , in addition to a weaker self-gravity in relation to the tidal and rotational accelerations.

5.5 Discussion

If Dimorphos's surface has an angle of repose of $\sim 35^\circ$, similar to that reported at Ryugu and Bennu (Barnouin et al., 2022; Watanabe et al., 2019), then we would expect significant landslides and shape changes in cases where θ exceeds this value. For the Dimorphos shape used in this study, this would only occur for lower densities and high β values. Without knowing the true shape of Dimorphos, however, it is impossible to say with certainty how probable any post-impact surface motion is. The aim of this paper is to demonstrate the plausibility of any dynamics-induced granular motion or shape change, and this topic will be revisited once Dimorphos's true shape is known.

Recent work focused on surface refreshment on Mars's moon Phobos indicates that a time-varying $\Delta\theta$ of only a few degrees can lead to a gradual creep motion of granular material, without the slope ever exceeding the formal angle of repose. Ballouz et al. (2019) combined dynamical modeling, granular physics, and geologic mapping of color units to demonstrate that regions of combined high values of θ and $\Delta\theta$ coincide with Phobos's blue units. This work indicated an active surface-refreshing process that could excavate pristine un-weathered material. Depending on Dimorphos's geophysical properties, it may be plausible that a similar creep motion process will occur following the DART impact. We note that surface refreshment could be currently ongoing, if Dimorphos is already in an NPA rotation state as predicted by Quillen et al. (2022a).

It is also important to consider that both β and ρ_S could lie outside the range explored in this paper. Of course, Dimorphos's real shape and surface geology are also unknown, so the results presented here are illustrative and meant to highlight the range of post-impact possibilities. After DART's impact, this phenomenon can be explored with higher fidelity, incorporating the initial

shape model and surface geology obtained with DART and LICIACube imagery. When Hera arrives, its optical instruments and CubeSats, especially the Juventas CubeSat and its onboard GRAvimeter for small Solar System bodies (GRASS) instrument, will measure the dynamical slopes as one of its science objectives (Karatekin et al., 2021; Michel et al., 2018; Ritter et al., 2021). The seismic pulse delivered by the DART impact may significantly alter surface features on Dimorphos (Quillen et al., 2022b; Thomas and Robinson, 2005). We also note that the global shape of Dimorphos may also be immediately altered by the DART impact itself (Raducan and Jutzi, 2022). In addition to affecting the system dynamics (Nakano et al., 2022), these processes will create a unique challenge in discerning the various surface refreshment mechanisms upon Hera's arrival.

The results of the work presented here have the following implications, in the context of the DART and Hera missions as well as binary asteroids in general:

Granular motion and surface changes. Through images and infrared measurements, Hera may identify refreshed areas of Dimorphos's surface exposed by dynamics-induced surface motion. Furthermore, a comparison of images taken by DART and Hera may be used to identify surface features that have moved or changed during the four years between the missions. If there is long-term boulder motion on the surface, Hera may detect the motion of boulders over the course of its six-month mission lifetime. Furthermore, this effect may noticeably alter the system's dynamics (Brack and McMahon, 2019).

Crater degradation. Impact craters (both natural craters and DART's crater) may degrade at different rates based on their location on the surface as surface slope changes are spatially dependent. This may have important implications for understanding crater morphology and the surface age of Dimorphos, a challenge that does not usually require consideration for single

asteroids due to their quasi-static spin states (Richardson et al., 2020; Sugita et al., 2019; Walsh et al., 2019).

Tidal dissipation. Granular surface motion may affect tidal dissipation in two ways. First, any material undergoing surface motion will dissipate energy through friction, potentially enhancing dissipation beyond what is assumed from traditional tidal theories (Goldreich and Sari, 2009; Nimmo and Matsuyama, 2019). Second, granular motion will change Dimorphos’s mass distribution and, therefore, its gravitational potential. This mechanism could subtly remove energy from the system, an effect not captured by simplified tidal treatments.

Binary formation and evolution. One proposed scenario of binary formation assumes the secondary forms through a spin-up fission event driven by the Yarkovsky-O’Keefe-Radzievskii-Paddack (YORP) effect and initially orbits chaotically. At some later time, the secondary must fission a second time, forming a short-lived triple system and liberating excess free energy in order to enter a stable, synchronous spin state (Jacobson and Scheeres, 2011a). Given the results presented herein, we might expect landslides on the surface well before a secondary fission event. This process may dissipate energy and reshape the secondary, allowing for synchronous rotation without the need to invoke additional fissions. Furthermore, if all secondaries undergo chaotic rotation at some point, then we might expect the population to have broadly similar shapes. However, this would largely depend on the relative timescales for tidal locking and surface refreshment, as well as other competing slope-altering processes such as meteorite impacts. In any case, rotation-driven surface motion, shape change, and energy dissipation may be important effects that should be accounted for in any binary asteroid formation scenario.

5.6 Conclusions

In this paper we have shown that perturbed post-impact spin and orbital dynamics may lead to significant fluctuations in Dimorphos's surface slopes. Depending on Dimorphos's shape, bulk density, surface geology, and β , we predict that this may trigger long-lived granular motion on the surface. The implications for dynamics-driven granular motion include a refreshment of Dimorphos's surface, impact crater degradation, and enhanced tidal dissipation. Understanding these effects will help guide and interpret the measurements Hera will obtain on Dimorphos's surface and interior. In addition, this effect may have implications for the formation and evolution of small binary systems in general.

Thanks to this initial study, post-impact granular motion will be explored more closely and with higher fidelity when Dimorphos's shape model first becomes available. Future work includes directly modeling granular motion on the surface in addition to coupling that motion back to the resulting dynamical evolution.

Chapter 6: Conclusions & Future Work

6.1 Conclusions

The results of this work highlight the dynamical complexity of the Didymos system, and for tight binary systems in general.

In Chapter 2, we benchmarked several simulation codes and explored the sensitivity of the system's dynamics to small perturbations in initial conditions. This work yielded three important results. The first is that dynamical simulations are limited in their predictive powers: they can predict general outcomes but cannot make specific predictions regarding the exact position or spin of the secondary component at later times simply due to the system's sensitivity to many initial conditions that are unknowable. The second is that we expect the libration state of Dimorphos to become excited as a result of the DART impact. Due to the near instantaneous change in orbit period, free librations will be excited as a result of the sudden mismatch in the mutual orbit period and Dimorphos's spin period. In addition, the increased eccentricity combined with a high degree of spin-orbit coupling will lead to forced librations. Finally, we determined that the General Use Binary Asteroid Simulator (GUBAS) was the optimal simulation code for future rigid-body dynamics studies of the Didymos system, owing to its computational speed and accuracy. However, discrete N -body codes like PKDGRAV can still be useful in special scenarios, despite the significantly increased computational cost.

Motivated by the results of Chapter 2, we studied Dimorphos’s post-impact spin state more closely in Chapter 3. Using both analytical and numerical methods, we determined that Dimorphos could become attitude unstable and enter a non-principal axis (NPA) rotation state, depending on its shape and the amount of momentum transferred by DART. Such an excited spin state is enabled by various resonances of Dimorphos’s natural frequencies of motion, which are largely dependent on Dimorphos’s unknown shape. Even if Dimorphos has a shape that is resistant to an attitude instability, the perturbation to the mutual orbit provided by DART, will significantly excite its libration state. If Dimorphos remains in an excited but stable libration state, then it may allow Hera to infer its moments of inertia through a measurement of the free libration frequency. If Dimorphos enters NPA rotation, then such a measurement may not be possible. In addition, NPA rotation could have implications for the binary’s secular evolution by effectively turning off the BYORP effect.

To better understand Dimorphos’s post-impact spin state and to verify the predictions of Chapter 3, we relaxed the rigid-body assumption to allow Didymos and Dimorphos to behave as gravitational aggregates of thousands of constituent particles in Chapter 4. First, we showed that for an approximately ellipsoidal Dimorphos, and for “typical” β values of ~ 3 , the rigid-body and rubble-pile predictions are nearly identical. This is simply because energy dissipation is not efficient enough on short (~ 1 yr) timescales and the dynamics are not excited to a high enough degree that Dimorphos would experience a measurable level of shape change. We then demonstrated that Dimorphos’s periapse distance is not expected to shrink enough to induce significant tidal distortion at its assumed size and bulk density unless β exceeds ~ 20 , which is unlikely. However, these simulations were performed over only a few orbit periods, which may not be sufficient to fully explore the problem as Dimorphos’s spin can get more excited at later

times due to spin-orbit coupling. Although tidal distortion or disruption is unlikely, it could be possible in a special circumstance in which Dimorphos's mass is lower than predicted and β is higher than expected. We also demonstrated the boulders could move around on the surface of Dimorphos, depending on its shape and β . However, the numerical method used for this portion of the study likely underestimates any surface motion so it only occurred for higher values of β ($\beta \gtrsim 5$).

Encouraged by the possibility of granular motion on Dimorphos's surface, Chapter 5 was a rapid study to understand the sensitivity of the surface slopes as a function of Dimorphos's bulk density and β . This study only considered a Dimorphos with a shape identical to Squannit, the secondary component of (66391) Moshup, so we did not explore the sensitivity to the shape itself. However, Squannit is arguably the best available analog for Dimorphos's shape, given the similarities between the two systems. For a Squannit-shaped Dimorphos, we found that the post-impact dynamics can excite the system, leading to time-varying tidal and rotational accelerations that can change the surface slope by several degrees on rapid timescales (~ 1 hr). Depending on the geophysical properties of Dimorphos (surface particle sizes, friction angle, cohesion, etc), the dynamics may be capable of driving granular motion on the surface. The possibility of surface motion will also depend significantly on Dimorphos's shape and bulk density as well as β . If this process occurs on Dimorphos, it may significantly alter its surface features, including the DART impact crater, by the time Hera arrives ~ 4 years later. Aside from the implications for the DART and Hera missions, this effect may influence geophysical and dynamical properties of the secondary components of other binary asteroids.

6.2 Future Work

In this section, we propose potential topics for future investigations related to binary asteroid dynamics and evolution.

Given that much of the results of this thesis depend heavily on some unknown properties of the Didymos system, the most obvious project will be to revisit the predictions of Chapters 3, 4, and 5. Shortly after this thesis is defended, DART will impact Dimorphos. Once a shape model for Dimorphos becomes available from the DART and LICIACube imagery, along with an estimate for β , it will be possible to make much more accurate predictions for Dimorphos's post-impact spin evolution. Furthermore, the images taken by DART and LICIACube can be used to constrain the geophysical properties of Dimorphos's surface, including the boulder size-frequency distribution, which can then be used to better estimate the possibility of granular motion on the surface, both before and after the DART impact. It will be important to revisit these predictions prior to Hera's arrival in late 2026, as Dimorphos's spin state may have important for Hera's operations. In addition, it may be possible to measure some of these phenomena, such as rotation-induced granular motion, with the Hera spacecraft if they occur.

One implication of dynamically triggered surface motion discussed in Chapter 5 is that it may be an efficient dissipation mechanism. First, the surface motion would gradually reshape the secondary, which changes its gravitational potential, making it a source or sink of kinetic energy. Second, any motion on the surface would be governed by frictional forces that would dissipate energy as well. It may be possible that these dissipation mechanisms could be more efficient than traditional tidal dissipation, especially in regimes where the secondary's spin is significantly excited. However, a quantitative study is still needed to fully understand how important this ef-

fect may be. If it is highly efficient, it may be a mechanism to allow for a chaotically rotating secondary to become tidally locked on short timescales, without the need to invoke more complicated processes to liberate excess free energy, such as a secondary fission process. Furthermore, if all secondaries undergo some level of chaotic rotation and resurfacing upon formation, should we expect these systems to have similarly shaped secondaries that are largely smoothed over and ellipsoidal?

Another idea related to binary formation regards multiple asteroid systems. The GUBAS code could be modified to allow for fully-coupled propagations of multiple irregularly shaped bodies to study in great detail how triple asteroids might form. After a binary is formed, it can evolve outwards through tides and BYORP. In principle, the primary could then spin up again to form an additional inner satellite. This satellite would then, depending on the direction of the BYORP torque, expand outwards faster than the outer satellite due to the stronger tides. Is there a reason why we haven't observed triple asteroids in mean-motion resonances (MMRs)? Would it be possible to form resonant chains of satellites? This problem will depend heavily on the YORP timescales, NEA dynamical lifetimes, and the probability of planetary encounters that would break any MMRs. It may be that YORP is simply not efficient enough to form multiple satellites within a typical NEA lifetime. By modifying GUBAS, one could also study how spin-spin and spin-orbit coupling among the satellite pairs might play a role in preventing stable configurations of multiple satellites on circular orbits.

Appendix A: Appendices for Chapter 3

A.1 The simplified 3D model

The “simplified” 3D model consists of the planar mutual orbit described in Appendix [A.1.1](#) combined with the 3D attitude of the secondary described in Appendix [A.1.2](#). This approach has the advantage of being an extremely fast approach to numerically model the system dynamics. However, it should be noted that the mutual orbit and secondary spin state are not fully coupled. The mutual separation and velocity is predetermined and set by the equations of motion in Appendix [A.1.1](#), and the secondary’s spin and attitude are then propagated based on equations [\(A.11\)](#)–[\(A.13\)](#).

A.1.1 The planar $J_2 +$ ellipsoid model

The planar “ J_2 +ellipsoid” model consists of two extended bodies, with masses M_1 and M_2 , that orbit and interact with each other via their mutual gravitational potential, as shown in Fig. [A.1](#). The primary is assumed to be an oblate spheroid with moments of inertia $A_1 = B_1 < C_1$, while the secondary is a triaxial ellipsoid with moments of inertia $A_2 < B_2 < C_2$. The Hamiltonian of the system reads,

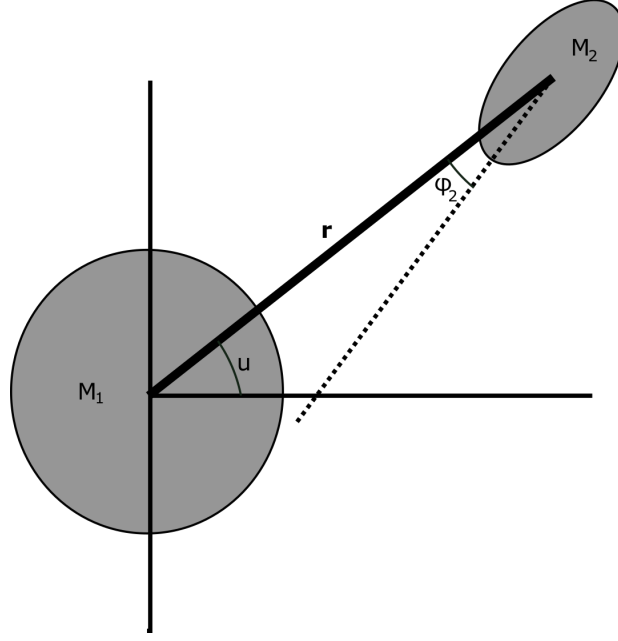


Figure A.1: The simplified configuration of the planar J_2 -ellipsoid model.

$$\mathcal{H} = \frac{1}{2} \left(\frac{P_{\phi_2}}{C_2} + \frac{(P_u - P_{\phi_2})^2}{r^2 \mu} + \frac{P_r^2}{\mu} \right) + V(r, \phi_2), \quad (\text{A.1})$$

where r is the distance between the two mass centers and ϕ_2 is the angle between the secondary's long axis and the radius vector r . The angle ϕ_2 is also known as the libration angle of the secondary. As shown in Fig. A.1, u is the angle of the radius vector with respect to an inertial system of reference. Then, P_r , P_{ϕ_2} , and P_u are the conjugate momenta and $\mu = M_1 M_2 / (M_1 + M_2)$.

The mutual potential, up to second-order expansion, is (McMahon and Scheeres, 2013),

$$\begin{aligned} V(r, \phi_2) = & -\frac{GM_1 M_2}{r} - \frac{GM_2}{2r^3} (2A_1 + C_1) - \frac{GM_1}{2r^3} (A_2 + B_2 + C_2) \\ & + \frac{3GM_2 A_1}{2r^3} + \frac{3GM_1}{4r^3} (A_2 + B_2 - (B_2 - A_2) \cos(2\phi_2)), \end{aligned} \quad (\text{A.2})$$

where G is the gravitational constant.

The angle u is ignorable and therefore the momentum P_u is a constant of the motion. For a fixed separation r_0 there exists an equilibrium solution, corresponding to a circular orbit with orbital frequency \dot{u}_{eq} (McMahon and Scheeres, 2013),

$$\dot{u}_{eq} = \sqrt{\frac{G(M_1 + M_2)}{r_0^3} \left(1 + \frac{3}{2r_0^2} \left(\frac{C_1 - A_1}{M_1} + \frac{B_2 + C_2 - 2A_2}{M_2} \right) \right)}, \quad (\text{A.3})$$

and the conjugate conserved momentum is,

$$P_u = (C_2 + r_0^2 \mu) \dot{u}_{eq}. \quad (\text{A.4})$$

Notice that if both the binary separation r and the orbital frequency are assumed to be known quantities, Eq. (A.3) could be solved to provide the total mass of the system ($M_1 + M_2$). This strategy was followed to obtain the relaxed equilibrium conditions assuming a constant-density ellipsoid with axial ratios a/b and b/c for Dimorphos.

A.1.2 The 3-dimensional rotation of the secondary

In order to study the attitude stability of Dimorphos with the simplified 3D model, we employ the 3-1-2 set of Euler angles¹ (θ, ϕ, ψ). Assuming a planar orbit for Dimorphos described

¹The simplified 3D model uses the 3-1-2 Euler angle set in its numerical integrations. However, the Euler angle plots in the manuscript use the 1-2-3 Euler angle set.

by $r(t)$ and $u(t)$, Euler's rigid body equations read (Wisdom et al., 1984),

$$A_2 \dot{\omega}_x - \omega_y \omega_z (B_2 - C_2) = -\frac{3GM_1}{r^3} \beta \gamma (B_2 - C_2), \quad (\text{A.5})$$

$$B_2 \dot{\omega}_y - \omega_z \omega_x (C_2 - A_2) = -\frac{3GM_1}{r^3} \alpha \gamma (C_2 - A_2), \quad (\text{A.6})$$

$$C_2 \dot{\omega}_z - \omega_x \omega_y (A_2 - B_2) = -\frac{3GM_1}{r^3} \alpha \beta (A_2 - B_2), \quad (\text{A.7})$$

where ω_x , ω_y and ω_z are the rotational angular velocity components with respect to the Dimorphos body-fixed axes x , y and z respectively. The direction cosines α , β and γ are given from the relations,

$$\alpha = \cos \psi \cos (\theta - u) - \sin \psi \sin \phi \sin (\theta - u), \quad (\text{A.8})$$

$$\beta = -\cos \phi \sin (\theta - u), \quad (\text{A.9})$$

$$\gamma = \sin \psi \cos (\theta - u) + \cos \psi \sin \phi \sin (\theta - u). \quad (\text{A.10})$$

Finally, the corresponding kinematic equations for the specific set of Euler angles read,

$$\dot{\theta} = \sec \phi (\omega_z \cos \psi - \omega_x \sin \psi), \quad (\text{A.11})$$

$$\dot{\phi} = \omega_x \cos \psi + \omega_z \sin \psi, \quad (\text{A.12})$$

$$\dot{\psi} = \omega_y - \omega_z \cos \psi \tan \phi + \omega_x \sin \psi \tan \phi. \quad (\text{A.13})$$

The planar solution for $r(t)$ and $u(t)$ is inserted into Euler's equations of motion and the 3-dimensional attitude dynamics are propagated. Given no out-of-plane excitation (i.e., $\phi = \psi =$

$\omega_x = \omega_y = 0$), then the computed librational solution is equivalent to the planar one,

$$\phi_{2,3D} = u(t) - \theta(t) = \phi_2(t).$$

If a small excitation is assumed in the out-of-plane rotation (i.e., $\omega_x = \omega_y = 10^{-15}$), then for some initial conditions $\phi_{2,3D} \approx \phi_2$ while in other cases the two solutions diverge. In order to study these instabilities in more detail, an analysis based on the linearized system of equations is required.

First the set of Euler's equations is cast into a Hamiltonian form via the Legendre transformation,

$$P_\theta = -A_2\omega_x \cos \phi \sin \psi + B_2\omega_y \sin \phi + C_2\omega_z \cos \phi \cos \psi, \quad (\text{A.14})$$

$$P_\phi = A_2\omega_x \cos \psi + C\omega_z \sin \psi, \quad (\text{A.15})$$

$$P_\psi = B_2\omega_y, \quad (\text{A.16})$$

and substituting ω_x , ω_y , and ω_z in the Hamiltonian of the rotation, we have,

$$\mathcal{H}_{rot} = \frac{1}{2}(A_2\omega_x^2 + B_2\omega_y^2 + C_2\omega_z^2) + V(r, u, \theta, \phi, \psi). \quad (\text{A.17})$$

with,

$$V(r, u, \theta, \phi, \psi) = \frac{3GM_1}{2r^5} \mathbf{r} \mathcal{A}_2^T I_2 \mathcal{A}_2 \mathbf{r}, \quad (\text{A.18})$$

where $I_2 = \text{diag}(A_2, B_2, C_2)$, $\mathbf{r} = (r \cos u, r \sin u, 0)$ and $\mathcal{A}_2 = R_y(\psi)R_x(\phi)R_z(\theta)$.

An equilibrium solution of the planar J_2 -ellipsoid Hamiltonian \mathcal{H} corresponds to a periodic

orbit of \mathcal{H}_{rot} . To determine the attitude stability, we also introduce a deviation vector,

$$\mathbf{w} = (\delta\theta, \delta\phi, \delta\psi, \delta P_\theta, \delta P_\phi, \delta P_\psi), \quad (\text{A.19})$$

and the system of variational equations as,

$$\dot{\mathbf{w}} = \mathcal{J}\mathbf{w}, \quad (\text{A.20})$$

where \mathcal{J} is the Jacobian of the flow. For a given trajectory ($r(t)$ and $u(t)$), the Hamiltonian equations for the rotation are solved along with the variational equations (Eq. (A.20)) and the stability is determined from the fast Lyapunov indicator (FLI) defined as (Froeschlé et al., 1997; Skokos, 2010),

$$\text{FLI}(t) = \sup_t \log_{10} \|\mathbf{w}(t)\|. \quad (\text{A.21})$$

A.1.3 Uncoupled natural frequencies

Let us assume a triaxial satellite, with moments of inertia ($A < B < C$), orbiting a primary on a Keplerian orbit. The natural rotational frequencies close to the synchronous state are

approximated by the following expressions (see for example Fleig (1970)):

$$k = 3\left(1 + \frac{3}{2}e^2 + \frac{15}{8}e^4\right) + \mathcal{O}(e^6),$$

$$r_1 = \frac{A}{C},$$

$$r_2 = \frac{B}{C},$$

$$a = r_1 r_2,$$

$$b = kr_1^2 - 2r_1 r_2 - (k - 1)r_1 + r_2 - 1,$$

$$c = (k + 1)(1 - r_1)(1 - r_2),$$

$$\omega_{\text{off},1} = n\sqrt{\frac{-b - \sqrt{b^2 - 4ac}}{2a}}, \quad (\text{A.22})$$

$$\omega_{\text{off},2} = n\sqrt{\frac{-b + \sqrt{b^2 - 4ac}}{2a}}, \quad (\text{A.23})$$

$$\omega_{\text{lib}} = n\sqrt{k(r_2 - r_1)}, \quad (\text{A.24})$$

where n is the mean motion, e is the eccentricity of the orbit, ω_{lib} is the planar libration frequency and $\omega_{\text{off},1}, \omega_{\text{off},2}$ are the two coupled off-plane frequencies related to the precession and nutation of the body. In the notation of this paper, we refer to $\omega_{\text{off},1}$ as ω_{prc}^{uc} .

A.2 Initial conditions optimization scheme

Due to the small uncertainty in the observed binary orbit period, we prioritize having the simulated pre-impact Didymos system match the observed binary orbit period as close as possible. The non-Keplerian nature of the system requires the use of a numerical optimization scheme to derive the initial conditions. Our procedure is described below.

In order to construct the nominal pre-impact state for a given choice in the secondary’s axial ratios, we make the simplifying assumption that the binary is in a dynamically relaxed state. This implies the following:

1. The binary orbit is circular or nearly circular ($e \approx 0.0$).
2. The mutual orbit pole is initially aligned with the primary’s spin pole.
3. The secondary’s rotation is synchronous with its orbit (i.e., tidally locked), and its spin pole is aligned with the mutual orbit pole.
4. The secondary’s libration amplitude has been damped to a minimum.

All of these assumptions are consistent (or at the very least not in disagreement) with current constraints of Didymos’ orbit (Naidu et al., 2020a; Scheirich and Pravec, 2009) and observations of other similar binary systems (Pravec et al., 2016). We also assume that both bodies have a uniform mass distribution and the same bulk density, which is appropriate if they have the same origin or if the secondary was created through YORP spin-up driven mass loss of the primary. Upon future observations, if it is found that any of these assumptions are incorrect, this optimization scheme can be changed accordingly.

Due to the non-spherical shapes and close proximity of the binary components, their motion is expected to be highly non-Keplerian. Therefore, estimating the binary mass with Kepler’s 3rd Law is only accurate to $\sim 1\%$, which is insufficient for reproducing the observed binary orbit period in simulations. Therefore, we implemented a simple optimization scheme to generate the initial conditions of the Didymos binary that best match the observed orbit period. The routine keeps the initial body positions, velocities, and spins fixed, while adjusting the bulk density (and

therefore the total mass, moments of inertia, etc.) until the desired orbit period is achieved. The routine has the following steps:

1. Set the primary's spin rate to its observed value and the secondary's spin rate equal to the *observed* mean motion with both bodies' spin poles aligned.
2. Set the separation between the mass centers equal to the observed semimajor axis.
3. Set the relative velocity between the two bodies such that their instantaneous orbital angular velocity is equal to the observed mean motion. The velocity should be orthonormal to the radial separation vector and in the direction such that orbit pole and spin poles are aligned.
4. Run a root-finding algorithm to determine the bulk density necessary to match the observed orbit period.

Root-finding algorithm

Once the relative positions, velocities, spins, and body orientations are set, we begin the optimization process. We use the secant method root-finding algorithm to find the bulk density that gives the correct orbit period. We are trying to find the root to the function,

$$f(\rho) = P_{\text{sim}}(\rho) - P_{\text{obs}}, \quad (\text{A.25})$$

where ρ is the system bulk density, $P_{\text{sim}}(\rho)$ is the simulated orbit period, and P_{obs} is the observed orbit period. The secant method is a finite difference version of Newton's method, where each successive guess for the bulk density is given by,

$$\rho_n = \rho_{n-1} - f(\rho_{n-1}) \frac{\rho_{n-1} - \rho_{n-2}}{f(\rho_{n-1}) - f(\rho_{n-2})} \quad (\text{A.26})$$

Each step in the root-finding process requires running a full-2-body-problem code for several orbital periods in order to calculate $P_{\text{sim}}(\rho)$. However, the secant method converges quickly in this case, matching the observed orbit period to within 10^{-6} s in ~ 5 iterations. Matching the orbit period to such high precision is not completely necessary, because the 3-sigma uncertainty on the measured orbit period is ~ 0.7 s. However, the optimization process is not computationally expensive so it requires a negligible amount of time.

An example of the scheme converging to a solution is shown in Fig. A.2. The top panel shows how accurately the simulated orbit period matches the observed orbit period. The remaining three panels show the system bulk density, maximum libration amplitude, and average separation, respectively. The bulk density for the initial guess (Iteration #0) is calculated using the 2nd-order equilibrium solution for a doubly synchronous binary (See Eq. 39 in Scheeres (2009)). Although the Didymos primary is not in synchronous rotation, this initial guess is a much better approximation than a Keplerian solution and is more than sufficient for a starting point.

Despite conserving the same total volume in each simulation, changing the shape of the secondary changes the mass distribution and therefore the mutual potential energy, which affects the orbit period. This sensitivity to the initial conditions requires that the optimization scheme is run for each choice in the secondary's shape that we want to study. Fig. A.3 shows the optimized bulk density for each choice in the secondary's axial ratios along with the resulting maximum libration amplitude. These changes are all very small, so the system mass never differs by more than $\sim \frac{1}{2}\%$ between two simulations.

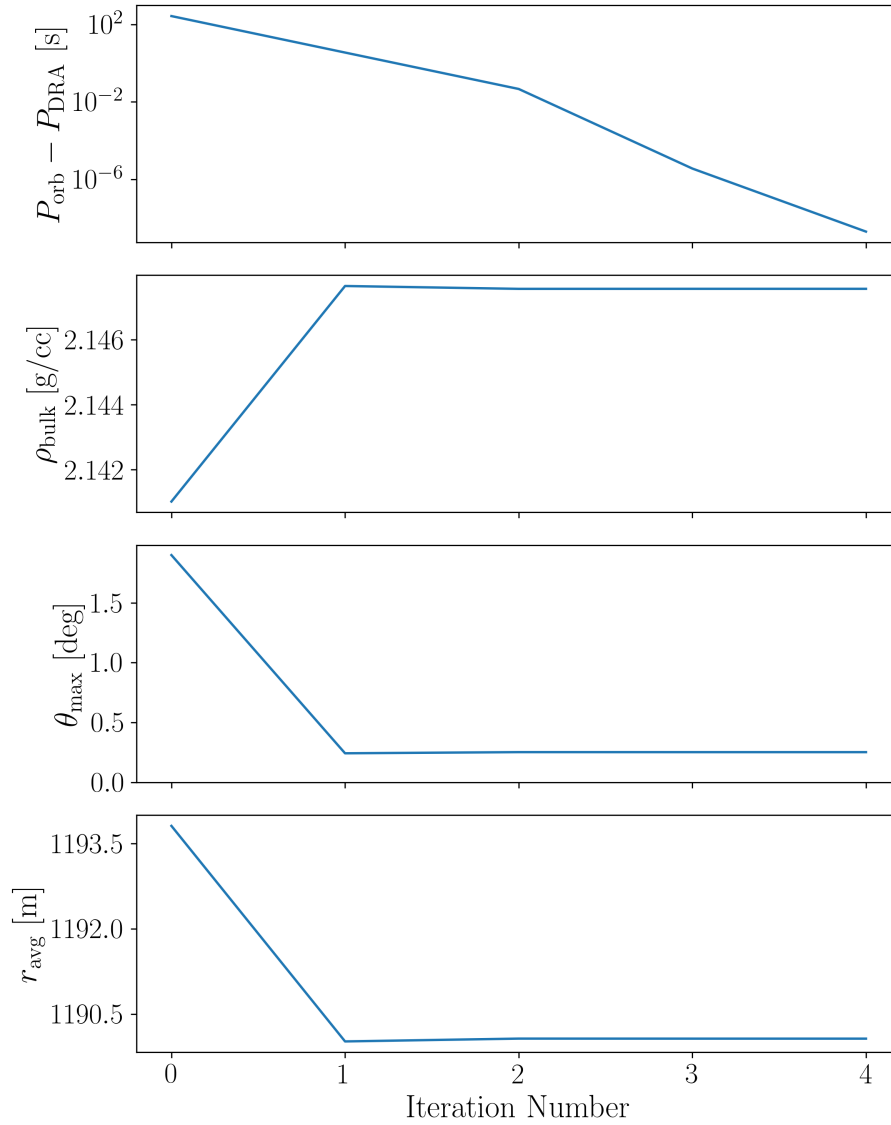
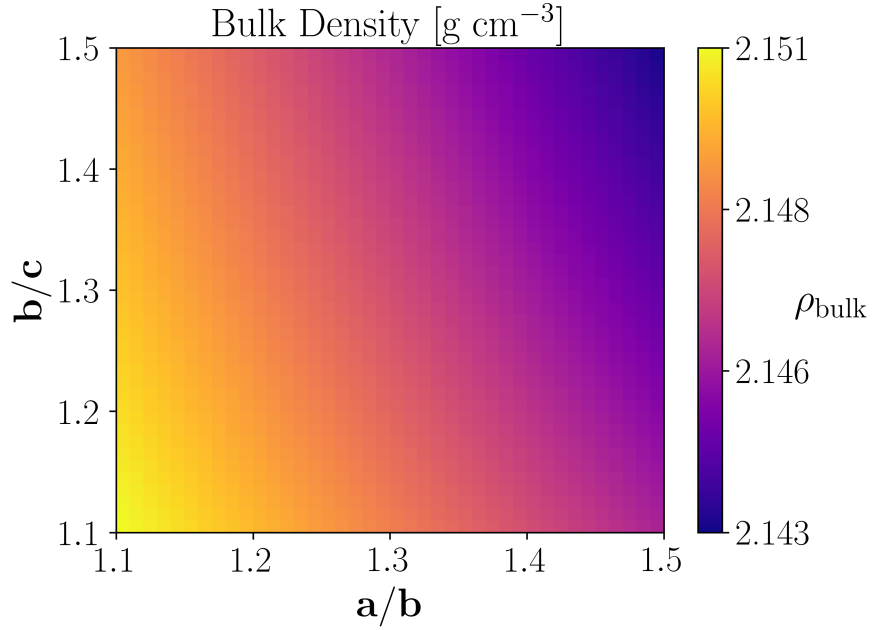
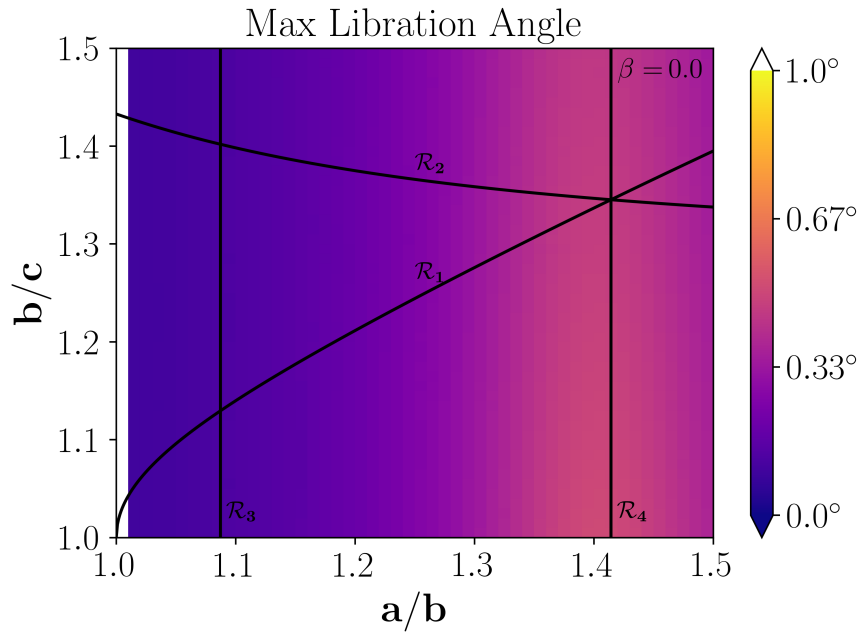


Figure A.2: A plot of the difference between the simulated and observed orbit periods, bulk density, maximum libration amplitude, and average separation as a function of each iteration in the optimization process. After the first iteration, the scheme gets a good solution, but continues making minute adjustments to the bulk density (which aren't discernible on this plot) until the orbit period is matched to high precision.



(a) Optimized bulk density.



(b) Resulting maximum libration amplitude.

Figure A.3: (A.3a) The bulk density resulting from the optimization scheme. Each shape of the secondary has a slightly different bulk density (and total mass) but all simulations have the same orbit period. (A.3b) The resulting libration amplitude after each optimized initial condition is run for 1 year. The libration amplitude has been minimized, with the peak near $a/b \simeq 1.4$ corresponding to the expected 1:1 resonance between the mean motion and free libration frequency (\mathcal{R}_4).

Appendix B: Appendices for Chapter 5

B.1 Calculation of surface accelerations and slopes

We provide additional details for how exactly the accelerations were computed over the surface of the secondary shape model. On each facet, all accelerations were evaluated at the midpoint (i.e., the center) of the given facet.

B.1.1 Gravitational accelerations

On a given facet, i , and at a given time, t , the two gravitational accelerations felt on the surface are due to self-gravity, $\mathbf{a}_{i,t}^{\text{grav}}$, and the tidal acceleration due to the presence of the primary, $\mathbf{a}_{i,t}^{\text{tides}}$.

The self-gravity was computed using an algorithm identical to that presented in Werner and Scheeres (1997). This method computes the exact gravitational acceleration due to a polyhedral shape model with uniform density. Though the calculation is somewhat computationally expensive, it only needs to be done once, as we assume that Dimorphos’s global shape does not undergo significant change. At each facet, $\mathbf{a}_{i,t}^{\text{grav}}$ was computed in Dimorphos’s body-fixed frame.

Unlike the self-gravity, the tidal acceleration must be computed at every facet at every timestep. Therefore, we turned to MacCullagh’s formula to approximate the tides to save com-

putational costs while still capturing effects due to Didymos's irregular shape. MacCullagh's formula is written as (MacCullagh, 1844a,b; Murray and Dermott, 2000)

$$V = \frac{GM}{r} - \frac{GM}{2r^5} f(A, B, C, x, y, z), \quad (\text{B.1})$$

where G is the gravitational constant, M is the body mass, r is the distance from the body's barycenter to the external field point, A , B , and C are the body's principal moments of inertia, x , y , and z are the coordinates of the external field point measured in the primary body-fixed frame, and f is defined as

$$f(A, B, C, x, y, z) = (B + C - 2A)x^2 + (C + A - 2B)y^2 + (A + B - 2C)z^2. \quad (\text{B.2})$$

The gravitational acceleration can be calculated by taking partial derivatives of V with respect to x , y , and z (see Chapter 5 of Murray and Dermott (2000)):

$$a_x = -\frac{\partial V}{\partial x} = -\frac{GMx}{r^3} + \frac{G(B + C - 2A)x}{r^5} - \frac{5Gx}{2r^7} f(A, B, C, x, y, z) \quad (\text{B.3})$$

$$a_y = -\frac{\partial V}{\partial y} = -\frac{GM y}{r^3} + \frac{G(A + C - 2B)y}{r^5} - \frac{5Gy}{2r^7} f(A, B, C, x, y, z) \quad (\text{B.4})$$

$$a_z = -\frac{\partial V}{\partial z} = -\frac{GMz}{r^3} + \frac{G(A + B - 2C)z}{r^5} - \frac{5Gz}{2r^7} f(A, B, C, x, y, z). \quad (\text{B.5})$$

In order to calculate the net gravitational acceleration felt at a point on Dimorphos's surface due to Didymos, we took the difference between the acceleration evaluated at a given surface point and the acceleration evaluated at Dimorphos's barycenter. This acceleration vector was

computed in the primary’s body-fixed frame before being rotated into the secondary’s body-fixed frame.

B.1.2 Rotational accelerations

The centrifugal acceleration at a given point on Dimorphos’s surface denoted with the index i can be written as

$$\mathbf{a}_{i,t}^{cent} = (\boldsymbol{\Omega}_t \times \mathbf{r}_i) \times \boldsymbol{\Omega}_t, \quad (\text{B.6})$$

where $\boldsymbol{\Omega}_t$ is the spin angular velocity vector of Dimorphos at a given time and \mathbf{r}_i is the position vector of the surface point, coordinated in Dimorphos’s body-fixed frame. Since Dimorphos’s spin rate is time varying, we also account for the Euler acceleration,

$$\mathbf{a}_{i,t}^{Euler} = \mathbf{r}_i \times \frac{d\boldsymbol{\Omega}_t}{dt}. \quad (\text{B.7})$$

Since GUBAS does not directly output the time derivative of the secondary’s spin, we calculated it in post-processing with a fourth-order central finite-difference scheme. At a 60 second timestep, the fourth-order approximation sufficiently approximates $\frac{d\boldsymbol{\Omega}}{dt}$.

B.2 Longer-term spin-orbit and surface slope evolution for the test case

Figure B.1 shows plots identical to those in Fig. 5.1 but with the time span increased to 365 d in order to show the longer-term evolution of the dynamics and slope. These plots indicate that the dominant mechanism for changing the surface slope is the NPA rotation of the secondary. We also see that Dimorphos is able to enter the “barrel instability,” a unique spin state where the

secondary remains tidally locked despite rolling about its long axis, as indicated by the roll angle hitting 180° (Ćuk et al., 2021). It seems that this does not significantly affect the surface slopes, however.

B.3 Additional surface slope plots

Here we provide supplemental plots of Dimorphos's spin and orbit, as well as its surface slope evolution, extending out to the full 365 days. The plots below are only for the nominal bulk density of $\rho_S = 2.2 \text{ g cm}^{-3}$. When $\beta = 1$ (Fig. B.2), the orbital eccentricity remains relatively low, keeping Dimorphos in a stable rotation state, which results in small changes to the surface slopes. When β is increased to 2 (Fig. B.3), Dimorphos becomes attitude unstable. Due to increased NPA rotation, we see much larger changes to the surface slopes. The slopes also vary chaotically since Dimorphos's spin state is chaotic. When $\beta = 3$ (Fig. B.4), Dimorphos is not only in NPA rotation, but it also enters the barrel instability, characterized by rotation about its long axis. As β increases further (Figs. B.5 and B.6), Dimorphos's spin and orbit are increasingly perturbed, leading to larger tidal and rotational accelerations that result in larger changes in the surface slopes.

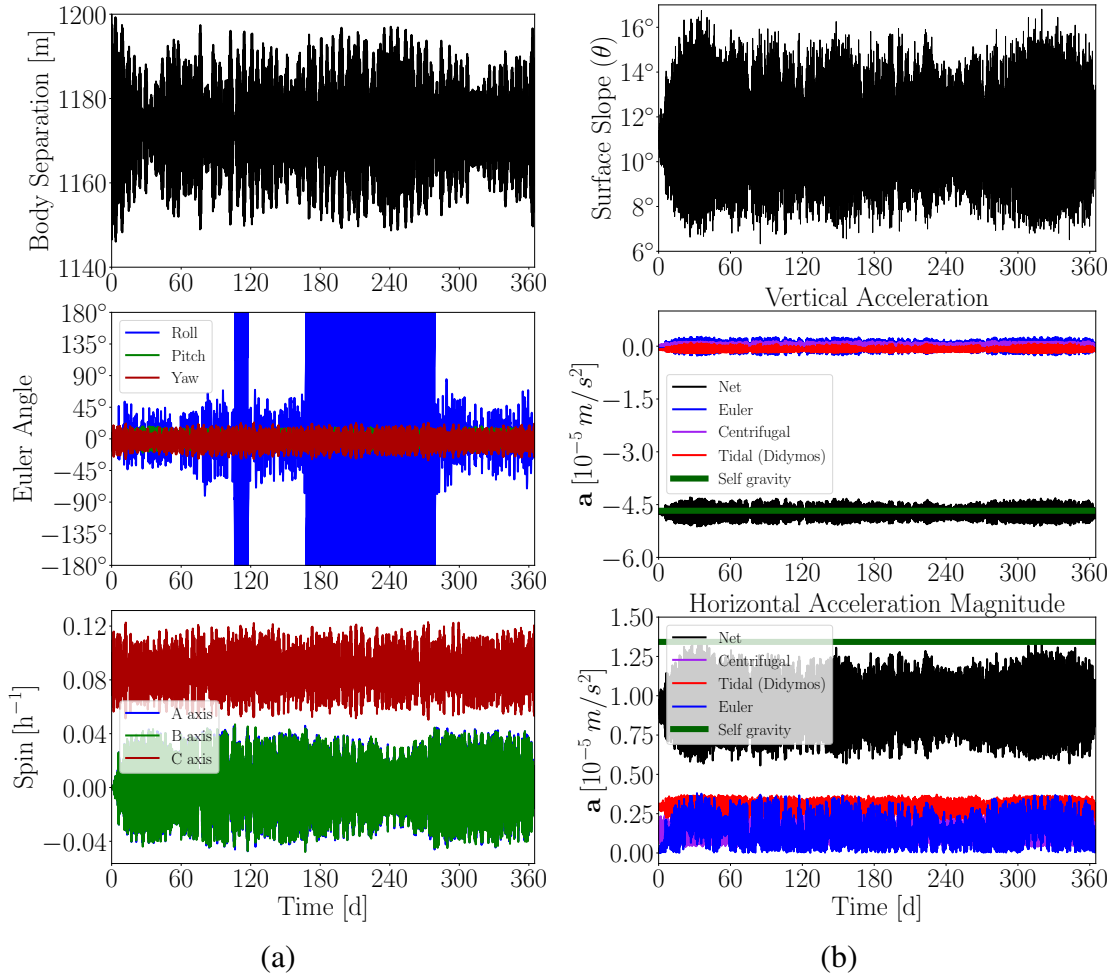


Figure B.1: Spin, orbit, and surface slope evolution for the Squannit-shaped Dimorphos when $\beta = 3$ ($e = 0.023$). (a) Body separation, Euler angles, and body spin of Dimorphos. (b) Slope and surface accelerations on a facet near $(\phi, \lambda) \approx (0^\circ, 45^\circ)$. These plots are identical to those of Fig. 5.1, coming from the same simulation, except they show a longer time duration to highlight how the evolving spin and orbital motion of Dimorphos influences the accelerations felt on the surface. Dimorphos’s NPA rotation (as indicated by the roll and pitch angles or spin about the A and B axes) leads to large increases in the centrifugal and Euler accelerations that are capable of driving large surface slope changes.

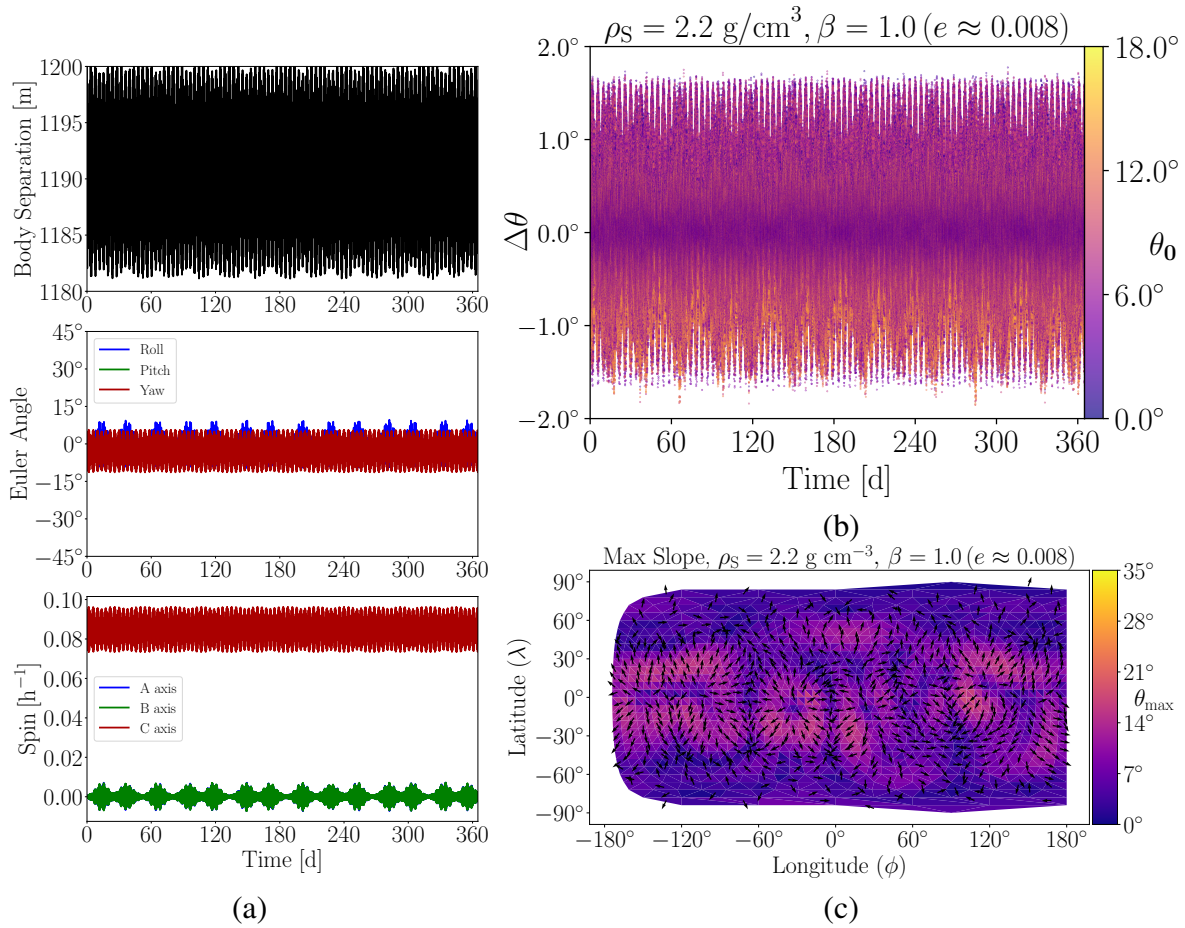


Figure B.2: The spin, orbit, and surface slope evolution for $\beta = 1$ and $\rho_S = 2.2 \text{ g cm}^{-3}$ over 365 days. (a) Body separation, Euler angles, and body spin of Dimorphos. (b) Corresponding change in slope ($\Delta\theta$) over time for each surface facet, colored by the starting slope (θ_0) of that facet. (c) Maximum surface slope achieved on each facet over the full 365 d simulation, with arrows pointing in the down-slope direction.

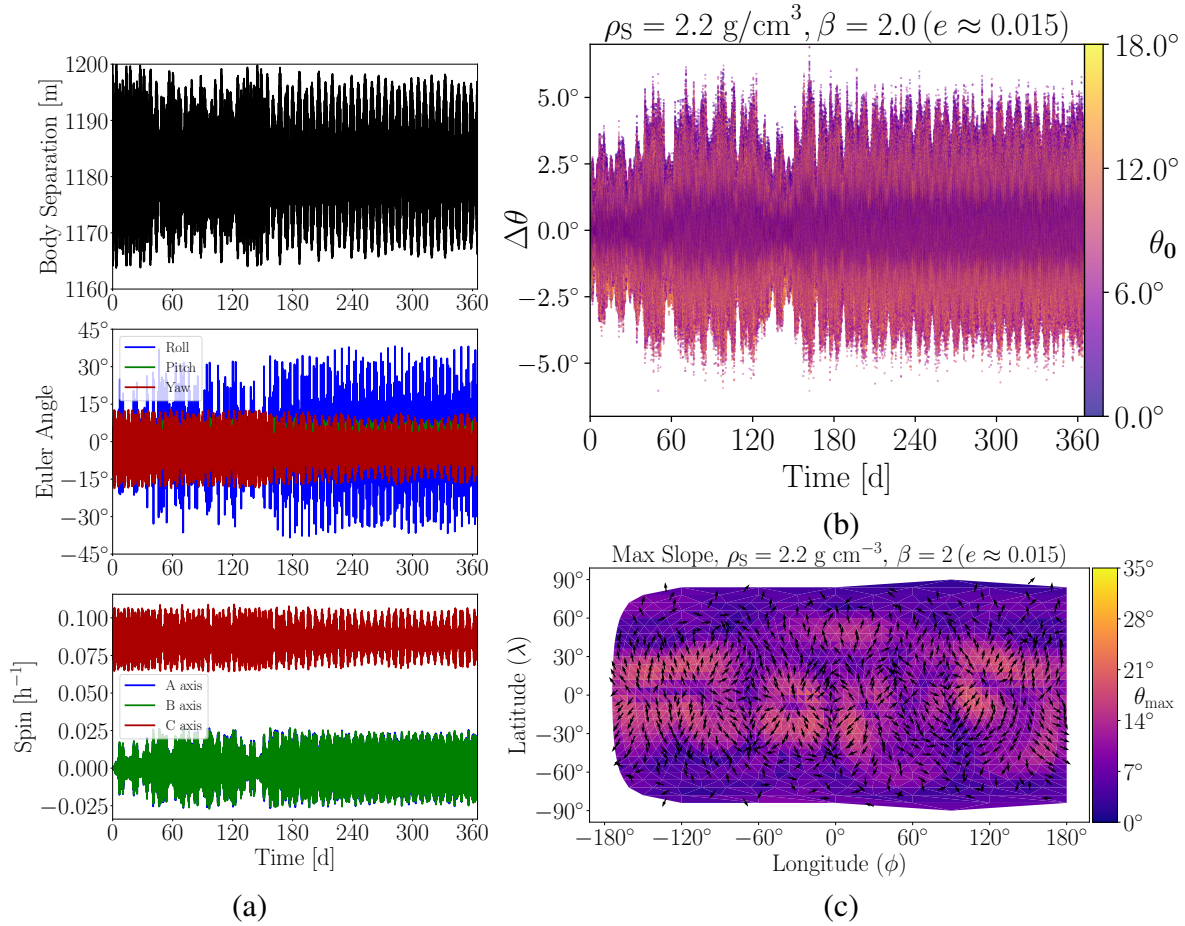


Figure B.3: The spin, orbit, and surface slope evolution for $\beta = 2$ and $\rho_S = 2.2 \text{ g cm}^{-3}$ over 365 days. (a) Body separation, Euler angles, and body spin of Dimorphos. (b) Corresponding change in slope ($\Delta\theta$) over time for each surface facet, colored by the starting slope (θ_0) of that facet. The spikes in $\Delta\theta$ correspond to periods of increased NPA rotation of Dimorphos. (c) Maximum surface slope achieved on each facet over the full 365 d simulation, with arrows pointing in the down-slope direction.

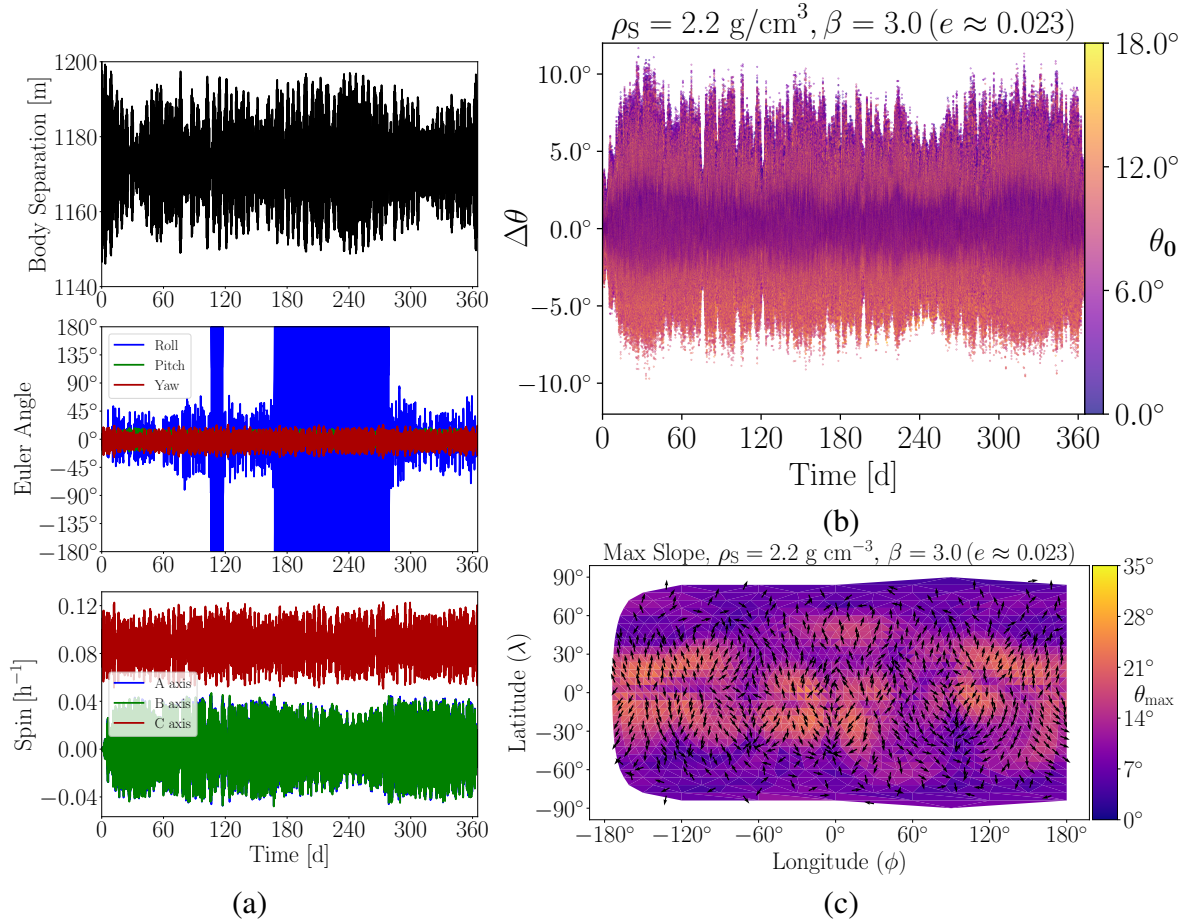


Figure B.4: The spin, orbit, and surface slope evolution for $\beta = 3$ and $\rho_s = 2.2 \text{ g cm}^{-3}$ over 365 days. (a) Body separation, Euler angles, and body spin of Dimorphos. (b) Corresponding change in slope ($\Delta\theta$) over time for each surface facet, colored by the starting slope (θ_0) of that facet. The surface slope evolution is dominated by NPA rotation. (c) Maximum surface slope achieved on each facet over the full 365 d simulation, with arrows pointing in the down-slope direction.

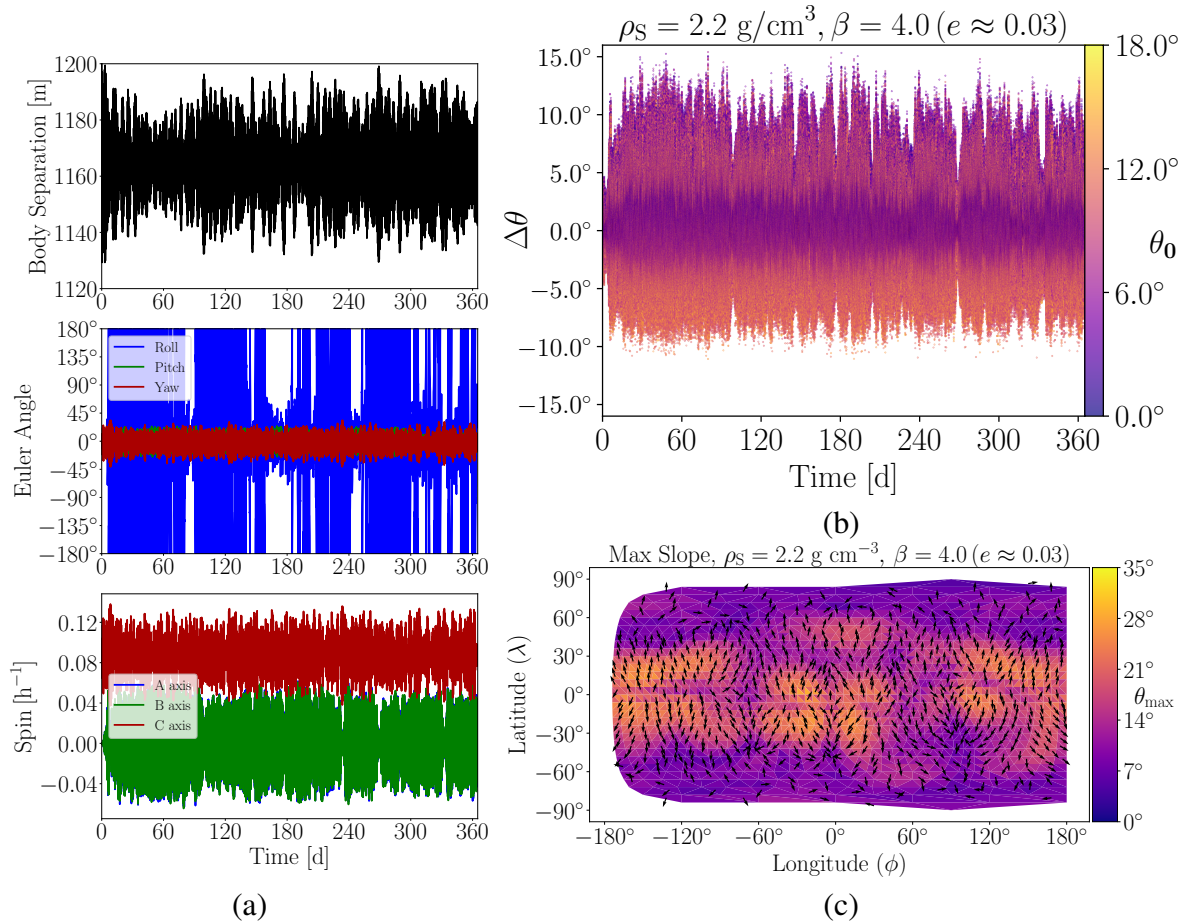


Figure B.5: The spin, orbit, and surface slope evolution for $\beta = 4$ and $\rho_S = 2.2 \text{ g cm}^{-3}$ over 365 days. (a) Body separation, Euler angles, and body spin of Dimorphos. (b) Corresponding change in slope ($\Delta\theta$) over time for each surface facet, colored by the starting slope (θ_0) of that facet. The surface slope evolution is dominated by NPA rotation. (c) Maximum surface slope achieved on each facet over the full 365 d simulation, with arrows pointing in the down-slope direction.

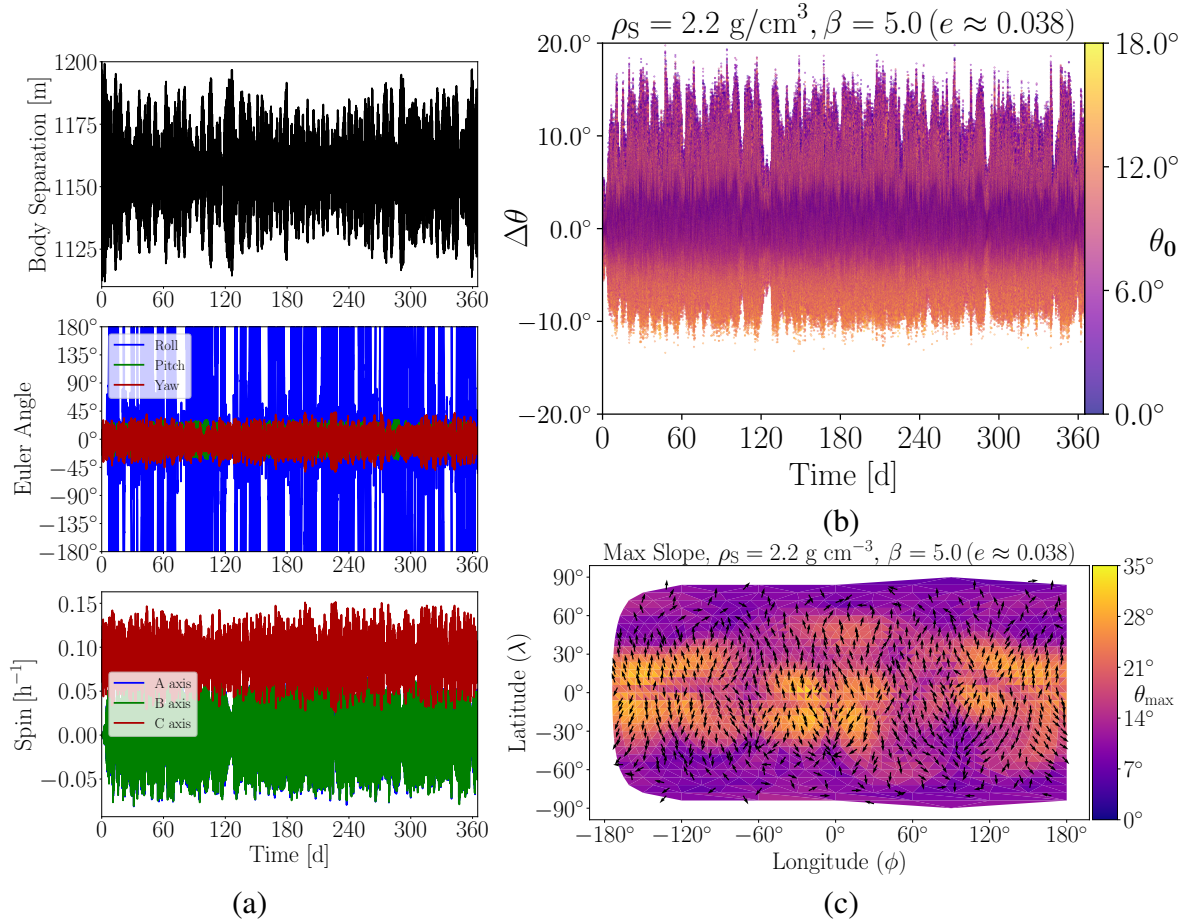


Figure B.6: The spin, orbit, and surface slope evolution for $\beta = 5$ and $\rho_s = 2.2 \text{ g cm}^{-3}$ over 365 days. (a) Body separation, Euler angles, and body spin of Dimorphos. (b) Corresponding change in slope ($\Delta\theta$) over time for each surface facet, colored by the starting slope (θ_0) of that facet. The surface slope evolution is dominated by NPA rotation. (c) Maximum surface slope achieved on each facet over the full 365 d simulation, with arrows pointing in the down-slope direction.

Appendix C: Facilities and Software used in this Thesis

Most of the simulations herein were carried out on The University of Maryland Astronomy Department's YORP cluster, administered by the Center for Theory and Computation. In addition, some simulations were run on the University of Maryland's Deeptought2 supercomputer, maintained by the Division of Information Technology.

Below is a list of open-source software used for this thesis:

1. Numpy (Harris et al., [2020](#))
2. Scipy (Virtanen et al., [2020](#))
3. Matplotlib (Caswell et al., [2020](#))
4. GUBAS¹ (Davis and Scheeres, [2020a](#), [2021](#))
5. PKDGRAV (Richardson et al., [2000](#); Schwartz et al., [2012](#); Zhang et al., [2017](#))
6. GRAINS (Ferrari et al., [2017](#))
7. POV-Ray (Persistence of Vision Raytracer)²

¹<https://github.com/alex-b-davis/gubas>

²<http://www.povray.org/>

Bibliography

- Agrusa, H. F., D. C. Richardson, A. B. Davis, E. Fahnestock, M. Hirabayashi, N. L. Chabot, A. F. Cheng, A. S. Rivkin, P. Michel, and DART Dynamics Working Group (2020). “A benchmarking and sensitivity study of the full two-body gravitational dynamics of the DART mission target, binary asteroid 65803 Didymos”. *Icarus* 349, 113849, p. 113849. DOI: 10.1016/j.icarus.2020.113849.
- Agrusa, H. F., I. Gkolias, K. Tsiganis, D. C. Richardson, A. J. Meyer, D. J. Scheeres, M. Ćuk, S. A. Jacobson, P. Michel, Ö. Karatekin, A. F. Cheng, M. Hirabayashi, Y. Zhang, E. G. Fahnestock, and A. B. Davis (2021). “The excited spin state of Dimorphos resulting from the DART impact”. *Icarus* 370, 114624, p. 114624. DOI: 10.1016/j.icarus.2021.114624.
- Agrusa, H. F., F. Ferrari, Y. Zhang, D. C. Richardson, and P. Michel (2022a). “Dynamical Evolution of the Didymos-Dimorphos Binary Asteroid as Rubble Piles following the DART Impact”. *The Planetary Science Journal* 3.7, p. 158. DOI: 10.3847/psj/ac76c1.
- Agrusa, H. F., R. Ballouz, A. J. Meyer, E. Tasev, G. Noiset, Ö. Karatekin, P. Michel, D. C. Richardson, and M. Hirabayashi (2022b). “Rotation-induced granular motion on the secondary component of binary asteroids: Application to the DART impact on Dimorphos”. *Astronomy and Astrophysics* 664, L3, p. L3. DOI: 10.1051/0004-6361/202244388.
- Albarède, F. (2009). “Volatile accretion history of the terrestrial planets and dynamic implications”. *Nature* 461.7268, pp. 1227–1233. DOI: 10.1038/nature08477.
- Alday, A., K. Moore, M. Tranilla, T. Goggia, V. Razo, A. Sylva, M. Ota, G. Fricke, J. Becker, J. Africano, P. Sydney, D. Nishimoto, D. O’Connell, P. Kervin, B. Kraszewski, V. Soo Hoo, J. Montani, J. V. Scotti, and G. V. Williams (1996). “1996 GT”. *Minor Planet Electronic Circulars* 1996-H02.
- Alvarez, L. W., W. Alvarez, F. Asaro, and H. V. Michel (1980). “Extraterrestrial Cause for the Cretaceous-Tertiary Extinction”. *Science* 208.4448, pp. 1095–1108. DOI: 10.1126/science.208.4448.1095.
- Asphaug, E. and W. Benz (1994). “Density of comet Shoemaker-Levy 9 deduced by modelling breakup of the parent ‘rubble pile’”. *Nature* 370.6485, pp. 120–124. DOI: 10.1038/370120a0.
- Ballouz, R.-L., N. Baresi, S. T. Crites, Y. Kawakatsu, and M. Fujimoto (2019). “Surface refreshing of Martian moon Phobos by orbital eccentricity-driven grain motion”. *Nature Geoscience* 12.4, pp. 229–234. DOI: 10.1038/s41561-019-0323-9.

- Barnouin, O. S., E. R. Jawin, R. T. Daly, R. -. Ballouz, M. G. Daly, J. A. Seabrook, P. Michel, Y. Zhang, C. L. Johnson, K. J. Walsh, M. M. Al Asad, R. Gaskell, J. Weirich, E. Palmer, E. B. Bierhaus, M. C. Nolan, C. W. V. Wolner, and D. S. Lauretta (2022). “Geologic Context of the OSIRIS-REx Sample Site from High-resolution Topography and Imaging”. *The Planetary Science Journal* 3.4, 75, p. 75. DOI: 10.3847/PSJ/ac5597.
- Belton, M. J. S., C. R. Chapman, P. C. Thomas, M. E. Davies, R. Greenberg, K. Klaasen, D. Byrnes, L. D’Amario, S. Synnott, T. V. Johnson, A. McEwen, W. J. Merline, D. R. Davis, J. -. Petit, A. Storrs, J. Veverka, and B. Zellner (1995). “Bulk density of asteroid 243 Ida from the orbit of its satellite Dactyl”. *Nature* 374.6525, pp. 785–788. DOI: 10.1038/374785a0.
- Berdeu, A., M. Langlois, and F. Vachier (2022). “First observation of a quadruple asteroid. Detection of a third moon around (130) Elektra with SPHERE/IFS”. *Astronomy and Astrophysics* 658, L4, p. L4. DOI: 10.1051/0004-6361/202142623.
- Binzel, R. P., A. S. Rivkin, J. S. Stuart, A. W. Harris, S. J. Bus, and T. H. Burbine (2004). “Observed spectral properties of near-Earth objects: results for population distribution, source regions, and space weathering processes”. *Icarus* 170.2, pp. 259–294. DOI: 10.1016/j.icarus.2004.04.004.
- Bottke, W. F. and H. J. Melosh (1996a). “Binary Asteroids and the Formation of Doublet Craters”. *Icarus* 124.2, pp. 372–391. DOI: 10.1006/icar.1996.0215.
- Bottke, W. F. and H. J. Melosh (1996b). “Formation of asteroid satellites and doublet craters by planetary tidal forces”. *Nature* 381.6577, pp. 51–53. DOI: 10.1038/381051a0.
- Bottke, W. F., D. Vokrouhlický, D. P. Rubincam, and M. Brož (2002). “The Effect of Yarkovsky Thermal Forces on the Dynamical Evolution of Asteroids and Meteoroids”. In: *Asteroids III*, pp. 395–408.
- Bottke, W. F., D. D. Durda, D. Nesvorný, R. Jedicke, A. Morbidelli, D. Vokrouhlický, and H. Levison (2005). “The fossilized size distribution of the main asteroid belt”. *Icarus* 175.1, pp. 111–140. DOI: 10.1016/j.icarus.2004.10.026.
- Bottke, W. F., D. Vokrouhlický, D. P. Rubincam, and D. Nesvorný (2006). “The Yarkovsky and Yorp Effects: Implications for Asteroid Dynamics”. *Annual Review of Earth and Planetary Sciences* 34, pp. 157–191. DOI: 10.1146/annurev.earth.34.031405.125154.
- Bottke, W. F., D. Vokrouhlický, and D. Nesvorný (2007). “An asteroid breakup 160Myr ago as the probable source of the K/T impactor”. *Nature* 449.7158, pp. 48–53. DOI: 10.1038/nature06070.
- Bottke, W. F., M. Brož, D. P. O’Brien, A. Campo Bagatin, A. Morbidelli, and S. Marchi (2015). “The Collisional Evolution of the Main Asteroid Belt”. In: *Asteroids IV*, pp. 701–724. DOI: 10.2458/azu_uapress_9780816532131-ch036.
- Boué, G. and J. Laskar (2009). “Spin axis evolution of two interacting bodies”. *Icarus* 201.2, pp. 750–767. DOI: 10.1016/j.icarus.2009.02.001.

- Brack, D. N. and J. W. McMahon (2019). “Modeling the coupled dynamics of an asteroid with surface boulder motion”. *Icarus* 333, pp. 96–112.
DOI: 10.1016/j.icarus.2019.05.038.
- Breakwell, J. V. and R. Pringle (1965). “Nonlinear resonances affecting gravity gradient stability”. In: *16th IAF International Congress*. Vol. 6. Athens, p. 305.
- Brozović, M., L. A. M. Benner, J. G. McMichael, J. D. Giorgini, P. Pravec, P. Scheirich, C. Magri, M. W. Busch, J. S. Jao, C. G. Lee, L. G. Snedeker, M. A. Silva, M. A. Slade, B. Semenov, M. C. Nolan, P. A. Taylor, E. S. Howell, and K. J. Lawrence (2018). “Goldstone and Arecibo radar observations of (99942) Apophis in 2012-2013”. *Icarus* 300, pp. 115–128.
DOI: 10.1016/j.icarus.2017.08.032.
- Caswell, T. A., M. Droettboom, A. Lee, J. Hunter, E. Sales de Andrade, E. Firing, T. Hoffmann, J. Klymak, D. Stansby, N. Varoquaux, J. Hedegaard Nielsen, B. Root, R. May, P. Elson, J. K. Seppänen, D. Dale, J.-J. Lee, D. McDougall, A. Straw, P. Hobson, C. Gohlke, T. S. Yu, E. Ma, A. F. Vincent, S. Silvester, C. Moad, hannah, N. Kniazev, E. Ernest, and P. Ivanov (2020). *matplotlib/matplotlib: REL: v3.3.3*. Zenodo. Version v3.3.3.
DOI: 10.5281/zenodo.4268928.
- Chapman, C. R., J. Veverka, P. C. Thomas, K. Klaasen, M. J. S. Belton, A. Harch, A. McEwen, T. V. Johnson, P. Helfenstein, M. E. Davies, W. J. Merline, and T. Denk (1995). “Discovery and physical properties of Dactyl, a satellite of asteroid 243 Ida”. *Nature* 374.6525, pp. 783–785. DOI: 10.1038/374783a0.
- Cheng, A. F., P. Michel, M. Jutzi, A. S. Rivkin, A. Stickle, O. Barnouin, C. Ernst, J. Atchison, P. Pravec, D. C. Richardson, and AIDA Team (2016). “Asteroid Impact & Deflection Assessment mission: Kinetic impactor”. *Planetary and Space Science* 121, pp. 27–35.
DOI: 10.1016/j.pss.2015.12.004.
- Cheng, A. F., A. S. Rivkin, P. Michel, J. Atchison, O. Barnouin, L. Benner, N. L. Chabot, C. Ernst, E. G. Fahnestock, M. Kueppers, P. Pravec, E. Rainey, D. C. Richardson, A. M. Stickle, and C. Thomas (2018). “AIDA DART asteroid deflection test: Planetary defense and science objectives”. *Planetary and Space Science* 157, pp. 104–115.
DOI: 10.1016/j.pss.2018.02.015.
- Cheng, A. F., A. M. Stickle, E. G. Fahnestock, E. Dotto, V. Della Corte, N. L. Chabot, and A. S. Rivkin (2020). “DART mission determination of momentum transfer: Model of ejecta plume observations”. *Icarus* 352, 113989, p. 113989.
DOI: 10.1016/j.icarus.2020.113989.
- Cheng, A. F., S. D. Raducan, E. G. Fahnestock, E. Dotto, V. Della Corte, and A. M. Stickle (2022). “Model of Double Asteroid Redirection Test Impact Ejecta Plume Observations”. *The Planetary Science Journal* 3.6, 131, p. 131. DOI: 10.3847/PSJ/ac66e9.
- Chyba, C. F., P. J. Thomas, and K. J. Zahnle (1993). “The 1908 Tunguska explosion: atmospheric disruption of a stony asteroid”. *Nature* 361.6407, pp. 40–44. DOI: 10.1038/361040a0.

- Cook, C. M., H. J. Melosh, and W. F. Bottke (2003). “Doublet craters on Venus”. *Icarus* 165.1, pp. 90–100. DOI: 10.1016/S0019-1035(03)00177-5.
- Correia, A. C. M. (2018). “Chaotic dynamics in the (47171) Lempo triple system”. *Icarus* 305, pp. 250–261. DOI: 10.1016/j.icarus.2018.01.008.
- Cotto-Figueroa, D., T. S. Statler, D. C. Richardson, and P. Tanga (2015). “Coupled Spin and Shape Evolution of Small Rubble-pile Asteroids: Self-limitation of the YORP Effect”. *The Astrophysical Journal* 803.1, 25, p. 25. DOI: 10.1088/0004-637X/803/1/25.
- Ćuk, M. and J. A. Burns (2005). “Effects of thermal radiation on the dynamics of binary NEAs”. *Icarus* 176.2, pp. 418–431. DOI: 10.1016/j.icarus.2005.02.001.
- Ćuk, M., S. Jacobson, and K. Walsh (2020). ““Barrel Instability” for Elongated Secondaries in Binary Asteroids”. In: *AAS/Division of Dynamical Astronomy Meeting*. Vol. 52. AAS/Division of Dynamical Astronomy Meeting, 103.04, p. 103.04.
- Ćuk, M., S. A. Jacobson, and K. J. Walsh (2021). “Barrel Instability in Binary Asteroids”. *The Planetary Science Journal* 2.6, 231, p. 231. DOI: 10.3847/PSJ/ac3093.
- Curtis, H. D. (2020). *Orbital Mechanics for Engineering Students*. 4th. Butterworth-Heinemann, pp. 479–542.
- Daly, R. T. and P. H. Schultz (2018). “The delivery of water by impacts from planetary accretion to present”. *Science Advances* 4.4, eaar2632. DOI: 10.1126/sciadv.aar2632.
- Daly, R. T., C. M. Ernst, O. S. Barnouin, R. W. Gaskell, E. E. Palmer, H. Nair, R. C. Espiritu, S. Hasnain, D. Waller, A. M. Stickle, M. C. Nolan, J. M. Trigo-Rodríguez, E. Dotto, A. Lucchetti, M. Pajola, S. Ieva, and P. Michel (2022). “Shape Modeling of Dimorphos for the Double Asteroid Redirection Test (DART)”. *The Planetary Science Journal* 3.9, p. 207. DOI: 10.3847/psj/ac7523.
- Davis, A. B. and D. J. Scheeres (2020a). “Doubly synchronous binary asteroid mass parameter observability”. 341, 113439, p. 113439. DOI: 10.1016/j.icarus.2019.113439.
- Davis, A. B. and D. J. Scheeres (2020b). “High-fidelity Modeling of Rotationally Fissioned Asteroids”. *The Planetary Science Journal* 1.1, 25, p. 25. DOI: 10.3847/PSJ/ab9a39.
- Davis, A. B. and D. J. Scheeres (2021). *GUBAS: General Use Binary Asteroid Simulator*.
- DeMartini, J. V., D. C. Richardson, O. S. Barnouin, N. C. Schmerr, J. B. Plescia, P. Scheirich, and P. Pravec (2019). “Using a discrete element method to investigate seismic response and spin change of 99942 Apophis during its 2029 tidal encounter with Earth”. *Icarus* 328, pp. 93–103. DOI: 10.1016/j.icarus.2019.03.015.
- Desch, S., A. Jackson, J. Noviello, and A. Anbar (2021). “The Chicxulub impactor: comet or asteroid?” *Astronomy and Geophysics* 62.3, pp. 3.34–3.37. DOI: 10.1093/astrogeo/atab069.
- Dotto, E., V. Della Corte, M. Amoroso, I. Bertini, J. R. Brucato, A. Capannolo, B. Cotugno, G. Cremonese, V. Di Tana, I. Gai, S. Ieva, G. Impresario, S. L. Ivanovski, M. Lavagna, A. Luc-

- chetti, E. Mazzotta Epifani, A. Meneghin, F. Miglioretti, D. Modenini, M. Pajola, P. Palumbo, D. Perna, S. Pirrotta, G. Poggiali, A. Rossi, E. Simioni, S. Simonetti, P. Tortora, M. Zannoni, G. Zanotti, A. Zinzi, A. F. Cheng, A. S. Rivkin, E. Y. Adams, E. L. Reynolds, and K. Fretz (2021). “LICIACube - The Light Italian Cubesat for Imaging of Asteroids In support of the NASA DART mission towards asteroid (65803) Didymos”. *Planetary and Space Science* 199, 105185, p. 105185. DOI: 10.1016/j.pss.2021.105185.
- Dunn, T. L., T. H. Burbine, W. F. Bottke, and J. P. Clark (2013). “Mineralogies and source regions of near-Earth asteroids”. *Icarus* 222.1, pp. 273–282. DOI: 10.1016/j.icarus.2012.11.007.
- Eapen, R. T., M. Majji, and K. T. Alfriend (2021). “Attitude dynamics of a rigid body in Keplerian motion”. *Celestial Mechanics and Dynamical Astronomy* 133.1, 2, p. 2. DOI: 10.1007/s10569-020-10000-w.
- Fahnestock, E. G. and D. J. Scheeres (2006). “Simulation of the full two rigid body problem using polyhedral mutual potential and potential derivatives approach”. *Celestial Mechanics and Dynamical Astronomy* 96.3-4, pp. 317–339. DOI: 10.1007/s10569-006-9045-6.
- Fahnestock, E. G. and D. J. Scheeres (2008). “Simulation and analysis of the dynamics of binary near-Earth Asteroid (66391) 1999 KW4”. *Icarus* 194.2, pp. 410–435. DOI: 10.1016/j.icarus.2007.11.007.
- Fang, J. and J.-L. Margot (2012). “Near-Earth Binaries and Triples: Origin and Evolution of Spin-Orbital Properties”. *The Astronomical Journal* 143.1, 24, p. 24. DOI: 10.1088/0004-6256/143/1/24.
- Farnocchia, D., S. R. Chesley, P. W. Chodas, M. Micheli, D. J. Tholen, A. Milani, G. T. Elliott, and F. Bernardi (2013). “Yarkovsky-driven impact risk analysis for asteroid (99942) Apophis”. *Icarus* 224.1, pp. 192–200. DOI: 10.1016/j.icarus.2013.02.020.
- Farnocchia, D., S. R. Chesley, A. Milani, G. F. Gronchi, and P. W. Chodas (2015). “Orbits, Long-Term Predictions, Impact Monitoring”. In: *Asteroids IV*, pp. 815–834. DOI: 10.2458/azu_uapress_9780816532131-ch041.
- Feldhacker, J. D., M. B. Syal, B. A. Jones, A. Doostan, J. McMahon, and D. J. Scheeres (2017). “Shape Dependence of the Kinetic Deflection of Asteroids”. *Journal of Guidance Control Dynamics* 40.10, pp. 2417–2431. DOI: 10.2514/1.G002270.
- Ferrari, F., A. Tasora, P. Masarati, and M. Lavagna (2017). “N-body gravitational and contact dynamics for asteroid aggregation”. *Multibody System Dynamics* 39.1, pp. 3–20. ISSN: 1573-272X. DOI: 10.1007/s11044-016-9547-2.
- Ferrari, F. and P. Tanga (2020). “The role of fragment shapes in the simulations of asteroids as gravitational aggregates”. *Icarus* 350, 113871, p. 113871. DOI: 10.1016/j.icarus.2020.113871.
- Ferrari, F., M. Lavagna, and E. Blazquez (2020). “A parallel-GPU code for asteroid aggregation problems with angular particles”. *Monthly Notices of the Royal Astronomical Society* 492 (1), pp. 749–761. ISSN: 0035-8711. DOI: 10.1093/mnras/stz3458.

- Ferrari, F. and P. Tanga (2022). “Interior of top-shaped asteroids with cohesionless surface”. *Icarus* 378, 114914, p. 114914. DOI: 10.1016/j.icarus.2022.114914.
- Fleig, A. J. (1970). *On the libration of a gravity gradient stabilized spacecraft in an eccentric orbit*. National Aeronautics and Space Administration.
- Fleischmann, J., R. Serban, D. Negrut, and P. Jayakumar (2015). “On the Importance of Displacement History in Soft-Body Contact Models”. *Journal of Computational and Nonlinear Dynamics* 11.4, pp. 044502–044502-5. ISSN: 1555-1415. DOI: 10.1115/1.4031197.
- Froeschlé, C., R. Gonczi, and E. Lega (1997). “The fast Lyapunov indicator: a simple tool to detect weak chaos. Application to the structure of the main asteroidal belt”. *Planetary and Space Science* 45.7, pp. 881–886. DOI: 10.1016/S0032-0633(97)00058-5.
- Fuentes-Muñoz, O. and D. J. Scheeres (2020). “Extremely long-term asteroid propagation”. In: *AIAA Scitech 2020 Forum*, p. 0464.
- Gao, Y., Y. Yu, B. Cheng, and H. Baoyin (2022). “Accelerating the finite element method for calculating the full 2-body problem with CUDA”. *Advances in Space Research* 69.5, pp. 2305–2318. DOI: 10.1016/j.asr.2021.11.037.
- Gehrels, T., J. D. Drummond, and N. A. Levenson (1987). “The absence of satellites of asteroids”. *Icarus* 70.2, pp. 257–263. DOI: 10.1016/0019-1035(87)90133-3.
- Geissler, P., J.-M. Petit, D. D. Durda, R. Greenberg, W. Bottke, M. Nolan, and J. Moore (1996). “Erosion and Ejecta Reaccretion on 243 Ida and Its Moon”. *Icarus* 120.1, pp. 140–157. DOI: 10.1006/icar.1996.0042.
- Giorgini, J. D., L. A. M. Benner, S. J. Ostro, M. C. Nolan, and M. W. Busch (2008). “Predicting the Earth encounters of (99942) Apophis”. *Icarus* 193.1, pp. 1–19. DOI: 10.1016/j.icarus.2007.09.012.
- Gkolias, I., C. Efthymiopoulos, A. Celletti, and G. Pucacco (2019). “Accurate modelling of the low-order secondary resonances in the spin-orbit problem”. *Communications in Nonlinear Science and Numerical Simulations* 77, pp. 181–202. DOI: 10.1016/j.cnsns.2019.04.015.
- Gladman, B., P. Michel, and C. Froeschlé (2000). “The Near-Earth Object Population”. *Icarus* 146.1, pp. 176–189. DOI: 10.1006/icar.2000.6391.
- Goldreich, P. and S. Soter (1966). “Q in the Solar System”. *Icarus* 5.1, pp. 375–389. DOI: 10.1016/0019-1035(66)90051-0.
- Goldreich, P. and R. Sari (2009). “Tidal Evolution of Rubble Piles”. *The Astrophysical Journal* 691.1, pp. 54–60. DOI: 10.1088/0004-637X/691/1/54.
- Gradie, J. and L. Flynn (1988). “A Search for Satellites and Dust Belts Around Asteroids: Negative Results”. In: *Lunar and Planetary Science Conference*. Vol. 19. Lunar and Planetary Science Conference, p. 405.

- Hammel, H. B., R. F. Beebe, A. P. Ingersoll, G. S. Orton, J. R. Mills, A. A. Simon, P. Chodas, J. T. Clarke, E. de Jong, T. E. Dowling, J. Harrington, L. F. Huber, E. Karkoschka, C. M. Santori, A. Toigo, D. Yeomans, and R. A. West (1995). “HST Imaging of Atmospheric Phenomena Created by the Impact of Comet Shoemaker-Levy 9”. *Science* 267.5202, pp. 1288–1296. DOI: 10.1126/science.7871425.
- Harris, A. W., E. G. Fahnestock, and P. Pravec (2009). “On the shapes and spins of “rubble pile” asteroids”. *Icarus* 199.2, pp. 310–318. DOI: 10.1016/j.icarus.2008.09.012.
- Harris, A. W., M. Boslough, C. R. Chapman, L. Drube, P. Michel, and A. W. Harris (2015). “Asteroid Impacts and Modern Civilization: Can We Prevent a Catastrophe?” In: *Asteroids IV*, pp. 835–854. DOI: 10.2458/azu_uapress_9780816532131-ch042.
- Harris, A. W. and G. D’Abramo (2015). “The population of near-Earth asteroids”. *Icarus* 257, pp. 302–312. DOI: 10.1016/j.icarus.2015.05.004.
- Harris, A. W. and P. W. Chodas (2021). “The population of near-earth asteroids revisited and updated”. *Icarus* 365, 114452, p. 114452. DOI: 10.1016/j.icarus.2021.114452.
- Harris, C. R., K. J. Millman, S. J. Van Der Walt, R. Gommers, P. Virtanen, D. Cournapeau, E. Wieser, J. Taylor, S. Berg, N. J. Smith, et al. (2020). “Array programming with NumPy”. *Nature* 585.7825, pp. 357–362.
- Hergenrother, C. W., C. K. Maleszewski, M. C. Nolan, J. -. Li, C. Y. Drouet D’Aubigny, F. C. Shelly, E. S. Howell, T. R. Kareta, M. R. M. Izawa, M. A. Barucci, E. B. Bierhaus, H. Campins, S. R. Chesley, B. E. Clark, E. J. Christensen, D. N. Dellagiustina, S. Fornasier, D. R. Golish, C. M. Hartzell, B. Rizk, D. J. Scheeres, P. H. Smith, X. -. Zou, D. S. Laretta, and OSIRIS-REx Team (2019). “The operational environment and rotational acceleration of asteroid (101955) Bennu from OSIRIS-REx observations”. *Nature Communications* 10, 1291, p. 1291. DOI: 10.1038/s41467-019-09213-x.
- Hirabayashi, M. and D. J. Scheeres (2013). “Recursive computation of mutual potential between two polyhedra”. *Celestial Mechanics and Dynamical Astronomy* 117.3, pp. 245–262. DOI: 10.1007/s10569-013-9511-x.
- Hirabayashi, M., S. R. Schwartz, Y. Yu, A. B. Davis, S. R. Chesley, E. G. Fahnestock, P. Michel, D. C. Richardson, S. P. Naidu, D. J. Scheeres, A. F. Cheng, A. S. Rivkin, and L. A. M. Benner (2017). “Constraints on the perturbed mutual motion in Didymos due to impact-induced deformation of its primary after the DART impact”. *Monthly Notices of the Royal Astronomical Society* 472.2, pp. 1641–1648. DOI: 10.1093/mnras/stx1992.
- Hirabayashi, M., A. B. Davis, E. G. Fahnestock, D. C. Richardson, P. Michel, A. F. Cheng, A. S. Rivkin, D. J. Scheeres, S. R. Chesley, Y. Yu, S. P. Naidu, S. R. Schwartz, L. A. M. Benner, P. Pravec, A. M. Stickle, M. Jutzi, DART Dynamical Group, and Physical Properties (WG3) Analysis Group (2019). “Assessing possible mutual orbit period change by shape deformation of Didymos after a kinetic impact in the NASA-led Double Asteroid Redirection Test”. *Advances in Space Research* 63.8, pp. 2515–2534. DOI: 10.1016/j.asr.2018.12.041.

- Hirabayashi, M. and D. J. Scheeres (2019). “Rotationally induced failure of irregularly shaped asteroids”. *Icarus* 317, pp. 354–364. DOI: 10.1016/j.icarus.2018.08.003.
- Hirabayashi, M., F. Ferrari, M. Jutzi, R. Nakano, S. D. Raducan, P. Sánchez, S. Soldini, Y. Zhang, O. S. Barnouin, D. C. Richardson, P. Michel, E. Dotto, A. Rossi, and A. R. Rivkin (2022). “Double Asteroid Redirection Test (DART): Structural and Dynamic Interactions between Asteroidal Elements of Binary Asteroid (65803) Didymos”. *The Planetary Science Journal* 3.6, 140, p. 140. DOI: 10.3847/PSJ/ac6eff.
- Holsapple, K. A. and P. Michel (2006). “Tidal disruptions: A continuum theory for solid bodies”. *Icarus* 183.2, pp. 331–348. DOI: 10.1016/j.icarus.2006.03.013.
- Holsapple, K. A. and P. Michel (2008). “Tidal disruptions. II. A continuum theory for solid bodies with strength, with applications to the Solar System”. *Icarus* 193.1, pp. 283–301. DOI: 10.1016/j.icarus.2007.09.011.
- Hou, X., D. J. Scheeres, and X. Xin (2017). “Mutual potential between two rigid bodies with arbitrary shapes and mass distributions”. *Celestial Mechanics and Dynamical Astronomy* 127.3, pp. 369–395. DOI: 10.1007/s10569-016-9731-y.
- Jacobson, S. A. and D. J. Scheeres (2011a). “Dynamics of rotationally fissioned asteroids: Source of observed small asteroid systems”. *Icarus* 214.1, pp. 161–178. DOI: 10.1016/j.icarus.2011.04.009.
- Jacobson, S. A. and D. J. Scheeres (2011b). “Long-term Stable Equilibria for Synchronous Binary Asteroids”. *The Astrophysical Journal* 736.1, L19, p. L19. DOI: 10.1088/2041-8205/736/1/L19.
- Jacobson, S. A., F. Marzari, A. Rossi, and D. J. Scheeres (2016). “Matching asteroid population characteristics with a model constructed from the YORP-induced rotational fission hypothesis”. *Icarus* 277, pp. 381–394. DOI: 10.1016/j.icarus.2016.05.032.
- Kane, T. R. (1965). “Attitude stability of earth-pointing satellites”. *AIAA Journal* 3.4, pp. 726–731. DOI: 10.2514/3.2955.
- Karatekin, Ö., E. Le Bras, S. Van wal, A. Herique, P. Tortora, B. Ritter, M. Scoubeau, and V. M. Moreno (2021). “Juventas Cubesat for the Hera mision”. In: *European Planetary Science Congress, EPSC2021-750, EPSC2021–750*. DOI: 10.5194/epsc2021-750.
- Kim, Y., M. Hirabayashi, R. P. Binzel, M. Brozović, D. J. FScheeres, and D. C. Richardson (2021). “The surface sensitivity of rubble-pile asteroids during a distant planetary encounter: Influence of asteroid shape elongation”. *Icarus* 358, 114205, p. 114205. DOI: 10.1016/j.icarus.2020.114205.
- Kulik, L. A. (1927). “Report of the meteorite expedition”. In: *Dokl. Akad. Nauka USSR*. Vol. 23, p. 399.
- Lee, T., M. Leok, and N. H. McClamroch (2007). “Lie group variational integrators for the full body problem in orbital mechanics”. *Celestial Mechanics and Dynamical Astronomy* 98.2, pp. 121–144. DOI: 10.1007/s10569-007-9073-x.

- Lowry, S. C., A. Fitzsimmons, P. Pravec, D. Vokrouhlický, H. Boehnhardt, P. A. Taylor, J.-L. Margot, A. Galád, M. Irwin, J. Irwin, and P. Kusnirák (2007). “Direct Detection of the Asteroidal YORP Effect”. *Science* 316.5822, p. 272. DOI: 10.1126/science.1139040.
- MacCullagh (1844a). “Further Remarks on the Rotation of a Solid Body”. *Proceedings of the Royal Irish Academy (1836-1869)* 2, pp. 542–545. ISSN: 03027597.
- MacCullagh (1844b). “On the Rotation of a Solid Body”. *Proceedings of the Royal Irish Academy (1836-1869)* 2, pp. 520–526. ISSN: 03027597.
- Makadia, R., S. D. Raducan, E. G. Fahnestock, and S. Eggl (2022). “Heliocentric Effects of the DART Mission on the (65803) Didymos Binary Asteroid System”. *The Planetary Science Journal* 3.8, p. 184. DOI: 10.3847/psj/ac7de7.
- Margot, J. L., M. C. Nolan, L. A. M. Benner, S. J. Ostro, R. F. Jurgens, J. D. Giorgini, M. A. Slade, and D. B. Campbell (2002). “Binary Asteroids in the Near-Earth Object Population”. *Science* 296.5572, pp. 1445–1448. DOI: 10.1126/science.1072094.
- McMahon, J. and D. Scheeres (2010). “Detailed prediction for the BYORP effect on binary near-Earth Asteroid (66391) 1999 KW4 and implications for the binary population”. *Icarus* 209.2, pp. 494–509. DOI: 10.1016/j.icarus.2010.05.016.
- McMahon, J. W. and D. J. Scheeres (2013). “Dynamic limits on planar libration-orbit coupling around an oblate primary”. *Celestial Mechanics and Dynamical Astronomy* 115.4, pp. 365–396. DOI: 10.1007/s10569-012-9469-0.
- Melnikov, A. V. (2001). “Bifurcation Regime of a Synchronous Resonance in the Translational-Rotational Motion of Nonspherical Natural Satellites of Planets”. *Cosmic Research* 39.1, pp. 68–77.
- Melosh, H. J. and J. A. Stansberry (1991). “Doublet craters and the tidal disruption of binary asteroids”. *Icarus* 94.1, pp. 171–179. DOI: 10.1016/0019-1035(91)90148-M.
- Merline, W. J., L. M. Close, C. Dumas, C. R. Chapman, F. Roddier, F. Menard, D. C. Slater, G. Duvert, C. Shelton, and T. Morgan (1999). “Discovery of a moon orbiting the asteroid 45 Eugenia”. *Nature* 401, p. 565. DOI: 10.1038/44089.
- Merline, W. J., S. J. Weidenschilling, D. D. Durda, J. L. Margot, P. Pravec, and A. D. Storrs (2002). “Asteroids Do Have Satellites”. In: *Asteroids III*, pp. 289–312.
- Meyer, A. J., I. Gkolias, M. Gaitanas, H. F. Agrusa, D. J. Scheeres, K. Tsiganis, P. Pravec, L. A. M. Benner, F. Ferrari, and P. Michel (2021). “Libration-induced Orbit Period Variations Following the DART Impact”. *The Planetary Science Journal* 2.6, 242, p. 242. DOI: 10.3847/PSJ/ac3bd1.
- Meyer, A. J. and D. J. Scheeres (2021). “The effect of planetary flybys on singly synchronous binary asteroids”. *Icarus* 367, 114554, p. 114554. DOI: 10.1016/j.icarus.2021.114554.
- Michel, P., M. Kueppers, H. Sierks, I. Carnelli, A. F. Cheng, K. Mellab, M. Granvik, A. Kestilä, T. Kohout, K. Muinonen, A. Näsilä, A. Penttilä, T. Tikka, P. Tortora, V. Ciarletti, A. Hérique,

- N. Murdoch, E. Asphaug, A. Rivkin, O. Barnouin, A. C. Bagatin, P. Pravec, D. C. Richardson, S. R. Schwartz, K. Tsiganis, S. Ulamec, and O. Karatekin (2018). “European component of the AIDA mission to a binary asteroid: Characterization and interpretation of the impact of the DART mission”. *Advances in Space Research* 62.8, pp. 2261–2272.
DOI: 10.1016/j.asr.2017.12.020.
- Michel, P., M. Küppers, A. C. Bagatin, B. Carry, S. Charnoz, J. de Leon, A. Fitzsimmons, P. Gordo, S. F. Green, A. Hérique, M. Juzzi, Ö. Karatekin, T. Kohout, M. Lazzarin, N. Murdoch, T. Okada, E. Palomba, P. Pravec, C. Snodgrass, P. Tortora, K. Tsiganis, S. Ulamec, J.-B. Vincent, K. Wünnemann, Y. Zhang, S. D. Raducan, E. Dotto, N. Chabot, A. F. Cheng, A. Rivkin, O. Barnouin, C. Ernst, A. Stickle, D. C. Richardson, C. Thomas, M. Arakawa, H. Miyamoto, A. Nakamura, S. Sugita, M. Yoshikawa, P. Abell, E. Asphaug, R.-L. Ballouz, W. F. Bottke, D. S. Lauretta, K. J. Walsh, P. Martino, and I. Carnelli (2022). “The ESA Hera Mission: Detailed Characterization of the DART Impact Outcome and of the Binary Asteroid (65803) Didymos”. *The Planetary Science Journal* 3.7, p. 160.
DOI: 10.3847/psj/ac6f52.
- Michikami, T., A. M. Nakamura, and N. Hirata (2010). “The shape distribution of boulders on Asteroid 25143 Itokawa: Comparison with fragments from impact experiments”. *Icarus* 207.1, pp. 277–284. DOI: 10.1016/j.icarus.2009.10.008.
- Michikami, T., C. Honda, H. Miyamoto, M. Hirabayashi, A. Hagermann, T. Irie, K. Nomura, C. M. Ernst, M. Kawamura, K. Sugimoto, E. Tatsumi, T. Morota, N. Hirata, T. Noguchi, Y. Cho, S. Kameda, T. Kouyama, Y. Yokota, R. Noguchi, M. Hayakawa, N. Hirata, R. Honda, M. Matsuoka, N. Sakatani, H. Suzuki, M. Yamada, K. Yoshioka, H. Sawada, R. Hemmi, H. Kikuchi, K. Ogawa, S.-i. Watanabe, S. Tanaka, M. Yoshikawa, Y. Tsuda, and S. Sugita (2019). “Boulder size and shape distributions on asteroid Ryugu”. *Icarus* 331, pp. 179–191.
DOI: 10.1016/j.icarus.2019.05.019.
- Möhlmann, D., K. J. Seidensticker, H.-H. Fischer, C. Faber, A. Flandes, M. Knapmeyer, H. Krüger, R. Roll, F. Scholten, K. Thiel, and W. Arnold (2018). “Compressive strength and elastic modulus at Agilkia on comet 67P/Churyumov-Gerasimenko derived from the SESAME/CASSE touchdown signals”. *Icarus* 303, pp. 251–264.
DOI: 10.1016/j.icarus.2017.09.038.
- Movshovitz, N., E. Asphaug, and D. Korycansky (2012). “Numerical Modeling of the Disruption of Comet D/1993 F2 Shoemaker-Levy 9 Representing the Progenitor by a Gravitationally Bound Assemblage of Randomly Shaped Polyhedra”. *The Astrophysical Journal* 759.2, 93, p. 93. DOI: 10.1088/0004-637X/759/2/93.
- Murray, C. D. and S. F. Dermott (2000). *Solar System Dynamics*.
DOI: 10.1017/CBO9781139174817.
- Naidu, S. P., L. A. M. Benner, M. Brozovic, M. C. Nolan, S. J. Ostro, J. L. Margot, J. D. Giorgini, T. Hirabayashi, D. J. Scheeres, P. Pravec, P. Scheirich, C. Magri, and J. S. Jao (2020a). “Radar observations and a physical model of binary near-Earth asteroid 65803 Didymos, target of the DART mission”. *Icarus* 348, 113777, p. 113777.
DOI: 10.1016/j.icarus.2020.113777.

- Naidu, S., S. Chesley, and D. Farnocchia (2020b). *Computation of the orbit of the satellite of binary near-Earth asteroid (65803) Didymos*. Jet Propulsion Laboratory Interoffice Memorandum 392R-20-001.
- Naidu, S. P. and J.-L. Margot (2015). “Near-Earth Asteroid Satellite Spins Under Spin-orbit Coupling”. *The Astronomical Journal* 149.2, 80, p. 80. DOI: 10.1088/0004-6256/149/2/80.
- Nakano, R., M. Hirabayashi, H. F. Agrusa, F. Ferrari, A. J. Meyer, P. Michel, S. D. Raducan, P. Sánchez, and Y. Zhang (2022). “NASA’s Double Asteroid Redirection Test (DART): Mutual Orbital Period Change Due to Reshaping in the Near-Earth Binary Asteroid System (65803) Didymos”. *The Planetary Science Journal* 3.7, p. 148. DOI: 10.3847/psj/ac7566.
- National Academies of Sciences, E. and Medicine (2022). *Origins, Worlds, and Life: A Decadal Strategy for Planetary Science and Astrobiology 2023-2032*. Washington, DC: The National Academies Press. ISBN: 978-0-309-47578-5. DOI: 10.17226/26522.
- Nimmo, F. and I. Matsuyama (2019). “Tidal dissipation in rubble-pile asteroids”. *Icarus* 321, pp. 715–721. DOI: 10.1016/j.icarus.2018.12.012.
- Nolan, M. C., J. -L. Margot, E. S. Howell, L. A. M. Benner, S. J. Ostro, R. F. Jurgens, J. D. Giorgini, and D. B. Campbell (2000). “2000 UG₁₁”. *International Astronomical Union Circular* 7518, p. 2.
- Ostro, S. J., J. -L. Margot, M. C. Nolan, L. A. M. Benner, R. F. Jurgens, and J. D. Giorgini (2000). “2000 DP107”. *International Astronomical Union Circular* 7496, p. 2.
- Ostro, S. J., J.-L. Margot, L. A. M. Benner, J. D. Giorgini, D. J. Scheeres, E. G. Fahnestock, S. B. Broschart, J. Bellerose, M. C. Nolan, C. Magri, P. Pravec, P. Scheirich, R. Rose, R. F. Jurgens, E. M. De Jong, and S. Suzuki (2006). “Radar Imaging of Binary Near-Earth Asteroid (66391) 1999 KW₄”. *Science* 314.5803, pp. 1276–1280. DOI: 10.1126/science.1133622.
- Pajola, M., O. S. Barnouin, A. Lucchetti, M. Hirabayashi, R.-L. Ballouz, E. Asphaug, C. M. Ernst, V. D. Corte, T. Farnham, G. Poggiali, J. M. Sunshine, E. M. Epifani, N. Murdoch, S. Ieva, S. R. Schwartz, S. Ivanovski, J. M. Trigo-Rodríguez, A. Rossi, N. L. Chabot, A. Zinzi, A. Rivkin, J. R. Brucato, P. Michel, G. Cremonese, E. Dotto, M. Amoroso, I. Bertini, A. Cappanolo, A. Cheng, B. Cotugno, M. Dall’Ora, R. T. Daly, V. D. Tana, J. D. P. Deshapriya, I. Gai, P. H. A. Hasselmann, G. Impresario, M. Lavagna, A. Meneghin, F. Miglioretti, D. Modenini, P. Palumbo, D. Perna, S. Pirrotta, E. Simioni, S. Simonetti, P. Tortora, M. Zannoni, and G. Zanotti (2022). “Anticipated Geological Assessment of the (65803) Didymos–Dimorphos System, Target of the DART–LICIACube Mission”. *The Planetary Science Journal* 3.9, p. 210. DOI: 10.3847/psj/ac880d.
- Pazouki, A., M. Kwarta, K. Williams, W. Likos, R. Serban, P. Jayakumar, and D. Negrut (2017). “Compliant contact versus rigid contact: A comparison in the context of granular dynamics”. *Physical Review E* 96.4, 042905, p. 042905. DOI: 10.1103/PhysRevE.96.042905.
- Popova, O. P., P. Jenniskens, V. Emel’yanenko, A. Kartashova, E. Biryukov, S. Khaibrakhmanov, V. Shuvalov, Y. Rybnov, A. Dudorov, V. I. Grokhovsky, D. D. Badyukov, Q.-Z. Yin, P. S. Gu-

- ral, J. Albers, M. Granvik, L. G. Evers, J. Kuiper, V. Kharlamov, A. Solovyov, Y. S. Rusakov, S. Korotkiy, I. Serdyuk, A. V. Korochantsev, M. Y. Larionov, D. Glazachev, A. E. Mayer, G. Gisler, S. V. Gladkovsky, J. Wimpenny, M. E. Sanborn, A. Yamakawa, K. L. Verosub, D. J. Rowland, S. Roeske, N. W. Botto, J. M. Friedrich, M. E. Zolensky, L. Le, D. Ross, K. Ziegler, T. Nakamura, I. Ahn, J. I. Lee, Q. Zhou, X.-H. Li, Q.-L. Li, Y. Liu, G.-Q. Tang, T. Hiroi, D. Sears, I. A. Weinstein, A. S. Vokhmintsev, A. V. Ishchenko, P. Schmitt-Kopplin, N. Hertkorn, K. Nagao, M. K. Haba, M. Komatsu, T. Mikouchi, and aff34 (2013). “Chelyabinsk Airburst, Damage Assessment, Meteorite Recovery, and Characterization”. *Science* 342.6162, pp. 1069–1073. DOI: 10.1126/science.1242642.
- Pravec, P. and G. Hahn (1997). “Two-Period Lightcurve of 1994 AW₁: Indication of a Binary Asteroid?” *Icarus* 127.2, pp. 431–440. DOI: 10.1006/icar.1997.5703.
- Pravec, P., M. Wolf, and L. Šarounová (1998). “Occultation/Eclipse Events in Binary Asteroid 1991 VH”. *Icarus* 133.1, pp. 79–88. DOI: 10.1006/icar.1998.5890.
- Pravec, P., M. Wolf, and L. Šarounová (1999). “How many binaries are there among the near-Earth asteroids?” In: *IAU Colloq. 173: Evolution and Source Regions of Asteroids and Comets*. Ed. by J. Svoren, E. M. Pittich, and H. Rickman, p. 159.
- Pravec, P. and A. W. Harris (2000). “Fast and Slow Rotation of Asteroids”. *Icarus* 148.1, pp. 12–20. DOI: 10.1006/icar.2000.6482.
- Pravec, P., L. A. M. Benner, M. C. Nolan, P. Kusnirak, D. Pray, J. D. Giorgini, R. F. Jurgens, S. J. Ostro, J. -. Margot, C. Magri, A. Grauer, and S. Larson (2003). “(65803) 1996 GT”. *International Astronomical Union Circular* 8244, p. 2.
- Pravec, P., P. Scheirich, P. Kušnirák, L. Šarounová, S. Mottola, G. Hahn, P. Brown, G. Esquerdo, N. Kaiser, Z. Krzeminski, D. P. Pray, B. D. Warner, A. W. Harris, M. C. Nolan, E. S. Howell, L. A. M. Benner, J. -. Margot, A. Galád, W. Holliday, M. D. Hicks, Y. N. Krugly, D. Tholen, R. Whiteley, F. Marchis, D. R. DeGraff, A. Grauer, S. Larson, F. P. Velichko, W. R. Cooney, R. Stephens, J. Zhu, K. Kirsch, R. Dyvig, L. Snyder, V. Reddy, S. Moore, Š. Gajdoš, J. Világi, G. Masi, D. Higgins, G. Funkhouser, B. Knight, S. Slivan, R. Behrend, M. Grenon, G. Burki, R. Roy, C. Demeautis, D. Matter, N. Waelchli, Y. Revaz, A. Klotz, M. Rieugné, P. Thierry, V. Cotrez, L. Brunetto, and G. Kober (2006). “Photometric survey of binary near-Earth asteroids”. *Icarus* 181.1, pp. 63–93. DOI: 10.1016/j.icarus.2005.10.014.
- Pravec, P. and A. W. Harris (2007). “Binary asteroid population. 1. Angular momentum content”. *Icarus* 190.1, pp. 250–259. DOI: 10.1016/j.icarus.2007.02.023.
- Pravec, P., P. Scheirich, P. Kušnirák, K. Hornoch, A. Galád, S. P. Naidu, D. P. Pray, J. Világi, Š. Gajdoš, L. Kornoš, Y. N. Krugly, W. R. Cooney, J. Gross, D. Terrell, N. Gaftonyuk, J. Pollock, M. Husárik, V. Chiorny, R. D. Stephens, R. Durkee, V. Reddy, R. Dyvig, J. Vraštil, J. Žížka, S. Mottola, S. Hellmich, J. Oey, V. Benishek, A. Kryszczyńska, D. Higgins, J. Ries, F. Marchis, M. Baek, B. Macomber, R. Inasaridze, O. Kvaratskhelia, V. Ayvazian, V. Rummyantsev, G. Masi, F. Colas, J. Lecacheux, R. Montaignut, A. Leroy, P. Brown, Z. Krzeminski, I. Molotov, D. Reichart, J. Haislip, and A. LaCluyze (2016). “Binary asteroid population. 3. Secondary

- rotations and elongations”. *Icarus* 267, pp. 267–295.
DOI: 10.1016/j.icarus.2015.12.019.
- Pravec, P., C. A. Thomas, A. S. Rivkin, P. Scheirich, N. Moskovitz, M. M. Knight, C. Snodgrass, J. de León, J. Licandro, M. Popescu, A. Thirouin, D. Föhring, C. O. Chandler, W. J. Oldroyd, C. A. Trujillo, E. S. Howell, S. F. Green, J. Thomas-Osip, S. S. Sheppard, T. L. Farnham, E. M. Epifani, E. Dotto, S. Ieva, M. Dall’Ora, R. Kokotanekova, B. Carry, and D. Souami (2022). “Photometric Observations of the Binary Near-Earth Asteroid (65803) Didymos in 2015–2021 Prior to DART Impact”. *The Planetary Science Journal* 3.7, p. 175.
DOI: 10.3847/psj/ac7be1.
- Quillen, A. C., A. LaBarca, and Y. Chen (2022a). “Non-principal axis rotation in binary asteroid systems and how it weakens the BYORP effect”. *Icarus* 374, 114826, p. 114826.
DOI: 10.1016/j.icarus.2021.114826.
- Quillen, A. C., M. Neiderbach, B. Suo, J. South, E. Wright, N. Skerrett, P. Sánchez, F. D. Cúñez, P. Miklavcic, and H. Askari (2022b). “Propagation and attenuation of pulses driven by low velocity normal impacts in granular media”. *Icarus* 386, p. 115139. ISSN: 0019-1035.
DOI: <https://doi.org/10.1016/j.icarus.2022.115139>.
- Raducan, S., M. Jutzi, T. Davison, M. DeCoster, D. Graninger, J. Owen, A. Stickle, and G. Collins (2022). “Influence of the projectile geometry on the momentum transfer from a kinetic impactor and implications for the DART mission”. *International Journal of Impact Engineering* 162, p. 104147. ISSN: 0734-743X.
DOI: <https://doi.org/10.1016/j.ijimpeng.2021.104147>.
- Raducan, S. D. and M. Jutzi (2022). “Global-scale Reshaping and Resurfacing of Asteroids by Small-scale Impacts, with Applications to the DART and Hera Missions”. *The Planetary Science Journal* 3.6, 128, p. 128. DOI: 10.3847/PSJ/ac67a7.
- Richardson, D. C., W. F. Bottke, and S. G. Love (1998). “Tidal Distortion and Disruption of Earth-Crossing Asteroids”. *Icarus* 134.1, pp. 47–76. DOI: 10.1006/icar.1998.5954.
- Richardson, D. C., T. Quinn, J. Stadel, and G. Lake (2000). “Direct Large-Scale N-Body Simulations of Planetesimal Dynamics”. *Icarus* 143.1, pp. 45–59.
DOI: 10.1006/icar.1999.6243.
- Richardson, D. C. and K. J. Walsh (2006). “Binary Minor Planets”. *Annual Review of Earth and Planetary Sciences* 34, pp. 47–81.
DOI: 10.1146/annurev.earth.32.101802.120208.
- Richardson, D. C., P. Michel, K. J. Walsh, and K. W. Flynn (2009). “Numerical simulations of asteroids modelled as gravitational aggregates with cohesion”. *Planetary and Space Science* 57.2, pp. 183–192. DOI: 10.1016/j.pss.2008.04.015.
- Richardson, D. C., H. F. Agrusa, B. Barbee, W. F. Bottke, A. F. Cheng, S. Eggl, F. Ferrari, M. Hirabayashi, Ö. Karatekin, J. McMahon, S. R. Schwartz, R.-L. Ballouz, A. C. Bagatin, E. Dotto, E. G. Fahnestock, O. Fuentes-Muñoz, I. Gkolias, D. P. Hamilton, S. A. Jacobson, M. Jutzi, J. Lyzhoft, R. Makadia, A. J. Meyer, P. Michel, R. Nakano, G. Noiset, S. D. Raducan,

- N. Rambaux, A. Rossi, P. Sánchez, D. J. Scheeres, S. Soldini, A. M. Stickle, P. Tanga, K. Tsiganis, and Y. Zhang (2022). “Predictions for the Dynamical States of the Didymos System before and after the Planned DART Impact”. *The Planetary Science Journal* 3.7, p. 157. DOI: 10.3847/psj/ac76c9.
- Richardson, J. E. and T. J. Bowling (2014). “Investigating the combined effects of shape, density, and rotation on small body surface slopes and erosion rates”. *Icarus* 234, pp. 53–65. DOI: 10.1016/j.icarus.2014.02.015.
- Richardson, J. E., K. J. Graves, A. W. Harris, and T. J. Bowling (2019). “Small body shapes and spins reveal a prevailing state of maximum topographic stability”. *Icarus* 329, pp. 207–221. DOI: 10.1016/j.icarus.2019.03.027.
- Richardson, J. E., J. K. Steckloff, and D. A. Minton (2020). “Impact-produced seismic shaking and regolith growth on asteroids 433 Eros, 2867 Šteins, and 25143 Itokawa”. *Icarus* 347, 113811, p. 113811. DOI: 10.1016/j.icarus.2020.113811.
- Ritter, B., Ö. Karatekin, J. A. Carrasco, M. Noeker, E. Ümit, E. Van Ransbeek, H. Alaves, E. Tasev, M. Goli, and M. Van Ruymbeke (2021). “Surface Gravimetry on Dimorphos with GRASS on Juventas”. In: *7th IAA Planetary Defense Conference*, 190, p. 190.
- Rivkin, A. S., N. L. Chabot, A. M. Stickle, C. A. Thomas, D. C. Richardson, O. Barnouin, E. G. Fahnestock, C. M. Ernst, A. F. Cheng, S. Chesley, S. Naidu, T. S. Statler, B. Barbee, H. Agrusa, N. Moskovitz, R. Terik Daly, P. Pravec, P. Scheirich, E. Dotto, V. Della Corte, P. Michel, M. Küppers, J. Atchison, and M. Hirabayashi (2021). “The Double Asteroid Redirection Test (DART): Planetary Defense Investigations and Requirements”. *The Planetary Science Journal* 2.5, 173, p. 173. DOI: 10.3847/PSJ/ac063e.
- Roche, E. (1847). *Acad. Sci. Lett. Montpellier. Mem. Section Sci.* 1, pp. 243–262.
- Rossi, A., F. Marzari, and P. Farinella (1999). “Orbital evolution around irregular bodies”. *Earth, Planets and Space* 51, pp. 1173–1180. DOI: 10.1186/BF03351592.
- Rubincam, D. P. (2000). “Radiative Spin-up and Spin-down of Small Asteroids”. *Icarus* 148.1, pp. 2–11. DOI: 10.1006/icar.2000.6485.
- Sarafian, A. R., S. G. Nielsen, H. R. Marschall, F. M. McCubbin, and B. D. Monteleone (2014). “Early accretion of water in the inner solar system from a carbonaceous chondrite-like source”. *Science* 346.6209, pp. 623–626. DOI: 10.1126/science.1256717.
- Schaub, H., J. L. Junkins, and J. A. Schetz (2009). *Analytical Mechanics of Space Systems, Second Edition*.
- Scheeres, D. J. (1994). “Dynamics about Uniformly Rotating Triaxial Ellipsoids: Applications to Asteroids”. *Icarus* 110.2, pp. 225–238. DOI: 10.1006/icar.1994.1118.
- Scheeres, D. J., F. Marzari, L. Tomasella, and V. Vanzani (1998). “ROSETTA mission: satellite orbits around a cometary nucleus”. *Planetary and Space Science* 46.6, pp. 649–671. DOI: 10.1016/S0032-0633(97)00200-6.

- Scheeres, D. J., E. G. Fahnestock, S. J. Ostro, J. -. Margot, L. A. M. Benner, S. B. Broschart, J. Bellerose, J. D. Giorgini, M. C. Nolan, C. Magri, P. Pravec, P. Scheirich, R. Rose, R. F. Jurgens, E. M. De Jong, and S. Suzuki (2006). “Dynamical Configuration of Binary Near-Earth Asteroid (66391) 1999 KW4”. *Science* 314.5803, pp. 1280–1283. DOI: 10.1126/science.1133599.
- Scheeres, D. J. (2006). “Relative Equilibria for General Gravity Fields in the Sphere-Restricted Full 2-Body Problem”. *Celestial Mechanics and Dynamical Astronomy* 94.3, pp. 317–349. DOI: 10.1007/s10569-005-6182-2.
- Scheeres, D. J. (2007). “Rotational fission of contact binary asteroids”. *Icarus* 189.2, pp. 370–385. DOI: 10.1016/j.icarus.2007.02.015.
- Scheeres, D. J. (2009). “Stability of the planar full 2-body problem”. *Celestial Mechanics and Dynamical Astronomy* 104.1-2, pp. 103–128. DOI: 10.1007/s10569-009-9184-7.
- Scheirich, P. and P. Pravec (2009). “Modeling of lightcurves of binary asteroids”. *Icarus* 200.2, pp. 531–547. DOI: 10.1016/j.icarus.2008.12.001.
- Scheirich, P., P. Pravec, S. A. Jacobson, J. Ďurech, P. Kušnirák, K. Hornoch, S. Mottola, M. Mommert, S. Hellmich, D. Pray, D. Polishook, Y. N. Krugly, R. Y. Inasaridze, O. I. Kvaratskhelia, V. Ayvazian, I. Slyusarev, J. Pittichová, E. Jehin, J. Manfroid, M. Gillon, A. Galád, J. Pollock, J. Licandro, V. Alí-Lagoa, J. Brinsfield, and I. E. Molotov (2015). “The binary near-Earth Asteroid (175706) 1996 FG₃ - An observational constraint on its orbital evolution”. *Icarus* 245, pp. 56–63. DOI: 10.1016/j.icarus.2014.09.023.
- Scheirich, P., P. Pravec, P. Kušnirák, K. Hornoch, J. McMahon, D. J. Scheeres, D. Čapek, D. P. Pray, H. Kučáková, A. Galád, J. Vraštil, Y. N. Krugly, N. Moskovitz, L. D. Avner, B. Skiff, R. S. McMillan, J. A. Larsen, M. J. Brucker, A. F. Tubbiolo, W. R. Cooney, J. Gross, D. Terrell, O. Burkhonov, K. E. Ergashev, S. A. Ehgamberdiev, P. Fatka, R. Durkee, E. L. Schunova, R. Y. Inasaridze, V. R. Ayvazian, G. Kapanadze, N. M. Gaftonyuk, J. A. Sanchez, V. Reddy, L. McGraw, M. S. Kelley, and I. E. Molotov (2021). “A satellite orbit drift in binary near-Earth asteroids (66391) 1999 KW4 and (88710) 2001 SL9 - Indication of the BYORP effect”. *Icarus* 360, 114321, p. 114321. DOI: 10.1016/j.icarus.2021.114321.
- Scheirich, P. and P. Pravec (2022). “Preimpact Mutual Orbit of the DART Target Binary Asteroid (65803) Didymos Derived from Observations of Mutual Events in 2003–2021”. *The Planetary Science Journal* 3.7, p. 163. DOI: 10.3847/psj/ac7233.
- Schwartz, S. R., D. C. Richardson, and P. Michel (2012). “An implementation of the soft-sphere discrete element method in a high-performance parallel gravity tree-code”. *Granular Matter* 14.3, pp. 363–380. ISSN: 1434-7636. DOI: 10.1007/s10035-012-0346-z.
- Seligman, D. and K. Batygin (2021). “The Onset of Chaos in Permanently Deformed Binaries from Spin-Orbit and Spin-Spin Coupling”. *The Astrophysical Journal* 913.1, 31, p. 31. DOI: 10.3847/1538-4357/abf248.
- Showalter, M. R. and D. P. Hamilton (2015). “Resonant interactions and chaotic rotation of Pluto’s small moons”. *Nature* 522.7554, pp. 45–49. DOI: 10.1038/nature14469.

- Skokos, C. (2010). “The Lyapunov Characteristic Exponents and Their Computation”. In: *Dynamics of Small Solar System Bodies and Exoplanets*. Ed. by J. J. Souchay and R. Dvorak. Berlin, Heidelberg: Springer Berlin Heidelberg, pp. 63–135. ISBN: 978-3-642-04458-8. DOI: 10.1007/978-3-642-04458-8_2.
- Stadel, J. G. (2001). “Cosmological N-body simulations and their analysis”. PhD thesis. University of Washington, United States.
- Statler, T. S. (2009). “Extreme sensitivity of the YORP effect to small-scale topography”. *Icarus* 202.2, pp. 502–513. DOI: 10.1016/j.icarus.2009.03.003.
- Stickle, A. M., M. Bruck Syal, A. F. Cheng, G. S. Collins, T. M. Davison, G. Gisler, N. Gülde-meister, T. Heberling, R. Luther, P. Michel, P. Miller, J. M. Owen, E. S. G. Rainey, A. S. Rivkin, T. Rosch, and K. Wünnemann (2020). “Benchmarking impact hydrocodes in the strength regime: Implications for modeling deflection by a kinetic impactor”. *Icarus* 338, 113446, p. 113446. DOI: 10.1016/j.icarus.2019.113446.
- Stickle, A. M., C. Burger, W. K. Caldwell, M. E. DeCoster, D. Graninger, K. M. Kumamoto, and R. Luther (2022). “Effects of impact and target parameters on the results of a kinetic im-pactor: predictions for the Double Asteroid Redirection Test (DART) mission”. *The Planetary Science Journal* (submitted).
- Sugita, S. et al. (2019). “The geomorphology, color, and thermal properties of Ryugu: Implica-tions for parent-body processes”. *Science* 364.6437, eaaw0422, eaaw0422. DOI: 10.1126/science.aaw0422.
- Susorney, H. C. M. and N. A. Teanby (2022). “Investigating the effects of density and spin period on surface slopes of asteroids”. *Icarus* 380, 114969, p. 114969. DOI: 10.1016/j.icarus.2022.114969.
- Tasora, A., R. Serban, H. Mazhar, A. Pazouki, D. Melanz, J. Fleischmann, M. Taylor, H. Sugiyama, and D. Negrut (2016). “Chrono: An Open Source Multi-physics Dynamics Engine”. In: *High Performance Computing in Science and Engineering*. Ed. by T. Kozubek, R. Blaheta, J. Šístek, M. Rozložník, and M. Čermák. Springer International Publishing, pp. 19–49. ISBN: 978-3-319-40361-8.
- Taylor, P. A., J.-L. Margot, D. Vokrouhlický, D. J. Scheeres, P. Pravec, S. C. Lowry, A. Fitzsim-mons, M. C. Nolan, S. J. Ostro, L. A. M. Benner, J. D. Giorgini, and C. Magri (2007). “Spin Rate of Asteroid (54509) 2000 PH5 Increasing Due to the YORP Effect”. *Science* 316.5822, p. 274. DOI: 10.1126/science.1139038.
- Thomas, P. C. and M. S. Robinson (2005). “Seismic resurfacing by a single impact on the asteroid 433 Eros”. *Nature* 436.7049, pp. 366–369. DOI: 10.1038/nature03855.
- van Flandern, T. C., E. F. Tedesco, and R. P. Binzel (1979). “Satellites of asteroids.” In: *Asteroids*. Ed. by T. Gehrels and M. S. Matthews, pp. 443–465.
- Vavilov, D. E., B. Carry, A. Lagain, A. Guimpier, S. Conway, H. Devillepoix, and S. Bouley (2022). “Evidence for widely-separated binary asteroids recorded by craters on Mars”. *Icarus* 383, 115045, p. 115045. DOI: 10.1016/j.icarus.2022.115045.

- Veillet, C., J. W. Parker, I. Griffin, B. Marsden, A. Doressoundiram, M. Buie, D. J. Tholen, M. Connelley, and M. J. Holman (2002). “The binary Kuiper-belt object 1998 WW31”. *Nature* 416.6882, pp. 711–713. DOI: 10.1038/416711a.
- Virtanen, P., R. Gommers, T. E. Oliphant, M. Haberland, T. Reddy, D. Cournapeau, E. Burovski, P. Peterson, W. Weckesser, J. Bright, et al. (2020). “SciPy 1.0: fundamental algorithms for scientific computing in Python”. *Nature methods* 17.3, pp. 261–272.
- Vokrouhlický, D., W. F. Bottke, S. R. Chesley, D. J. Scheeres, and T. S. Statler (2015). “The Yarkovsky and YORP Effects”. In: *Asteroids IV*, pp. 509–531. DOI: 10.2458/azu_uapress_9780816532131-ch027.
- Walker, J. D., S. Chocron, D. J. Grosch, S. Marchi, and A. M. Alexander (2022). “Momentum Enhancement from a 3 cm Diameter Aluminum Sphere Striking a Small Boulder Assembly at 5.4 km s⁻¹”. *The Planetary Science Journal* 3.9, p. 215. DOI: 10.3847/psj/ac854f.
- Walsh, K. J. and D. C. Richardson (2006). “Binary near-Earth asteroid formation: Rubble pile model of tidal disruptions”. *Icarus* 180.1, pp. 201–216. DOI: 10.1016/j.icarus.2005.08.015.
- Walsh, K. J. and D. C. Richardson (2008). “A steady-state model of NEA binaries formed by tidal disruption of gravitational aggregates”. *Icarus* 193.2, pp. 553–566. DOI: 10.1016/j.icarus.2007.08.020.
- Walsh, K. J., D. C. Richardson, and P. Michel (2008). “Rotational breakup as the origin of small binary asteroids”. *Nature* 454.7201, pp. 188–191. DOI: 10.1038/nature07078.
- Walsh, K. J., D. C. Richardson, and P. Michel (2012). “Spin-up of rubble-pile asteroids: Disruption, satellite formation, and equilibrium shapes”. *Icarus* 220.2, pp. 514–529. DOI: 10.1016/j.icarus.2012.04.029.
- Walsh, K. J. and S. A. Jacobson (2015). “Formation and Evolution of Binary Asteroids”. In: *Asteroids IV*, pp. 375–393. DOI: 10.2458/azu_uapress_9780816532131-ch020.
- Walsh, K. J. (2018). “Rubble Pile Asteroids”. *Annual Review of Astronomy and Astrophysics* 56, pp. 593–624. DOI: 10.1146/annurev-astro-081817-052013.
- Walsh, K. J., E. R. Jawin, R. Ballouz, O. S. Barnouin, E. B. Bierhaus, H. C. Connolly, J. L. Molaro, T. J. McCoy, M. Delbo, C. M. Hartzell, M. Pajola, S. R. Schwartz, D. Trang, E. Asphaug, K. J. Becker, C. B. Beddingfield, C. A. Bennett, W. F. Bottke, K. N. Burke, B. C. Clark, M. G. Daly, D. N. Dellagiustina, J. P. Dworkin, C. M. Elder, D. R. Golish, A. R. Hildebrand, R. Malhotra, J. Marshall, P. Michel, M. C. Nolan, M. E. Perry, B. Rizk, A. Ryan, S. A. Sandford, D. J. Scheeres, H. C. M. Susorney, F. Thuillet, D. S. Lauretta, and Osiris-Rex Team (2019). “Craters, boulders and regolith of (101955) Bennu indicative of an old and dynamic surface”. *Nature Geoscience* 12.4, pp. 242–246. DOI: 10.1038/s41561-019-0326-6.

- Warner, B. D. and A. W. Harris (2007). “Lightcurve Studies of Small Asteroids”. In: *AAS/Division for Planetary Sciences Meeting Abstracts #39*. Vol. 39. AAS/Division for Planetary Sciences Meeting Abstracts, 13.03, p. 13.03.
- Watanabe, S., M. Hirabayashi, N. Hirata, N. Hirata, R. Noguchi, Y. Shimaki, H. Ikeda, E. Tatsu-
sumi, M. Yoshikawa, S. Kikuchi, H. Yabuta, T. Nakamura, S. Tachibana, Y. Ishihara, T. Mo-
rota, K. Kitazato, N. Sakatani, K. Matsumoto, K. Wada, H. Senshu, C. Honda, T. Michikami,
H. Takeuchi, T. Kouyama, R. Honda, S. Kameda, T. Fuse, H. Miyamoto, G. Komatsu, S.
Sugita, T. Okada, N. Namiki, M. Arakawa, M. Ishiguro, M. Abe, R. Gaskell, E. Palmer, O. S.
Barnouin, P. Michel, A. S. French, J. W. McMahan, D. J. Scheeres, P. A. Abell, Y. Yamamoto,
S. Tanaka, K. Shirai, M. Matsuoka, M. Yamada, Y. Yokota, H. Suzuki, K. Yoshioka, Y. Cho,
S. Tanaka, N. Nishikawa, T. Sugiyama, H. Kikuchi, R. Hemmi, T. Yamaguchi, N. Ogawa,
G. Ono, Y. Mimasu, K. Yoshikawa, T. Takahashi, Y. Takei, A. Fujii, C. Hirose, T. Iwata, M.
Hayakawa, S. Hosoda, O. Mori, H. Sawada, T. Shimada, S. Soldini, H. Yano, R. Tsukizaki,
M. Ozaki, Y. Iijima, K. Ogawa, M. Fujimoto, T. -. Ho, A. Moussi, R. Jaumann, J. -. Bib-
ring, C. Krause, F. Terui, T. Saiki, S. Nakazawa, and Y. Tsuda (2019). “Hayabusa2 arrives
at the carbonaceous asteroid 162173 Ryugu—A spinning top-shaped rubble pile”. *Science*
364.6437, pp. 268–272. DOI: 10.1126/science.aav8032.
- Weaver, H. A., P. D. Feldman, M. F. A’Hearn, C. Arpigny, R. A. Brown, E. F. Helin, D. H. Levy,
B. G. Marsden, K. J. Meech, S. M. Larson, K. S. Noll, J. V. Scotti, Z. Sekanina, C. S. Shoemaker,
E. M. Shoemaker, T. E. Smith, A. D. Storrs, D. K. Yeomans, and B. Zellner (1994).
“Hubble Space Telescope Observations of Comet P/Shoemaker-Levy 9 (1993e)”. *Science*
263.5148, pp. 787–791. DOI: 10.1126/science.263.5148.787.
- Weidenschilling, S. J., P. Paolicchi, and V. Zappala (1989). “Do asteroids have satellites?” In:
Asteroids II. Ed. by R. P. Binzel, T. Gehrels, and M. S. Matthews, pp. 643–658.
- Werner, R. A. and D. J. Scheeres (1997). “Exterior Gravitation of a Polyhedron Derived and Com-
pared with Harmonic and Mascon Gravitation Representations of Asteroid 4769 Castalia”.
Celestial Mechanics and Dynamical Astronomy 65.3, pp. 313–344.
- Werner, R. A. and D. J. Scheeres (2005). “Mutual Potential of Homogeneous Polyhedra”. *Celestial
Mechanics and Dynamical Astronomy* 91.3-4, pp. 337–349.
DOI: 10.1007/s10569-004-4621-0.
- Wisdom, J., S. J. Peale, and F. Mignard (1984). “The chaotic rotation of Hyperion”. *Icarus* 58.2,
pp. 137–152. DOI: 10.1016/0019-1035(84)90032-0.
- Wisdom, J. (1987a). “Rotational Dynamics of Irregularly Shaped Natural Satellites”. *The Astro-
nomical Journal* 94, p. 1350. DOI: 10.1086/114573.
- Wisdom, J. (1987b). “Urey prize lecture: Chaotic dynamics in the solar system”. *Icarus* 72.2,
pp. 241–275. DOI: 10.1016/0019-1035(87)90175-8.
- Yu, Y., D. C. Richardson, P. Michel, S. R. Schwartz, and R.-L. Ballouz (2014). “Numerical pre-
dictions of surface effects during the 2029 close approach of Asteroid 99942 Apophis”. *Icarus*
242, pp. 82–96. DOI: 10.1016/j.icarus.2014.07.027.

- Yu, Y., B. Cheng, M. Hayabayashi, P. Michel, and H. Baoyin (2019). “A finite element method for computational full two-body problem: I. The mutual potential and derivatives over bilinear tetrahedron elements”. *Celestial Mechanics and Dynamical Astronomy* 131.11, 51, p. 51. DOI: 10.1007/s10569-019-9930-4.
- Zhang, Y., D. C. Richardson, O. S. Barnouin, C. Maurel, P. Michel, S. R. Schwartz, R.-L. Ballouz, L. A. M. Benner, S. P. Naidu, and J. Li (2017). “Creep stability of the proposed AIDA mission target 65803 Didymos: I. Discrete cohesionless granular physics model”. *Icarus* 294, pp. 98–123. DOI: 10.1016/j.icarus.2017.04.027.
- Zhang, Y., D. C. Richardson, O. S. Barnouin, P. Michel, S. R. Schwartz, and R.-L. Ballouz (2018). “Rotational Failure of Rubble-pile Bodies: Influences of Shear and Cohesive Strengths”. *The Astrophysical Journal* 857.1, 15, p. 15. DOI: 10.3847/1538-4357/aab5b2.
- Zhang, Y. and P. Michel (2020). “Tidal distortion and disruption of rubble-pile bodies revisited”. *Astronomy & Astrophysics* 640, A102. DOI: 10.1051/0004-6361/202037856.
- Zhang, Y., P. Michel, D. C. Richardson, O. S. Barnouin, H. F. Agrusa, K. Tsiganis, C. Manzoni, and B. H. May (2021). “Creep stability of the DART/Hera mission target 65803 Didymos: II. The role of cohesion”. *Icarus* 362, 114433, p. 114433. DOI: 10.1016/j.icarus.2021.114433.